

Linear Parameter-Varying Control of Full-Vehicle Vertical Dynamics
using Semi-Active Dampers

M.Sc. Michael Fleps-Dezasse

Vollständiger Abdruck der von der Fakultät für Luft- und Raumfahrttechnik der Universität der Bundeswehr München zur Erlangung des akademischen Grades eines

Doktor-Ingenieurs (Dr.-Ing.)

genehmigten Dissertation.

Gutachter/Gutachterin:

1. Univ.-Prof. Dr.-Ing. Ferdinand
Svaricek
2. Univ.-Prof. Dr.-Ing. Herbert
Werner

Die Dissertation wurde am 17.11.2017 bei der Universität der Bundeswehr München eingereicht und durch die Fakultät für Luft- und Raumfahrttechnik am 08.05.2018 angenommen. Die mündliche Prüfung fand am 29.05.2018 statt.

Acknowledgment

The last six year at the Institute of System Dynamics and Control (SR) of the German Aerospace Center (DLR) in Oberpfaffenhofen have been an exciting and valuable experience. This time has been a great benefit for my personal development not only because I could develop profound skills in automatic control and vehicle dynamics, but also because of the magnificent team work within the department. I would like to thank all those who have made this possible.

First, I would like to thank Dr. Johann Bals, the institute director of SR, and Jonathan Brembeck, my department leader, for providing excellent conditions for scientific work and their financial support throughout my stay at the DLR.

Second, I would like to thank Professor Ferdinand Svaricek, my advisor, for his insight and suggestions regarding control theory and his detailed feedback regarding my scientific work. I would also like to thank Professor Werner, my second advisor, especially for his valuable comments on LPV theory and nonlinear systems in general.

At my department, I would like to thank Dr. Tilman Bunte and Dr. Ricardo de Castro for their consistent encouragement and many fruitful discussions. In particular, the reviews of my articles and of my thesis prepared by Dr. Ricardo de Castro significantly improved the quality of my work. The ROboMObil project at SR has been the one big thing that took a lot of time during my stay at the DLR. Nevertheless, working with the enthusiastic ROMO team has been great fun! Therefore, I would like to sincerely thank Dr. Lok Man Ho, Dr. Clemens Satzger, Dr. Alexander Schaub, Michael Panzirsch, Daniel Baumgartner, Christoph Winter, Johannes Ultsch and Peter Ritzer.

The cooperation with KW automotive has been the enabler for the experimental part of my work and I would like to thank Michael Rohn and Thomas Wurst of KW automotive for a great and successful cooperation. Moreover, I would like to thank Uwe Bleck for his advice on vehicle dynamics and his great job as our test driver. I would also like to thank the Central Innovation Management for Small and Medium Sized Enterprises for its financial support.

I address my special thanks to my parent, Michael Fleps and Elfriede Katharina Fleps, for their consistent emotional support and their imperturbable belief in my ability to accomplish this thesis. Last, I would like to express my deepest gratitude to my wife Bernadette Dezasse for her abundant love, her unending patience and support, and the many evenings I could not spend with her but at the desk preparing this thesis.

Kurzfassung

Semi-aktive Fahrwerke bergen im Vergleich zu passiven großes Potential zur Verbesserung wesentlicher Fahrzeugeigenschaften, wie Fahrkomfort, Straßenhaftung und Fahrverhalten. Die Ausnutzung dieses Potentials verlangt nach geeigneten Regelungsalgorithmen, welche das nichtlineare Eingangssignal-zu-Dämpferkraft Verhalten und die Passivitätsbeschränkung semi-aktiver Dämpfer berücksichtigen. Im Besonderen die Passivitätsbeschränkung impliziert enge, zustandsabhängige Aktuatorkraftbegrenzungen und sollte daher im Regelungsentwurf direkt berücksichtigt werden. Der Entwurf performanter semi-aktiver Fahrwerkregelungen stellt eine große Herausforderung dar, da Störungen aufgrund von Straßenunebenheiten und Lastwechseln unterschiedliche Anforderungen an die Regelung stellen, und zusätzlich in einer Gesamtfahrzeuganwendung auch ein Regelungsentwurf basierend auf einem Gesamtfahrzeugmodell benötigt wird.

Im Gegensatz zu konventionellen viertelfahrzeug-basierten Fahrwerkregelungsansätzen, welche häufig in der Literatur zu finden sind, zielt der Gesamtfahrzeugregelungsansatz dieser Dissertation auf die explizite Berücksichtigung der Hub-, Wank und Nickbewegung des Aufbaus. Darüber hinaus ermöglicht der Gesamtfahrzeugansatz die Entwicklung von fehlertoleranten Reglern, welche die schwache Aktuatorredundanz der vier Dämpfer nutzen. Die vorliegende Dissertation befasst sich mit linear parameter-variablen (LPV) Regelungsmethoden zur Lösung des oben beschriebenen komplexen Regelungsproblems. Die Kraftbegrenzungen der semi-aktiven Dämpfer werden mittels Sättigungsindikatoren modelliert und diese dann als variable Parameter in den LPV Regelungsentwurf integriert. Zusätzlich wird der LPV Regler um eine Dämpferkraftrekonfiguration erweitert, so dass der Regler den Dämpferkraftverlust im Falle einer Dämpferfehlfunktion mit den verbleibenden gesunden Dämpfern kompensiert. Der Regelungsentwurf begegnet den unterschiedlichen Anforderungen von Straßen- und Lastwechselstörungen durch eine Zweifreiheitsgradregelung bestehend aus einem LPV Regler und einer LPV Vorsteuerung. Dabei fokussiert sich der LPV Regler auf die Verminderung des Effekts der Straßenunebenheiten und die LPV Vorsteuerung verringert den Effekt der Lastwechselstörungen. Auf diese Weise zeigt die Zweifreiheitsgradregelung das gewünschte Verhalten trotz dieser beiden konträren Störungen.

Die Wirksamkeit der vorgeschlagenen Zweifreiheitsgradregelung wird durch Experimente auf einem Stempelprüfstand und durch Straßenversuche validiert. Die Ergebnisse zeigen eine Verbesserung des klassischen Zielkonflikts der Fahrwerksregelung zwischen Fahrkomfort und Straßenhaftung durch die LPV Gesamtfahrzeugregelung. Insbesondere erzielt die LPV Gesamtfahrzeugregelung eine 10 % ige Verbesserung von Fahrkomfort und Straßenhaftung im Vergleich zu einer Skyhook-Groundhook Gesamtfahrzeugregelung. Des Weiteren verdeutlicht ein Experiment mit einem simulierten Dämpferfehler die Vorteile der fehlertoleranten LPV Regelung. Abschließend wird anhand von Spurwechselversuchen die Wirksamkeit der LPV Vorsteuerung zur Verbesserung von Fahrkomfort, Straßenhaftung und Fahrverhalten bei dynamischen Lenkwinkleingaben des Fahrers demonstriert.

Abstract

Semi-active suspensions offer a large potential to improve essential vehicle properties like ride comfort, road-holding and vehicle handling compared to passive suspensions. The exploitation of this potential relies on suitable semi-active suspension control algorithms which consider the nonlinear control signal to damper force characteristic and the passivity constraint of the semi-active damper. In particular, the passivity constraint introduces a restrictive state-dependent actuator force limitation and should be explicitly considered during the control design. The design of high-performance semi-active damper controllers constitutes a challenging task due to the different requirements of an optimal control design regarding road disturbances and load disturbances induced by the driver inputs, and the needed full-vehicle control approach to realize the performance potential of vehicles equipped with semi-active suspensions.

In contrast to the conventional quarter-vehicle based suspension control approaches commonly found in the literature, the full-vehicle control approach proposed in this dissertation aims at taking into account the body heave, roll and pitch motions. Moreover, the full-vehicle control approach facilitates the development of active fault-tolerant controllers by exploring the weak input redundancy provided by four semi-active dampers. The dissertation addresses this complex control problem by linear-parameter varying (LPV) control methods. The force constraints of the semi-active damper are modeled by saturation indicators and these are treated as scheduling parameters in the LPV design. Additionally, the LPV controller is augmented by a damper force reconfiguration such that the controller compensates for the damper force loss in case of saturation or failure by the remaining healthy dampers. The different requirements of an optimal control design regarding road disturbances and driver-induced disturbances are met by a two-degree-of-freedom control approach comprised of an LPV feedback controller and an LPV feedforward filter. The LPV feedback controller focuses on the attenuation of road disturbances, while the LPV feedforward filter reduces the effect of driver-induced disturbances. In this way, the two-degree-of-freedom control provides good performance regarding both disturbances.

The effectiveness of the proposed two-degree-of-freedom LPV controller is validated by experiments on a four-post test-rig and by road tests. The results show the improved trade-off between ride comfort and road-holding of the full-vehicle LPV controller. In particular, the full-vehicle LPV controller achieves a 10 % improvement of ride comfort and road-holding compared to a full-vehicle Skyhook-Groundhook controller. Furthermore, an experiment with an assumed damper failure emphasizes the benefit of the active fault-tolerant full-vehicle LPV controller. Finally, the results of the double lane change manoeuvres performed during the road tests illustrate the enhanced ride comfort and handling properties of the vehicle with two-degree-of-freedom LPV control compared to the set-up without feedforward filter.

Contents

List of Figures	XI
List of Tables	XV
List of Symbols	XVII
1 Introduction	1
1.1 State-of-the-Art in Semi-Active Damper Control	5
1.1.1 Skyhook Control	5
1.1.2 Groundhook Control	6
1.1.3 Clipped Control	6
1.1.4 Model-Predictive Control	7
1.1.5 Linear Parameter-Varying Control	7
1.1.6 Vertical Dynamics Vehicle Models	8
1.1.7 Experimental Validation	9
1.2 Linear Parameter-Varying Control	11
1.3 Control Design Methodology	13
1.4 Problem Statement and Contribution	15
1.5 Outline	18
2 LPV Control with Actuator Constraints	19
2.1 Definition of LPV Systems	19
2.2 Basics of LPV Control Design	20
2.3 LPV Modeling of Actuator Constraints	21
2.4 LPV Control Design with Actuator Constraints	24
2.5 Saturation Indicator Grid Density Assessment	28
3 Quarter-Vehicle Control Design	31
3.1 Quarter-Vehicle Control Structure	31
3.2 Performance Criteria	32
3.3 LTI Quarter-Vehicle Model	34
3.4 Skyhook-Groundhook Control	38
3.5 Quarter-Vehicle LPV Control Design	39
3.5.1 State-Observer Design	41
3.5.2 DI Controller Design	44
3.6 Multi-Objective Controller Tuning	50
3.7 Simulation Results	52
3.8 Experimental Results	53
3.9 Discussion and Conclusion	54

4	Full-Vehicle Control Design	56
4.1	Full-Vehicle Control Structure	58
4.2	Performance Criteria	58
4.3	LTI Full-Vehicle Model	60
4.4	Full-Vehicle Skyhook-Groundhook Controller	63
4.5	Full-Vehicle LPV Control Design	64
4.5.1	State-Observer Design	66
4.5.2	DI Controller Design	67
4.6	Fault-Tolerant Control Augmentation	71
4.6.1	Stability of the Nominal Controller	72
4.6.2	Augmentation of the Nominal Controller	72
4.6.3	Verification of the Augmented Controller	76
4.7	Multi-Objective Controller Tuning	79
4.8	Four-Post Test-Rig Experiments	85
4.8.1	Experiments without Damper Malfunction	86
4.8.2	Experiments with Damper Malfunction	93
4.9	Discussion and Conclusion	94
5	Roll Disturbance Feedforward Control	97
5.1	Roll Disturbance Feedforward Control Structure	98
5.2	Vehicle Model with Roll Disturbance Input	99
5.3	Roll Disturbance Feedforward Control Design	100
5.4	Simulation Results	105
5.5	Experimental Results	108
5.6	Discussion and Conclusion	112
6	Conclusion and Outlook	113
6.1	Conclusion	113
6.2	Outlook and Future Work	114
	Appendix	117
A	LPV Control Design	117
A.1	Definition of LPV Systems	117
A.2	Stability of LPV Systems	118
A.2.1	Quadratic Lyapunov Stability	119
A.2.2	Parameter-Dependent Lyapunov Stability	119
A.3	Induced L_2 -Norm Performance	120
A.4	LPV Controller Synthesis	122
A.4.1	State-Feedback Problem	125
A.4.2	State-Observer Problem	127

A.4.3	Separation Principle	129
A.4.4	Special Control Problem: Disturbance-Information	130
A.4.5	Special Control Problem: Full-Information	134
A.4.6	Computational Considerations	136
B	Semi-Active Force Actuator	138
B.1	Semi-Active Damper Technology	139
B.2	Semi-Active Damper Model	140
B.3	Inverse Semi-Active Damper Model	143
B.4	Results of Semi-Active Damper Model Assessment	145
C	Vertical Dynamics Road Excitations	147
C.1	Stochastic Road Excitation	147
C.2	Sine Sweep Excitation	148
D	The Quarter-Vehicle Test-Rig	150
D.1	Hardware and Software Setup	150
D.2	Modeling and Simulation	152
E	The SC3-Bulli Experimental Vehicle	154
E.1	Hardware and Software Setup	154
E.2	Modeling and Simulation	155
F	Estimation of the Roll Disturbance Moment	158
G	Gain-Scheduled H_∞ Control vs LPV Control	161
G.1	γ -Performance Level Comparison	161
G.2	Ride Comfort and Road-holding Performance Comparison	162
H	Robust Performance of the Full-Vehicle LPV Controller	164
I	Implementation in Simulink	165
	References	169

List of Figures

1.1	Schematic Pareto diagram of the trade-off between ride comfort and road-holding	2
1.2	Example of force characteristic of passive damper and set of admissible semi-active damper forces	3
1.3	Overview of functions of vertical dynamics control algorithms	4
1.4	<i>SC3-Bulli</i> experimental vehicle of SR on four-post test-rig	5
1.5	Comparison of LPV control to gain-scheduled control	11
1.6	<i>Design-by-Simulation</i> methodology	13
1.7	Two degree-of-freedom control configuration	15
1.8	Structure of the thesis	18
2.1	General control configuration	21
2.2	Closed-loop of plant with actuator constraints and controller	22
2.3	Types of control signal constraints	23
2.4	Structure of LPV controller without saturation indicator dependent weighting filters	25
2.5	Structure of LPV controller with proposed saturation indicator dependent weighting filters	26
2.6	Spring-mass system used to illustrate the advantages of the proposed control effort weight	27
2.7	LPV control design example emphasizing the advantages of the proposed control effort weight	28
3.1	Disturbance-Information structure of quarter-vehicle LPV controller	32
3.2	Sketch of the quarter-vehicle model	34
3.3	Waterbed effect of frequency responses of quarter-vehicle subject to road disturbances due to variation of damping coefficient	36
3.4	Effect of tire damping on frequency responses of quarter-vehicle with suspension force input	37
3.5	Control structure of quarter-vehicle semi-active suspension control	40
3.6	Transformation of actuator force limits by time-varying nominal damping coefficient called saturation transformer	41
3.7	Weighting scheme of quarter-vehicle state-observer design	42
3.8	General control configuration of quarter-vehicle state-observer problem . .	43
3.9	Mixed sensitivity weighting scheme of quarter-vehicle LPV controller design	44
3.10	Open-loop frequency responses of plant from road disturbance input to: body motion, wheel motion, and dynamic wheel load	48
3.11	Saturation indicator dependence of weighting filters	49
3.12	Process diagram of multi-objective controller tuning	51
3.13	Sine-sweep simulation: PSD of body acceleration, dynamic wheel load and damper velocity	53

3.14	Stochastic road simulation according to ISO (8608:1995) road type D at a vehicle speed of 100 km/h: ride comfort, road-holding and damper deflection	53
3.15	Sine-sweep simulation: control signal over time	54
3.16	Sine-sweep experiment: PSD of body acceleration, dynamic wheel load and damper velocity	55
3.17	Stochastic road experiment according to ISO (8608:1995) road type D at a vehicle speed of 100 km/h: ride comfort, road-holding and damper deflection	55
4.1	Interconnection of generalized plant with nominal controller (left) and re-configured controller (right)	57
4.2	Disturbance-Information structure of full-vehicle LPV controller	58
4.3	Directions of comfort assessment defined by ISO 2631-1:1997	59
4.4	Weighting filters of translational heave acceleration and angular roll and pitch accelerations according to ISO (2631-1:1997)	60
4.5	Sketch of quarter-vehicle model (left) and full-vehicle model (right)	61
4.6	Control structure of full-vehicle semi-active suspension control	64
4.7	Weighting scheme of full-vehicle state-observer design	66
4.8	Mixed sensitivity weighting scheme of full-vehicle Disturbance-Information controller design	68
4.9	Left - structure of the nominal controller without force reconfiguration; right - structure of the augmented controller with force reconfiguration . .	73
4.10	Results of sweep simulations with damper failure:body heave, body roll, body pitch and normalized control signals	78
4.11	Effect of sample time on ride comfort and road-holding performance of SH/GH controller	81
4.12	Result of Pareto optimization of ride comfort and road-holding with non-linear full-vehicle model subject to stochastic road excitation	82
4.13	Normalized frequency responses of open-loop and closed-loop with full-vehicle from road disturbance to: body heave velocity, body roll velocity and body pitch velocity	83
4.14	Normalized frequency responses of open-loop and closed-loop with full-vehicle from heave road disturbance to wheel velocity	83
4.15	Normalized frequency responses of open-loop and closed-loop with full-vehicle from disturbances to body heave velocity	84
4.16	Normalized frequency responses of open-loop and closed-loop with full-vehicle from disturbance to: body roll velocity and body pitch velocity . .	85
4.17	Normalized frequency responses of open-loop and closed-loop with full-vehicle from disturbance to wheel velocity	85
4.18	Normalized frequency responses of open-loop and closed-loop with full-vehicle from heave acceleration disturbance to control signal	86
4.19	Frequency response of body heave acceleration of experimental vehicle subject to heave sweep excitation	87

4.20	Frequency response of dynamic wheel load of experimental vehicle subject to heave sweep excitation	88
4.21	Frequency response of damper velocity of experimental vehicle subject to heave sweep excitation	88
4.22	Post displacements stochastic road, Spanish bumps and country road with long-wave bump excitation	89
4.23	Post displacement and body accelerations of experimental vehicle subject to large bump excitation	91
4.24	Dynamic wheel load of experimental vehicle subject to large bump excitation	91
4.25	Damper velocities of experimental vehicle subject to large bump excitation	92
4.26	Damper current of experimental vehicle subject to large bump excitation .	92
4.27	Post displacement and body accelerations of experimental vehicle with rear right damper failure subject to large bump excitation	94
4.28	Dynamic wheel load of experimental vehicle with rear right damper failure subject to large bump excitation	95
4.29	Damper current of experimental vehicle with rear right damper failure subject to large bump excitation	95
5.1	Two degree-of-freedom control structure of full-vehicle equipped with four semi-active suspensions	99
5.2	Transfer function from roll disturbance input to angular roll velocity of vehicle body	100
5.3	Two-degree-of-freedom closed-loop interconnection	102
5.4	Weighting scheme of feedforward control design	104
5.5	Frequency response of plant from roll disturbance moment input to angular roll velocity with and without feedforward filter	104
5.6	Simulation of lane change manoeuvre: lateral acceleration, body roll angle and angular velocity	106
5.7	Simulation of lane change manoeuvre: damper velocity	107
5.8	Simulation of lane change manoeuvre: dyn. wheel load	107
5.9	Simulation of lane change manoeuvre: control signal	108
5.10	Experiment set-up ISO (3888-2:2011) lane change	109
5.11	ISO (3888-2:2011) double lane change at a vehicle speed of 50 km/h: lateral acceleration and steering angle	110
5.12	ISO (3888-2:2011) double lane change at a vehicle speed of 50 km/h: body roll angle and angular velocity	111
5.13	ISO (3888-2:2011) double lane change at a vehicle speed of 50 km/h: damper current	111
A.1	Induced L_2 -Norm of LPV system	121
A.2	General control configuration	122
A.3	General control configuration state-feedback problem	126
A.4	General control configuration state-observer problem	128

A.5	General control configuration Disturbance-Information (DI) problem	132
A.6	General control configuration Full-Information (FI) problem	134
A.7	Equivalence of Full-Information controller and Disturbance-Information controller	135
B.1	Conflict triangle of suspension types	138
B.2	Schematic of semi-active dampers with controllable electro-hydraulic valves	140
B.3	Force map of semi-active damper with normalized control signal	142
B.4	Inversion of force map damper model	143
B.5	Control signal map of inverse semi-active damper model	144
B.6	Accuracy of reproducing measurement data of Bouc-Wen and force map damper models for constant control signals	146
B.7	Accuracy of reproducing control signal steps of Bouc-Wen and force map damper models for constant damper velocities	146
C.1	Road profile power spectral density	148
C.2	Illustration of sine sweep excitation with amplitude spectrum similar to stochastic road excitations according to ISO 8608:1995	149
D.1	Quarter-vehicle test-rig of the <i>University of the Federal Armed Forces</i> in Munich	150
D.2	Block diagram illustrating the test-rig operation	152
D.3	Force map of semi-active damper at quarter-vehicle test-rig	153
E.1	Left - suspension spring characteristic, right - semi-active damper charac- teristic of <i>SC3-Bulli</i>	155
E.2	Left - damper deflection over vertical wheel position, right - height sensor output over vertical wheel position	156
F.1	Estimation error of single-track model with parameters according to Table F.1 during quasi steady-state cornering at a constant radius	160
F.2	Estimation error of single-track model with parameters according to Table F.1 during steering angle steps	160
G.1	Comparison of frequency responses of body and wheel velocity of closed- loop with H_∞ control of the unconstrained system and closed-loop with LPV control of system with frozen saturation indicators	162
G.2	Comparison of Pareto fronts of ride comfort and road-holding of full-vehicle gain-scheduled H_∞ controller and LPV controller	163
H.1	Robust performance investigation of full-vehicle LPV controller	164
I.1	Overview of Simulink implementation of the vertical dynamics algorithm .	166
I.2	Simulink implementation of the full-vehicle LPV controller with feedforward	167

List of Tables

4.1	Performance degradation due to failure of front left (FL) or rear left (RL) damper	77
4.2	Performance degradation due to false alarm (FA) of damper failure front left (FL) or rear left (RL)	79
4.3	Performance assessment of stochastic excitation experiment	90
4.4	Performance assessment of Spanish bumps experiment	90
4.5	Performance assessment of country road with long-wave bump experiment	90
4.6	Performance assessment of large bump excitation experiment with rear right damper failure	93
5.1	Performance assessment of two-degree-of-freedom controller with feedforward filter during simulation of lane-change scenario	105
5.2	Parameters of lane change manoeuvres according to ISO (3888-2:2011)	109
5.3	ISO (3888-2:2011) double lane change at a vehicle speed of 50 km/h: performance assessment of two-degree-of-freedom controller with feedforward filter	110
B.1	Classification of electronically controlled suspensions	139
D.1	Quarter-vehicle test-rig model: symbols and parameters	152
E.1	Sensor specification <i>SC3-Bulli</i>	155
E.2	Symbols and parameters of <i>SC3-Bulli</i> vehicle model	156
F.1	Single-track model: symbols and parameters	158

List of Symbols

The List of Symbols is structured into the two first sections which introduces the basic mathematical and control related symbols used in this thesis. The following sections present the specific symbols employed in the chapters of the thesis. Basic symbols, which are used with indices, are not repeated as long as their meaning is clear from the context. Throughout the thesis bold lower case symbols represent vectors, bold upper case symbols represent matrices and light symbols represent scalars. Symbols which are introduced in a previous section are not explained in the consecutive section as long as their meaning stays the same. The time derivative of a signal \mathbf{x} is denoted by $\dot{\mathbf{x}} = \frac{d\mathbf{x}}{dt}$. Similarly, the partial derivative of \mathbf{x} with respect to \mathbf{z} is denoted by $\frac{\delta \mathbf{x}}{\delta \mathbf{z}}$. Throughout the thesis only SI units are used for variables and parameters.

Mathematical Symbols

\mathbb{R}	set of real numbers
\mathbb{R}^+	set of non-negative, real numbers
\mathbb{R}^n	set of n -dimensional real vectors
$\mathbb{R}^{n \times m}$	set of n by m matrices with elements in \mathbb{R}
\mathbf{M}^T	transpose of matrix \mathbf{M}
\mathbf{M}^{-1}	inverse of invertible matrix \mathbf{M}
$\text{eig}(\mathbf{M})$	eigenvalues of n by n matrix \mathbf{M}
$\text{diag}(\mathbf{m})$	n by n diagonal matrix with elements of vector \mathbf{m} of length n on the diagonal line
$\text{Ker } \mathbf{M}$	kernel of matrix \mathbf{M}
\mathbf{I}_n	n -dimensional identity matrix
$\mathbf{0}_{n \times m}$	n by m matrices with zero elements
$\mathbf{M} > 0$	symmetric matrix \mathbf{M} is positive definite
$\mathbf{M} < 0$	symmetric matrix \mathbf{M} is negative definite
$\ \cdot\ _2$	L_2 -norm
$\ \cdot\ _\infty$	H_∞ -norm
$\ \cdot\ _{i2}$	induced L_2 -norm
$\mathcal{PC}(\mathbb{R}^+, \mathbb{R}^{n \times m})$	set of piecewise continuous matrix-valued functions of dimension n by m
$\mathcal{C}_0(\mathbb{R}^+, \mathbb{R}^{n \times m})$	set of continuous matrix-valued functions of dimension n by m
$\mathcal{C}_1(\mathbb{R}^+, \mathbb{R}^{n \times m})$	set of continuously differentiable matrix-valued functions of dimension n by m

Basic Control related Symbols

t	time variable
s	Laplace variable
ω	frequency variable
\mathbf{G}	linear (LTV, LPV or LTI) system
\mathbf{x}	state vector of length n_x of linear system
\mathbf{u}	control input vector of length n_u of linear system
\mathbf{d}	disturbance input vector of length n_d of linear system
\mathbf{y}	measurement output vector of length n_y of linear system
\mathbf{A}	n_x by n_x dynamics matrix of linear system
\mathbf{B}	n_x by n_u input matrix of linear system
\mathbf{C}	n_y by n_x output matrix of linear system
\mathbf{D}	n_y by n_u feedthrough matrix of linear system
\mathbf{K}	controller of dimension n_K
\mathbf{O}	state-observer of dimension n_O
\mathbf{F}	n_u by n_x state-feedback gain of state-feedback controller
$\hat{\mathbf{x}}$	state of length n_x of Luenberger observer
\mathbf{L}	n_x by n_y state-observer gain of Luenberger observer
Φ	n_x by n_x state transition matrix of linear system
\mathbf{P}	generalized plant
\mathbf{e}	performance output vector of length n_e of generalized plant
Γ_{ed}	LPV system with disturbance inputs \mathbf{d} and performance outputs \mathbf{e}
$\Gamma_{ed}(\mathbf{P}, \mathbf{K})$	LPV system of closed-loop interconnection of generalized plant \mathbf{P} with controller \mathbf{K}
v	Lyapunov function
$\mathbf{Z}, \mathbf{Y}, \mathbf{X}, \mathbf{V}$	n_x by n_x Lyapunov matrix of quadratic Lyapunov functions
$\sigma(\cdot)$	saturation function

Introduction

k_b	suspension spring stiffness
d_b	suspension damping
F_d	damper force
v_d	damper velocity
\mathcal{D}	set of admissible semi-active damper forces
\mathbf{K}_{lpv}	linear parameter-varying controller
\mathbf{K}_{gs}	gain-scheduled H_∞ controller
\mathbf{N}_k	feedforward filter processing the known disturbances \mathbf{d}_k
\mathbf{K}_u	feedback controller processing the measurements \mathbf{y}

LPV Control with Actuator Constraints

$\boldsymbol{\rho}$	scheduling parameter vector of length n_ρ of LPV system
$\dot{\boldsymbol{\rho}}_{\max}$	rate bounds of scheduling parameters
\mathcal{P}	set of admissible scheduling parameters
\mathcal{F}_ρ	set of time-varying trajectories of scheduling parameters $\boldsymbol{\rho}$ with rate bounds $\dot{\boldsymbol{\rho}}_{\max}$
γ	induced L_2 -norm performance level
\mathbf{W}_d	shaping filter of disturbance input \mathbf{d} of generalized plant \mathbf{P}
\mathbf{W}_e	shaping filter of performance outputs \mathbf{e} of generalized plant \mathbf{P}
\mathbf{e}_a	performance signals of structured performance output \mathbf{e}
\mathbf{e}_u	control effort signals of structured performance output \mathbf{e}
$\boldsymbol{\theta}$	saturation indicator parameters
$\boldsymbol{\Theta}$	saturation indicator matrix
u_i^{\min}	minimum actuator force limit
u_i^{\max}	maximum actuator force limit
\mathbf{W}_a	shaping filter of performance signals \mathbf{e}_a of generalized plant \mathbf{P}
\mathbf{W}_u	shaping filter of control effort \mathbf{e}_u of generalized plant \mathbf{P}
\mathbf{H}_Θ	auxiliary matrix of proof of minimum grid density for quadratic stability analysis
\mathbf{M}_Θ	auxiliary matrix of proof of minimum grid density for quadratic stability analysis

Quarter-Vehicle Control Design

F_{sa}	damper force control signal of semi-active suspension controller
u_d	damper current control signal
T	interval length
J_c	ride comfort criterion of quarter-vehicle
$F_{t,xy}$	longitudinal and lateral tire force potential
μ_r	friction coefficient of road
$F_{t,z}$	vertical tire force
$F_{wl,stat}$	static wheel load
$F_{wl,dyn}$	dynamic wheel load
F_{wl}	wheel load
J_{rh}	road-holding criterion
J_d	suspension deflection criterion (suspension deflection usage)
\bar{m}_b	body mass of quarter-vehicle
m_w	wheel mass
F_s	suspension force acting between body and wheel
k_w	tire spring stiffness
d_w	tire damping
d_g	road disturbance
F_d	damper force
f_{FM}	force map damper model
f_{2D}	2D look-up table
g_{2D}	inversion of 2D look-up table f_{2D}
$F_{sa,SH}$	Skyhook force control signal
F_{SH}	Skyhook force
d_{SH}	Skyhook damping
$F_{sa,GH}$	Groundhook force control signal
F_{GH}	Groundhook force
d_{GH}	Groundhook damping
u_{F_d}	virtual control force of LPV controller
F_0	nominal damper force
d_0	nominal damping
ω_d	bandwidth of semi-active damper
\mathbf{d}_n	measurement disturbances
\mathbf{W}_n	weighting matrix of measurement disturbances \mathbf{d}_n

v_v	vehicle speed
v_{ref}	reference vehicle speed
α_r	parameter of road model
β_r	parameter of road model
\mathbf{y}_a	performance outputs of plant \mathbf{G}
\mathbf{S}_a	augmented sensitivity function
$\mathbf{W}_1, \mathbf{W}_1, \mathbf{V}_1, \mathbf{V}_2$	auxiliary functions of mixed sensitivity problem representation
\mathbf{S}	sensitivity function
J_{opt}	cost function of multi-objective optimization of tuning parameters of control design
$\boldsymbol{\varphi}$	vector of tuning parameters of optimization
λ_{max}	upper bound of eigenvalues of frozen LPV systems
ϑ	auxiliary parameter of optimization problem

Full-Vehicle Control Design

\mathbf{r}	reference controller input signal
J_{cISO}	ride comfort criterion of full-vehicle
$W_{\text{cISO,heave}}$	weighting filter of body heave acceleration
$W_{\text{cISO,rot}}$	weighting filter of body roll and pitch accelerations
m_b	body mass of full-vehicle
I_{xx}	body roll inertia
I_{yy}	body pitch inertia
\mathbf{T}_{bs}	geometric transformation matrix to wheel centers
$l_{x,f}$	distance front axle to body center of gravity
$l_{x,r}$	distance rear axle to body center of gravity
$l_{y,f}$	vehicle track width front
$l_{y,r}$	vehicle track width rear
$d_{\text{SH,heave}}$	body heave velocity related Skyhook damping
$d_{\text{SH,roll}}$	body roll velocity related Skyhook damping
$d_{\text{SH,pitch}}$	body pitch velocity related Skyhook damping
\mathbf{T}_{ba}	geometric transformation matrix to body acceleration sensor positions
\mathbf{M}_η	actuator efficiency matrix
$\boldsymbol{\eta}$	actuator efficiencies
\mathbf{u}_δ	control signal loss in the event of malfunction or saturation
\mathbf{T}	force reconfiguration matrix
\mathbf{T}_u	force redistribution matrix
α_u	tuning parameter of the amount of force redistribution
\mathbf{u}_0	control signal of healthy actuators
F_{sf}	sliding friction force
T_{nFVM}	step size of full-vehicle simulation model
Δ_{obs}	relative mean square error (MSE) of observer
T_s	sample time of dSPACE MicroAutoBox II
T_{log}	sample time of data logging

Roll Disturbance Feedforward Control

N_{Θ}	LPV feedforward filter
\mathbf{u}_J	control signal of two-degree-of-freedom controller
ϵ_y	input of feedback controller in two-degree-of-freedom structure
ϵ_u	output of feedback controller in two-degree-of-freedom structure
a_y	lateral vehicle acceleration
d_r	body roll disturbance resulting from lateral vehicle acceleration
a_{yS}	lateral vehicle acceleration at position S
δ_F	front wheel steer angle
\mathbf{J}_m	auxiliary matrix of two-degree-of-freedom control structure
J_h	vehicle handling criterion

1 Introduction

A well tuned suspension system significantly contributes to the vehicle's driving safety by promoting a good tire road contact. From the driver perspective the tire road contact itself is not of major importance, but rather the road-holding ability, which e.g. affects the braking distance during emergency braking or the cornering capabilities. These two aspects, however, can be characterized by the transmissible longitudinal and lateral tire forces and are therefore directly related to the tire road contact. Besides driving safety, ride comfort is an important customer requirement of a modern vehicle (Mitschke and Wallentowitz, 2004). Here, the suspension system also has a substantial effect, firstly on the amount of road excitations transmitted to the vehicle body and secondly on the magnitudes of roll and pitch motions of the vehicle body induced by the steering and braking inputs of the driver.

Passive suspension systems allow only a compromise between the conflicting demands ride comfort and road-holding. On the one hand ride comfort for example can be achieved by small vehicle body amplitudes around the body resonance frequency and consequently a stiff spring and high damper forces, whereas on the other hand good isolation of the vehicle body against road excitations beyond the wheel resonance frequency requires a soft spring and small damper forces. The trade-off between ride comfort and road-holding is shown in a schematic way in Figure 1.1. There, the dotted black lines illustrate the evolution of the design objectives ride comfort and road-holding if the body damper is varied while the body spring is kept constant. Conversely, the dashed black lines depict the evolution of both design objectives if the body spring is varied and the body damper is kept constant. Furthermore, the solid black line represents the Pareto front of ride comfort and road-holding of a passive suspension system, i.e. the optimal settings of the body spring stiffness and body damping. No other spring stiffness and damping combination can yield a better trade-off between ride comfort and road-holding than the realizations belonging to the Pareto front. A detailed introduction to vehicle suspension systems, its components and the design objectives can be found in Mitschke and Wallentowitz (2004, p. 249 ff.), Heißing and Ersoy (2011), Rajamani (2012, p. 287 ff.), Rill (2012) and Venhovens (1994).

Compared to passive suspension systems, active and semi-active suspension systems enable the mitigation of the above described conflicting requirements by the continuous control of the respective actuators. These actuators are in case of an active suspension e.g. a hydraulic cylinder or in case of a semi-active suspension a controllable damper (Tseng and Hrovat, 2015). In either case, ride comfort and road-holding can be improved compared to passive suspensions resulting in a better overall performance. Figure 1.1 also shows the idealized Pareto fronts of an active suspension depicted by the dot-dashed blue line and a semi-active suspension depicted by the dashed green line. From the three variants an active suspension generally provides the best trade-off between ride comfort and road-holding followed by a semi-active suspension. The disadvantages of both systems are firstly an increase in suspension cost due to additional and complex components like electronic control units (ECU), sensors, wiring and the actuators themselves. Secondly,

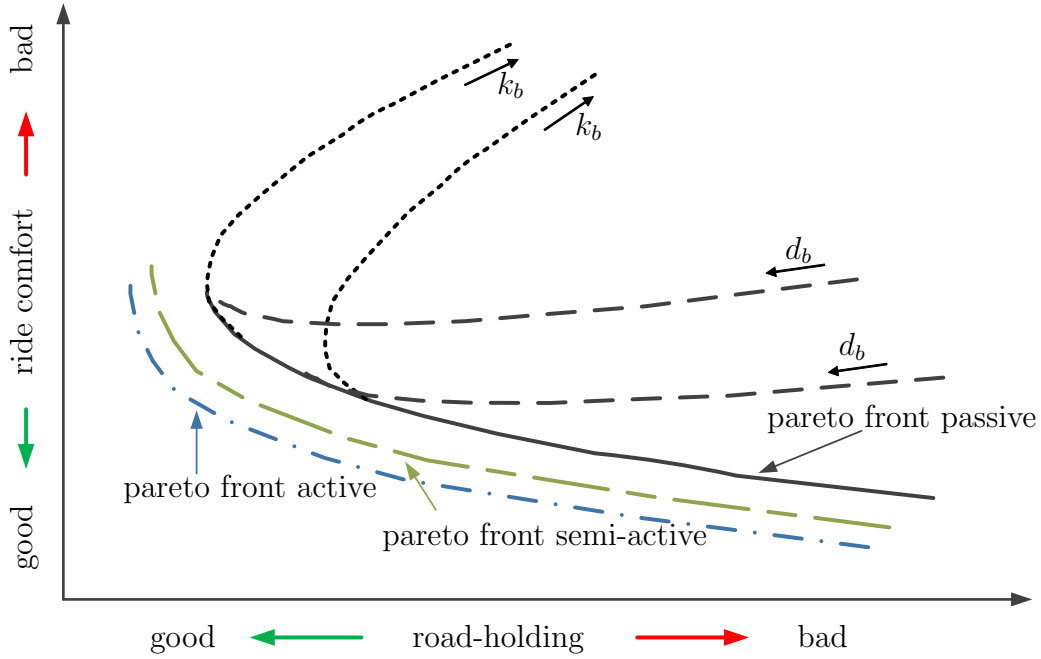


Figure 1.1: Schematic Pareto diagram of the trade-off between ride comfort and road-holding (spring stiffness denoted by k_b and body damping by d_b)

active and semi-active suspension systems also increase the energy consumption of the vehicle due to the needed energy supply. These negative properties are more challenging for active suspension systems, therefore active suspension systems are only offered in premium cars with a strong focus on ride comfort like the *Mercedes Benz S-class*, which offers an active suspension system called *Magic Body Control* (Weist et al., 2013). In contrast to fully-active suspensions, semi-active suspensions offer a good compromise between the additional energy consumption and the system complexity on the one side and ride comfort and road-holding improvements on the other side. Moreover, the system costs of semi-active suspensions are much lower than that of active suspension systems resulting in a very good cost versus benefit calculation (Savaresi et al., 2010, p. 4 ff.). Thus, semi-active suspension systems are not only offered in premium cars like the *VW T6 Multivan*, but also in middle class cars like the *VW Golf VII*. Additionally, the low energy consumption of semi-active suspensions makes their application in electric vehicles very appealing in the near future.

The vital performance benefit of semi-active suspensions compared to passive suspensions results from the high bandwidth and large controllable force range of contemporary semi-active dampers. In contrast to the initial expectation, the Pareto front of a semi-active suspension essentially differs from the damping variation curve (dashed black lines) of passive dampers. As illustrated in Figure 1.1, the Pareto front of semi-active suspensions is rather comparable to the Pareto front of active suspension systems. To understand this

property, a semi-active damper has to be considered as a force actuator with constraints, rather than as a damper with modifiable damping coefficient. Even though, a semi-active damper is limited by the passivity constraint and thus can only dissipate energy like any ordinary passive damper, as illustrated in Figure 1.2, its damper forces F_d can be freely selected within the set of admissible damper forces \mathcal{D} . In contrast, the forces $F_{d,p}$ of a passive damper are defined by a single curve. The inherent actuator force constraints, however, bound the achievable ride comfort and road-holding performance of semi-active suspensions and constitute a crucial restriction which has to be handled during controller design.

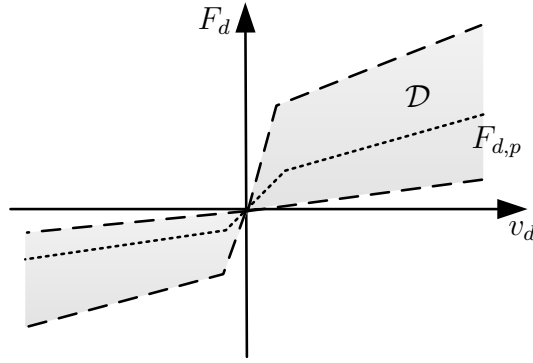


Figure 1.2: Example of force characteristic of passive damper (dotted line) and set \mathcal{D} of admissible semi-active damper forces (gray area)

Figure 1.3 gives an overview of typical functions of a semi-active suspension control algorithm from a software implementation perspective. This thesis scientifically investigates the core functions *feedback controller* and *roll feedforward control*, and presents new developments with improved performance. The main design goal of the feedback control path is the attenuation of road disturbances, while the roll and pitch feedforward control paths focus on the attenuation of load disturbances induced by the steering, brake and acceleration inputs of the driver. Thus, the core functions of the vertical dynamics control algorithm resemble a two-degree-of freedom control structure with the feedback control dealing with the unknown road disturbances and the feedforward control with the known driver-induced disturbances. The functions *inverse damper model*, *local damper controller* and *sensor signal processing* are realized according to the state-of-the-art with minor adaptations to the application. This work does not investigate *control adaptations*, e.g. depending on the selected *user mode*, the *vehicle speed* and the *road type*, but of course they are considered during the design of the core functions such that the controller provides the necessary interfaces.

The effectiveness of the newly developed semi-active damper control algorithms is demonstrated by experimental results of the *VW T5* van experimental vehicle called *SC3-Bulli* of the *Institute of System Dynamics and Control* (SR) of the *German Aerospace Center*

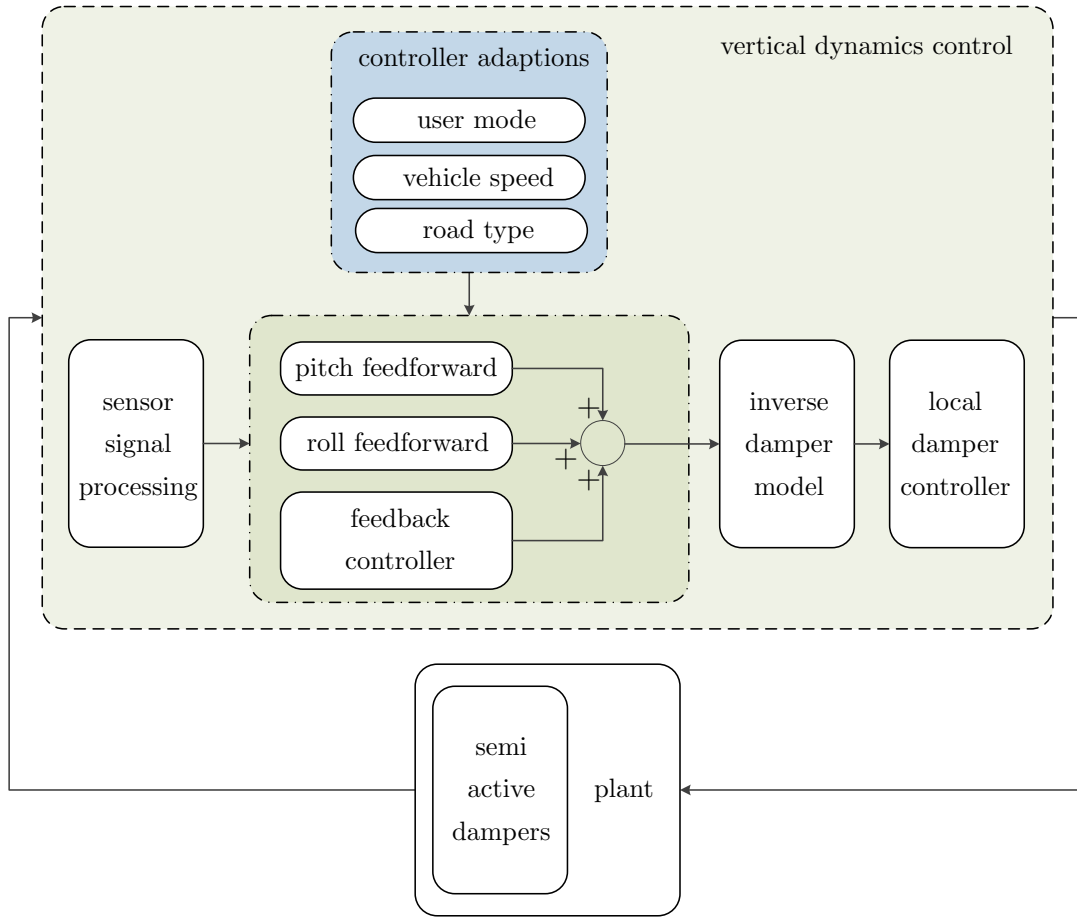


Figure 1.3: Overview of functions of vertical dynamics control algorithms

(DLR). Two types of experiments are performed with the *SC3-Bulli* depicted in Figure 1.4. The performance regarding road disturbances is validated on the four-post test-rig of the *KW automotive GmbH* (KW) and the performance regarding driver-induced disturbances is proven by lane change experiments on the automotive testing area of the *University of the Federal Armed Forces* in Munich.

As a major step before the actual full-vehicle experiments, the control algorithms were investigated on the quarter-vehicle test-rig of the *Institute of Control Engineering* of the *Department of Aerospace Engineering* at the *University of the Federal Armed Forces* in Munich. These experiments enabled a first detailed evaluation of the proposed control algorithms and a targeted further development towards the full-vehicle experiments.



Figure 1.4: *SC3-Bulli* experimental vehicle of SR on four-post test-rig

1.1 State-of-the-Art in Semi-Active Damper Control

1.1.1 Skyhook Control

In the literature, a lot of control approaches for semi-active suspensions like Skyhook, Groundhook and clipped control concepts have been investigated since 1974 when Karnopp et al. (1974) first published their famous work on “Vibration Control Using Semi-Active Force Generators”. There, the to-date state-of-the-art in comfort-oriented semi-active suspension control used in production vehicles, the Skyhook control concept, was described for the first time. Within this concept, a hypothetical damper between sky and vehicle body, the Skyhook damper, is approximated by the actual semi-active damper. In this way, the controlled damper stabilizes the vehicle body and at the same time also improves the isolation of the vehicle body from road excitations. The theoretical motivation for the Skyhook control concept is derived from the optimal control policy of a fully-active one-mass system using quadratic performance criteria. The resulting optimal feedback law consists of two terms: one term proportional to the body velocity and a second term proportional to the relative position between body and ground. In many application, e.g. vehicle suspensions, the later term can be realized by a spring between body and ground, while the exact realization of the first term, the Skyhook damper, is not possible. The patent Ahmadian et al. (2000) describes an approximation of the Skyhook damper by a switching rule using the body and damper velocity. In particular, the algorithm results in jerk free damper forces and thus achieves excellent ride comfort of the vehicle. In Savaresi and Spelta (2007) the Skyhook concept is combined with the Acceleration Driven Damping (ADD) concept through a frequency selector defining a cross-over frequency from the Skyhook controller to the ADD controller. The authors show that these two concepts feature complementary behavior to the effect that the Skyhook controller performs well

around the body resonance frequency and the ADD controller in the intermediate and high frequency range. Additionally, the ride comfort performance of the mixed Skyhook-ADD controller is compared to an optimal ride-comfort benchmark (lower bound) derived from the solution of an optimal predictive control problem under the assumption of a known road profile as presented in Poussot-Vassal et al. (2010). In this investigation, the authors show that the mixed Skyhook-ADD controller achieves a ride comfort performance close to the optimal lower bound despite its simple structure and lack of road profile information. The same design goal is addressed by a different approach in Yi and Song (1999). In this article, the authors propose a frequency dependent scheduling of the Skyhook controller gain such that the Skyhook controller improves its performance in the intermediate and high frequency range.

Recent developments as presented in the patents Nedachi et al. (2016) and Unger (2017) augment the Skyhook control policy to obtain a desired pitch behavior or add preview information about the road profile to the controller.

1.1.2 Groundhook Control

The counterpart of the Skyhook control concept, the road-holding oriented Groundhook control concept, was first published by Valášek et al. (1997). In this article, a hypothetical damper, the Groundhook damper, between ground and wheel carrier is introduced aiming at a reduction of the tire deflection magnitude, which is directly related to road-holding. Subsequently, the approximation of the Groundhook damper by an actual semi-active suspension damper is described. In comparison with the Skyhook concept, the implementation of the Groundhook control concept is complicated by the fact that the current tire deflection is unknown in many applications because it cannot be measured easily. Consequently, the desired Groundhook damper force cannot be determined. The authors in Koo et al. (2004) analyze the desired Groundhook damper forces under several conditions and develop an approximate, switching Groundhook control policy based on damper velocity and wheel velocity signals without the need of tire deflection information. An extensive survey of Skyhook and Groundhook control approaches including numeric evaluations of the controller performance can be found in Savaresi et al. (2010) and Poussot-Vassal et al. (2012).

1.1.3 Clipped Control

The clipped control concept adopts control approaches from fully-active suspension systems for semi-active suspension control by simply clipping the actuator force demand according to the current damper force constraints (Margolls, 1982; Karnopp, 1983). The basic idea of this approach can be summarized as follows: the actuator force demand from the fully-active control policy is applied whenever possible i.e. the demanded actuator force is realizable by the semi-active damper and otherwise the control policy selects the best approximation of the demanded actuator force. In Hrovat (1997) the clipped

control approach is used to develop a linear quadratic (LQ) controller for semi-active suspensions. This clipped LQ approach, also denoted clipped-optimal, is widely used in scientific applications (Unger et al., 2013; Tseng and Hrovat, 2015) because ride comfort and road-holding can be quantified based on the L_2 -norm of linear combinations of the system states. If the focus is shifted towards robust control and loop-shaping, clipped H_∞ control offers a well-established framework to adopted developments from H_∞ control of fully-active suspensions (Sammier et al., 2003), to the case of semi-active suspensions. An example of the clipped H_∞ approach represents the clipped, adaptive, robust, gain-scheduled H_∞ controller given in Ahmed and Svaricek (2013). The huge disadvantage of all controllers design according to the clipping policy arises from the ad-hoc controller adjustment. As a result, a loss of stability might occur when the actuator limits are reached. Nevertheless, good performance of the clipped controllers is reported in the above publications and the question is raised how far the performance of the clipped-optimal controller deviates from an optimal controller which explicitly accounts for the actuator constraints.

1.1.4 Model-Predictive Control

In Giorgetti et al. (2006) the question of optimal performance is addressed by the comparison of the clipped LQ approach with a model-predictive control (MPC) approach for hybrid systems. During the MPC design the force constraints of the semi-active damper are explicitly considered by including suitable inequality constraints in the formulation of the optimization problem. The online optimization algorithm utilized inside the MPC controller limits any solution of the demanded actuator force to reachable damper forces. Firstly, the authors show that the clipped LQ controller and the MPC controller with prediction horizon $N = 1$ correspond to each other and secondly that the MPC controller can achieve a significantly better performance for prediction horizons $N > 1$. A similar MPC approach with a stronger focus on a real-time implementation on rapid control prototyping (RCP) hardware, called “fast” MPC, is investigated in Canale et al. (2006). In this article, the authors circumvent the online-optimization problem, an inherent part of model-predictive control, by an approximation based on the set membership approach of nonlinear function estimation.

1.1.5 Linear Parameter-Varying Control

As an alternative approach in recent years, the design of semi-active suspension controllers based on linear parameter-varying (LPV) control theory are investigated. LPV control methods offer a flexible theoretical framework for the design of nonlinear controllers, e.g. LPV techniques features the possibility firstly to easily incorporate plant nonlinearities like an air spring characteristic or vehicle speed dependencies and secondly to integrate controller adaptations like a suspension deflection or a road type dependency (Fialho and Balas, 2000, 2002). The application of polytopic LPV methods to semi-active suspension control goes back to Poussot-Vassal et al. (2008). The quarter-vehicle LPV control approach

presented there relies on the appropriate selection of scheduling parameter-dependent weighting filters such that the final controller always stays within the actuator limits. In the follow-up research in Do et al. (2010, 2012) and Nguyen et al. (2015a), the polytopic LPV framework is used to approximate the nonlinear input-to-output characteristic of the semi-active damper by an LPV model and subsequently directly incorporate the LPV damper model in the quarter-vehicle plant model. The approach assumes a bi-viscous hysteresis behavior of the semi-active damper such that the damper can be described by a *Shuqi Guo* model. In this way, the semi-active damper control problem is converted from a problem with passivity constraint, i.e. state-dependent input constraints, into a problem with constant input constraints. Moreover, parameter-dependent weighting filters as in Poussot-Vassal et al. (2008) are no longer mandatory and parameter-independent ones are used. Do et al. (2013) compare the performance of both control approaches in a numerical analysis based on a quarter-vehicle model and show that similar results are obtained. Furthermore, Do et al. (2010, 2011) and Nguyen et al. (2015a) present extensions of the control approach with LPV damper model introduced in Do et al. (2010). The travel of a suspension system is typically limited by bump stops in order to prevent physical damage from the suspension components due to collisions. In Do et al. (2010) the suspension deflection issue is addressed by introducing a deflection dependent scheduling of the controller such that the damper forces are increased if the deflection limits are approached. Alternatively, Do et al. (2011) and Nguyen et al. (2015a) develop a systematic approach to avoid the deflection limits by adding a deflection inequality constraint to the controller synthesis problem. To improve the controller performance and reduce conservatism, the authors in Nguyen et al. (2015a) also modify the polytopic LPV controller synthesis based on Finsler's Lemma such that two Lyapunov function are utilized: one that characterizes stability in the admissible scheduling parameter range and another that defines performance of the unconstrained controller.

1.1.6 Vertical Dynamics Vehicle Models

When looking at the models employed during the controller design, most works cited above focus on a simple two-degree-of-freedom quarter-vehicle model with reference to the sufficiently good approximation of the vehicle vertical dynamics. The quarter-vehicle model already covers most of the fundamental vehicle vertical dynamics properties like the passivity constraint of the semi-active damper, of course, but also the invariant points e.g. involved when modifying the body spring stiffness and damping coefficient (Savaresi et al., 2010, p. 46 ff.). Therefore, most results obtained within quarter-vehicle applications can be generalized to full-vehicle applications, especially if the main purpose is a proof-of-concept or the presentation of a single dedicated innovation. Detailed introductions on vertical vehicle dynamics models can be found in e.g. Mischke and Wallentowitz (2004); Rajamani (2012); Rill (2012); Savaresi et al. (2010) and Guglielmino et al. (2008). Examples for the utilization of a quarter-vehicle model to illustrate theoretical advances are the publications of Poussot-Vassal et al. (2008) and Do et al. (2013). The application

of higher-order vehicle models like a half-vehicle model with four-degrees-of-freedom or a full-vehicle model with seven-degrees-of-freedom, complicates the control design problem. Therefore, higher-order models are generally only used if the theoretical contribution requires such a complex model like in Smith and Wang (2002); Lu and DePoyster (2002) and Gáspár and Szabó (2013) or if the work aims at the development of high performance controllers for real vehicles (Unger, 2012; Unger et al., 2013). In Smith and Wang (2002), e.g. the authors present a special controller parametrization, which allows to decouple the disturbance response of the closed-loop system subject to road disturbances and to load disturbances like longitudinal and lateral vehicle accelerations.

1.1.7 Experimental Validation

The final aspect to be highlighted in this chapter is the experimental evaluation of semi-active damper controllers. With respect to this point it has to be distinguished between gain-scheduled Skyhook controllers and more sophisticated model-based controllers e.g. clipped LQ, MPC or LPV controllers discussed above. The former have been available in production vehicles since many years, while field tests of the latter controllers are rare. The reason for this difference is firstly the validated very good performance of gain-scheduled Skyhook controllers, which constitutes a high entry barrier for other control algorithms especially in industry and secondly the significantly increased effort and cost of field tests compared to numerical investigations. This substantial effort emerges during planning, constructing and commissioning of the test-rig and vehicle hard- and software. Additionally, the plant model used in simulation is always a simplified approximation of the real plant which ideally models the most important subset of plant dynamics, disturbances, uncertainties and nonlinearities. Therefore, the reproducibility of the performance of controllers verified with simple simulation models, like the LPV controllers proposed in Do et al. (2011) and Nguyen et al. (2015a) or the MPC controllers developed in Canale et al. (2006), on a test-rig or in a vehicle application is highly uncertain.

Some examples of successful quarter-vehicle test-rig experiments are the investigation of a combined Skyhook-Groundhook controller in Ahmadian and Pare (2000) or the investigation of clipped H_∞ controllers in Ahmed and Svaricek (2013, 2014). Savaresi et al. (2010) and Spelta et al. (2010) present results achieved with Skyhook, ADD and mixed Skyhook-ADD controllers on a two-post motorcycle test-rig. The experiments cover a wide range of excitations like sine sweep, stochastic road and bump excitations and thus give a detailed comparison of the performance of these control methods. Examples of experimental investigations in a full-vehicle context are the application of a Groundhook policy in order to reduce road damage in Valášek et al. (1998), the evaluation of electro-rheological dampers using a Skyhook controller in Choi et al. (2001) or the investigation of a combined Skyhook-Groundhook controller in a light commercial vehicle in Sankaranarayanan et al. (2008). Guglielmino et al. (2008) analyze the achievable performance benefit using rather uncommon friction dampers with a clipped position and velocity feedback control approach on a four-post test-rig. A particularly interesting application of a clipped LQ

control policy based on a full-vehicle observer and state-feedback controller is presented in Unger (2012) and Unger et al. (2013). These works discuss many practical aspects like the effect of ascending and descending roads and give an experimental evaluation of the proposed clipped LQ controller on a four-post test-rig.

1.2 Linear Parameter-Varying Control

LPV control theory provides a mathematically rigorous framework to the design of non-linear controllers for a family of linear time-varying plants. These time-varying plants are characterized by certain assumptions on the exogenous scheduling parameters, such as bounds on their magnitudes and rate of variations, and the availability of a measured or estimated value of the current scheduling parameters during operation. The latter assumption reflects the close relation between LPV control and classical gain-scheduled control in the sense that the LPV controller is also gain-scheduled by time-varying exogenous parameters. The close relationship gets even clearer when looking at the early work on LPV control in Shamma (1988) and Shamma and Athans (1991). There, analysis methods for one special type of gain-scheduled control system, namely a linear system satisfying the LPV assumptions, are proposed in order to guarantee that the stability, robustness and performance properties of the gain-scheduled control system carry over the entire operation range. Gain-scheduled controllers are widely used in real-world applications as “they offer a cheap and fairly transparent way of carrying out nonlinear control” to cite Prof. P. Apkarian (Mohammadpour and Scherer, 2012, p. v-vi). The main drawbacks of classical gain-scheduling are firstly the necessity of detailed engineering insight in order to determine ad-hoc scheduling rules for the exogenous parameters and secondly these techniques ignore the nonstationary nature of parameter variations. In contrast as illustrated in Figure 1.5, LPV controllers are automatically gain-scheduled and parameter variations are explicitly considered during the controller synthesis. These properties make LPV controllers a viable alternative to classical gain-scheduling despite the increased complexity of the controller synthesis problem.

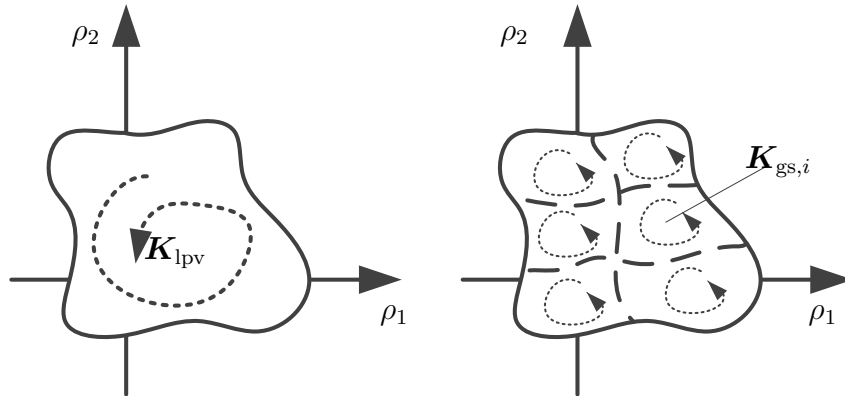


Figure 1.5: Comparison of LPV control to gain-scheduled control with index i denoting the scheduling parameter grid points

The theoretical base of LPV methods was developed in the early- and mid-nineties when Shamma and Athans (1991), Becker and Packard (1994), Apkarian et al. (1995) and Apkarian and Gahinet (1995) published their works on LPV control. The control design presented in this work is based on the follow-up research of Becker and Packard (1994), Wu

(1995) and Wu et al. (1996) on gridding-based LPV controller synthesis. An introduction to LPV control design starting with some fundamental properties of linear time-varying systems can be found in Amato (2006). More recent books such as Mohammadpour and Scherer (2012) and Sename et al. (2013) provide an overview over past, recent and novel methods on modeling, identification, and control design of LPV systems. Additionally, they present an extensive collection of applications in diverse domains like aerospace and road vehicles. A vital supplement to these books can be found in the survey article of Hoffmann and Werner (2015), which discusses polytopic, gridding-based and linear fractional transformation (LFT) based LPV control methods and gives corresponding application examples.

1.3 Control Design Methodology

The control development presented in the subsequent sections strongly relies on simulation investigations and simulation-based tuning of the controller parameters. This approach has been successfully applied to many different topics like control of semi-active dampers (Kortüm et al., 2002) and control of industrial manipulators (Saupe, 2013) at SR. The major advantage of such a *Design-by-Simulation* methodology (Kortüm et al., 2002) arises from short development cycles due to the reduced number of necessary hardware experiments for controller tuning and validation. In particular, the controller tuning in simulation allows for an extensive analysis of the controller stability, performance and robustness under various use cases and with respect to all relevant uncertainties and disturbances. In this process, the employed plant model becomes crucial meaning that on the one hand the model has to be a sufficiently good approximation of the real plant, and on the other hand the model should be as simple as possible to keep the complexity and the computational effort at a reasonable level. According to Kortüm et al. (2002), the virtual control design can be divided into the five consecutive steps depicted in Figure 1.6. In the context of the development of vertical dynamics controllers, the first step consists of establishing a nonlinear quarter-vehicle model of the test-rig and of developing a nonlinear full-vehicle model of the experimental vehicle. Starting from these plant models, in the next step, an LPV representation must be derived for controller synthesis. In the third step, the LPV model is then used in a mixed sensitivity loop-shaping design and in the fourth step the tuning parameters of the control design are optimized by simulating the high-fidelity plant model and the controller in closed-loop. The optimization itself is implemented as a Pareto optimization seeking the optimal trade-off between ride comfort

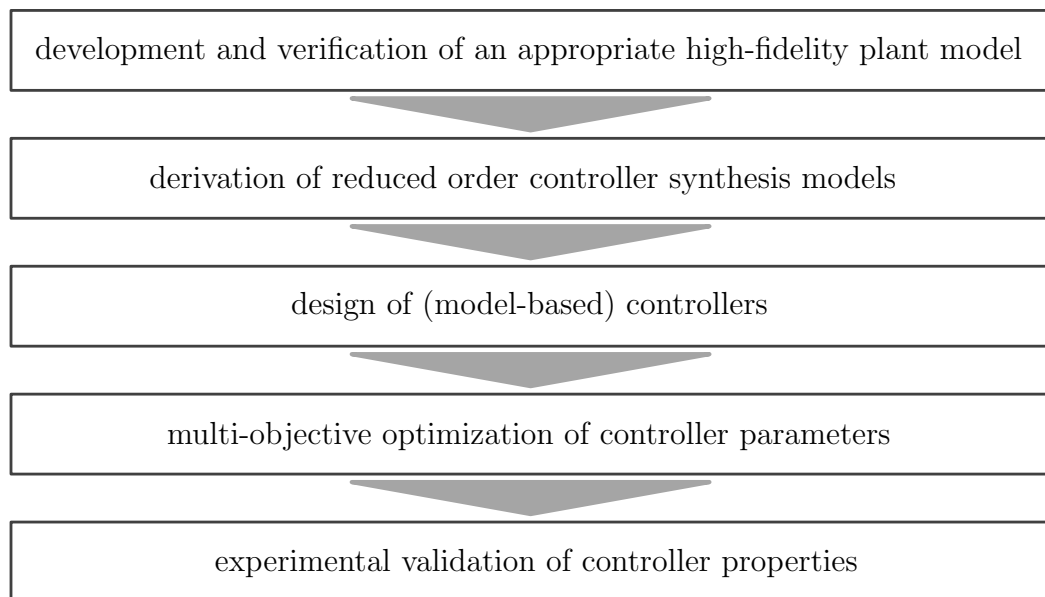


Figure 1.6: *Design-by-Simulation* methodology

and road-holding. Finally, the properties of the controller, like performance and stability, are validated during experiments with the test-rig and experimental vehicle.

1.4 Problem Statement and Contribution

As previously discussed, semi-active suspensions offer a large potential to improve essential vehicle properties like ride comfort, road-holding and vehicle handling compared to passive suspensions. The exploitation of this potential relies on suitable semi-active suspension control algorithms which consider the nonlinear control signal to damper force characteristic and the passivity constraint of the semi-active damper. In particular, the passivity constraint introduces a restrictive state-dependent actuator force limitation and should be explicitly considered during the control design. Figure 1.7 shows the two degree-of-freedom control configuration of the semi-active suspension control algorithm developed in this work. The control-loop consists of the two degree-of-freedom LPV controller \mathbf{K} , the plant model \mathbf{G}_{sa} and the disturbance model \mathbf{G}_d . The disturbance signal \mathbf{d} driving \mathbf{G}_d gathers the known and unknown disturbances \mathbf{d}_k and \mathbf{d}_u . The two degree-of-freedom LPV controller \mathbf{K} , which generates the control signal \mathbf{u} , is composed of the feedforward filter \mathbf{N}_k processing the known disturbances \mathbf{d}_k and the feedback controller \mathbf{K}_u processing the measurements \mathbf{y} . Subsequently, the saturation block limits the control signal \mathbf{u} to the saturated signal $\boldsymbol{\sigma}(\mathbf{u})$.

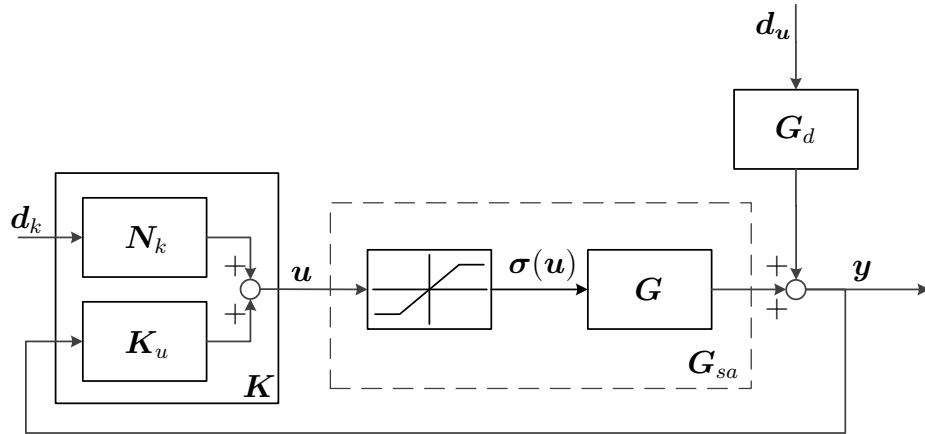


Figure 1.7: Two degree-of-freedom control configuration

As illustrated in Figure 1.7, there exists no reference signal which has to be tracked, but the control design should focus on the rejection of road disturbances as well as driver-induced disturbances. These two disturbances have distinct frequency ranges meaning that the relevant frequency range of road disturbances is 0.5 - 20 Hz, while the relevant frequency range of driver-induced disturbances is 0.1 - 3 Hz. Furthermore, road disturbances denoted by \mathbf{d}_u are unknown during runtime, but driver-induced disturbances \mathbf{d}_k can be estimated from the driver inputs by a planar vehicle model like the single-track model (Schramm et al., 2014, p. 223 ff.). As illustrated in Figure 1.1, the optimal values of the design objectives ride comfort and road-holding cannot be simultaneously realized and the control design always has to seek the best trade-off between them. Moreover, controllers which

minimize the effect of road disturbances only achieve medium ride comfort, road-holding and handling regarding driver-induced disturbances and vice versa.

This work addresses the above described challenges by the anti-windup LPV control approach proposed by Wu et al. (2000). The approach utilizes saturation indicator parameters to directly model the actuator constraints in the LPV plant. The resulting LPV controller features guaranteed closed-loop performance and stability in the presence of saturation nonlinearities. The conflicting design requirements regarding road disturbances and driver-induced disturbances are overcome by the two-degree-of-freedom LPV control approach described in Prempain and Postlethwaite (2001). The separate design of the LPV feedback control part and the LPV feedforward control part proposed there, perfectly matches the semi-active control problem at hand as driver-induced disturbances are known during runtime and consequently their effect can be reduced by an appropriate feedforward filter, while road disturbances are unknown during runtime and their effect has to be minimized by feedback control.

This thesis extends control methods and semi-active suspension control by the following vital scientific contributions:

Section 2.4 presents a new saturation indicator dependent control effort weight resulting in an LPV controller which linearly reduces its control signal according to the saturation status.

Section 2.5 derives a minimum grid density of the LPV representation of the saturation indicator parameters to guarantee quadratic stability of the closed-loop system for all admissible saturation indicator parameters.

Section 3.5 proposes a time-varying saturation transformer parameter to extend the saturation indicator concept to arbitrary, time-varying actuator constraints. In the quarter-vehicle, semi-active suspension control design, the saturation transformer has the physical interpretation of a time-varying nominal damping.

Sections 4.5 and 4.6 develop an active fault-tolerant, full-vehicle, semi-active suspension LPV controller. In particular, the sections discuss a new saturation indicator dependent performance signal weight in addition to the saturation indicator dependent control effort weight of Section 2.4. Moreover, the sections present the integration of the saturation indicator and the actuator efficiency concepts and a fault-tolerant control augmentation.

Section 5.3 presents the design of an LPV feedforward filter to reduce the effect of vehicle roll disturbances induced by the steering inputs of the driver based on a Full-Information problem approach.

Additionally, this thesis presents extensive experimental results of the quarter-vehicle controller of Chapter 3, the full-vehicle controller of Chapter 4 and the feedforward control of Chapter 5. In particular:

Section 3.8 gives experimental results of the quarter-vehicle LPV controller with saturation indicator and saturation transformer gathered at the quarter-vehicle test-rig of the *University of the Federal Armed Forces* in Munich.

Section 4.8 emphasizes the performance improvement of the active fault-tolerant, full-vehicle LPV controller with saturation indicators compared to a state-of-the-art Skyhook-Groundhook controller by experiments gathered with the *SC3-Bulli* experimental vehicle at a four-post test-rig.

Section 5.5 shows the vital benefit of combining feedback control with feedforward control by double lane change manoeuvres with the *SC3-Bulli* experimental vehicle.

1.5 Outline

The thesis presents a step-wise development of the two-degree-of-freedom LPV controller. It is structured into the six chapters visualized in Figure 1.8. Starting with the introduction of the semi-active suspension control problem and a brief state-of-the-art review in Chapter 1, Chapter 2 describes the anti-windup LPV approach and establishes the saturation indicator concept.

Subsequently, Chapter 3 introduces the semi-active control problem and emphasizes the nonlinear actuator characteristics. Additionally, Chapter 3 presents the design of a quarter-vehicle semi-active suspension controller and its assessment by experiments on the quarter-vehicle test-rig of the *University of the Federal Armed Forces* in Munich. Chapter 4 extends the quarter-vehicle controller of Chapter 3 to an active fault-tolerant, full-vehicle controller and gives an investigation of the controller performance and its fault-tolerance capabilities by experiments on a four-post test-rig. Finally, Chapter 5 adds a feedforward control part to the controller of Chapter 4 such that the entire controller performs well regarding road disturbances and driver-induced disturbances. Chapter 6 closes the thesis with a summary of the presented control design and an outlook about future topics. Additionally, Chapter 6 discusses the cooperation of the proposed control algorithm with planar vehicle dynamics control and describes the next steps towards the integration of the control algorithm into the development process of car manufactures.

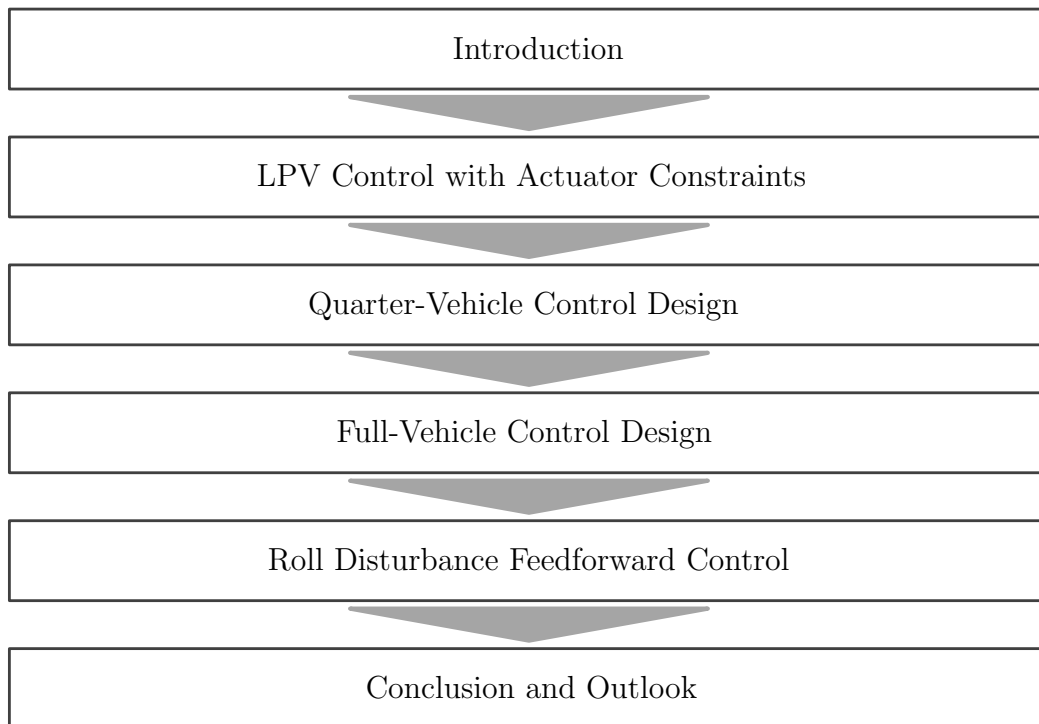


Figure 1.8: Structure of the thesis

2 LPV Control with Actuator Constraints

The inherent physical constraints limit the actuator capacity in all real-world applications leading to a difference between the controller output and the actual plant input if the controller output exceeds the actuator capacity. This has long been acknowledged as a major issue during control design and numerous literature addressing actuator constraints like magnitude and rate limitations can be found like Doyle et al. (1987), Åström and Rundqwist (1989) and Hu and Lin (2001). A simple but conservative approach to handle actuator limitations is the avoidance of saturation by the design of low-gain controllers. The essential drawback of low-gain controllers is poor performance because the control signal has to stay within its limits even for worst-case disturbances. An alternative approach consists in extending a predetermined controller with a so-called anti-windup augmentation to reduce the adverse effects. The augmentation is necessary if the predetermined controller is ill-suited for the input nonlinearity, e.g. if the controller states wind-up to excessively large values in the event of saturation. Classical realizations of anti-windup augmentations for PID controllers are presented in Åström and Murray (2008, p. 306). A more involved augmentation with dynamic anti-windup compensators is developed in Grimm et al. (2003). The latter work especially focuses on guaranteeing a prescribed performance level of the augmented closed-loop system. Moreover, as shown in Giorgetti et al. (2006) and Canale et al. (2006), MPC approaches readily consider actuator limitations as inequality constraints of the online-optimization problem.

The control design in this work is performed along the anti-windup control method proposed by Wu et al. (2000). The approach utilizes so-called saturation indicator scheduling parameters to model the actuator constraints in an LPV plant. Subsequently, the LPV plant facilitates the systematic design of an anti-windup LPV controller, which is directly scheduled by the saturation indicators. This LPV method for plants with input constraints features some desirable properties like guaranteed closed-loop system stability, smooth degradation of unconstrained performance in the presence of actuator saturation and recovery of unconstrained design specifications in the absence of saturation. Furthermore, the approach is well-suited for the sophisticated design of anti-windup controllers of MIMO systems.

Remark. In the following the term *unconstrained* is used to indicate the absence of saturation, e.g. unconstrained closed-loop system refers to the closed-loop system if the controller output can be realized by the actuator.

2.1 Definition of LPV Systems

LPV systems generalize LTI systems to linear plants with time-varying parameters $\boldsymbol{\rho}(t)$ called scheduling parameters. The scheduling parameters are assumed to continuously evolve in time and to be measurable or estimable in real-time. Furthermore, the rates of

variation of the scheduling parameters are assumed to be bounded according to

$$|\dot{\rho}_i(t)| \leq \dot{\rho}_{\max,i} \quad \forall i \in \{1, 2, \dots, n_\rho\} \quad \forall t \in \mathbb{R}^+ \quad (2.1)$$

with n_ρ the number of scheduling parameters and the rate bounds $\dot{\rho}_{\max,i} > 0$. The scheduling parameter vector itself belongs to a compact set $\mathcal{P} \subset \mathbb{R}^{n_\rho}$. Definition 2.1 states a general continuous-time LPV system whose state-space matrices are continuous functions of the scheduling parameters $\boldsymbol{\rho}$ and their derivatives $\dot{\boldsymbol{\rho}}$.

Definition 2.1. An n_x -th order linear parameter-varying (LPV) system Γ_{ed} with disturbance input \mathbf{d} and performance output \mathbf{e} is given by

$$\begin{bmatrix} \dot{\mathbf{x}} \\ \mathbf{e} \end{bmatrix} = \begin{bmatrix} \mathbf{A}(\boldsymbol{\rho}, \dot{\boldsymbol{\rho}}) & \mathbf{B}(\boldsymbol{\rho}, \dot{\boldsymbol{\rho}}) \\ \mathbf{C}(\boldsymbol{\rho}, \dot{\boldsymbol{\rho}}) & \mathbf{D}(\boldsymbol{\rho}, \dot{\boldsymbol{\rho}}) \end{bmatrix} \begin{bmatrix} \mathbf{x} \\ \mathbf{d} \end{bmatrix}, \quad (2.2)$$

with $\boldsymbol{\rho} \in \mathcal{F}_\rho$, $\mathbf{A} \in \mathcal{C}_0(\mathbb{R}^{n_\rho} \times \mathbb{R}^{n_\rho}, \mathbb{R}^{n_x \times n_x})$, $\mathbf{B} \in \mathcal{C}_0(\mathbb{R}^{n_\rho} \times \mathbb{R}^{n_\rho}, \mathbb{R}^{n_x \times n_d})$, $\mathbf{C} \in \mathcal{C}_0(\mathbb{R}^{n_\rho} \times \mathbb{R}^{n_\rho}, \mathbb{R}^{n_e \times n_x})$, and $\mathbf{D} \in \mathcal{C}_0(\mathbb{R}^{n_\rho} \times \mathbb{R}^{n_\rho}, \mathbb{R}^{n_e \times n_d})$ and the vectors \mathbf{x} , \mathbf{e} and \mathbf{d} of appropriate dimension. The notation $\boldsymbol{\rho} \in \mathcal{F}_\rho$ denotes time-varying trajectories with bounded rates in the parameter variation set \mathcal{F}_ρ .

Compared to LTV systems whose system matrices $\mathbf{A}(t)$, $\mathbf{B}(t)$, $\mathbf{C}(t)$, and $\mathbf{D}(t)$ are general functions of time, the system matrices of LPV systems feature a prescribed dependence on the scheduling parameters $\boldsymbol{\rho}$. The interest in LPV systems is motivated by the fact that nonlinear dynamics can be often cast into LPV systems by choosing a suitable set of scheduling variables. LPV systems whose scheduling parameters are functions of the system state $\boldsymbol{\rho}(t) = f(\mathbf{x}(t))$ are called quasi-LPV systems. During controller synthesis, the state-dependent scheduling parameters of quasi-LPV systems are treated as exogenous signals just as scheduling parameters of ordinary LPV systems. The drawback of this approximation may be a more conservative controller, however, the advantages of LPV methods outweigh in most applications (Huang and Jadbabaie, 1999, p. 87). In the remainder, this thesis does not distinguish between quasi-LPV systems and LPV systems.

2.2 Basics of LPV Control Design

The LPV controller synthesis is carried out in MATLAB using the LPVTools toolbox (Hjartarson et al., 2013, 2015). This toolbox pursues a gridding-based LPV approach which specifies performance by the closed-loop input-to-output response (Apkarian et al., 1995; Apkarian and Gahinet, 1995; Wu et al., 1996; Becker and Packard, 1994). The controller design interconnects the open-loop LPV plant \mathbf{P} and the LPV controller \mathbf{K} according to the general control configuration illustrated in Figure 2.1. The resulting closed-loop system is denoted by $\Gamma_{ed}(\mathbf{P}, \mathbf{K})$. In this configuration, the measurements \mathbf{y} of the open-loop plant \mathbf{P} drive the controller \mathbf{K} yielding the control signal \mathbf{u} . The performance of the controller is specified by the induced L_2 -norm of the closed-loop system Γ_{ed} with the disturbance input \mathbf{d} shaped by the filter \mathbf{W}_d and the performance output \mathbf{e}

weighted by the filter \mathbf{W}_e . The induced L_2 -norm of the closed-loop system $\mathbf{\Gamma}_{ed}$ is defined as

$$\|\mathbf{\Gamma}_{ed}(\mathbf{P}, \mathbf{K})\|_{i2} = \sup_{\substack{\rho \in \mathcal{F}_\rho, \|\mathbf{d}\|_2 \neq 0, \\ \mathbf{d} \in \mathcal{L}_2}} \frac{\|\mathbf{e}\|_2}{\|\mathbf{d}\|_2} = \sup_{\substack{\rho \in \mathcal{F}_\rho, \|\mathbf{d}\|_2 \neq 0, \\ \mathbf{d} \in \mathcal{L}_2}} \frac{\|\mathbf{\Gamma}_{ed}(\mathbf{P}, \mathbf{K}) \mathbf{d}\|_2}{\|\mathbf{d}\|_2} < \gamma, \quad (2.3)$$

with the induced L_2 -norm performance level γ . The conditions $\|\mathbf{d}\|_2 \neq 0$ and $\mathbf{d} \in \mathcal{L}_2$ ensure that the L_2 -norm of the input signal \mathbf{d} is well defined. A proof of the existence of an upper bound of the induced L_2 -norm of a stable LPV system $\mathbf{\Gamma}_{ed}$, i.e. $\gamma < \infty$, can be found in Wu (1995, p. 61 ff.).

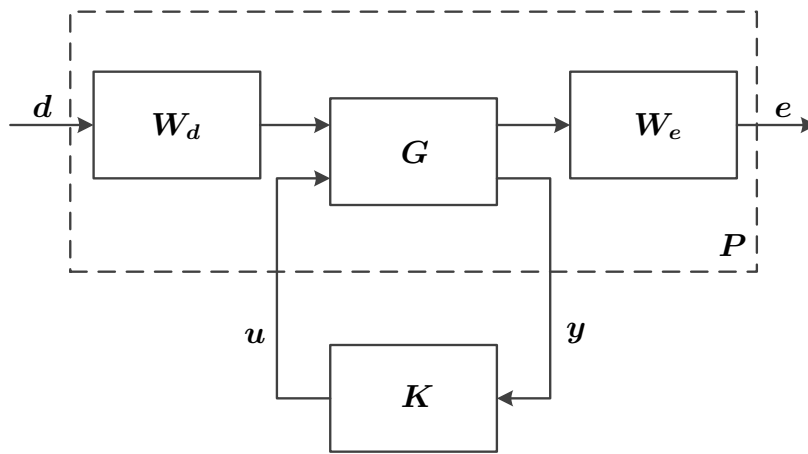


Figure 2.1: General control configuration

The close relation of the induced L_2 -norm and the \mathcal{H}_∞ -norm facilitates the application of loop-shaping techniques during the design of LPV controllers. Hence, LPV controllers can be developed according to the two-stage loop-shaping design process well-established in \mathcal{H}_∞ control, see e.g. Kwakernaak (1993, p. 261 ff.) and Skogestad and Postlethwaite (2005, p. 399 ff.). In this process, the original open-loop LPV plant \mathbf{G} is augmented by input and output weighting filters \mathbf{W}_d and \mathbf{W}_e to specify the desired closed-loop shape. A detailed introduction to LPV control design is presented in Appendix A. Additional overviews of LPV control theory and lots of application examples are given in Amato (2006); Sename et al. (2013); Mohammadpour and Scherer (2012) and Hoffmann and Werner (2015).

2.3 LPV Modeling of Actuator Constraints

Figure 2.2 illustrates the general control configuration of a closed-loop with actuator constraints. The open-loop plant \mathbf{G}_Θ consists of the unconstrained open-loop plant \mathbf{G} and the saturation block. The control signals \mathbf{u} of the controller \mathbf{K}_Θ are fed into the saturation block yielding the saturated control signals $\boldsymbol{\sigma}(\mathbf{u})$. Mathematically, saturation

of the i -th actuator can be described by

$$\sigma(u_i) = \begin{cases} u_i & u_i^{\min} < u_i < u_i^{\max} \\ u_i^{\min} & u_i^{\min} \geq u_i \\ u_i^{\max} & u_i^{\max} \leq u_i \end{cases} \quad (2.4)$$

with the upper actuator limitation $u_i^{\max} > 0$ and the lower actuator limitation $u_i^{\min} < 0$. The saturation indicator parameter θ_i is introduced as the quotient of the saturated control signal $\sigma(u_i)$ and the original control signal u_i according to

$$\theta_i = \frac{\sigma(u_i)}{u_i} \quad \forall i \in \{1, 2, \dots, n_u\}. \quad (2.5)$$

A saturation indicator value of $\theta_i = 1$ represents the situation when the control signal u_i can be realized by the actuator and $\theta_i < 1$ reflects the degree of saturation. The saturation indicators θ_i are assumed to continuously evolve over time, to be either measurable or estimable in real-time, and to lie in the range $\theta_i \in (0, 1] \quad \forall i \in \{1, 2, \dots, n_u\}$. As mentioned in the introduction of this chapter, the saturation indicators are introduced as additional scheduling parameters into the plant. They are gathered in the saturation matrix Θ given by

$$\Theta = \text{diag}(\boldsymbol{\theta}), \quad (2.6)$$

with the saturation indicator vector $\boldsymbol{\theta} = [\theta_1 \ \theta_2 \ \dots \ \theta_{n_u}]^T$. This saturation matrix assumes decoupled actuator constraints, i.e. the control signal of one actuator has no influence on the saturated control signals of other actuators. The saturation matrix Θ can be used to express the saturated control signals as

$$\boldsymbol{\sigma}(\mathbf{u}) = \Theta \mathbf{u}. \quad (2.7)$$

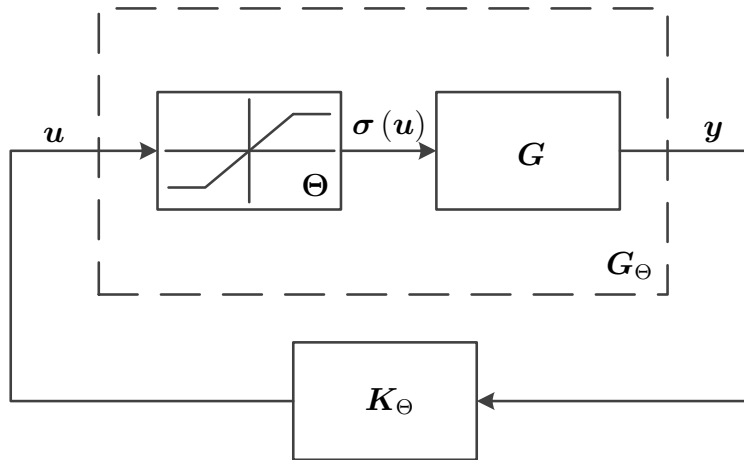


Figure 2.2: Closed-loop of plant G_Θ with actuator constraints and controller K_Θ

The state-space realization of a generalized plant \mathbf{P}_Θ with the scheduling parameter vector $\boldsymbol{\rho}$ comprised of the original scheduling parameters $\bar{\boldsymbol{\rho}}$ and the saturation indicators $\boldsymbol{\theta}$ according to

$$\boldsymbol{\rho} = [\bar{\boldsymbol{\rho}}^T \ \boldsymbol{\theta}^T]^T, \quad (2.8)$$

can then be stated by

$$\begin{bmatrix} \dot{\mathbf{x}} \\ \mathbf{e} \\ \mathbf{y} \end{bmatrix} = \begin{bmatrix} \mathbf{A}(\bar{\boldsymbol{\rho}}, \boldsymbol{\theta}) & \mathbf{B}_1(\bar{\boldsymbol{\rho}}, \boldsymbol{\theta}) & \bar{\mathbf{B}}_2(\bar{\boldsymbol{\rho}}) \boldsymbol{\Theta} \\ \mathbf{C}_1(\bar{\boldsymbol{\rho}}, \boldsymbol{\theta}) & \mathbf{0} & \bar{\mathbf{D}}_{12}(\bar{\boldsymbol{\rho}}, \boldsymbol{\theta}) \boldsymbol{\Theta} \\ \mathbf{C}_2(\bar{\boldsymbol{\rho}}) & \mathbf{D}_{21}(\bar{\boldsymbol{\rho}}, \boldsymbol{\theta}) & \mathbf{0} \end{bmatrix} \begin{bmatrix} \mathbf{x} \\ \mathbf{d} \\ \mathbf{u} \end{bmatrix}. \quad (2.9)$$

The corresponding state-space matrices are continuous functions of the scheduling parameters $\boldsymbol{\rho} \in \mathcal{F}_\rho$ and of appropriate dimensions with $\mathbf{x} \in \mathbb{R}^{n_x}$, $\mathbf{d} \in \mathbb{R}^{n_d}$, $\mathbf{e} \in \mathbb{R}^{n_e}$, $\mathbf{u} \in \mathbb{R}^{n_u}$, and $\mathbf{y} \in \mathbb{R}^{n_y}$. The formulation of \mathbf{P}_Θ uses the definition of the saturated control signal (2.7) to incorporate the input constraints in the LPV plant. Additionally, the saturation indicators may occur in $\mathbf{A}(\bar{\boldsymbol{\rho}}, \boldsymbol{\theta})$, $\mathbf{B}_1(\bar{\boldsymbol{\rho}}, \boldsymbol{\theta})$, $\mathbf{C}_1(\bar{\boldsymbol{\rho}}, \boldsymbol{\theta})$, $\bar{\mathbf{D}}_{12}(\bar{\boldsymbol{\rho}}, \boldsymbol{\theta})$ and $\mathbf{D}_{21}(\bar{\boldsymbol{\rho}}, \boldsymbol{\theta})$ if the control design employs saturation indicator dependent weighting filters $\mathbf{W}_e(\bar{\boldsymbol{\rho}}, \boldsymbol{\theta})$ and $\mathbf{W}_d(\bar{\boldsymbol{\rho}}, \boldsymbol{\theta})$. More details on the assumptions and structure of generalized plants for LPV control design can be found in Appendix A.4.

Even though Wu et al. (2000) only consider constant symmetric actuator limitations, i.e. $|u_i^{\min}| = |u_i^{\max}| \ \forall i \in \{1, 2, \dots, n_u\}$, the approach can be readily extended to general time-dependent actuator limitations. Figure 2.3 depicts examples of 1) constant actuator limitations, 2) time-dependent actuator limitations, and the special case of 3) state-dependent actuator limitations. In any case, the actuator limitations must satisfy $u_i^{\max} > 0$ and $u_i^{\min} < 0$ to keep the saturation indicators well defined and within their parameter space given by $\theta_i \in (0, 1]$.

In the context of semi-active damper control, the actuator limits are nonlinear functions

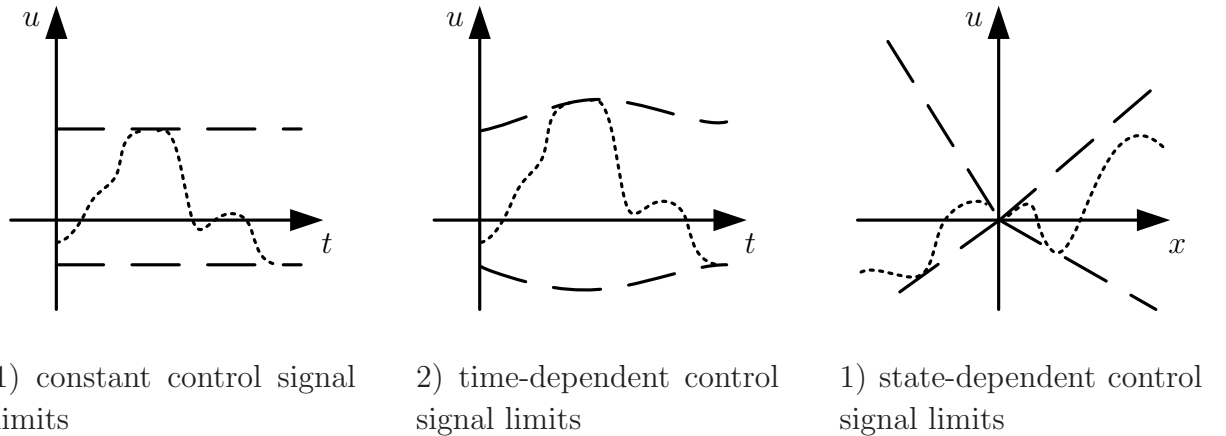


Figure 2.3: Types of control signal constraints; dashed lines represent actuator limitations and dotted lines saturated control signals

of the plant states and can be expressed as

$$u_i^{\min}(\mathbf{x}) = f_{\min}(\mathbf{x}) \quad (2.10a)$$

$$u_i^{\max}(\mathbf{x}) = f_{\max}(\mathbf{x}). \quad (2.10b)$$

Remark. This thesis assumes that the actuator limitation of each actuator is relevant during control design. Therefore, the number of saturation indicators is considered equal to the number of actuators n_u . Nevertheless, actuators with large capacity whose limits are not reached can readily be treated by the presented anti-windup LPV control approach by adjusting their saturation indicators to one.

2.4 LPV Control Design with Actuator Constraints

The LPV control problem formulated by the generalized plant \mathbf{P}_Θ can be solved by LPV methods as introduced in Appendix A.4. The resulting controller depends on the saturation indicators and thus is gain-scheduled by the saturation status. As emphasized in Wu et al. (2000, p. 1109), a saturation indicator dependent weighting scheme is necessary to achieve a successful control design. The weighting scheme should specify different performance requirements for the unconstrained and constrained closed-loop system. In particular, Wu et al. (2000) show that controllers synthesized with plants $\bar{\mathbf{P}}_\Theta$ given by

$$\begin{bmatrix} \dot{\mathbf{x}} \\ \mathbf{e} \\ \mathbf{y} \end{bmatrix} = \begin{bmatrix} \mathbf{A}(\bar{\rho}) & \mathbf{B}_1(\bar{\rho}) & \bar{\mathbf{B}}_2(\bar{\rho}) \boldsymbol{\Theta} \\ \mathbf{C}_1(\bar{\rho}) & \mathbf{0} & \bar{\mathbf{D}}_{12}(\bar{\rho}) \boldsymbol{\Theta} \\ \mathbf{C}_2(\bar{\rho}) & \mathbf{D}_{21}(\bar{\rho}) & \mathbf{0} \end{bmatrix} \begin{bmatrix} \mathbf{x} \\ \mathbf{d} \\ \mathbf{u} \end{bmatrix}, \quad (2.11)$$

without saturation indicator dependent weights upscale their control signal by $\boldsymbol{\Theta}^{-1}$ in the event of saturation. This property holds for general output-feedback controllers $\bar{\mathbf{K}}_\Theta$ as well as state-feedback controllers $\bar{\mathbf{K}}_{\Theta,x}$. The corresponding gain $\bar{\mathbf{F}}(\bar{\rho}, \boldsymbol{\theta})$ of the state-feedback controller $\bar{\mathbf{K}}_{\Theta,x}$ is given by

$$\bar{\mathbf{F}}(\bar{\rho}, \boldsymbol{\theta}) = -\boldsymbol{\Theta}^{-1} \underbrace{\left(\bar{\mathbf{D}}_{12}^T(\bar{\rho}) \bar{\mathbf{D}}_{12}(\bar{\rho}) \right)^{-1} \left(\gamma^2 \bar{\mathbf{B}}_2^T(\bar{\rho}) \mathbf{Z}(\bar{\rho}, \boldsymbol{\theta}) + \bar{\mathbf{D}}_{12}^T(\bar{\rho}) \mathbf{C}_1(\bar{\rho}) \right)}_{= -\bar{\mathbf{K}}_{\rho,x}}, \quad (2.12)$$

with parameter-dependent Lyapunov function $\mathbf{Z}(\bar{\rho}, \boldsymbol{\theta})$. The difference to the state-feedback gain $\mathbf{F}(\boldsymbol{\rho})$ introduced in (A.25) arises from the augmented matrices $\mathbf{B}_2(\bar{\rho}, \boldsymbol{\theta}) = \bar{\mathbf{B}}_2(\bar{\rho}) \boldsymbol{\Theta}$, and $\mathbf{D}_{12}(\bar{\rho}, \boldsymbol{\theta}) = \bar{\mathbf{D}}_{12}(\bar{\rho}) \boldsymbol{\Theta}$ in the plant with saturation indicators. The structure of the state-feedback controller $\bar{\mathbf{K}}_{\Theta,x}$ in closed-loop with its plant $\mathbf{G}_{\Theta,x}$ is visualized in Figure 2.4. To highlight the effect of the saturation indicators, the figure shows the inner structure of $\bar{\mathbf{K}}_{\Theta,x}$ comprised of $\bar{\mathbf{K}}_{\rho,x}$ and the inverse saturation indicator matrix $\boldsymbol{\Theta}^{-1}$. From Figure 2.4 it is obvious that state-feedback controllers $\bar{\mathbf{K}}_{\Theta,x}$ synthesized without saturation indicator dependent weights simply cancel the saturation indicators of the open-loop plant. The resulting closed-loop features no saturation indicators at all. In real world applications, the controller output is a physical signal, e.g. a force demand. Consequently, the controller output should stay finite even if saturation occurs. Unfortunately,

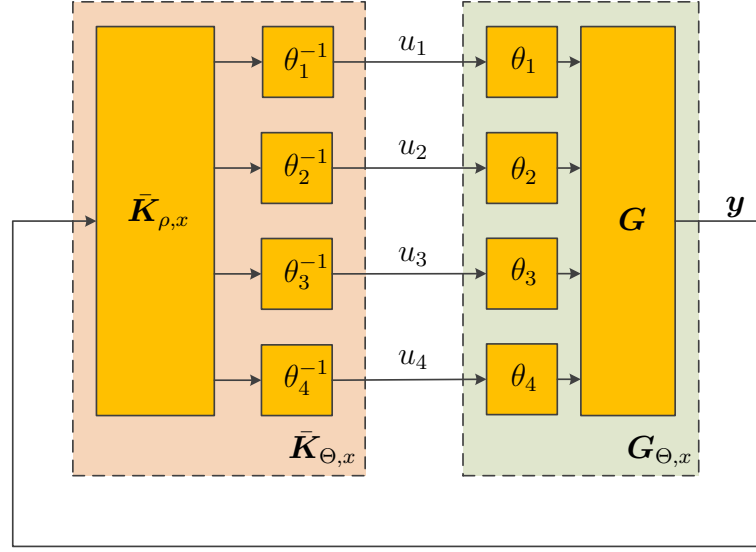


Figure 2.4: Structure of LPV controller without saturation indicator dependent weighting filters

controller $\bar{K}_{\Theta,x}$ is unstable regarding the saturation indicators; once saturation occurs the controller increases its control signal to infinity.

To overcome the issue, this work proposes a new saturation indicator dependent control effort weight $\mathbf{W}_u(\theta)$. The control effort weight $\mathbf{W}_u(\theta)$ shapes the control effort performance output \mathbf{e}_u according to

$$\mathbf{e}_u = \mathbf{W}_u(\theta) \Theta \mathbf{u}. \quad (2.13)$$

The idea is to distinguish the performance requirements of the unconstrained and constrained closed-loop system by realizing the control effort weight as

$$\mathbf{W}_u(\theta) = \Theta^{-1}, \quad (2.14)$$

with $\Theta = \text{diag}(\theta)$ and $\theta_i \in (0, 1] \forall i \in \{1, 2, \dots, n_u\}$ and consequently Θ always invertible. This control effort weight increases the penalty of large control signals if saturation occurs and yields the control effort performance output equal to the control signal $\mathbf{e}_u = \mathbf{u}$. The generalized plant \mathbf{P}_Θ with $\mathbf{W}_u = \Theta^{-1}$ can be expressed as

$$\begin{bmatrix} \dot{\mathbf{x}} \\ \begin{bmatrix} \mathbf{e}_a \\ \mathbf{e}_u \end{bmatrix} \\ \mathbf{y} \end{bmatrix} = \begin{bmatrix} \mathbf{A}(\bar{\rho}, \theta) & \mathbf{B}_1(\bar{\rho}, \theta) & \bar{\mathbf{B}}_2(\bar{\rho}) \Theta \\ \begin{bmatrix} \mathbf{C}_{11}(\bar{\rho}, \theta) \\ \mathbf{0} \end{bmatrix} & \begin{bmatrix} \mathbf{0} \\ \mathbf{0} \end{bmatrix} & \begin{bmatrix} \mathbf{0} \\ \mathbf{I} \end{bmatrix} \\ \mathbf{C}_2(\bar{\rho}) & \mathbf{D}_{21}(\bar{\rho}) & \mathbf{0} \end{bmatrix} \begin{bmatrix} \mathbf{x} \\ \mathbf{d} \\ \mathbf{u} \end{bmatrix}. \quad (2.15)$$

This representation of \mathbf{P}_Θ emphasizes the structure of the performance signal $\mathbf{e} = [\mathbf{e}_a^T \mathbf{e}_u^T]^T$ as in (A.11) and its corresponding performance weight

$$\mathbf{W}_e(\theta) = \begin{bmatrix} \mathbf{W}_a(\theta) & \mathbf{0} \\ \mathbf{0} & \mathbf{W}_u(\theta) \end{bmatrix} \quad (2.16)$$

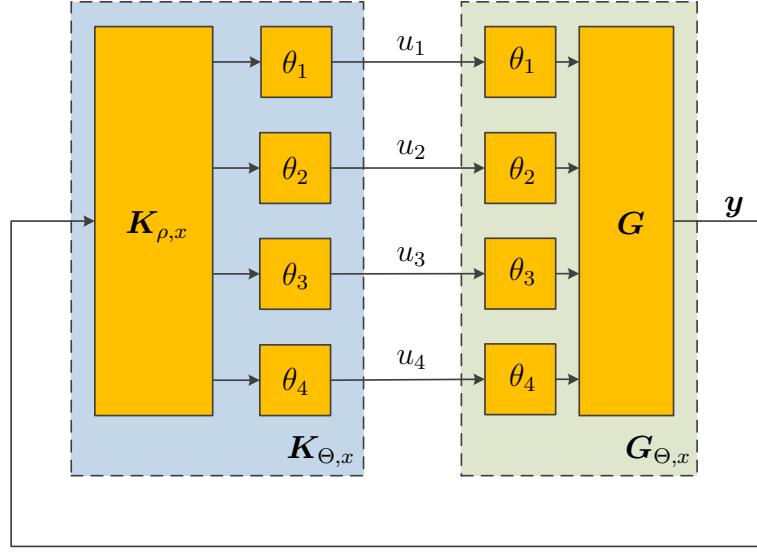


Figure 2.5: Structure of LPV controller with proposed saturation indicator dependent weighting filters

introduced in Figure 2.1. Compared to the generalized plant (2.11), the augmented generalized plant (2.15) with $\mathbf{W}_u(\boldsymbol{\theta})$ as defined in (2.14) recovers the simplifying assumptions $\mathbf{D}_{12} = [\mathbf{0} \ \mathbf{I}_{n_u}]^T$ and $\mathbf{C}_{12} = \mathbf{0}$. In contrast to LPV controllers synthesized without saturation indicator dependent weights, general output-feedback controllers \mathbf{K}_{Θ} as well as state-feedback controllers $\mathbf{K}_{\Theta,x}$ designed with $\mathbf{W}_u = \boldsymbol{\Theta}^{-1}$ linearly reduce their control signals \mathbf{u} by $\boldsymbol{\Theta}$. The corresponding gain $\mathbf{F}(\bar{\boldsymbol{\rho}}, \boldsymbol{\theta})$ of the state-feedback controller $\mathbf{K}_{\Theta,x}$ is then given by

$$\mathbf{F}(\bar{\boldsymbol{\rho}}, \boldsymbol{\theta}) = -\boldsymbol{\Theta} \underbrace{\gamma^2 \bar{\mathbf{B}}_2^T(\bar{\boldsymbol{\rho}}) \mathbf{Z}(\bar{\boldsymbol{\rho}}, \boldsymbol{\theta})}_{-\mathbf{K}_{\rho,x}}. \quad (2.17)$$

The closed-loop system with controller $\mathbf{K}_{\Theta,x}$ with gain $\mathbf{F}(\bar{\boldsymbol{\rho}}, \boldsymbol{\theta})$ according to (2.17) is visualized in Figure 2.5. Due to the proposed control effort weight each control signal u_i is downscaled by θ_i in the event of saturation and hence, the controller is stable regarding the saturation indicators and avoids excessively large control signals.

The following example emphasizes the advantages of the proposed control effort weight $\mathbf{W}_u(\boldsymbol{\theta})$ in (2.14). The example presents the design of two LPV state-feedback controllers for the LTI spring-mass system with input constraints illustrated in Figure 2.6. The control design minimizes the induced L_2 -norm from the ground disturbance d_g to the body velocity \dot{x}_b . The resonance magnitude of the open-loop spring-mass system is infinite due to the missing damping of the body mass. Consequently, the \mathcal{H}_{∞} -norm of the open-loop system is not defined. The parameters of the spring-mass system are the body mass $m_b = 250$ kg and the spring stiffness $k_b = 30000$ N/m. For the control design, the control force u is scaled to kilo Newton.

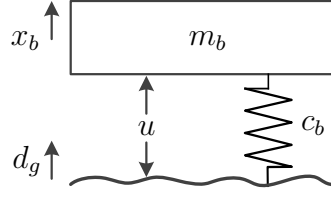


Figure 2.6: Spring-mass system used to illustrate the advantages of the proposed control effort weight $\mathbf{W}_u(\theta)$

The first controller $\bar{\mathbf{K}}_{\theta,x}$ is synthesized from plant $\bar{\mathbf{P}}_{\theta,x}$ given by

$$\begin{bmatrix} \dot{x}_b \\ \ddot{x}_b \\ e_a \\ e_u \end{bmatrix} = \begin{bmatrix} 0 & 1 & 0 & 0 \\ -\frac{k_b}{m_b} & 0 & \frac{k_b}{m_b} & \frac{1000}{m_b}\theta \\ 0 & 0.1\theta & 0 & 0 \\ 0 & 0 & 0 & \theta \end{bmatrix} \begin{bmatrix} x_b \\ \dot{x}_b \\ d_g \\ u \end{bmatrix}, \quad (2.18)$$

with the constant control effort weight $W_u = 1$ and the performance weight $W_a = \theta/10$. This performance weight linearly mitigates the performance requirements depending on the saturation indicator. The second controller $\mathbf{K}_{\theta,x}$ is synthesized from plant $\mathbf{P}_{\theta,x}$ given by

$$\begin{bmatrix} \dot{x}_b \\ \ddot{x}_b \\ e_a \\ e_u \end{bmatrix} = \begin{bmatrix} 0 & 1 & 0 & 0 \\ -\frac{k_b}{m_b} & 0 & \frac{k_b}{m_b} & \frac{1000}{m_b}\theta \\ 0 & 0.1\theta & 0 & 0 \\ 0 & 0 & 0 & 1 \end{bmatrix} \begin{bmatrix} x_b \\ \dot{x}_b \\ d_g \\ u \end{bmatrix}, \quad (2.19)$$

with the control effort weight $W_u = \theta^{-1}$ as proposed in (2.14) and the same performance weight $W_a = \theta/10$. Figure 2.7-top left illustrates the frequency responses from disturbance d_g to body velocity \dot{x}_b of the open-loop plant, and the closed-loop plants with controller $\bar{\mathbf{K}}_{\theta,x}$ and $\mathbf{K}_{\theta,x}$. Due to the cancellation of the saturation indicators in the closed-loop plant with $\bar{\mathbf{K}}_{\theta,x}$, the closed-loop $\Gamma_{ed}(\bar{\mathbf{P}}_{\theta,x}, \bar{\mathbf{K}}_{\theta,x})$ is independent of θ and Figure 2.7-top left shows only one curve. Conversely, the closed-loop system $\Gamma_{ed}(\mathbf{P}_{\theta,x}, \mathbf{K}_{\theta,x})$ depends on the saturation indicator and its frequency behavior is visualized by the frozen closed-loop systems with θ_{\min} and θ_{\max} . Figure 2.7-top right and bottom show a simulation of the decay of the body velocity of the system with an initial body displacement $x_b = 0.1$ m. During the simulation the ground disturbance d_g is zero all the time. The force constraint of the control force u is adjusted to 0.5 kN. The simulation emphasizes the inappropriate behavior of controller $\bar{\mathbf{K}}_{\theta,x}$. In particular, as illustrated in Figure 2.7-bottom left, its control force u increases towards infinity as soon as the control force reaches the force constraint. Accordingly, its saturation indicator violates the specified saturation indicator range $\theta \in [0.1, 1]$ and the LPV controller operates outside its validity range. In contrast, the controller $\mathbf{K}_{\theta,x}$ linearly reduces its control force u depending on the saturation indicator if the control force violates the force constraint. In this way, the

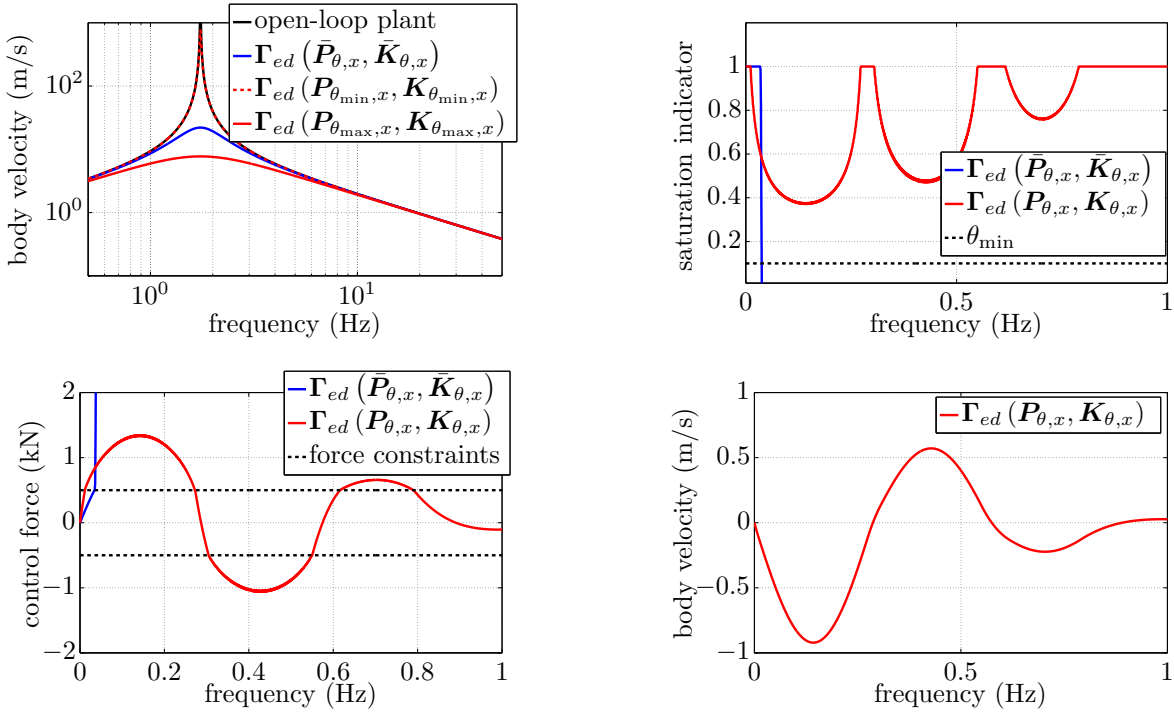


Figure 2.7: LPV control design example emphasizing the advantages of the proposed control effort weight $\mathbf{W}_u(\theta)$: top left - frequency response of frozen LPV systems, top right - saturation indicator trajectory, bottom left - control force, and bottom right - body velocity

control force stays finite and the saturation indicator trajectory depicted in Figure 2.7-top right keeps the validity range of the saturation indicator.

Remark. From the controller equations in (2.12) and (2.17) it can be concluded that the performance weight $\mathbf{W}_a(\theta)$ has no effect on the structure of the controller comparable to the control effort weight $\mathbf{W}_u(\theta)$. Nevertheless, a saturation indicator dependent performance weight $\mathbf{W}_a(\theta)$ should be employed to relax the performance specification in the event of saturation to honor stability over performance.

2.5 Saturation Indicator Grid Density Assessment

As discussed in Appendix A, the grid density is an important design parameter during a gridding-based LPV control approach. On the one hand a fine-meshed grid constitutes a good approximation of the continuous operating range of the controller, while on the other hand a wide-meshed grid with few grid points reduces the computational complexity of the controller synthesis and implementation. The complexity of the synthesis problem is of major interest as it badly scales with the number of states and the number of grid points. This is especially obstructive during the synthesis of LPV controllers with high-order MIMO plant models. Firstly, the high-order plant model yields large LMI conditions and secondly the synthesis problem involves several of these LMI conditions

as discussed in Appendix A.4.6. To emphasize the complexity issue, (2.20) shows the number of LMIs h_P of a synthesis problem with constant Lyapunov matrix and a uniform scheduling parameter grid with h_0 grid points per scheduling parameter ρ_i . The number of LMIs is then determined by

$$h_P = h_0^{n_\rho}, \quad (2.20)$$

and it is obvious that the number of LMIs grows exponentially.

In the special case of a controller design with a constant Lyapunov function, the structure of the closed-loop system can be exploited to state a necessary and sufficient condition for the number of grid points of the saturation indicators $\boldsymbol{\theta}$ guaranteeing quadratic stability of the closed-loop system. Theorem 2.1 states this condition for the state-feedback problem with state-feedback plant $\mathbf{P}_{\Theta,x}$ given by

$$\begin{bmatrix} \dot{\mathbf{x}} \\ \begin{bmatrix} \mathbf{e}_a \\ \mathbf{e}_u \end{bmatrix} \end{bmatrix} = \begin{bmatrix} \mathbf{A}(\bar{\rho}) & \mathbf{B}_1(\bar{\rho}, \boldsymbol{\theta}) & \bar{\mathbf{B}}_2(\bar{\rho}) \boldsymbol{\Theta} \\ \begin{bmatrix} \mathbf{C}_{11}(\bar{\rho}, \boldsymbol{\theta}) \\ \mathbf{0} \end{bmatrix} & \begin{bmatrix} \mathbf{0} \\ \mathbf{0} \end{bmatrix} & \begin{bmatrix} \mathbf{0} \\ \mathbf{I}_{n_u} \end{bmatrix} \end{bmatrix} \begin{bmatrix} \mathbf{x} \\ \mathbf{d} \\ \mathbf{u} \end{bmatrix}. \quad (2.21)$$

This state-feedback plant is derived from (2.15) and thus includes the control effort weight $\mathbf{W}_u(\boldsymbol{\theta}) = \boldsymbol{\Theta}^{-1}$. Compared to (2.15), however, plant (2.21) additionally features a saturation indicator independent system matrix $\mathbf{A}(\bar{\rho})$. This assumptions can be easily satisfied by a proper definition of the saturation indicator dependent weighting function $\mathbf{W}_a(\boldsymbol{\theta})$.

Theorem 2.1 (Minimum grid density for quadratic stability analysis). *Given the open-loop plant $\mathbf{P}_{\Theta,x}$ in (2.21), the scheduling parameters $\boldsymbol{\rho} = [\bar{\rho}^T \boldsymbol{\theta}^T]^T \in \mathcal{P}$ and the performance level $\gamma > 0$. The closed-loop system $\boldsymbol{\Gamma}_{ed}(\mathbf{P}_{\Theta,x}, \mathbf{K}_{\Theta,x})$ is quadratically stable for all $\boldsymbol{\rho} \in \mathcal{P}$ if and only if there exists a positive-definite Lyapunov matrix $\mathbf{Z} > 0$ with $\mathbf{Z} \in \mathbb{R}^{n_x \times n_x}$ and saturation indicators $\boldsymbol{\theta}$ with $\theta_i \in (\theta_{\min}, 1] \quad \forall i \in \{1, 2, \dots, n_u\}$ and $\theta_{\min} \in (0, 1)$ such that the closed-loop $\boldsymbol{\Gamma}_{ed}(\mathbf{P}_{\Theta_{\min},x}, \mathbf{K}_{\Theta_{\min},x})$ with $\boldsymbol{\theta} = \boldsymbol{\theta}_{\min}$ is quadratically stable for all $\bar{\rho} \in \bar{\mathcal{P}}$, i.e.*

$$\mathbf{A}_F^T(\bar{\rho}, \boldsymbol{\theta}_{\min}) \mathbf{Z} + \mathbf{Z} \mathbf{A}_F(\bar{\rho}, \boldsymbol{\theta}_{\min}) < 0, \quad (2.22)$$

with $\mathbf{A}_F(\bar{\rho}, \boldsymbol{\theta}_{\min}) = \mathbf{A}(\bar{\rho}) + \bar{\mathbf{B}}_2(\bar{\rho}) \boldsymbol{\Theta}_{\min} \mathbf{F}(\bar{\rho}, \boldsymbol{\theta}_{\min})$.

Proof. The quadratic stability condition of the closed-loop system $\boldsymbol{\Gamma}_{ed}(\mathbf{P}_{\Theta,x}, \mathbf{K}_{\Theta,x})$ according to (A.6) can be stated as

$$\mathbf{A}_F^T(\bar{\rho}, \boldsymbol{\theta}) \mathbf{Z} + \mathbf{Z} \mathbf{A}_F(\bar{\rho}, \boldsymbol{\theta}) < 0. \quad (2.23)$$

After substituting $\mathbf{A}_F(\bar{\rho}, \boldsymbol{\theta})$ and $\mathbf{F}(\bar{\rho}, \boldsymbol{\theta})$ into (2.23), the condition can be expressed by

$$\mathbf{A}^T(\bar{\rho}) \mathbf{Z} + \mathbf{Z} \mathbf{A}(\bar{\rho}) - \gamma^2 (\bar{\mathbf{B}}_2(\bar{\rho}) \boldsymbol{\Theta} \boldsymbol{\Theta}^T \bar{\mathbf{B}}_2^T(\bar{\rho}) \mathbf{Z})^T \mathbf{Z} - \gamma^2 \mathbf{Z} \bar{\mathbf{B}}_2(\bar{\rho}) \boldsymbol{\Theta} \boldsymbol{\Theta}^T \bar{\mathbf{B}}_2^T(\bar{\rho}) \mathbf{Z} < 0, \quad (2.24)$$

and subsequently using $\mathbf{Z} = \mathbf{Z}^T$ as

$$\mathbf{A}^T(\bar{\rho}) \mathbf{Z} + \mathbf{Z} \mathbf{A}(\bar{\rho}) - 2\gamma^2 \mathbf{Z} \bar{\mathbf{B}}_2(\bar{\rho}) \boldsymbol{\Theta} \boldsymbol{\Theta}^T \bar{\mathbf{B}}_2^T(\bar{\rho}) \mathbf{Z} < 0. \quad (2.25)$$

The third term in (2.25) is positive-definite for all $\bar{\rho} \in \mathcal{P}$ due to

$$\mathbf{H}_\Theta(\bar{\rho}, \boldsymbol{\theta}) = \gamma^2 \mathbf{Z} \bar{\mathbf{B}}_2(\bar{\rho}) \boldsymbol{\Theta} \boldsymbol{\Theta}^T \bar{\mathbf{B}}_2^T(\bar{\rho}) \mathbf{Z} = \mathbf{M}_\Theta(\bar{\rho}, \boldsymbol{\theta}) \mathbf{M}_\Theta^T(\bar{\rho}, \boldsymbol{\theta}) > 0, \quad (2.26)$$

with $\mathbf{M}_\Theta(\bar{\rho}, \boldsymbol{\theta}) = \gamma \mathbf{Z} \bar{\mathbf{B}}_2(\bar{\rho}) \boldsymbol{\Theta}$ and $\gamma > 0$. Using the definition of $\mathbf{H}_\Theta(\bar{\rho}, \boldsymbol{\theta})$, condition (2.25) can be rewritten as

$$\mathbf{A}^T(\bar{\rho}) \mathbf{Z} + \mathbf{Z} \mathbf{A}(\bar{\rho}) - 2\mathbf{H}_\Theta(\bar{\rho}, \boldsymbol{\theta}) < 0. \quad (2.27)$$

The diagonal structure of $\boldsymbol{\Theta}$ introduced in (2.6) can now be exploited to show that

$$\mathbf{H}_\Theta(\bar{\rho}, \boldsymbol{\theta}) > \mathbf{H}_\Theta(\bar{\rho}, \boldsymbol{\theta}_{\min}) > 0. \quad (2.28)$$

To this end, $\mathbf{H}_\Theta(\bar{\rho}, \boldsymbol{\theta})$ must be reformulated as

$$\mathbf{H}_\Theta(\bar{\rho}, \boldsymbol{\theta}) = \gamma^2 \sum_{i=1}^{n_u} \theta_i^2 \mathbf{Z} \bar{\mathbf{B}}_2(\bar{\rho}) \mathbf{E}_i \bar{\mathbf{B}}_2^T(\bar{\rho}) \mathbf{Z} > 0, \quad (2.29)$$

with \mathbf{E}_i defined such that

$$\boldsymbol{\Theta} = \sum_{i=1}^{n_u} \theta_i \mathbf{E}_i, \quad (2.30)$$

e.g. $\mathbf{E}_1 = \text{diag}([1, 0, \dots, 0]^T)$. Each term of (2.29) itself is positive-definite, i.e.

$$\theta_i^2 \mathbf{Z} \bar{\mathbf{B}}_2(\bar{\rho}) \mathbf{E}_i \bar{\mathbf{B}}_2^T(\bar{\rho}) \mathbf{Z} > 0 \quad \forall i \in \{1, 2, \dots, n_u\}, \quad (2.31)$$

and each term of (2.29) is upscaled by θ_i . These properties of $\mathbf{H}_\Theta(\bar{\rho}, \boldsymbol{\theta})$ can be used to conclude that $\mathbf{H}_\Theta(\bar{\rho}, \boldsymbol{\theta}) > \mathbf{H}_\Theta(\bar{\rho}, \boldsymbol{\theta}_{\min})$ as stated in (2.28). Consequently, any positive-definite Lyapunov matrix \mathbf{Z} that renders the closed-loop system $\boldsymbol{\Gamma}_{ed}(\mathbf{P}_{\Theta_{\min}, x}, \mathbf{K}_{\Theta_{\min}, x})$ quadratically stable for all $\bar{\rho} \in \bar{\mathcal{P}}$, also renders the closed-loop system $\boldsymbol{\Gamma}_{ed}(\mathbf{P}_{\Theta, x}, \mathbf{K}_{\Theta, x})$ quadratically stable for all $\bar{\rho} \in \mathcal{P}$. \square

Remark. Even though Theorem 2.1 only states a stability condition and does not consider the induced L_2 -norm performance of the closed-loop system, it essentially facilitates the design of high-order MIMO controllers for plants with actuator saturation. Due to the a priori known grid point $\boldsymbol{\theta} = \boldsymbol{\theta}_{\min}$ required to guarantee quadratic stability, the LPV controller can be synthesized with a loose saturation indicator grid containing $\boldsymbol{\theta} = \boldsymbol{\theta}_{\min}$ for quadratic stability and some additional grid points as required for performance.

Remark. Theorem 2.1 says nothing about the required grid density regarding the scheduling parameters $\bar{\rho}$. Thus the required grid density of these parameters has to be determined during a preliminary analysis as described in Appendix A.4.6.

3 Quarter-Vehicle Control Design

For fundamental investigations, the well-known two-degree-of-freedom quarter-vehicle represents a sufficiently good approximation of the vehicle vertical dynamics. Most constraints and limitations like invariant points are already captured by this rather simple model. Therefore, results and insights obtained within quarter-vehicle applications can be transferred to full-vehicle applications, see e.g. Savaresi et al. (2010) and Guglielmino et al. (2008) for details. As discussed in Chapter 1, the semi-active suspension control problem has been intensively investigated due to its high relevance in automotive suspension development. Most of these investigation have been performed in quarter-vehicle set-ups, as the quarter-vehicle features the following advantages compared to a full-vehicle:

- single control input,
- single road disturbance input,
- medium number of states,
- well-understood system dynamics,
- large and solid collection of control policies, and
- reasonable effort to build a test-rig.

The first three items simplify the control design due to the manageable problem complexity and the following two points facilitate the design of controllers using sophisticated control theory like MPC and LPV due to the vast availability of expert knowledge. The last item concerns the experimental assessment of developed controllers because experimental validation is the mandatory last step to demonstrate a successful control design.

Regarding the development of a full-vehicle controller, which is the ultimate target of this work, the initial development of a quarter-vehicle controller constitutes a good starting point. Firstly, because four quarter-vehicle controllers each applied to one suspension unit of the vehicle can be gathered to form a full-vehicle controller and secondly because the control design methods developed in quarter-vehicle applications can be readily extended to the design of full-vehicle controllers.

3.1 Quarter-Vehicle Control Structure

The structure of the Disturbance-Information (DI) LPV controller consisting of the state-observer and the state-feedback controller is illustrated in Figure 3.1. The state-observer estimates the current plant states $\hat{\mathbf{x}}$ using the plant measurements \mathbf{y} and the exogenous scheduling parameter $\boldsymbol{\rho}$. Based on the estimated states $\hat{\mathbf{x}}$ and the exogenous scheduling parameters $\boldsymbol{\rho}$, the state-feedback controller calculates the optimal damper force F_{sa} . As discussed later on in Section 3.5, the augmented plant used for the LPV control design gathers the saturation block, the inverse damper model and the plant. In this way, the

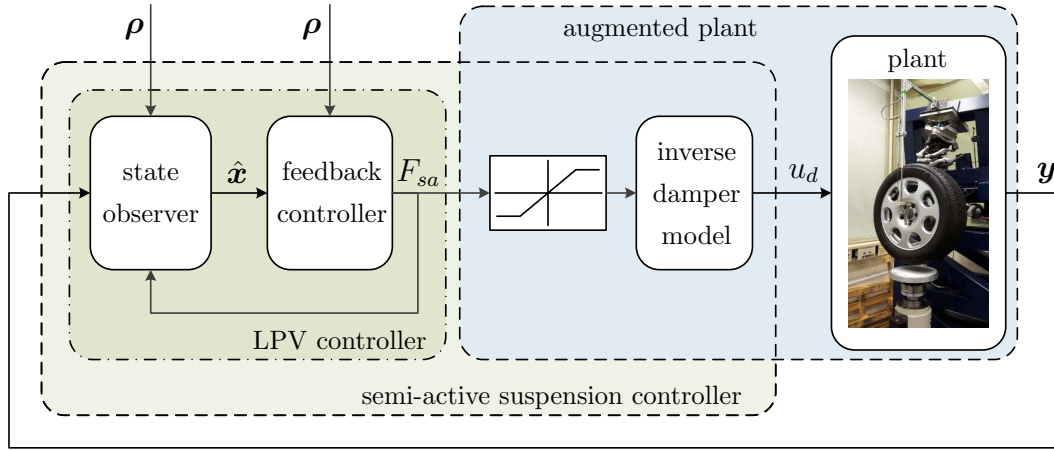


Figure 3.1: Disturbance-Information structure of quarter-vehicle LPV controller

damper force F_{sa} forms the interface between the LPV controller and the augmented plant. The inverse damper subsystem transforms the constrained damper force demand $\sigma(F_{sa})$ of the controller into the current demand u_d of the semi-active damper using the estimated states $\hat{\mathbf{x}}$. The actual implementation of the semi-active suspension controller depicted in light green is comprised of the LPV controller, the saturation block and the inverse damper subsystem.

3.2 Performance Criteria

A systematic system design necessitates the quantitative description of the design goals of the system. In the suspension design context, the major design objectives are ride comfort and road-holding. Additionally, the suspension deflection can become relevant in applications with restrictive minimum and maximum suspension deflection bounds.

According to ISO (2631-1:1997), ride comfort of vehicle passengers can be characterized by their experienced accelerations. In general, this includes translational and rotational accelerations along all six degrees-of-freedom (DoF). In a quarter-vehicle application, however, the body mass has just the vertical, translational DoF and the best approximation of ride comfort is achieved by assuming that the accelerations experienced by the passenger are equal to the body mass accelerations of the quarter-vehicle. These accelerations can be stochastically evaluated as described in ISO (2631-1:1997) by the root mean square (RMS) value of the signal. In contrast to the sophisticated procedure of ISO (2631-1:1997), the ride comfort criterion calculation employed in this section neglects the band-limiting prefiltering step and also the frequency weighting of the signal. The quantitative representation of ride comfort J_c is given by

$$J_c = \sqrt{\frac{1}{T} \int_0^T |\ddot{x}_b|^2 dt}. \quad (3.1)$$

The road-holding capability defines the longitudinal and lateral force potential $F_{t,xy}$ of the

vehicle tires and is directly related to ride safety. The dependence of the force potential $F_{t,xy}$ on the vertical tire force $F_{t,z}$, called wheel load, through the road friction coefficient μ_r is given by

$$F_{t,xy} = \mu_r F_{t,z}, \quad (3.2)$$

with the total wheel load comprised of the static wheel load $F_{wl,stat}$ and the dynamic wheel load $F_{wl,dyn}$ according to

$$F_{t,z} = F_{wl,stat} + F_{wl,dyn}. \quad (3.3)$$

The static wheel load of a tire is solely determined by the vehicle mass and its distribution to the front, rear, left and right suspensions. Generally, the static wheel load cannot be influenced by suspension elements like springs, dampers or actuators. Conversely, the dynamic wheel load is affected by these suspension elements and of essential interest during the design of suspension systems. In the following only the road-holding ability regarding the dynamic wheel load is considered as design criterion and the notation wheel load is used for the dynamic wheel load, i.e. $F_{wl} = F_{wl,dyn}$. Eq. (3.2) immediately suggests to define the road-holding criterion as the integral of the dynamic wheel load such that a maximization of the criterion improves road-holding. Unfortunately, this criterion is difficult to evaluate because it distinguishes between the sign of the dynamic wheel load and cannot be formulated as a signal norm. Additionally, for the most common road excitations, namely stochastic road excitations, the integral of the dynamic wheel load over infinite time is zero, meaning that the positive dynamic wheel loads, which improve road-holding, cannot be increased without equivalently increasing the negative dynamic wheel loads, which deteriorate road-holding. Therefore, the variation of the dynamic wheel load should be reduced and the road-holding criterion J_{rh} can be quantitatively represented by the RMS value of the dynamic wheel load according to

$$J_{rh} = \sqrt{\frac{1}{T} \int_0^T |F_{wl}|^2 dt}. \quad (3.4)$$

This definition of the road-holding criterion can be also found in Savaresi et al. (2010, p. 95).

The exploitation of the minimum and maximum suspension deflection constitutes the third criterion to be considered during suspension design. The suspension deflection is bounded by bump-stops leading to large suspension forces and large body accelerations when these bump-stops are reached during operation. Consequently, excessively large suspension deflections deteriorate ride comfort and reduce the durability of the suspension system. The exploitation of the suspension deflection range, called deflection usage J_d , can quantitatively be characterized by the RMS value of the suspension deflection x_d according to

$$J_d = \sqrt{\frac{1}{T} \int_0^T |x_d|^2 dt}. \quad (3.5)$$

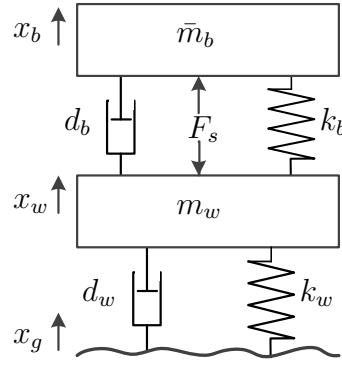


Figure 3.2: Sketch of the quarter-vehicle model

When stochastically evaluated, the criteria J_c , J_{rh} and J_d determine the *one sigma* bound of their corresponding signals, which is tantamount to the signal values being 68.3 % of the time smaller than the criteria value.

3.3 LTI Quarter-Vehicle Model

From a mechanical point of view the linear quarter-vehicle model is essentially a two-mass spring-damper system as depicted in Figure 3.2. The upper mass denoted by \bar{m}_b represents the vehicle body and the lower mass denoted by m_w represents the wheel. In the general configuration of Figure 3.2, both masses are coupled by a linear spring-damper element with spring stiffness k_b and damping coefficient d_b . Additionally, a suspension force F_s can act between both masses. The tire transmits the road disturbances d_g to the wheel. The tire is approximated as a linear spring-damper element with spring stiffness k_w and damping coefficient d_w . The position of the body mass \bar{m}_b and the wheel mass m_w with respect to the equilibrium point of the two-mass system are labeled by x_b and x_w . A detailed introduction to the quarter-vehicle and to suspension systems can be found in Mitschke and Wallentowitz (2004), Isermann (2005) and Savaresi et al. (2010, p. 41 ff.). The quarter-vehicle dynamics equation can be derived by applying Newtons' second law to the body and wheel masses. After reformulating these two equations, the differential equation of the quarter-vehicle can be expressed as

$$\dot{\mathbf{x}} = \mathbf{A}\mathbf{x} + \mathbf{B}_1 d_g + \mathbf{B}_2 F_s, \quad (3.6)$$

with the system states $\mathbf{x} = [x_b \ \dot{x}_b \ x_w \ \dot{x}_w \ x_g]^T$, and the matrices

$$\mathbf{A} = \begin{bmatrix} 0 & 1 & 0 & 0 & 0 \\ \frac{-k_b}{\bar{m}_b} & \frac{-d_b}{\bar{m}_b} & \frac{k_b}{\bar{m}_b} & \frac{d_b}{\bar{m}_b} & 0 \\ 0 & 0 & 0 & 1 & 0 \\ \frac{k_b}{m_w} & \frac{d_b}{m_w} & \frac{-k_b - k_w}{m_w} & \frac{-d_b - d_w}{m_w} & \frac{k_w}{m_w} \\ 0 & 0 & 0 & 0 & 0 \end{bmatrix}, \quad (3.7)$$

$$\mathbf{B}_1 = \begin{bmatrix} 0 & 0 & 0 & \frac{d_w}{m_w} & 1 \end{bmatrix}^T \text{ and} \quad (3.8)$$

$$\mathbf{B}_2 = \begin{bmatrix} 0 & \frac{1}{m_b} & 0 & \frac{-1}{m_w} & 0 \end{bmatrix}^T. \quad (3.9)$$

The quarter-vehicle has some interesting properties which affect the design of a semi-active suspension controller. The first property to be discussed concerns the calculation of the dynamic wheel load. On the one hand, the dynamic wheel load can be calculated from the tire properties according to

$$F_{wl} = -k_w x_t - d_w \dot{x}_t, \quad (3.10)$$

with the tire deflection x_t defined as the difference between the wheel and road position $x_t = x_w - x_g$. On the other hand, the dynamic wheel load can be expressed as a function of the body and wheel accelerations without any knowledge of the tire properties according to

$$F_{wl} = \bar{m}_b \ddot{x}_b + m_w \ddot{x}_w. \quad (3.11)$$

The latter equation of the dynamic wheel load establishes a direct relation between the body acceleration, the wheel acceleration and the dynamic wheel load and emphasizes the coupling between the ride comfort and road-holding criteria. In particular, (3.11) shows that a reduction of the body acceleration while maintaining the same wheel acceleration yields an improvement of both criteria. Unfortunately, during the design of a semi-active suspension the body acceleration cannot be reduced without interference to the wheel acceleration.

The frequency responses of the body acceleration and the dynamic wheel load of a passive suspension are subject to a waterbed effect. Therefore, it is impossible to simultaneously reduce the frequency response magnitude at all frequencies. Figure 3.3 illustrates the waterbed effect for a variation of the body damping coefficient d_b of the quarter-vehicle. This analysis shows the limits of suspension systems with passive dampers and presents some helpful insights into the system dynamics. Additionally, passive suspension configurations will be extensively used as benchmark for the evaluation of the LPV controllers. The transfer functions from the road disturbance to the body acceleration, Figure 3.3-top left, and to the dynamic wheel load, Figure 3.3-top right, have two magnitudes, which are invariant against variations of the damping coefficient. This property was theoretically investigated in Hedrick and Butsuen (1990) and is discussed in detail in (Savaresi et al., 2010, p. 46 ff.). In the example shown in Figure 3.3, the first invariant point is located at a frequency slightly higher than the resonance peak of the body mass and the second invariant point is located near the resonance frequency of the wheel mass. As obvious from Figure 3.3 the waterbed effect leads to a simultaneous increase in magnitude in the intermediate and high frequency range if the resonance peaks are reduced by a higher damping coefficient. Consequently, the design of a passive suspension regarding ride comfort and

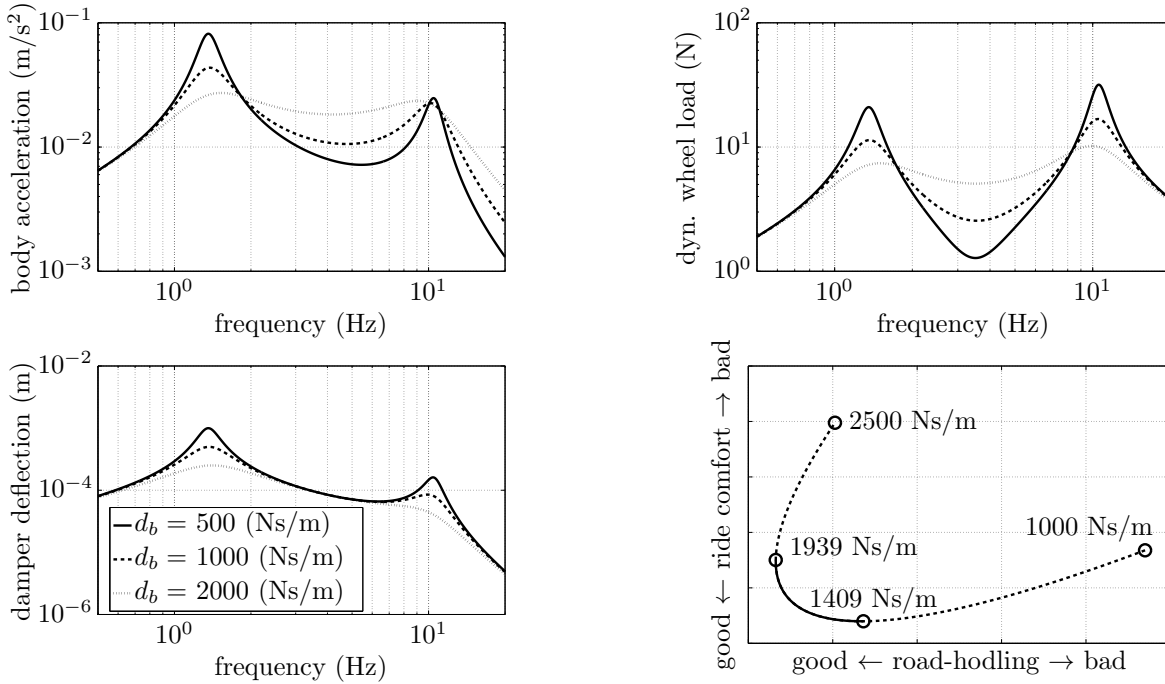


Figure 3.3: Waterbed effect of frequency responses of quarter-vehicle subject to road disturbances d_g due to variation of damping coefficient d_b ; top left - frequency response of body acceleration, top right - frequency response of dynamic wheel load, bottom left - frequency response of damper deflection, and bottom right - trade-off ride comfort vs road-holding

road-holding involves a trade-off between small resonance peak magnitudes, especially of the body mass resonance peak, and the deterioration of the isolation against road disturbances in the intermediate and high frequency range. Figure 3.3-bottom right shows the conflict diagram corresponding to a variation of the damping coefficient from $d_b = 1000$ Ns/m to $d_b = 2500$ Ns/m. The conflict diagram confirms the observation from (3.11) that ride comfort and road-holding can be improved simultaneously (dashed black line) if the damping coefficient is far from the optimum, but optimal ride comfort and road-holding cannot be achieved at the same time (solid black line). During the design of semi-active suspensions, the area of interest in the conflict diagram is mainly the trade-off region between ride comfort and road-holding represented by the solid black line. In contrast to the frequency responses of body acceleration and dynamic wheel load, the frequency response of the damper deflection $x_d = x_b - x_w$ shows no waterbed effect and an increase in damping yields a consistent reduction of the damper deflection magnitude. Nevertheless, there is a design conflict between ride comfort and road-holding on the one side and damper deflection on the other, because ride comfort and road-holding drastically deteriorate once the damping coefficient increases beyond a certain level.

In model-based semi-active damper control, the damper is considered as a force actuator with input constraints rather than as a device to continuously change the damping. The

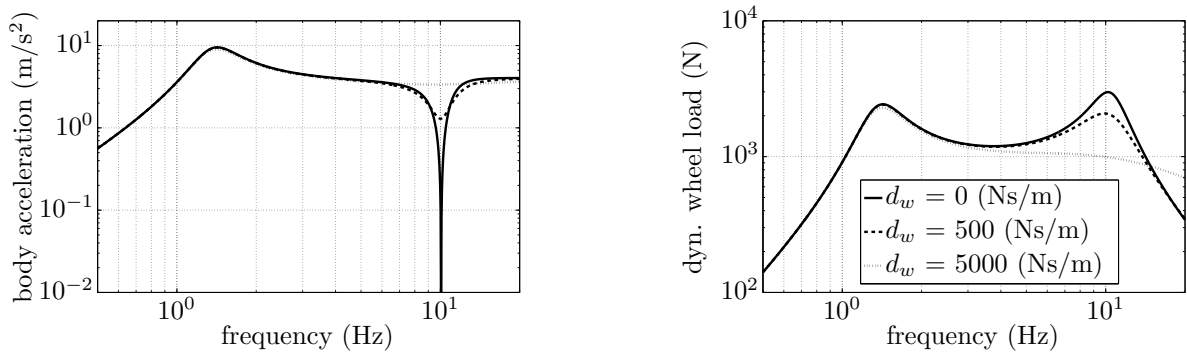


Figure 3.4: Effect of tire damping on frequency responses of quarter-vehicle with suspension force input F_s ; left - frequency response of body acceleration, right - frequency response of dynamic wheel load

interpretation as force actuator with constraints is natural, because a semi-active damper can generate arbitrary forces inside its limits. The analysis of the system behavior subject to a varying damping coefficient given in Figure 3.3 only provides the first part of the necessary system understanding. The second part presents the analysis of the system properties considering the suspension force F_s as input which is depicted in Figure 3.4. The transfer function on the left of Figure 3.4 shows a transmission zero of the suspension force F_s regarding the body acceleration for zero tire damping $d_w = 0$ Ns/m. The reduction of the gain of the suspension force on the body acceleration stays significant for a tire damping up to $d_w = 500$ Ns/m. In vehicle applications, the tire damping is normally smaller than $d_w = 500$ Ns/m. Most investigations in the literature even neglect the tire damping at all, e.g. Savaresi et al. (2010, p. 44 ff.). The efficiency loss of the suspension force regarding the body acceleration near the wheel mass resonance peak imposes vital challenges during an induced L_2 -norm control design, because the input-output behavior of the system can hardly be changed by the suspension actuator. Conversely, the transfer function of the dynamic wheel load shows no efficiency loss of the suspension actuator. Based on the quarter-vehicle system properties, the following performance specification for semi-active suspension control design can be derived:

ride comfort: performance outputs related to ride comfort should emphasize the body resonance peak and roll-off at about 3 Hz,

road-holding: performance outputs related to road-holding should emphasize the body and wheel resonance peaks, and roll-off beyond the wheel resonance frequency,

suspension usage: performance outputs related to suspension usage should emphasize the body and wheel resonance peaks, and roll-off beyond the wheel resonance frequency.

The specification regarding ride comfort is obvious from Figure 3.3-top left and Figure 3.4-left. In the frequency range between both resonance peaks the smallest body acceleration

magnitudes are achieved by the smallest possible damper forces. This cannot be overcome by a semi-active damper due to its inherent force limits. Additionally, the frequency response magnitude of the wheel resonance peak can hardly be reduced due to the poor actuator efficiency in this frequency region. Consequently, the best that a ride comfort oriented controller can achieve is to roll-off after the body resonance frequency. Regarding road-holding and suspension usage the performance specification is not that involved. The control objective is simply a reduction of both resonance peaks with a simultaneous sufficiently fast controller roll-off.

3.4 Skyhook-Groundhook Control

The Skyhook (SH) control policy introduced by Karnopp et al. (1974) constitutes the to-date state-of-the-art in semi-active suspension control in production vehicles. It follows from a result of optimal quadratic control of a one-mass system which states that the body velocity can be best minimized by a Skyhook damper, i.e. a damper between the body mass and an inertial reference frame. In the context of vehicle applications, a Skyhook damper cannot be realized, but it can be approximated by a semi-active damper mounted between body and wheel mass. The semi-active suspension operated by the Skyhook control policy aims at a reduction of the body resonance peak and hence at improved ride comfort.

Conversely, the Groundhook (GH) control policy developed in Valášek et al. (1997) aims at a reduction of the dynamic wheel load to improve road-holding. This is achieved by approximating a Groundhook damper acting between ground and wheel by the semi-active damper. Savaresi et al. (2010, p. 108 ff.) provide an overview about the Skyhook and Groundhook control concepts and give a performance evaluation of both concepts compared to passive suspension setups. In this thesis, the Skyhook and Groundhook controllers are implemented in the control structure shown in Figure 3.1. The output signal of the controllers is a damper force demand similar to Unger et al. (2013, p. 4). Starting from Savaresi et al. (2010, p. 108 ff.), the Skyhook control law can be expressed by

$$F_{sa,SH} = \begin{cases} F_{d,\min} & \dot{x}_b \dot{x}_d \leq 0 \\ F_{SH} & \dot{x}_b \dot{x}_d > 0 \end{cases}, \quad (3.12)$$

with the Skyhook force $F_{SH} = d_{SH} \dot{x}_b$ computed from the body velocity \dot{x}_b and the Skyhook damping $d_{SH} \geq 0$. Similarly, the Groundhook control law can be expressed by

$$F_{sa,GH} = \begin{cases} F_{d,\min} & -\dot{x}_w \dot{x}_d \leq 0 \\ F_{GH} & -\dot{x}_w \dot{x}_d > 0 \end{cases}, \quad (3.13)$$

with the Groundhook force $F_{GH} = d_{GH} \dot{x}_w$ computed from the wheel velocity \dot{x}_w and the Groundhook damping $d_{GH} \geq 0$. In (3.12) and (3.13), $F_{d,\min}$ denotes the minimum absolute damper forces.

As proposed by Ahmadian and Blanchard (2011, p. 223), a combined Skyhook-Groundhook (SH/GH) control policy can be realized by superposition of the Skyhook controller given in (3.12) and the Groundhook controller given in (3.13) according to

$$F_{sa} = F_{sa,SH} + F_{sa,GH}. \quad (3.14)$$

The hybrid controller collapses to the pure Skyhook controller given in (3.12) for $d_{GH} = 0$ and to the pure Groundhook controller given in (3.13) for $d_{SH} = 0$. Skyhook and Groundhook damping values larger than zero yield a controller that simultaneously approximates the Skyhook damper and the Groundhook damper.

3.5 Quarter-Vehicle LPV Control Design

This section presents the design of a quarter-vehicle DI LPV controller as introduced in Chapter 2 and Appendix A. The DI problem represents a special type of output-feedback control problem. It is extensively discussed in Doyle et al. (1989) and Prempain and Postlethwaite (2001) where it is referred to as Disturbance-Feedforward problem. One advantageous property of DI controllers is that they can be constructed by the sequential synthesis of a full-order state-observer and a state-feedback controller. In contrast to ad-hoc observer-based state-feedback controllers, DI controllers achieve a guaranteed performance index γ of the closed-loop equivalently to general output-feedback controllers. Specifically, this section particularizes the quarter-vehicle semi-active LPV control approach published in Fleps-Dezasse et al. (2016).

As a first step, the LTI quarter-vehicle state-space model \mathbf{G}_{qv} with general suspension force input F_s discussed in Section 3.3 is adapted to a semi-active damper force input F_{sa} as depicted in Figure 3.5. The augmented quarter-vehicle plant $\bar{\mathbf{G}}_{sa}$ with semi-active damper force input considers the damper force dynamics $G_{u_d}(s)$ and the damper force limitations. The nonlinear control signal to damper force behavior of the force map f_{2D} of the semi-active damper, however, is canceled by the control signal map g_{2D} as described in (B.5).

According to the passivity constraint of the semi-active damper, the damper force F_{sa} is limited to the first and third quadrant of the force map shown in Appendix B Figure B.3. This asymmetry is obstructive for the synthesis of an LPV controller using saturation indicators to model the actuator force limits. To obtain an eligible representation the QVM plant $\bar{\mathbf{G}}_{sa}$ is transformed as follows: the damper force F_{sa} generated by the semi-active damper is split into a virtual control force u_{F_d} and a nominal damper force F_0

$$F_{sa} = F_0 + u_{F_d}, \quad (3.15)$$

with $F_0 = -d_0(\mathbf{x}(t))\dot{x}_d$ and the damper velocity $\dot{x}_d = \dot{x}_b - \dot{x}_w$. For a suitable problem formulation, the force constraints of the virtual control signal u_{F_d} should be such that the upper force limit $u_{F_d,\max}$ is greater than zero $u_{F_d,\max} > 0$ and the lower force limit $u_{F_d,\min}$ is smaller than zero $u_{F_d,\min} < 0$. For general semi-active damper force maps, this can be

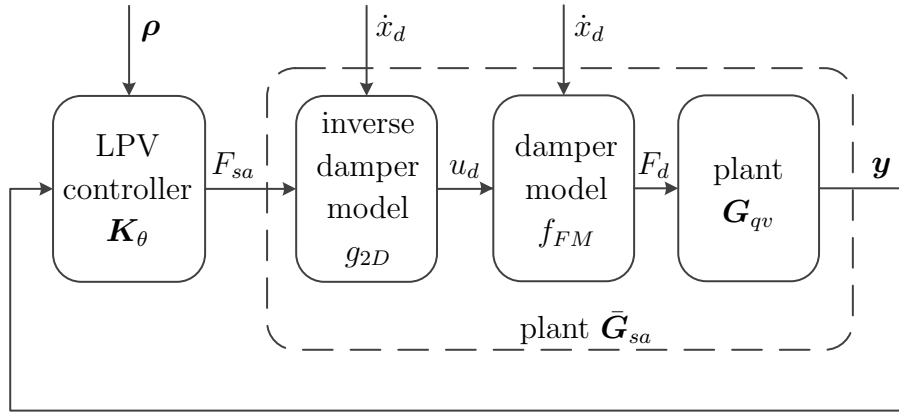


Figure 3.5: Control structure of quarter-vehicle semi-active suspension control

realized by utilizing a nonlinear nominal damper force characteristic with a time-varying damping coefficient $d_0(\mathbf{x}(t))$. Figure 3.6 illustrates the effect of the nonlinear nominal damper force F_0 on the force limits of the virtual control force u_{F_d} . Compared to the original force limits of F_{sa} , the force limits of u_{F_d} are shifted to all four quadrants of the force map. In contrast to previous works utilizing such a shift towards a virtual control input with a constant nominal damping like Poussot-Vassal et al. (2008, p. 1525), a time-varying nominal damping coefficient $d_0(\mathbf{x}(t))$ readily extends the anti-windup LPV controller design presented in Wu et al. (2000) to general semi-active damper applications. According to Section 2.3, the constrained virtual control force $\sigma(u_{F_d})$ can now be expressed as a function of the saturation indicator θ by

$$\sigma(u_{F_d}) = \theta u_{F_d}, \quad (3.16)$$

with

$$\theta = \frac{\sigma(u_{F_d})}{u_{F_d}}. \quad (3.17)$$

The dynamics of control signal changes modeled by $G_{u_d}(s)$ in the force map damper model f_{FM} is approximated by a first-order dynamics of the virtual control force u_{F_d} with bandwidth ω_d according to

$$\dot{x}_{F_d} = \omega_d (u_{F_d} - x_{F_d}), \quad (3.18)$$

with the virtual damper force state x_{F_d} . The LPV plant $\bar{\mathbf{G}}_{sa}$ with the saturation indicator θ and saturation transformer d_0 can be stated by

$$\dot{\mathbf{x}} = \mathbf{A}(d_0) \mathbf{x} + \bar{\mathbf{B}}_2 \theta u_{F_d}, \quad (3.19)$$

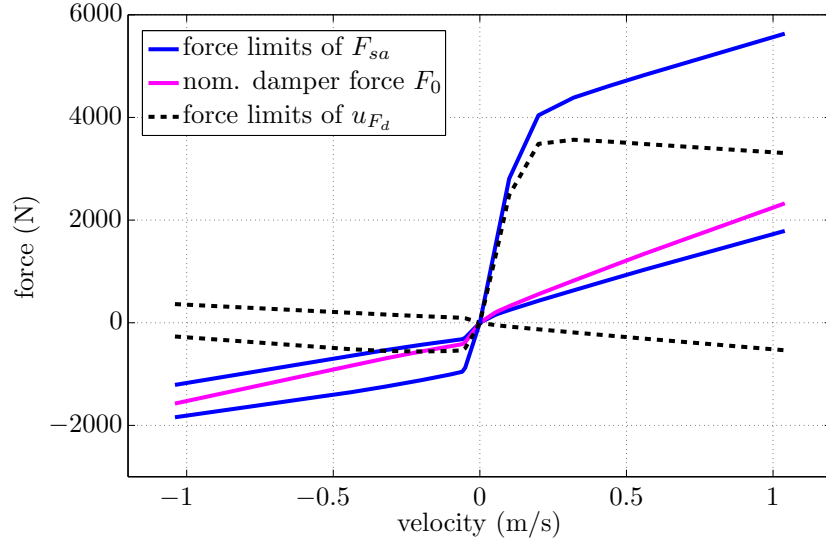


Figure 3.6: Transformation of actuator force limits by time-varying nominal damping coefficient $d_0(\mathbf{x}(t))$ called saturation transformer

with the system states $\mathbf{x} = [x_b \ \dot{x}_b \ x_w \ \dot{x}_w \ x_{F_d}]^T$, and the matrices

$$\mathbf{A}(d_0) = \begin{bmatrix} 0 & 1 & 0 & 0 & 0 \\ \frac{-k_b}{m_b} & \frac{-d_0}{m_b} & \frac{k_b}{m_b} & \frac{d_0}{m_b} & \frac{1}{m_b} \\ 0 & 0 & 0 & 1 & 0 \\ \frac{k_b}{m_w} & \frac{d_0}{m_w} & \frac{-k_b - k_w}{m_w} & \frac{-d_0 - d_w}{m_w} & -\frac{1}{m_w} \\ 0 & 0 & 0 & 0 & -\omega_d \end{bmatrix} \quad \text{and} \quad (3.20)$$

$$\bar{\mathbf{B}}_2 = [0 \ 0 \ 0 \ 0 \ \omega_d]^T. \quad (3.21)$$

Remark. The control force transformation by saturation transformers can be easily used to achieve an eligible virtual control force u_{virtual} of force actuators with arbitrary time-varying constraints. In the general case, the control force shift is then performed by a saturation transformer $\delta_u(t)$ according to

$$u_{\text{original}} = \delta_u(t) + u_{\text{virtual}}. \quad (3.22)$$

3.5.1 State-Observer Design

The state-observer of the open-loop plant $\bar{\mathbf{G}}_{sa}$ is synthesized according to Appendix A.4.1 and A.4.2. Figure 3.7 shows the detailed general control structure of the observer problem with the road disturbance input d_g , the measurement disturbances \mathbf{d}_n and the performance output $\Delta \mathbf{e}$. For the observer design, the performance output simply consists of the estimation error between the plant states \mathbf{x} and the observer states $\hat{\mathbf{x}}$ according to

$$\Delta \mathbf{e} = \mathbf{W}_e (\mathbf{x} - \hat{\mathbf{x}}). \quad (3.23)$$

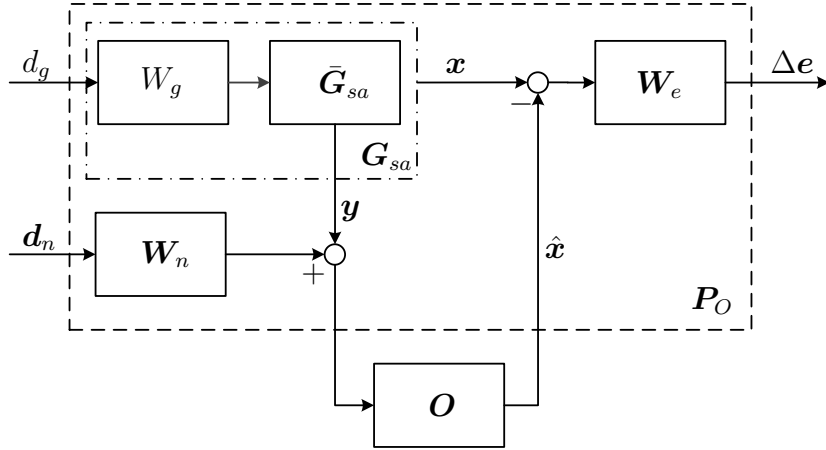


Figure 3.7: Weighting scheme of quarter-vehicle state-observer design

The diagonal weighting matrix $\mathbf{W}_e = \text{diag}([w_{e,1}, \dots, w_{e,n_x}]^T)$ prioritizes the estimation error of distinct states according to the values of the diagonal entries $w_{e,i}$. In the same way, the diagonal weighting matrix $\mathbf{W}_n = \text{diag}([w_{n,1}, \dots, w_{n,n_y}]^T)$ scales the measurement disturbances \mathbf{d}_n . The road disturbance weight W_g is realized as stated in (C.6) as a first-order filter that shapes the road disturbance amplitudes according to the power spectral densities (PSD) of real roads reported by ISO (8608:1995). This weighting filter introduces an additional state x_g into $\bar{\mathbf{G}}_{sa}$ which is also estimated by the observer \mathbf{O} as shown in Figure 3.7. Instead of the vehicle speed, the disturbance input filter W_g uses a fixed reference velocity, i.e. $v_v = v_{\text{ref}}$ such that the vehicle speed dependence of the road model does not introduce an additional scheduling parameter. Due to this approximation the velocity dependent increase in magnitude of the road disturbances is neglected and the observer design only considers a static trade-off between road disturbances and measurement disturbances. The reference velocity v_{ref} should thus be selected around 100 km/h to give a good approximation of the entire velocity related operating range of passenger cars.

The state-observer design assumes measurements of the body acceleration $y_{\ddot{x}_b}$, the wheel acceleration $y_{\ddot{x}_w}$ and the damper velocity $y_{\dot{x}_d}$. According to (A.30), the generalized plant \mathbf{P}_O of the observer synthesis can be stated by

$$\begin{bmatrix} \Delta \dot{\mathbf{x}} \\ \Delta \mathbf{e} \\ \Delta \mathbf{y} \end{bmatrix} = \begin{bmatrix} \mathbf{A}(d_0) & \mathbf{B}_1 & \mathbf{I} \\ \mathbf{C}_1 & \mathbf{0} & \mathbf{0} \\ \mathbf{C}_2(d_0) & \mathbf{D}_{21} & \mathbf{0} \end{bmatrix} \begin{bmatrix} \Delta \mathbf{x} \\ \mathbf{d} \\ \Delta \mathbf{v} \end{bmatrix}. \quad (3.24)$$

with $\Delta \mathbf{x}$ the difference between the plant and observer states and $\Delta \mathbf{y}$ the difference between the plant measurements and the estimated measurements of the observer. The disturbance inputs \mathbf{d} of \mathbf{P}_O are $\mathbf{d} = [d_g \ d_{n,\ddot{x}_b} \ d_{n,\ddot{x}_w} \ d_{n,\dot{x}_d}]^T$ and the system matrices are

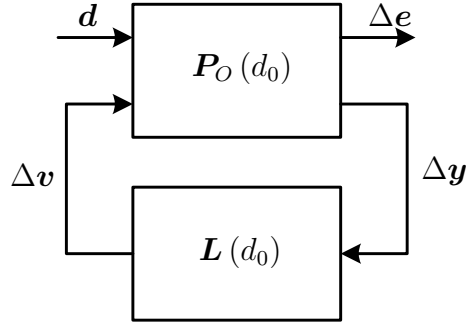


Figure 3.8: General control configuration of quarter-vehicle state-observer problem

given by

$$\mathbf{A}(d_0) = \begin{bmatrix} 0 & 1 & 0 & 0 & 0 & 0 \\ \frac{-k_b}{m_b} & \frac{-d_0}{m_b} & \frac{k_b}{m_b} & \frac{d_0}{m_b} & \frac{1}{m_b} & 0 \\ 0 & 0 & 0 & 1 & 0 & 0 \\ \frac{k_b}{m_w} & \frac{d_0}{m_w} & \frac{-k_b-k_w}{m_w} & \frac{-d_0-d_w}{m_w} & -\frac{1}{m_w} & \frac{k_w-d_w\beta_r v_{\text{ref}}}{m_w} \\ 0 & 0 & 0 & 0 & -\omega_d & 0 \\ 0 & 0 & 0 & 0 & 0 & -\beta_r v_{\text{ref}} \end{bmatrix}, \quad (3.25)$$

$$\mathbf{B}_1 = \begin{bmatrix} 0 & 0 & 0 & \frac{d_w \alpha_r v_{\text{ref}}}{m_w} & 0 & \alpha_r v_{\text{ref}} \\ 0 & 0 & 0 & 0 & 0 & 0 \\ 0 & 0 & 0 & 0 & 0 & 0 \\ 0 & 0 & 0 & 0 & 0 & 0 \end{bmatrix}^T, \quad (3.26)$$

$$\mathbf{C}_1 = \mathbf{W}_e = \text{diag}([w_{e,1}, \dots, w_{e,n_x}]^T), \quad (3.27)$$

$$\mathbf{C}_2(d_0) = \begin{bmatrix} \frac{-k_b}{m_b} & \frac{-d_0}{m_b} & \frac{k_b}{m_b} & \frac{d_0}{m_b} & \frac{1}{m_b} & 0 \\ \frac{k_b}{m_w} & \frac{d_0}{m_w} & \frac{-k_b-k_w}{m_w} & \frac{-d_0-d_w}{m_w} & -\frac{1}{m_w} & \frac{k_w-d_w\beta_r v_{\text{ref}}}{m_w} \\ 0 & 1 & 0 & -1 & 0 & 0 \end{bmatrix} \text{ and} \quad (3.28)$$

$$\mathbf{D}_{21} = \begin{bmatrix} 0 & w_{n,\ddot{x}_b} & 0 & 0 \\ \frac{d_w \alpha_r v_{\text{ref}}}{m_w} & 0 & w_{n,\ddot{x}_w} & 0 \\ 0 & 0 & 0 & w_{n,\dot{x}_d} \end{bmatrix}. \quad (3.29)$$

The states \mathbf{x} of the open-loop plant \mathbf{G}_{sa} are $\mathbf{x} = [x_b \dot{x}_b x_w \dot{x}_w x_{F_d} x_g]^T$ and the corresponding measurements are $\mathbf{y} = [y_{\ddot{x}_b} y_{\ddot{x}_w} y_{\dot{x}_d}]^T$. The generalized plant \mathbf{P}_O given in (3.24) - (3.29) exhibits just the saturation transformer scheduling parameter d_0 because the saturation indicator θ only occurs in the input matrix $\mathbf{B}_2 = \bar{\mathbf{B}}_2 \theta$. Consequently, the LPV observer synthesis considers one scheduling parameter, namely d_0 as illustrated in Figure

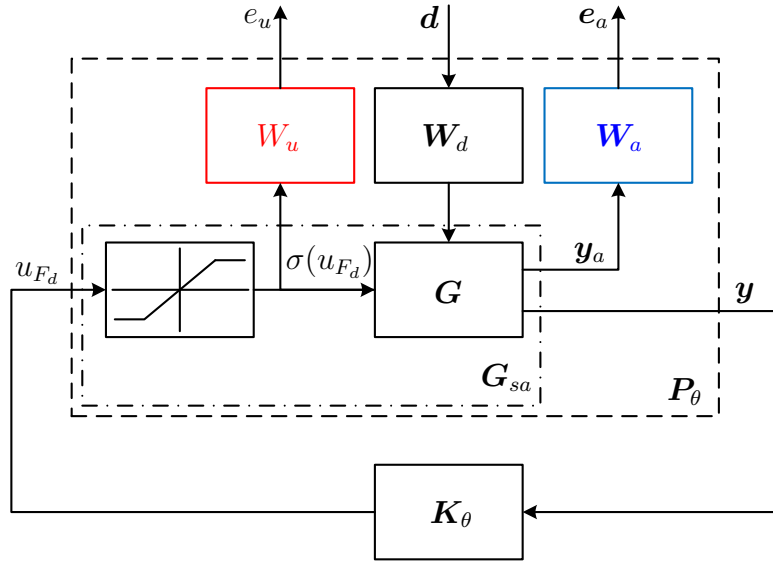


Figure 3.9: Mixed sensitivity weighting scheme of quarter-vehicle LPV controller design

3.8. The observer synthesis is performed with a linear parameter-dependent Lyapunov matrix $\mathbf{Y}(d_0)$ stated by

$$\mathbf{Y}(d_0) = \mathbf{Y}_0 + d_0 \mathbf{Y}_1, \quad (3.30)$$

and a grid density of two points. After determination of the tuning parameters, the observer synthesis is verified with a denser grid featuring $h_P = 10$ grid points.

The tuning parameters of the observer problem are

- the scaling factors of the state-estimation errors $w_{e,1}, \dots, w_{e,n_x}$,
- the scaling factors of the measurement disturbances $w_{n,1}$, $w_{n,2}$ and $w_{n,3}$, and
- the parameters of the road model β_r , α_r and v_{ref} .

The determination of optimal values of these tuning parameters is discussed later on in Section 3.6.

3.5.2 DI Controller Design

This section presents the actual semi-active suspension DI LPV controller design based on the theory introduced in Section 2.4 and Appendix A.4.4. The controller is designed along a mixed sensitivity S/KS loop shaping scheme as discussed in Kwakernaak (1993, p. 261) and Skogestad and Postlethwaite (2005, p. 392 ff.). The design scheme is adapted to the special case of semi-active suspension control, e.g. pure disturbance rejection without any reference tracking.

Figure 3.9 illustrates the detailed general control configuration of the mixed sensitivity S/KS scheme consisting of the unconstrained open-loop plant \mathbf{G} , the constrained open-loop plant \mathbf{G}_{sa} , the generalized plant \mathbf{P}_θ , and the DI controller \mathbf{K}_θ . The constrained open-loop plant \mathbf{G}_{sa} is excited by the disturbances \mathbf{d} shaped by the weighting function \mathbf{W}_d . According to the mixed sensitivity S/KS scheme, the overall performance outputs \mathbf{e} are distinct into the control effort e_u shaped by \mathbf{W}_u and the actual performance signals \mathbf{e}_a shaped by \mathbf{W}_a . The S/KS mixed sensitivity design problem of Figure 3.9 with the closed-loop system denoted by $\mathbf{\Gamma}_{ed}(\mathbf{P}_\theta, \mathbf{K}_\theta)$ can be stated as

$$\|\mathbf{\Gamma}_{ed}(\mathbf{P}_\theta, \mathbf{K}_\theta)\|_{i2} = \left\| \begin{bmatrix} \mathbf{W}_1 & \mathbf{0} \\ \mathbf{0} & \mathbf{W}_2 \end{bmatrix} \mathbf{S}_a \begin{bmatrix} \mathbf{V}_1 \\ \mathbf{V}_2 \end{bmatrix} \right\|_{i2} < \gamma, \quad (3.31)$$

with γ the least upper bound of the induced L_2 -norm of $\mathbf{\Gamma}_{ed}(\mathbf{P}_\theta, \mathbf{K}_\theta)$. The functions \mathbf{W}_1 , \mathbf{W}_2 , \mathbf{V}_1 and \mathbf{V}_2 can be determined from Figure 3.9 using an augmented sensitivity function \mathbf{S}_a . The augmented sensitivity function \mathbf{S}_a describes the mapping of the closed-loop system $\mathbf{\Gamma}_{ed}(\mathbf{P}_\theta, \mathbf{K}_\theta)$ from the disturbance inputs \mathbf{d} to the augmented measurement outputs $\mathbf{y}_P = [\mathbf{y}_a \ \mathbf{y}]^T$ according to

$$\begin{bmatrix} \mathbf{y}_a \\ \mathbf{y} \end{bmatrix} = \mathbf{S}_a \begin{bmatrix} \mathbf{G}_{ad} \\ \mathbf{G}_{yd} \end{bmatrix} \mathbf{W}_d \mathbf{d}. \quad (3.32)$$

The indices ad and yd of the plant \mathbf{G} describe the plant input and output signals, namely the input signals \mathbf{d} and the output signals \mathbf{y}_a and \mathbf{y} , respectively. Starting from the control structure in Figure 3.9, the augmented sensitivity function \mathbf{S}_a given by

$$\mathbf{S}_a = \begin{bmatrix} \mathbf{I} & -\mathbf{G}_{au}\theta\mathbf{K}_\theta\mathbf{S} \\ \mathbf{0} & \mathbf{S} \end{bmatrix}, \quad (3.33)$$

can be derived from

$$\begin{bmatrix} \mathbf{y}_a \\ \mathbf{y} \end{bmatrix} = \begin{bmatrix} \mathbf{G}_{ad} \\ \mathbf{G}_{yd} \end{bmatrix} \mathbf{W}_d \mathbf{d} + \begin{bmatrix} \mathbf{G}_{au} \\ \mathbf{G}_{yu} \end{bmatrix} \theta [\mathbf{0} \ \mathbf{K}_\theta] \begin{bmatrix} \mathbf{y}_a \\ \mathbf{y} \end{bmatrix}, \quad (3.34)$$

using the closed-loop mapping \mathbf{S} of output disturbances to the measurement signals. For LTI systems, the closed-loop mapping \mathbf{S} is referred to as sensitivity function (Skogestad and Postlethwaite, 2005, p. 24). The mixed sensitivity problem defined in (3.31) can now be expressed by

$$\|\mathbf{\Gamma}_{ed}(\mathbf{P}_\theta, \mathbf{K}_\theta)\|_{i2} = \left\| \begin{bmatrix} \mathbf{W}_a & \mathbf{0} \\ \mathbf{0} & \mathbf{W}_u\theta\mathbf{K}_\theta \end{bmatrix} \begin{bmatrix} \mathbf{I} & -\mathbf{G}_{au}\theta\mathbf{K}_\theta\mathbf{S} \\ \mathbf{0} & \mathbf{S} \end{bmatrix} \begin{bmatrix} \mathbf{G}_{ad}\mathbf{W}_d \\ \mathbf{G}_{yd}\mathbf{W}_d \end{bmatrix} \right\|_{i2} < \gamma. \quad (3.35)$$

Even though the controller synthesis problem is formulated in generalized plant notation as introduced in Appendix A.4, the mixed sensitivity problem representation in (3.35) provides some insight into the performance specification. The triangle inequality of norms described in Skogestad and Postlethwaite (2005, p. 549) imposes that each individual row

of (3.35) has to be at least smaller than γ , i.e. the induced L_2 -norm from the disturbances \mathbf{d} to the performance signals \mathbf{e}_a has to satisfy

$$\|\mathbf{W}_a (\mathbf{G}_{ad} - \mathbf{G}_{au} \theta \mathbf{K}_\theta \mathbf{S} \mathbf{G}_{yd}) \mathbf{W}_d\|_{i_2} < \gamma, \quad (3.36)$$

and simultaneously the induced L_2 -norm from the disturbances \mathbf{d} to the controller effort e_u has to satisfy

$$\|W_u \theta \mathbf{K}_\theta \mathbf{S} \mathbf{G}_{yd} \mathbf{W}_d\|_{i_2} < \gamma. \quad (3.37)$$

According to Kwakernaak (1993, p. 261), (3.36) and (3.37) can be exploited to specify the design targets of \mathbf{e}_a and e_u by appropriately choosing the weighting functions \mathbf{W}_a , W_u and \mathbf{W}_d . In particular, a large \mathbf{W}_a at low frequencies and a large W_u at high frequencies often has the effect that (3.36) dominates the resulting closed-loop at low frequencies and (3.37) at high frequencies.

The DI controller design introduced in Section 2.4 predetermines the control effort weighting function W_u to

$$W_u = \theta^{-1}, \quad (3.38)$$

to achieve the desired controller structure. As described in Section 2.4, this choice of W_u yields a controller that linearly reduces its control signal in the event of saturation. In addition to the structural motivation of $W_u = \theta^{-1}$ of Section 2.4, the inspection of (3.35) also suggests this control effort function, because $W_u = \theta^{-1}$ cancels θ and consequently the control effort e_u is equal to the controller output u_{F_d} . This entails that the control effort e_u is not downscaled by θ and the design imposes the same control effort bound for the constrained and unconstrained system.

The DI controller design also predetermines the disturbances \mathbf{d} , the disturbance weighting function \mathbf{W}_d and the disturbance models \mathbf{G}_{yd} and \mathbf{G}_{ad} according to the DI plant assumptions

$$(a1) \quad \mathbf{D}_{11}(\boldsymbol{\rho}) = \mathbf{0},$$

$$(b1) \quad (\mathbf{A}(\boldsymbol{\rho}) - \mathbf{B}_1(\boldsymbol{\rho}) \mathbf{C}_2(\boldsymbol{\rho})) \text{ parameter-dependent stable, and}$$

$$(b2) \quad \mathbf{D}_{21}(\boldsymbol{\rho}) = \mathbf{I}.$$

Assumption (b2) can be satisfied by

$$\mathbf{G}_{yd} = \mathbf{I}, \quad (3.39)$$

and

$$\mathbf{W}_d = \mathbf{I}. \quad (3.40)$$

Assumptions (a1) and (b1) restrict the disturbance model \mathbf{G}_{ad} given by

$$\begin{bmatrix} \dot{\mathbf{x}}_a \\ \mathbf{y}_a \end{bmatrix} = \begin{bmatrix} \mathbf{A}_a & \mathbf{B}_a \\ \mathbf{C}_a & \mathbf{D}_a \end{bmatrix} \begin{bmatrix} \mathbf{x}_a \\ \mathbf{d} \end{bmatrix} \quad (3.41)$$

to have the same dynamics matrix as the open-loop plant \mathbf{G}_{sa} , i.e. $\mathbf{A}_a = \mathbf{A}$, and the feedthrough matrix $\mathbf{D}_a = \mathbf{0}$. Furthermore, an input matrix \mathbf{B}_a equal to the observer gain $\mathbf{L}(d_0)$, i.e. $\mathbf{B}_a = \mathbf{L}(d_0)$, satisfies assumption (b1).

The choice of the performance signals \mathbf{e}_a and their weighting function \mathbf{W}_a is crucial during the controller design. The main objectives determining the performance signals are:

- the performance goals ride comfort and road-holding introduced in Section 3.2, and
- the computational cost during controller synthesis and code execution on real-time hardware.

According to the ride comfort and road-holding criteria introduced in (3.1) and (3.4), the first point refers to a reduction of the body acceleration \ddot{x}_b and dynamic wheel load F_{wl} . The second point is mainly influenced by the controller order and consequently the number of states of the generalized plant \mathbf{P}_θ . The presented controller design employs the body velocity \dot{x}_b and the wheel velocity \dot{x}_w as performance signal. To motivate this choice, Figure 3.10 shows the quarter-vehicle frequency responses of body and wheel velocity and acceleration, and the corresponding dynamic wheel load. As discussed in Section 3.3, the ride comfort related performance signals should emphasized the body resonance peak and roll-off at higher frequencies. The body acceleration which directly characterizes ride comfort according to (3.1) does not meet this requirement as the wheel resonance peak is almost as high as the body resonance peak. Do et al. (2010, p. 4656) overcome this issue by shaping the body acceleration with a second-order low-pass filter. This approach introduces two additional states into the generalized plant which is not desired in the control design in this work. The body velocity, however, inherently provides a better distinction between the body and wheel resonance peaks and consequently, a first-order shaping filter is sufficient. Regarding road-holding, Do et al. (2010, p. 4656) propose the dynamic wheel load as performance signal again shaped by a second-order low-pass filter. In contrast to this approach, a wheel velocity performance signal sufficiently emphasizes the wheel resonance peak and features a one decade steeper roll-off than the dynamic wheel load. In the proposed performance signal scheme, the dynamic wheel load is indirectly minimized through the body and wheel velocities according to (3.11). In summary, the proposed weighting scheme reduces the number of states of the generalized plant by 30 % compared to Do et al. (2010). Thus, the number of controller states is also reduced by 30 % because the controller order is equal to the generalized plant order as discussed in Appendix A. Moreover, the proposed performance signals

$$\mathbf{e}_a = \begin{bmatrix} e_{\dot{x}_b} \\ e_{\dot{x}_w} \end{bmatrix} = \begin{bmatrix} W_{a,b} & 0 \\ 0 & W_{a,w} \end{bmatrix} \begin{bmatrix} \dot{x}_b \\ \dot{x}_w \end{bmatrix} \quad (3.42)$$

with weighting functions $W_{a,b}$ and $W_{a,w}$ provide the necessary degrees-of-freedom (DoF) to tune ride comfort and road-holding. In particular, the selected performance signals correspond to the two DoFs of the quarter-vehicle model such that the body resonance

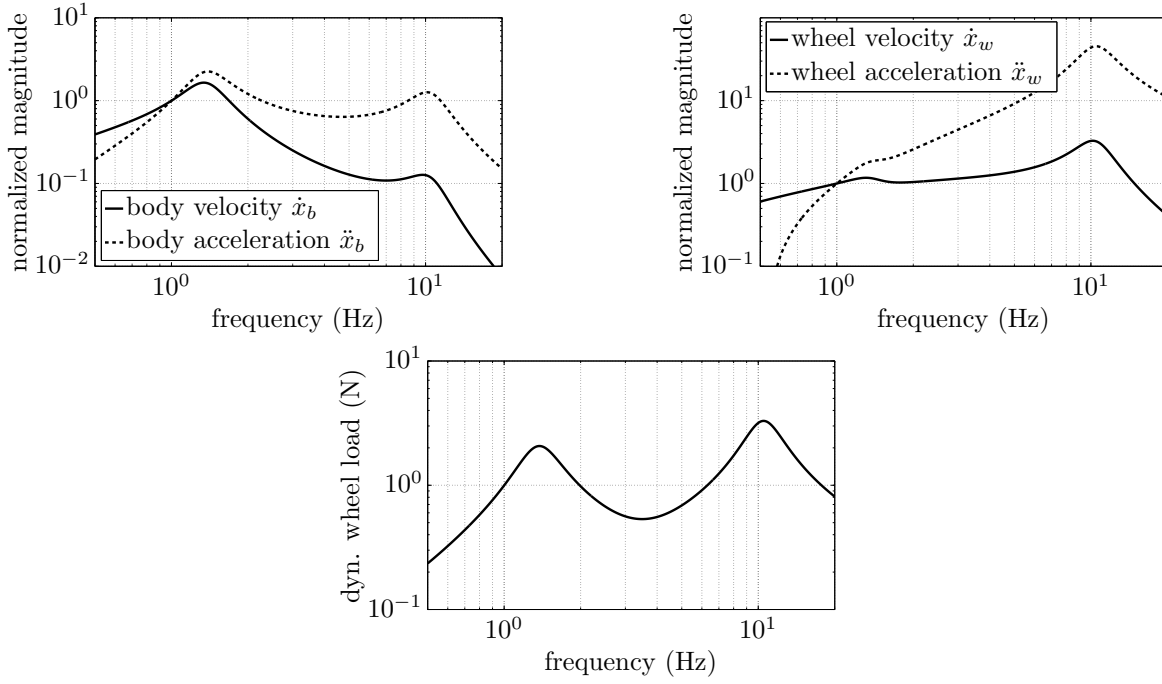


Figure 3.10: Open-loop frequency responses of plant \mathbf{G}_{sa} from road disturbance input d_g to: left - body motion, right - wheel motion, and bottom - dynamic wheel load

peak is tuned by $e_{\dot{x}_b}$ with the first-order weighting function $W_{a,b}$ with bandwidth ω_b given by

$$\begin{bmatrix} \dot{x}_{a,b} \\ e_{\dot{x}_b} \end{bmatrix} = \begin{bmatrix} -\omega_b & 1 \\ \theta w_b \omega_b & 0 \end{bmatrix} \begin{bmatrix} x_{a,b} \\ \dot{x}_b \end{bmatrix}, \quad (3.43)$$

and the wheel resonance peak by $e_{\dot{x}_b}$ with the weighting function $W_{a,w}$ given by

$$W_{a,w} = \theta w_w. \quad (3.44)$$

The scalars w_b and w_w offer a means to tune the controller and trade-off ride comfort against road-holding.

Eq. (3.36) and (3.37) impose upper bounds on the performance signals \mathbf{y}_a such that

$$\mathbf{y}_a < \gamma \begin{bmatrix} W_{a,b} & 0 \\ 0 & W_{a,w} \end{bmatrix}^{-1}, \quad (3.45)$$

and on the constrained controller output $\sigma(u_{F_d})$ such that

$$\sigma(u_{F_d}) < \gamma W_u^{-1}(\theta). \quad (3.46)$$

This property is exploited to reduce the weighting functions $W_{a,b}(\theta)$ and $W_{a,w}(\theta)$ by θ to relax the performance requirements and simultaneously to increase the control effort

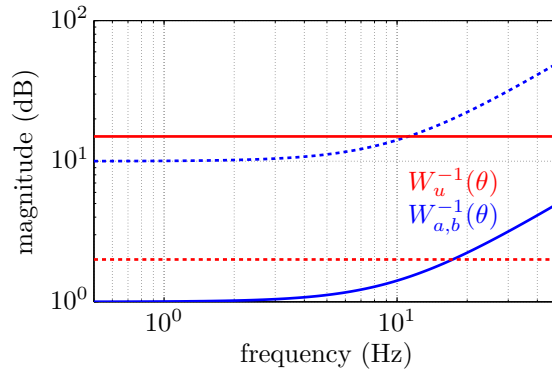


Figure 3.11: Saturation indicator dependence of weighting filters $W_{a,b}$ and W_u ; solid line $\theta = 1$ and dashed line $\theta = \theta_{\min}$

weight $W_u(\theta)$ by θ^{-1} to reduce the control signal usage, when actuator saturation occurs. Figure 3.11 exemplifies the saturation indicator dependence of the weighting functions $W_{a,b}(\theta)$ and $W_u(\theta)$.

The generalized plant \mathbf{P}_θ , which is used for controller synthesis, can now be stated by

$$\begin{bmatrix} \dot{\mathbf{x}} \\ \begin{bmatrix} \mathbf{e}_a \\ \mathbf{e}_u \end{bmatrix} \\ \mathbf{y} \end{bmatrix} = \begin{bmatrix} \mathbf{A}(d_0) & \bar{\mathbf{L}}(d_0) & \bar{\mathbf{B}}_2\theta \\ \begin{bmatrix} \mathbf{C}_{11}(\theta) \\ \mathbf{0} \end{bmatrix} & \begin{bmatrix} \mathbf{0} \\ \mathbf{0} \end{bmatrix} & \begin{bmatrix} \mathbf{0} \\ I \end{bmatrix} \\ \mathbf{C}_2(d_0) & \mathbf{I} & \mathbf{0} \end{bmatrix} \begin{bmatrix} \mathbf{x} \\ \mathbf{d} \\ u_{F_d} \end{bmatrix}. \quad (3.47)$$

with the observer gain $\bar{\mathbf{L}}(d_0) = [\mathbf{L}(d_0) \ 0]^T$ which extends from the original observer gain \mathbf{L} of Section 3.5.1 by one row of zeros to account for the additional state introduced by the weighting function $W_{a,b}$. Equally, the system matrix $\mathbf{A}(d_0)$ and the input matrix $\bar{\mathbf{B}}_2$ are also adjusted according to $W_{a,b}$. The DI controller \mathbf{K}_θ obtained by the controller synthesis described in Appendix A.4.4 with \mathbf{P}_θ can be expressed as

$$\begin{bmatrix} \dot{\mathbf{x}}_K \\ u_{F_d} \end{bmatrix} = \begin{bmatrix} \mathbf{A}(d_0) + \bar{\mathbf{B}}_2\theta\mathbf{F}(d_0, \theta) & \bar{\mathbf{L}}(d_0) \\ \mathbf{F}(d_0, \theta) & \mathbf{0} \end{bmatrix} \begin{bmatrix} \mathbf{x}_K \\ \mathbf{y} \end{bmatrix}, \quad (3.48)$$

with state-feedback gain $\mathbf{F}(d_0, \theta)$ according to (A.26) given by

$$\mathbf{F}(d_0, \theta) = -\theta\gamma^2\bar{\mathbf{B}}_2^T\mathbf{Z}(d_0). \quad (3.49)$$

Likewise to the observer synthesis, a Lyapunov function $\mathbf{Z}(d_0)$ given by

$$\mathbf{Z}(d_0) = \mathbf{Z}_0 + d_0\mathbf{Z}_1, \quad (3.50)$$

with a linear dependence on the saturation transformer d_0 is employed in the feedback controller design. During controller tuning, a grid density of two points is employed for the saturation indicator θ and the saturation transformer d_0 . After determination of the tuning parameters, the controller synthesis is verified with a denser grid featuring $h_{d_0} = 10$ grid points for the saturation transformer d_0 .

The tuning parameters of the DI problem are

- the scaling w_b of the body velocity \dot{x}_b , and
- the scaling w_w of the wheel velocity \dot{x}_w .

The optimal values of these tuning parameters are obtained as discussed in Section 3.6.

3.6 Multi-Objective Controller Tuning

An additional Pareto optimization loop is implemented around the LPV controller synthesis to find the tuning parameters for optimal ride comfort and road-holding performance of the controller. As visualized in Figure 3.12, the optimization updates the control design during each iteration by synthesizing the state-observer and the DI controller with the updated tuners. Subsequently, the optimization evaluates the controller in closed-loop with the nonlinear reference quarter-vehicle model and quantifies the constraints and performance criteria ride comfort and road-holding. The stopping criterion analyzes the progression of the performance criteria and decides whether the optimization reached an optimum. The combination of the controller synthesis with the additional optimization loop simplifies the determination of the tuning parameters. On the one hand, the performance index γ obtained during the LPV controller synthesis is not directly related to the ride comfort and road-holding criteria of Section 3.2 and on the other hand the reference quarter-vehicle considers nonlinearities like the semi-active damper or bump stops. Additionally, during simulation, the reference vehicle can be excited by realistic road profiles as introduced in Appendix C leading to realistic damper force saturation conditions. In this way, the LPV controller can be tuned for optimal performance despite the very restrictive damper force constraints, which make saturated operation a common system state.

The optimization is formulated by

$$\min_{\varphi} J_{\text{opt}}(J_c, J_{rh}) \quad \text{subject to} \quad (3.51a)$$

$$\max(|\text{eig}(\mathbf{\Gamma}_{ed}(\mathbf{P}_{\theta,k}, \mathbf{K}_{\theta,k}))|) < \lambda_{\max}, \quad (3.51b)$$

as a Pareto optimization with parameter $\vartheta \in [0, 1]$ and cost function

$$J_{\text{opt}}(J_c, J_{rh}) = \vartheta J_c + (1 - \vartheta) J_{rh}, \quad (3.52)$$

as described in Savaresi et al. (2010, p. 99). The inequality constraint (3.51b) restricts the distance of the maximum eigenvalue of frozen closed-loop systems $\mathbf{\Gamma}_{ed}(\mathbf{P}_{\theta,k}, \mathbf{K}_{\theta,k})$ to the origin to values smaller than λ_{\max} . This ensures that the controller is implementable on real-time hardware with a given sample time $T_s = 1$ ms. The decision parameter vector φ gathers the tuning parameters of the state-observer and LPV controller design presented in Section 3.5.1 and 3.5.2 according to

$$\varphi = [w_{e,1} \ \dots \ w_{e,n_x} \ w_{n,\ddot{x}_b} \ w_{n,\ddot{x}_w} \ w_{n,\dot{x}_d} \ w_b \ w_w]^T. \quad (3.53)$$

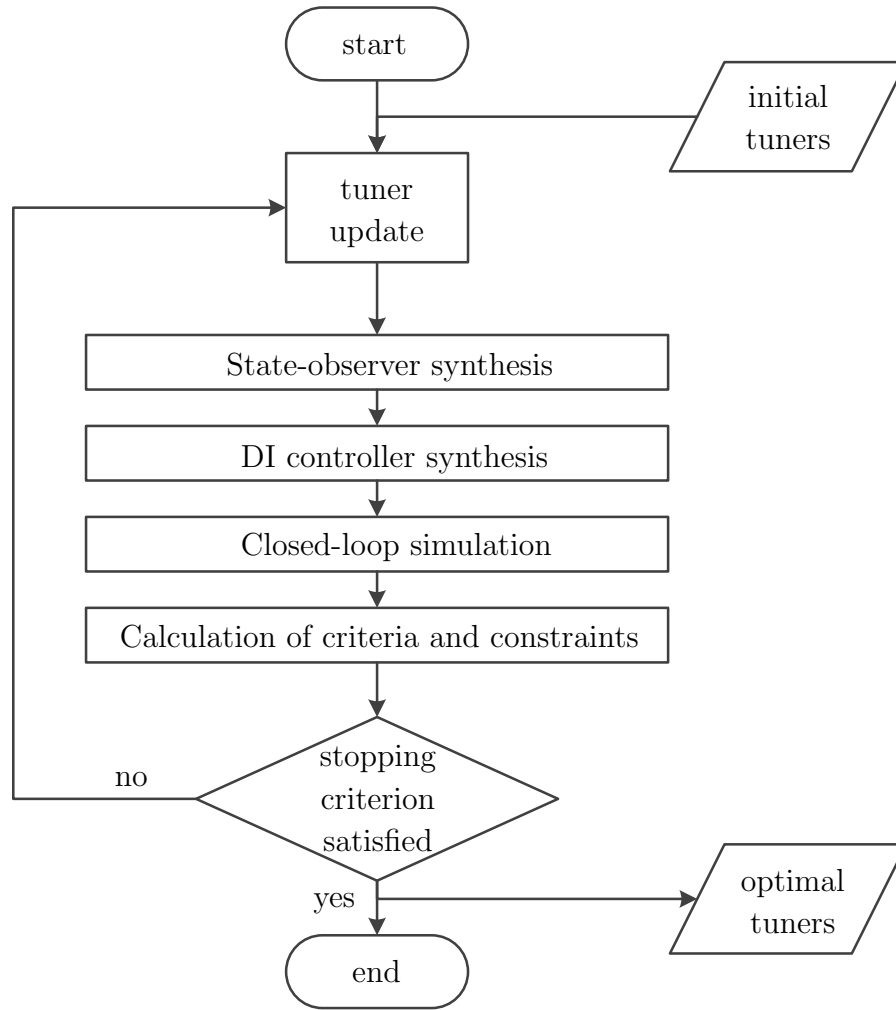


Figure 3.12: Process diagram of multi-objective controller tuning

The appropriate parameters of the road model β_r , α_r and v_{ref} are determined by a preliminary optimization.

During the optimization the reference vehicle is excited by the sine sweep signal with constant velocity amplitude introduced in Appendix C. This signal excites the body and wheel resonances with appropriate amplitudes and covers the relevant frequency range between 1 Hz and 20 Hz. The optimization itself is carried out in MATLAB using the DLR MOPS toolbox with a genetic algorithm and a subsequent local downhill method (Joos et al., 2002). The initial values of the tuning parameters related to the observer design are determined by a preceding optimization setup which minimizes the observation error between the body and wheel velocities estimated by the observer and the corresponding signals of the nonlinear reference model. Due to the large number of tuning parameters in (3.53), the genetic optimization algorithm has to be parametrized with a large population size. As a rule of thumb, the population size should be at least twice as large as the

number of tuning parameters. Thus, the genetic algorithm needs several hundred function evaluations. However, this is not a major restriction as the function evaluations of one population of the genetic algorithm can be performed in parallel. At the Institute of System Dynamics and Control the local Linux cluster can be used to implement the optimization such that up to 32 function evaluations can be performed in parallel which drastically speeds up the entire optimization process.

3.7 Simulation Results

As a performance benchmark for the LPV controller, a Skyhook-Groundhook (SH/GH) controller is implemented using the control structure in Figure 3.5. For the SH/GH control configuration, the state estimation is replaced by a simple low-pass and high-pass filtering of the measurements. The SH/GH controller itself is implemented according to Section 3.4 such that the controller provides a damper force F_{sa} which is then processed by the inverse damper subsystem. The gains of the SG/GH controller are tuned with the optimization framework described in the previous section.

The investigation of the PSD of the sine sweep simulations of passive and controlled suspensions shows that the passive suspension configuration denoted by *min. damping* offers the best ride comfort and road-holding behavior in the frequency range above 3 Hz as obvious from the top and middle plots of Figure 3.13. Even the passive configuration, called *ref. damping*, which applies very high damper forces and therefore drastically deteriorates ride comfort, can only slightly reduce the wheel load resonance amplitude. At the same time, the wheel load amplitudes in the intermediate frequency range are much higher and consequently the overall road-holding performance of the *ref. damping* configuration is worse than that of *min. damping*. Regarding the LPV controller this implies that the controller should roll-off at around 3 Hz and the bandwidth ω_b of the weighting filter W_{e,\dot{x}_b} should be chosen accordingly. Furthermore, the saturation transformer d_0 should closely reflect the *min. damping* characteristic as the frequency response of the LPV controller above 3 Hz is determined by the saturation transformer.

The simulation results with the reference quarter-vehicle excited by a sine-sweep signal and a stochastic road signal according to ISO (8608:1995) type D show that the LPV controller outperforms the SH/GH controller and both passive suspension configurations. The LPV controller especially features the smallest magnitudes of body acceleration and dynamic wheel load in the frequency range below 3 Hz. In comparison to the sine sweep experiment, the road excitation experiment is stochastically evaluated using the RMS criteria introduced in Section 3.2. The corresponding bar plot depicted in Figure 3.14 confirms the benefit of the LPV controller which achieves the lowest RMS values regarding ride comfort and road-holding. Furthermore, the LPV controller achieves smaller damper deflections for the sine sweep and stochastic road excitations than the SH/GH controller and the *min. damping* configuration.

In addition to the performance criteria, the controller roll-off can be analyzed by the sine sweep experiment as depicted in Figure 3.15. The sine sweep features a frequency range

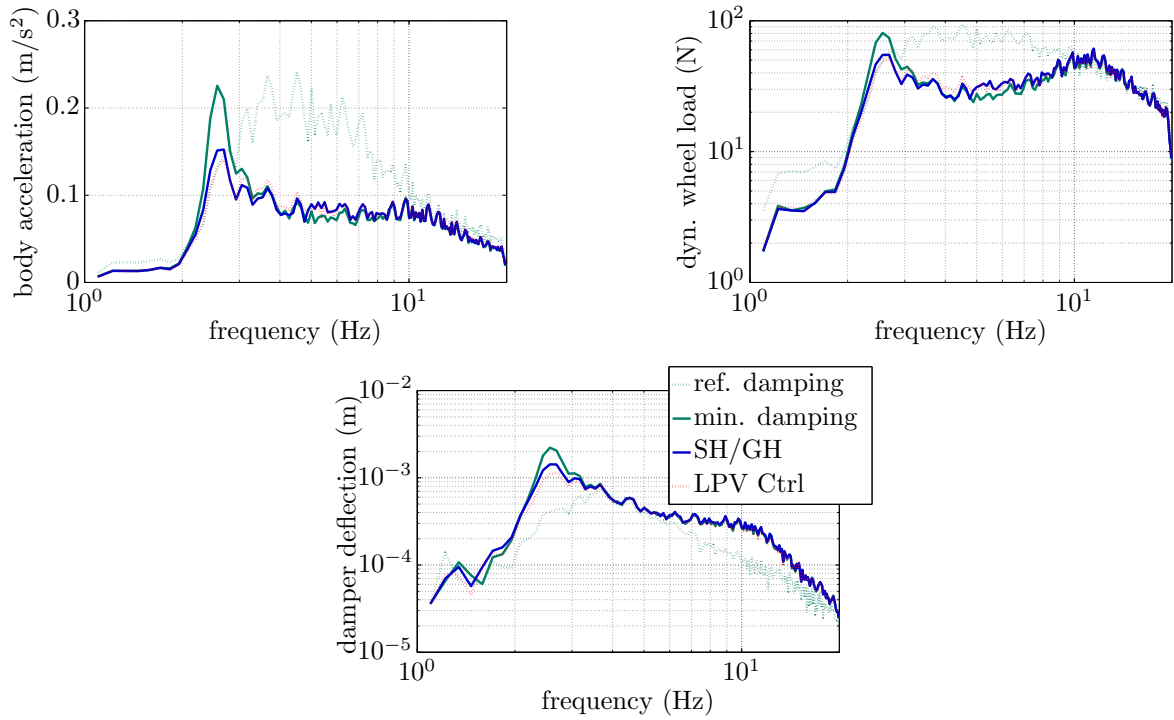


Figure 3.13: Sine-sweep simulation: top - PSD of body acceleration, middle - PSD of dynamic wheel load, and bottom PSD of damper velocity

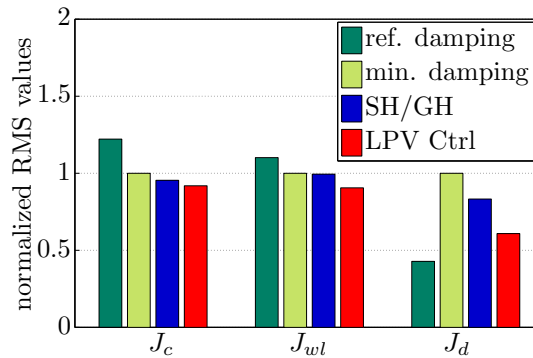


Figure 3.14: Stochastic road simulation according to ISO (8608:1995) road type D at a vehicle speed of 100 km/h: ride comfort J_c , road-holding J_{rh} and damper deflection J_d

of 1-20 Hz over a duration of 60 s. After 10 s, the excitation frequency reaches 3.6 Hz and as desired the control signal of the SH/GH and the LPV controller rise to almost 1.8 A which corresponds to *min. damping*.

3.8 Experimental Results

The experimental assessment was carried out using the sine sweep and stochastic road profile from the simulation study. In order to facilitate a comparison of the results obtained on the test-rig and during controller tuning, the experimental results are illustrated in

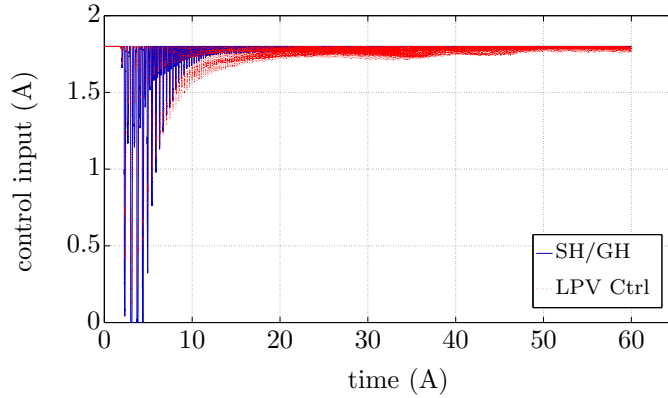


Figure 3.15: Sine-sweep simulation: control signal u_d over time

the same way as the simulation results in the previous Section. This visualization of the experimental results helps to verify the robustness of the controllers with respect to model uncertainties and sensor disturbances. The evaluation of the closed-loop PSD of the LPV controller, the SH/GH controller and both passive suspension configurations shows that the LPV controller outperforms the SH/GH controller and the passive suspension configurations *min. damping* and *ref. damping*, but the benefit of the LPV controller is not as large as expected from the simulation. In particular, the amplitude reduction of the body acceleration and dynamic wheel load in Figure 3.16 are smaller than during the simulation study. This deviation results from the approximated quarter-vehicle dynamics by the virtual body mass at the test-rig and from the suspension friction which has been neglected by the reference quarter-vehicle. Nevertheless, the improvement of the LPV controller with respect to both ride comfort and road-holding can be noticed in the frequency range from 2 Hz to 3 Hz.

Figure 3.17 shows the performance criteria in case of a stochastic road profile excitation according to ISO (8608:1995) type D at a vehicle speed of 100 km/h. In this experiment the LPV controller achieves small improvements regarding road-holding and damper deflection with similar ride comfort as the SH/GH controller and the *min. damping* configuration.

3.9 Discussion and Conclusion

This section presents an LPV controller for a semi-active quarter-vehicle suspension system. The LPV controller explicitly considers the state-dependent actuator constraints of the semi-active damper within a rigorous LPV control framework. Therefore, a saturation indicator and a saturation transformer are introduced into the LPV plant model as exogenous scheduling parameters. The LPV controller is designed along a mixed sensitivity scheme with saturation indicator dependent weighting filters. The tuning parameters of the control design are determined using a genetic optimization algorithm and a simulation

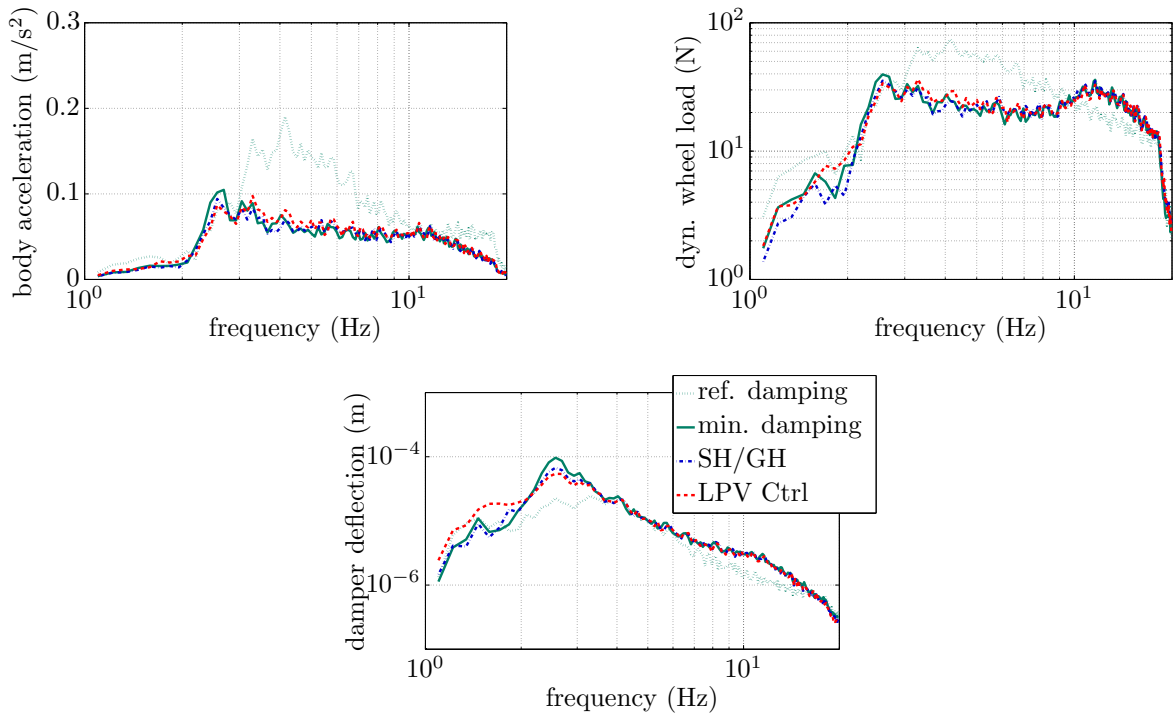


Figure 3.16: Sine-sweep experiment: top - PSD of body acceleration, middle - PSD of dynamic wheel load, and bottom PSD of damper velocity

environment with a nonlinear quarter-vehicle model.

The LPV controller is compared to a state-of-the-art Skyhook-Groundhook controller and two passive suspension configurations by means of quarter-vehicle simulations and experiments on a quarter-vehicle test-rig. The results show that the LPV controller offers a better trade-off between ride comfort and road-holding than the Skyhook-Groundhook controller and the passive suspension configurations with a simultaneous reduction of the damper deflection.

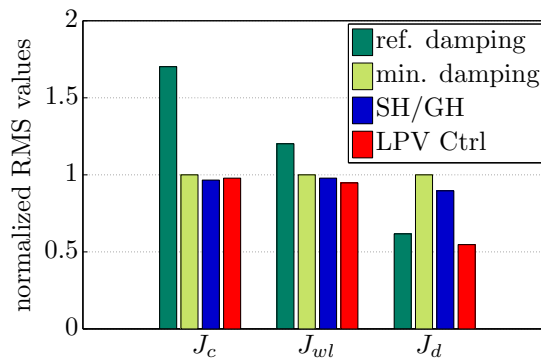


Figure 3.17: Stochastic road experiment according to ISO (8608:1995) road type D at a vehicle speed of 100 km/h: ride comfort J_c , road-holding J_{rh} and damper deflection J_d

4 Full-Vehicle Control Design

Exploiting the performance potential of vehicles equipped with semi-active dampers constitutes a complex control problem because of

- the well-known design conflict between ride comfort and road-holding as depicted in the conflict diagram in Figure 1.1,
- the highly nonlinear actuator, in particular the passivity constraint of the semi-active damper,
- the full-vehicle model necessary to accurately model the vehicle vertical dynamics and to individually tune heave, roll and pitch of the vehicle body during control design, and
- the sophisticated augmentation of the controller to explore the weak input redundancy in case of damper malfunction or saturation.

Here, these challenges are addressed by a DI LPV controller using a full-vehicle synthesis model. The controller gathers the developments published in Fleps-Dezasse and Brembeck (2016), Fleps-Dezasse et al. (2016) and Fleps-Dezasse et al. (2017). Equally to the quarter-vehicle control design presented in Chapter 3, the damper force constraints are incorporated in the synthesis model by saturation indicator parameters according to the anti-windup LPV control method introduced in Wu et al. (2000). The full-vehicle model allows for individually penalizing heave, roll and pitch of the vehicle body during control design and further for augmenting the controller with a force reconfiguration. The saturation indicators readily describe damper failures like e.g. oil leakage which extends the LPV controller validity from normal operation to faulty operation modes. The force reconfiguration explores the weak input redundancy provided by four force actuators in a full-vehicle. It is inspired by the fault-tolerant control (FTC) schemes in Sename et al. (2013) and Tudón-Martinez et al. (2013).

FTC has gained vital importance in automotive applications because mechatronic systems like semi-active suspensions are comprised of many components like sensors, actuators, power electronics and electronic control units. This component variety increases system complexity and contributes to a greater likelihood of component or system failure (Isermann, 2006). The fault-tolerant operation can be addressed in several ways depending on the type of failure, e.g. by component redundancy or backup operation modes. Regarding the control algorithms, control reconfiguration offers a promising approach to address component malfunction as described in Lunze and Richter (2008). Control reconfiguration, also referred to as fault-tolerant control, requires the control loop to maintain certain system properties like stability and satisfactory performance in the event of component failures (Zhang and Jiang, 2008). The basic principle of the control reconfiguration approach is illustrated in Figure 4.1 in case of an actuator malfunction. After the detection

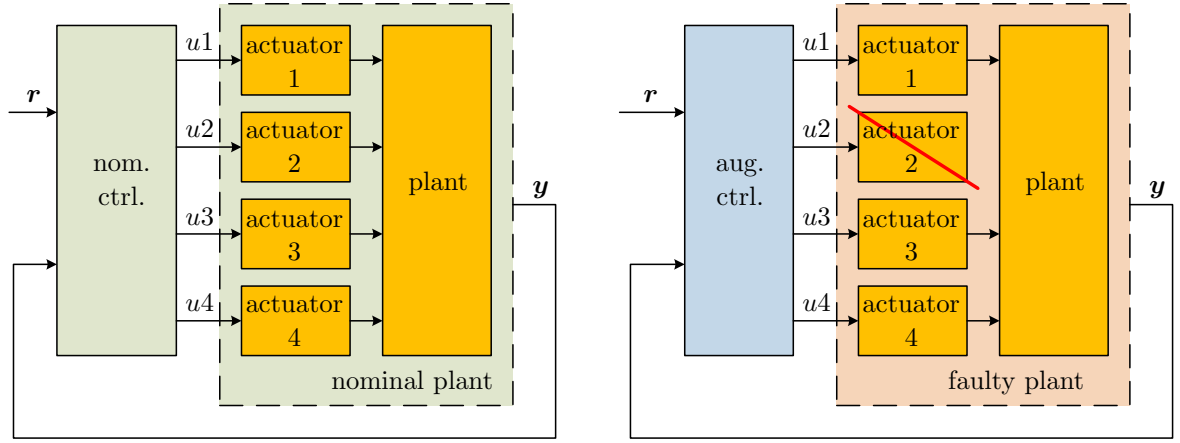


Figure 4.1: Interconnection of generalized plant with nominal controller (left) and re-configured controller (right)

of the actuator failure, the nominal controller is reconfigured such that it does not use actuator 2.

The LPV control design adopts the gridding-based LPV approach introduced in Chapter 2 and applied during the quarter-vehicle control design in Chapter 3. Together with the full-vehicle synthesis model and four saturation indicators, the gridding-based LPV control approach leads to a large controller synthesis problem. Therefore, the computational cost of the controller synthesis becomes a significant issue and the control design pursues two countermeasures:

- firstly, the control design exploits a Disturbance-Information output-feedback problem structure which allows for the separate synthesis of state-observer and state-feedback controller as introduced in Appendix A.4.4, and
- secondly, the control design uses a loose saturation indicator grid density based on the theoretical investigation of the minimum required saturation indicator grid density presented in Section 2.5.

As shown in Appendix A.4.4, the DI controller provides guaranteed performance, even though the controller can be assembled from the subsequent solutions of a state-observer and a state-feedback problem. In this way, the DI synthesis problem complexity is significantly smaller than the equivalent general output-feedback controller synthesis problem. Full-vehicle control design approaches are hardly found in the literature due to the essentially more complex vehicle model compared to quarter-vehicle approaches. As an exception, Unger et al. (2013) developed an LQG semi-active suspension controller using the clipping approach and presented promising experimental results gathered on a four-post test-rig. Regarding LPV control methods, Nguyen et al. (2015b) and Fleps-Dezasse and Brembeck (2016) provide simulation investigations involving a full-vehicle. Nguyen

et al. (2015b) presents a polytopic LPV state-feedback controller design which only focuses on a minimization of the vehicle roll acceleration. In contrast, this chapter extends the full-vehicle LPV control approach presented in Fleps-Dezasse and Brembeck (2016) and Fleps-Dezasse et al. (2017), and provides extensive results from experiments on a four-post test-rig.

4.1 Full-Vehicle Control Structure

The structure of the full-vehicle LPV controller employed in this section is depicted in Figure 4.2. The central LPV controller consisting of state-observer and state-feedback controller generates the damper forces \mathbf{F}_{sa} which are separately processed by saturation blocks and inverse damper subsystems yielding the damper current \mathbf{u}_d . Similar to the quarter-vehicle control design of Chapter 3, the saturation block and the inverse damper model are gathered in an augmented plant, which is then employed for the LPV control design. As a benchmark, a full-vehicle Skyhook-Groundhook (SH/GH) controller and a full-vehicle LPV controller gathering four quarter-vehicle LPV controllers, called quarter-vehicle FVC, are implemented in the control structure of Figure 4.2. The quarter-vehicle FVC assumes that the full-vehicle vertical dynamics can be approximated by four separate quarter-vehicle models, i.e. one quarter-vehicle for each suspension system of the vehicle. This approximation condenses the body mass, and the roll and pitch inertia into the mass of the quarter-vehicle body.

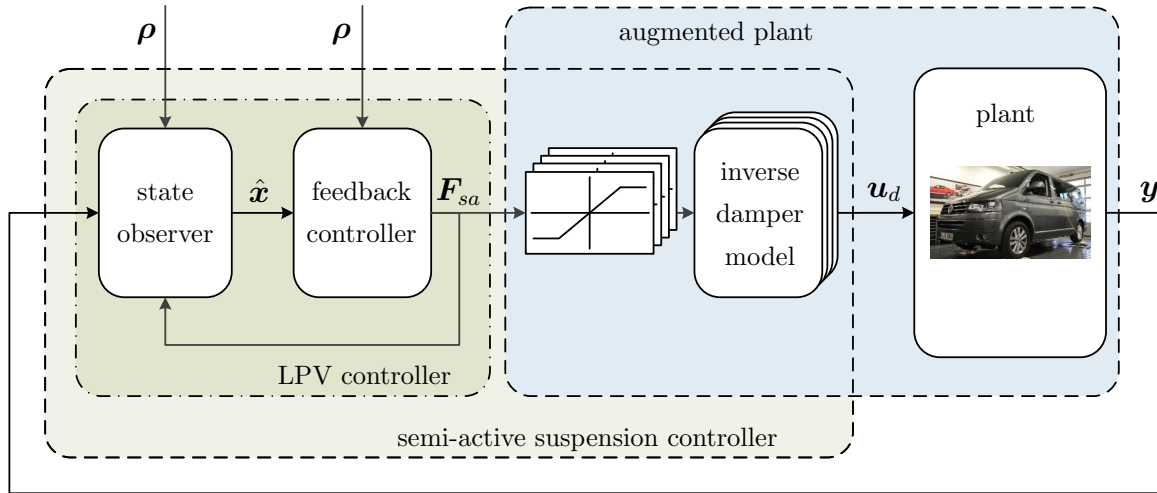


Figure 4.2: Disturbance-Information structure of full-vehicle LPV controller

4.2 Performance Criteria

In a full-vehicle context ride comfort is not solely characterized by the vehicle body heave acceleration, but also by the angular roll and pitch accelerations. ISO (2631-1:1997)

gives a detailed description of the effect of accelerations on human comfort and health. According to ISO (2631-1:1997) the accelerations have to be distinguished by their point of application, e.g. seat-surface or feat, and their direction, e.g. translational along z-axis or rotational around x-axis as illustrated in Figure 4.3.

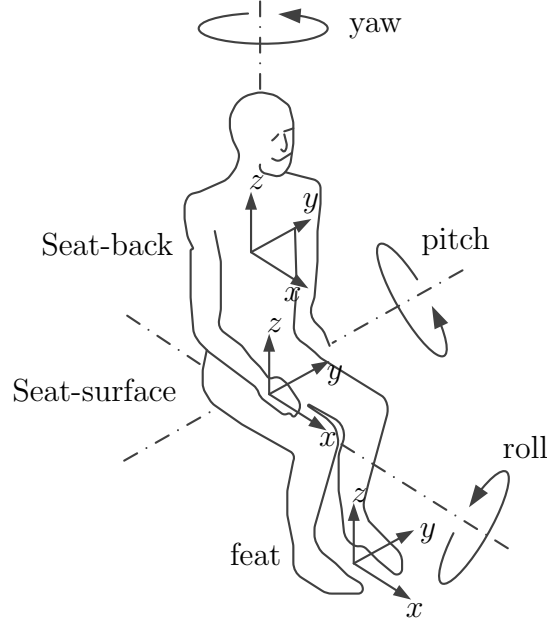


Figure 4.3: Directions of comfort assessment defined by ISO 2631-1:1997

Regarding the vehicle vertical dynamics only the translational body acceleration along the vehicle z-axis $\ddot{x}_{b,\text{CoG}}$ and the rotational body accelerations $\ddot{x}_{b,\text{roll}}$ and $\ddot{x}_{b,\text{pitch}}$ around the roll and pitch axes are of interest. The ride comfort criteria J_{cISO} given by ISO (2631-1:1997) can be calculated from these signals according to

$$J_{\text{cISO}} = \sqrt{(k_1 \text{RMS}(\ddot{x}_{b,\text{CoG}}))^2 + (k_2 \text{RMS}(\ddot{x}_{b,\text{roll}}))^2 + (k_3 \text{RMS}(\ddot{x}_{b,\text{pitch}}))^2}, \quad (4.1)$$

with the scaling factors $k_1 = 1$, $k_2 = 0.63$ and $k_3 = 0.4$. The RMS values $\text{RMS}(\ddot{x}_{b,\text{CoG}})$, $\text{RMS}(\ddot{x}_{b,\text{roll}})$ and $\text{RMS}(\ddot{x}_{b,\text{pitch}})$ are computed from the filtered body heave acceleration \ddot{x}_b obtained from

$$\ddot{x}_{b,\text{CoG}} = W_{\text{ISO,heave}} \ddot{x}_{b,\text{CoG}}, \quad (4.2)$$

the filtered angular roll acceleration $\ddot{x}_{b,\text{roll}}$ obtained from

$$\ddot{x}_{b,\text{roll}} = W_{\text{ISO,rot}} \ddot{x}_{b,\text{roll}}, \quad (4.3)$$

and filtered angular pitch acceleration $\ddot{x}_{b,\text{pitch}}$ obtained from

$$\ddot{x}_{b,\text{pitch}} = W_{\text{ISO,rot}} \ddot{x}_{b,\text{pitch}}. \quad (4.4)$$

Figure 4.4 shows the transfer functions of the weighting filters $W_{\text{ISO,heave}}$ and $W_{\text{ISO,rot}}$. They emphasize the amplitudes of the acceleration signals according to human sensitivity. The filter $W_{\text{ISO,rot}}$ focuses on the frequency range between 0.5 Hz and 2 Hz, while the filter $W_{\text{ISO,heave}}$ distinguishes between the low frequency range from 0.5 Hz to 3 Hz and the slightly more important medium frequency range from 4 Hz to 10 Hz. The parametrization of the weighting filters can be found in ISO (2631-1:1997).

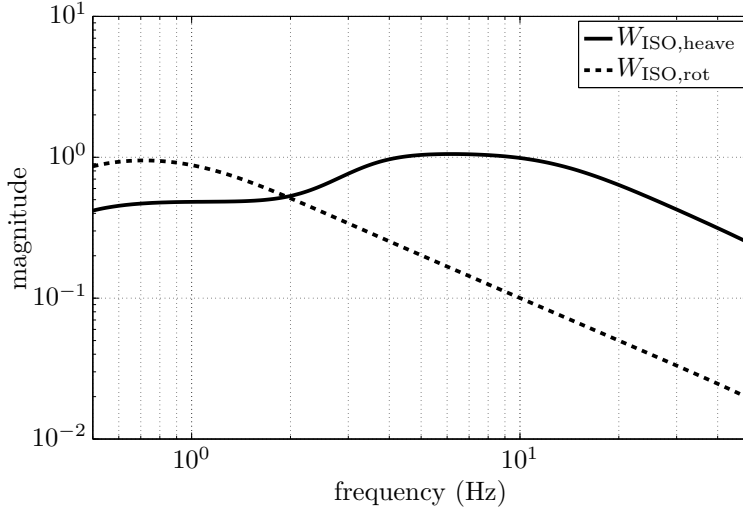


Figure 4.4: Weighting filters of translational heave acceleration and angular roll and pitch accelerations according to ISO (2631-1:1997)

Similar to the quarter-vehicle control design, the road-holding performance J_{rh} is characterized by the RMS value of the dynamic wheel loads. In contrast to the quarter-vehicle, however, the dynamic wheel loads \mathbf{F}_{wl} are a vector comprised of the dynamic wheel loads of the four tires according to

$$\mathbf{F}_{wl} = [F_{wl,1} \ F_{wl,2} \ F_{wl,3} \ F_{wl,4}]^T. \quad (4.5)$$

The RMS value of the vectorial dynamic wheel load signal \mathbf{F}_{wl} can be computed by

$$J_{rh} = \sqrt{\frac{1}{T} \int_0^T \sum_i |F_{wl,i}(t)|^2 dt}, \quad (4.6)$$

as described in (Skogestad and Postlethwaite, 2005, p. 558). Likewise, the suspension deflection usage J_d can be calculated from the damper deflection vector \mathbf{x}_d by

$$J_d = \sqrt{\frac{1}{T} \int_0^T \sum_i |x_{d,i}(t)|^2 dt}. \quad (4.7)$$

4.3 LTI Full-Vehicle Model

The full-vehicle vertical dynamics comprises seven degrees-of-freedom, namely vehicle body heave, roll and pitch and vertical wheel motion. Its equation of motion can be

derived from Newtons' second law using the notation introduced in Figure 4.5. The considered full-vehicle model assumes a left/ right symmetrical vehicle similar to Mitschke and Wallentowitz (2004, p. 439 ff.) and (Unger et al., 2013, p. 2-3) and equal tires at the front and rear suspensions. The full-vehicle model features similar parameters as the quarter-vehicle model namely the body spring stiffnesses $k_{b,i}$, body dampings $d_{b,i}$, tire stiffness k_w and tire damping d_w .

Remark. In the full-vehicle application, the number of semi-active dampers and the number of suspensions is identical, thus the index $i = 1, 2, 3, 4$ denotes both the respective damper and suspension unit with $i = 1$ referring to front left, $i = 2$ to front right, $i = 3$ to rear left, and $i = 4$ to rear right.

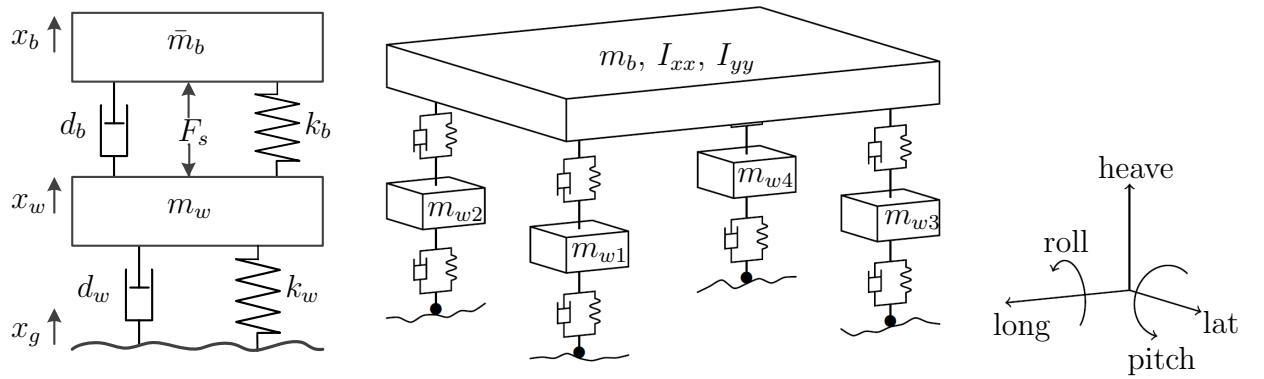


Figure 4.5: Sketch of quarter-vehicle model (left) and full-vehicle model (right)

The equation of motion of wheel i is given by

$$m_{w,i} \ddot{x}_{w,i} = k_{b,i} (x_{bs,i} - x_{w,i}) + d_{b,i} (\dot{x}_{bs,i} - \dot{x}_{w,i}) + k_w (x_{g,i} - x_{w,i}) + d_w (\dot{x}_{g,i} - \dot{x}_{w,i}) - F_{s,i}, \quad (4.8)$$

with $x_{bs,i}$ the body position above the wheel contact point at the respective suspension unit and the suspension force input $F_{s,i}$. According to Lu and DePoyster (2002, p. 809), the body position $x_{bs,i}$ can be calculated from the body position $x_{b,CoG}$ at the center of gravity (CoG), the body roll angle $x_{b,roll}$ and the body pitch angle $x_{b,pitch}$ using the geometric transformation matrix \mathbf{T}_{bs} by

$$\begin{bmatrix} x_{bs,1} \\ x_{bs,2} \\ x_{bs,3} \\ x_{bs,4} \end{bmatrix} = \underbrace{\begin{bmatrix} 1 & \frac{l_{y,f}}{2} & -l_{x,f} \\ 1 & -\frac{l_{y,f}}{2} & -l_{x,f} \\ 1 & \frac{l_{y,r}}{2} & l_{x,r} \\ 1 & -\frac{l_{y,r}}{2} & l_{x,r} \end{bmatrix}}_{\mathbf{T}_{bs}} \begin{bmatrix} x_{b,CoG} \\ x_{b,roll} \\ x_{b,pitch} \end{bmatrix}, \quad (4.9)$$

with $l_{y,f}$ and $l_{y,r}$ the front and rear track widths, and $l_{x,f}$ and $l_{x,r}$ the distances from the front and rear wheels to the body CoG. The geometric transformation of (4.9) uses small angle approximations of the roll and pitch angles of the vehicle body.

The equation of motion of the vehicle body heave is given by

$$m_b \ddot{x}_{b,\text{CoG}} = \sum_i (k_{b,i} (x_{w,i} - x_{bs,i}) + d_{b,i} (\dot{x}_{w,i} - \dot{x}_{bs,i}) + F_{s,i}), \quad (4.10)$$

the equation of body roll by

$$I_{xx} \ddot{x}_{b,\text{roll}} = \sum_i l_{\text{roll},i} (k_{b,i} (x_{w,i} - x_{bs,i}) + d_{b,i} (\dot{x}_{w,i} - \dot{x}_{bs,i}) + F_{s,i}), \quad (4.11)$$

with $l_{\text{roll}} = \left[\frac{l_{y,f}}{2} \quad -\frac{l_{y,f}}{2} \quad \frac{l_{y,r}}{2} \quad -\frac{l_{y,r}}{2} \right]^T$ and of body pitch by

$$I_{yy} \ddot{x}_{b,\text{pitch}} = \sum_i l_{\text{pitch},i} (k_{b,i} (x_{w,i} - x_{bs,i}) + d_{b,i} (\dot{x}_{w,i} - \dot{x}_{bs,i}) + F_{s,i}), \quad (4.12)$$

with $l_{\text{pitch}} = \left[-\frac{l_{x,f}}{2} \quad -\frac{l_{x,f}}{2} \quad \frac{l_{x,r}}{2} \quad \frac{l_{x,r}}{2} \right]^T$.

The vehicle model \mathbf{G}_{fv} represented by the equations (4.8) - (4.12) and including the road disturbance model introduced in (C.6) can be summarized in state-space notation by

$$\dot{\mathbf{x}} = \mathbf{A}\mathbf{x} + \mathbf{B}_1 \mathbf{d}_g + \mathbf{B}_2 \mathbf{F}_s, \quad (4.13)$$

with the state vector \mathbf{x} given by

$$\mathbf{x} = [x_{b,\text{CoG}} \quad \dot{x}_{b,\text{CoG}} \quad x_{b,\text{roll}} \quad \dot{x}_{b,\text{roll}} \quad x_{b,\text{pitch}} \quad \dot{x}_{b,\text{pitch}} \quad x_{w,1} \quad \dot{x}_{w,1} \quad \dots \quad x_{w,4} \quad \dot{x}_{w,4} \quad x_{g,1} \quad \dots \quad x_{g,4}], \quad (4.14)$$

the suspension forces \mathbf{F}_s of each suspension system given by

$$\mathbf{F}_s = [F_{s,1} \quad F_{s,2} \quad F_{s,3} \quad F_{s,4}]^T, \quad (4.15)$$

and the independent road disturbance inputs \mathbf{d}_g given by

$$\mathbf{d}_g = [d_{g,1} \quad d_{g,2} \quad d_{g,3} \quad d_{g,4}]^T, \quad (4.16)$$

The full-vehicle model feature similar properties as the quarter-vehicle model as discussed in Hedrick and Butsuen (1990). Equally to the quarter-vehicle case, the dynamic wheel loads can be computed from the tire deflections according to (3.10) and furthermore the dynamic wheel loads are a function of the body and wheel accelerations. Unfortunately, the dynamic wheel loads of the full-vehicle are coupled through the vehicle body and hence the dynamic wheel load of one wheel cannot be expressed as an explicit function of the body and wheel accelerations. Nevertheless, as described for the quarter-vehicle, a reduction of the body and wheel acceleration amplitudes simultaneously reduces the dynamic wheel loads. The frequency responses of the body heave, roll and pitch accelerations as well as of the dynamic wheel loads of the passive full-vehicle are also subject to the waterbed effect for variations of the body damping d_b . Additionally, the suspension force inputs \mathbf{F}_s also lose efficiency at frequencies near the wheel resonance frequency. The efficiency loss increases if the tire damping d_w approaches zero and results in a transmission zero for $d_w = 0$ Ns/m. Therefore, equal performance specifications than in the quarter-vehicle control design have to be imposed for the full-vehicle control design:

ride comfort: performance outputs related to ride comfort should emphasize the body resonance peak and roll-off at about 3 Hz,

road-holding: performance outputs related to road-holding should emphasize the body and the wheel resonance peak, and roll-off beyond the wheel resonance frequency,

suspension usage: performance outputs related to suspension usage should emphasize the body and the wheel resonance peak, and roll-off beyond the wheel resonance frequency.

This specification regarding ride comfort correspond well to the weighting filter $W_{\text{ISO,rot}}$ employed for the angular roll and pitch accelerations in the ride comfort criteria definition of ISO (2631-1:1997), but the weighting filter $W_{\text{ISO,heave}}$ emphasizes the frequency range between 4 Hz and 10 Hz. In this intermediate frequency range, however, a semi-active suspension controller achieves the best ride comfort performance by commanding the minimum damper forces.

4.4 Full-Vehicle Skyhook-Groundhook Controller

The basic principle of the Skyhook control policy introduced in Section 3.4 can be generalized to a full-vehicle application. Karnopp et al. (1974) showed that in the quarter-vehicle application the optimal body damping should be applied between an inertial frame and the vehicle body. In a full-vehicle application, the body cannot only move in the vertical direction, but also rotate around the roll and pitch axes. The optimal damping of these rotations is again a Skyhook damper between inertial frame and vehicle body as discussed in Unger et al. (2013, p. 4). Therefore, the full-vehicle Skyhook force \mathbf{F}_{SH} is computed from the body heave, roll and pitch velocities according to

$$\mathbf{F}_{\text{SH}} = \mathbf{T}_{bs} \begin{bmatrix} d_{\text{SH,heave}} & 0 & 0 \\ 0 & d_{\text{SH,roll}} & 0 \\ 0 & 0 & d_{\text{SH,pitch}} \end{bmatrix} \begin{bmatrix} \dot{x}_{b,\text{CoG}} \\ \dot{x}_{b,\text{roll}} \\ \dot{x}_{b,\text{pitch}} \end{bmatrix}, \quad (4.17)$$

using the Skyhook damping parameters $d_{\text{SH,heave}}$, $d_{\text{SH,roll}}$ and $d_{\text{SH,pitch}}$ related to heave, roll and pitch, respectively. Subsequently the control force of the i -th damper is calculated by

$$F_{sa,\text{SH},i} = \begin{cases} F_{d,\text{min},i} & F_{\text{SH},i} \dot{x}_d \leq 0 \\ F_{\text{SH},i} & F_{\text{SH},i} \dot{x}_d > 0 \end{cases}, \quad (4.18)$$

with $i \in \{1, 2, 3, 4\}$. This full-vehicle Skyhook policy recovers the quarter-vehicle Skyhook policy if $d_{\text{SH,heave}} = d_{\text{SH,roll}} = d_{\text{SH,pitch}}$.

As in the quarter-vehicle case, the combined Skyhook-Groundhook controller (SH/GH) with Groundhook part stated in (3.13) results from the superposition of the Skyhook and Groundhook control signals $\mathbf{F}_{sa,\text{SH}}$ and $\mathbf{F}_{sa,\text{GH}}$ according to

$$\mathbf{F}_{sa} = \mathbf{F}_{sa,\text{SH}} + \mathbf{F}_{sa,\text{GH}}. \quad (4.19)$$

4.5 Full-Vehicle LPV Control Design

This section presents the design of a full-vehicle DI LPV controller as introduced in Chapters 2 and Appendix A. The presented control design extends the quarter-vehicle control design of Section 3.5 and elaborates the full-vehicle semi-active LPV control approach published in Fleps-Dezasse and Brembeck (2016) and Fleps-Dezasse et al. (2017). The design process exploits the special structure of the DI problem introduced in Appendix A.4.4 and assembles the DI controller from the consecutive synthesis of a state-observer and a state-feedback controller to mitigate the computational complexity of the LPV control synthesis. The complexity issue constitutes an essential limitation during the application of LPV methods with high-order plants and numerous scheduling parameters. In addition to the simplifications of the DI controller design, the control design exploits Theorem 2.1 presented in Section 2.5 to determine the number of saturation indicator grid points. Theorem 2.1 is especially helpful in applications with several actuators like full-vehicle semi-active suspension control because the number of overall grid points scales exponentially with the number of actuators as described in (2.20).

The full-vehicle LTI state-space model \mathbf{G}_{fv} with general suspension force input F_s discussed in Section 4.3 is adapted to a semi-active damper force input \mathbf{F}_{sa} yielding the full-vehicle plant \mathbf{G}_{sa} as presented in Section 3.5. Figure 4.6 shows the corresponding full-vehicle control structure.

Due to its physical principle of converting kinetic energy into heat by means of hydraulic valves any damper is subject to the passivity constraint. These restrictive actuator force limits are considered during control design as presented in Section 3.5 by saturation indicator scheduling parameters $\boldsymbol{\theta}$. In the full-vehicle control design with four semi-active dampers, the four saturation indicators are gathered in the saturation indicator matrix $\boldsymbol{\Theta}$ given in (2.6). As discussed in Section 2.3, this saturation indicator matrix assumes decoupled actuator constraints which is perfectly valid during full-vehicle semi-active suspension control. The full-vehicle plant \mathbf{G}_{sa} also includes the damper force dynamics $\mathbf{G}_{u_d}(s)$ and the transformation of the semi-active damper force \mathbf{F}_{sa} by a nominal

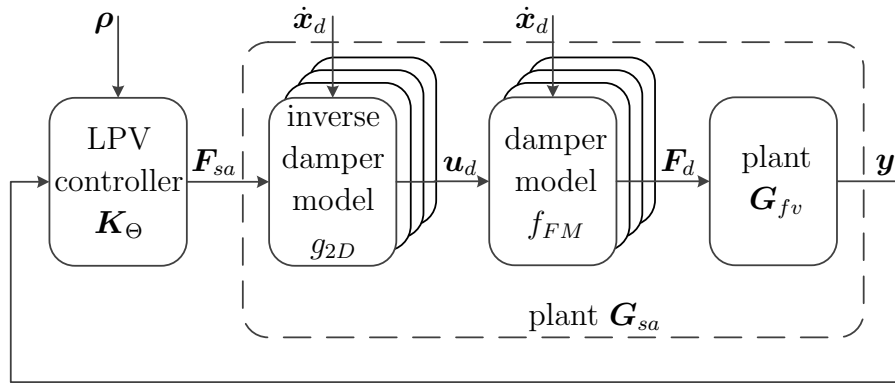


Figure 4.6: Control structure of full-vehicle semi-active suspension control

damper force \mathbf{F}_0 to the virtual damper force \mathbf{x}_{F_d} according to

$$\mathbf{F}_{sa} = \mathbf{F}_0 + \mathbf{x}_{F_d}. \quad (4.20)$$

In contrast to Section 3.5, however, this transformation is realized by linear nominal damper forces with constant nominal damping coefficients $d_{0,f}$ and $d_{0,r}$ of the front and rear suspensions given by

$$\mathbf{F}_0 = \begin{bmatrix} -d_{0,f} & 0 & 0 & 0 \\ 0 & -d_{0,f} & 0 & 0 \\ 0 & 0 & -d_{0,r} & 0 \\ 0 & 0 & 0 & -d_{0,r} \end{bmatrix} \begin{bmatrix} \dot{x}_{d,1} \\ \dot{x}_{d,2} \\ \dot{x}_{d,3} \\ \dot{x}_{d,4} \end{bmatrix}. \quad (4.21)$$

The constant nominal damping coefficients reduce the number of scheduling parameters of the LPV control design because no saturation transformer parameters are required, but simultaneously restrict the presented full-vehicle control design to semi-active dampers with approximately linear minimum damping.

The full-vehicle plant \mathbf{G}_{sa} can now be expressed by

$$\dot{\mathbf{x}} = \mathbf{A}\mathbf{x} + \mathbf{B}_1\mathbf{d}_g + \bar{\mathbf{B}}_2\Theta\mathbf{u}_{F_d}, \quad (4.22)$$

with the system states given by

$$\mathbf{x} = [x_{b,\text{CoG}} \ \dot{x}_{b,\text{CoG}} \ x_{b,\text{roll}} \ \dot{x}_{b,\text{roll}} \ x_{b,\text{pitch}} \ \dot{x}_{b,\text{pitch}} \\ x_{w,1} \ \dot{x}_{w,1} \ \dots \ x_{w,4} \ \dot{x}_{w,4} \ x_{g,1} \ \dots \ x_{g,4} \ x_{F_d,1} \ \dots \ x_{F_d,4}]. \quad (4.23)$$

Remark. Due to the kinematics of the suspension systems of passenger cars like McPherson or Double-Wishbone, the damper and spring deflection is not equivalent to the difference between the vertical body and wheel position. Therefore, the spring and damper deflections and forces have to be converted to their equivalent deflections and forces acting between body and wheel as depicted in Figure 4.5-right. The suspension spring force $F_{\text{spring},i}$ used in the plants \mathbf{G}_{fv} and \mathbf{G}_{sa} is computed from the linearized suspension spring stiffness $\bar{k}_{b,i}$ by

$$F_{\text{spring},i} = \underbrace{r_{\text{spring},i}^2}_{k_{b,i}} \bar{k}_{b,i} (x_{w,i} - x_{bs,i}), \quad (4.24)$$

with $r_{\text{spring},i}$ the conversion factor of the respective spring deflection. Similarly, the semi-active damper force \mathbf{F}_{sa} is computed by

$$F_{sa,i} = \underbrace{r_{\text{damper},i}^2}_{d_{0,i}} \bar{d}_{0,i} (\dot{x}_{w,i} - \dot{x}_{bs,i}) + \underbrace{r_{\text{damper},i}}_{u_{F_d,i}} \bar{u}_{F_d,i}, \quad (4.25)$$

with $r_{\text{damper},i}$ the conversion factor of the respective damper deflection and $\bar{u}_{F_d,i}$ the virtual damper force at the damper mounting position.

4.5.1 State-Observer Design

As presented in Appendix A.4.4, the first step of a DI control design consists of finding a suitable observer gain. This task simplifies to a classical \mathcal{H}_∞ state-observer design problem, due to the constant nominal damping coefficients. Figure 3.8 shows the weighting scheme of the full-vehicle observer design problem. Compared to the quarter-vehicle problem of Section 3.5.1, the full-vehicle problem considers four separate road disturbance inputs \mathbf{d}_g . The corresponding road disturbance weight \mathbf{W}_g comprises one first-order weighting filters according to (C.6) for each disturbance input and shapes the road disturbance amplitudes of each disturbance input according to the PSDs of real roads reported by ISO (8608:1995). As in the quarter-vehicle design, the diagonal weighting matrix $\mathbf{W}_e = \text{diag}([w_{e,1}, \dots, w_{e,n_x}]^T)$ prioritizes the estimation error of distinct states and the diagonal weighting matrix $\mathbf{W}_n = \text{diag}([w_{n,1}, \dots, w_{n,n_y}]^T)$ scales the measurement disturbances \mathbf{d}_n .

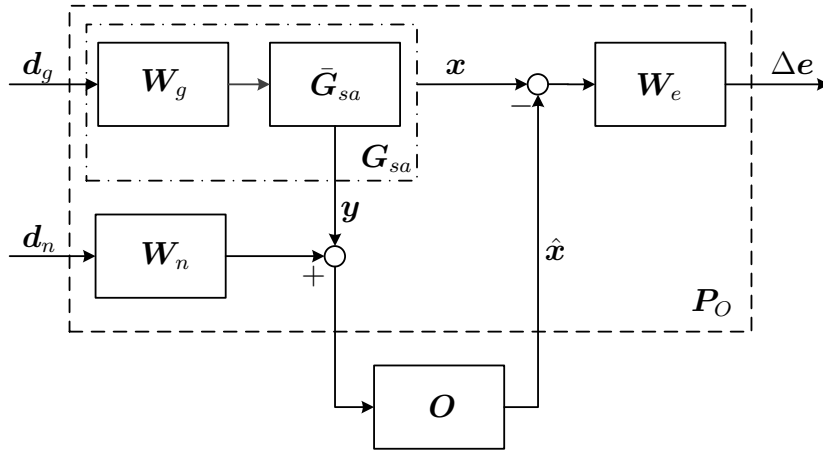


Figure 4.7: Weighting scheme of full-vehicle state-observer design

The full-vehicle state-observer design assumes measurements of the body accelerations $\mathbf{y}_{\ddot{x}_{ba}}$ near each suspension unit, the wheel accelerations $\mathbf{y}_{\ddot{x}_w}$ and the damper velocities $\mathbf{y}_{\dot{x}_d}$. The body acceleration measurements are related to the body heave, roll and pitch accelerations by

$$\begin{bmatrix} y_{\ddot{x}_{ba},1} \\ y_{\ddot{x}_{ba},2} \\ y_{\ddot{x}_{ba},3} \\ y_{\ddot{x}_{ba},4} \end{bmatrix} = \underbrace{\begin{bmatrix} 1 & l_{ba1,y} & -l_{ba1,x} \\ 1 & -l_{ba2,y} & -l_{ba2,x} \\ 1 & l_{ba3,y} & l_{ba3,x} \\ 1 & -l_{ba4,y} & l_{ba4,x} \end{bmatrix}}_{\mathbf{T}_{ba}} \begin{bmatrix} \ddot{x}_{b,\text{CoG}} \\ \ddot{x}_{b,\text{roll}} \\ \ddot{x}_{b,\text{pitch}} \end{bmatrix}, \quad (4.26)$$

with $l_{bai,y}$ denoting the y-distance of the respective sensor mounting position from the body CoG and $l_{bai,x}$ denoting the corresponding x-distance. The damper velocities can

be computed from the body velocities at each suspension \mathbf{x}_{bs} and the wheel velocities \mathbf{x}_w using the constant conversion factors $r_{\text{damper},i}$ according to

$$y_{\dot{x}_d,i} = r_{\text{damper},i} (x_{bs,i} - x_{w,i}). \quad (4.27)$$

The resulting generalized plant \mathbf{P}_O of the observer synthesis can be expressed by

$$\begin{bmatrix} \Delta \dot{\mathbf{x}} \\ \Delta \mathbf{e} \\ \Delta \mathbf{y} \end{bmatrix} = \begin{bmatrix} \mathbf{A} & \mathbf{B}_1 & \mathbf{I} \\ \mathbf{C}_1 & \mathbf{0} & \mathbf{0} \\ \mathbf{C}_2 & \mathbf{D}_{21} & \mathbf{0} \end{bmatrix} \begin{bmatrix} \Delta \mathbf{x} \\ \mathbf{d} \\ \Delta \mathbf{v} \end{bmatrix}. \quad (4.28)$$

with the disturbance inputs \mathbf{d} given by

$$\mathbf{d} = [\mathbf{d}_g \ \mathbf{d}_{n,\ddot{x}_{ba}} \ \mathbf{d}_{n,\ddot{x}_w} \ \mathbf{d}_{n,\dot{x}_d}]^T. \quad (4.29)$$

The states of the open-loop plant \mathbf{G}_{sa} are given in (4.23) and the corresponding measurements \mathbf{y} are given by

$$\mathbf{y} = [\mathbf{y}_{\ddot{x}_{ba}}^T \ \mathbf{y}_{\ddot{x}_w}^T \ \mathbf{y}_{\dot{x}_d}^T]^T. \quad (4.30)$$

The state-observer can be synthesized according to Appendix A.4.1 and A.4.2. The tuning parameters of the observer problem are

- the scaling factors of the state-estimation errors $w_{e,1}, \dots, w_{e,n_x}$,
- the scaling factors of the measurement disturbances $w_{n,1}, \dots, w_{n,n_y}$, and
- the parameters of the road model β_r , α_r and v_{ref} .

Equally to the quarter-vehicle control design, the vehicle speed v_v of the road model is fixed to a reference speed v_{ref} to avoid a vehicle speed scheduling parameter. The determination of optimal values of these tuning parameters is discussed later on in Section 4.7.

4.5.2 DI Controller Design

This section extends the quarter-vehicle control design presented in Section 3.5.2 to a full-vehicle application. The controller is designed along the same mixed sensitivity S/KS loop shaping scheme as employed in Section 3.5.2. Figure 4.8 illustrates the elements of the design scheme with unconstrained open-loop plant \mathbf{G} , constrained open-loop plant \mathbf{G}_{sa} and generalized plant \mathbf{P}_Θ . The open-loop plant \mathbf{G}_{sa} is excited by the disturbances \mathbf{d} shaped by the weighting function \mathbf{W}_d . The control effort \mathbf{e}_u is weighted by the saturation indicator dependent weight $\mathbf{W}_u(\boldsymbol{\theta})$ and the performance signals \mathbf{e}_a are weighted by the saturation indicator dependent weight $\mathbf{W}_a(\boldsymbol{\theta})$. According to Section 3.5.2, the S/KS mixed sensitivity design problem depicted in Figure 4.8 with closed-loop system $\Gamma_{ed}(\mathbf{P}_\Theta, \mathbf{K}_\Theta)$ can be expressed by



This representation is based on the augmented sensitivity function \mathbf{S}_a introduced in (3.33) given by

with the closed-loop mapping \mathbf{S} of output disturbances to the measurement signals. In Skogestad and Postlethwaite (2005), the closed-loop mapping \mathbf{S} of an LTI system is referred to as sensitivity function. The indices ad and yd of the plant \mathbf{G} describe the plant input and output signals, namely the input signals \mathbf{d} and the output signals \mathbf{y}_a and \mathbf{y} , respectively. As described in Section 3.5.2, representation (4.31) is helpful during the specification of performance signals and corresponding weighting functions as (4.31) imposes

and simultaneously

The DI control design introduced in Section 2.4 defines the control effort weighting function

$$\mathbf{W}_u(\boldsymbol{\theta}) = \mathbf{\Theta}^{-1}, \quad (4.35)$$

to achieve the desired controller behavior, i.e the controller linearly reduces its output with increasing actuator saturation. Furthermore, the DI control problem structure restricts the disturbances \mathbf{d} , the disturbance weighting function \mathbf{W}_d and the disturbance models \mathbf{G}_{yd} and \mathbf{G}_{ad} according to the DI plant assumptions introduced in Appendix A.4.4. The exact determination of these quantities can be performed analogous to the quarter-vehicle case described in Section 3.5.2.

In a full-vehicle application, the body not only moves in vertical direction, but also rotates around the roll and pitch axes. As presented in Section 4.2, the corresponding accelerations, namely body heave acceleration $\ddot{x}_{b,\text{CoG}}$, angular roll acceleration $\ddot{x}_{b,\text{roll}}$ and angular pitch acceleration $\ddot{x}_{b,\text{pitch}}$ determine ride comfort. Instead of the scalar body-related performance signal of the quarter-vehicle control design, the full-vehicle control design employs all three velocities $\dot{x}_{b,\text{CoG}}$, $\dot{x}_{b,\text{roll}}$ and $\dot{x}_{b,\text{pitch}}$ as performance signals. These signals complemented by the four wheel velocities $\dot{\mathbf{x}}_w$ form the overall performance signals according to

$$\mathbf{e}_a = \mathbf{W}_a \begin{bmatrix} \dot{x}_{b,\text{CoG}} & \dot{x}_{b,\text{roll}} & \dot{x}_{b,\text{pitch}} & \dot{\mathbf{x}}_w^T \end{bmatrix}^T. \quad (4.36)$$

The velocity signals are again preferred over the corresponding acceleration signals because the velocity signals directly emphasize the required frequency range of each signal as illustrated in Figure 3.10. In this way, no high-order weighting functions are needed for the design target specification and simple, first-order weighting functions as employed during the quarter-vehicle control design are sufficient. The weighting function $\mathbf{W}_{a,b}$ of the body signals $\dot{x}_{b,\text{CoG}}$, $\dot{x}_{b,\text{roll}}$ and $\dot{x}_{b,\text{pitch}}$ is defined as

$$\mathbf{W}_{a,b}(\boldsymbol{\theta}) = \left(\frac{1}{n_u} \sum_{i=1}^{n_u} \theta_i \right) \begin{bmatrix} w_{b,h} & 0 & 0 \\ 0 & w_{b,r} & 0 \\ 0 & 0 & w_{b,p} \end{bmatrix} \mathbf{G}_{pt1,b}, \quad (4.37)$$

with $\mathbf{G}_{pt1,b}$ a diagonal weighting filter matrix comprised of three first-order filters similar to (3.43) with bandwidths $w_{b,h}$, $w_{b,r}$ and $w_{b,p}$. The performance signals $\mathbf{e}_{a,b}$ are scaled by the mean value of the saturation indicators $\boldsymbol{\theta}$. This definition of the θ -dependence of $\mathbf{W}_{a,b}(\boldsymbol{\theta})$ gradually decreases the gain of $\mathbf{W}_{a,b}(\boldsymbol{\theta})$ to account for the reduced performance potential in the event of actuator saturation. Conversely, the wheel motion is essentially influenced by the attached damper and thus the performance requirement of each wheel velocity signal should be individually reduced according to the saturation status of the attached damper. This can be realized by defining $\mathbf{W}_{a,w}(\boldsymbol{\theta})$ as

$$\mathbf{W}_{a,w}(\boldsymbol{\theta}) = w_w \boldsymbol{\Theta}, \quad (4.38)$$

with the tuning parameter w_w .

The generalized plant \mathbf{P}_Θ gathering the full-vehicle plant \mathbf{G}_{sa} and the weighting functions

can be stated by

$$\begin{bmatrix} \dot{\mathbf{x}} \\ \begin{bmatrix} \mathbf{e}_a \\ \mathbf{e}_u \\ \mathbf{y} \end{bmatrix} \end{bmatrix} = \begin{bmatrix} \mathbf{A} & \bar{\mathbf{L}} & \bar{\mathbf{B}}_2 \boldsymbol{\Theta} \\ \begin{bmatrix} \mathbf{C}_{11}(\boldsymbol{\theta}) \\ \mathbf{0} \\ \mathbf{C}_2 \end{bmatrix} & \begin{bmatrix} \mathbf{0} \\ \mathbf{0} \\ \mathbf{I} \end{bmatrix} & \begin{bmatrix} \mathbf{0} \\ \mathbf{I} \\ \mathbf{0} \end{bmatrix} \end{bmatrix} \begin{bmatrix} \mathbf{x} \\ \mathbf{d} \\ \mathbf{u}_{F_d} \end{bmatrix}. \quad (4.39)$$

with the observer gain $\bar{\mathbf{L}} = [\mathbf{L} \mathbf{0}]^T$ which extends from the original observer gain \mathbf{L} of Section 4.5.1 by three rows of zeros to account for the additional states introduced by the weighting function $\mathbf{W}_{a,b}$. Similarly, the system matrix \mathbf{A} and the input matrix $\bar{\mathbf{B}}_2$ are also adjusted according to $\mathbf{W}_{a,b}$. The DI controller \mathbf{K}_Θ obtained by the controller synthesis described in Appendix A with plant \mathbf{P}_Θ has the form

$$\begin{bmatrix} \dot{\mathbf{x}}_K \\ \mathbf{u}_{F_d} \end{bmatrix} = \begin{bmatrix} \mathbf{A} + \bar{\mathbf{B}}_2 \boldsymbol{\Theta} \mathbf{F}(\boldsymbol{\theta}) & \bar{\mathbf{L}} \\ \mathbf{F}(\boldsymbol{\theta}) & \mathbf{0} \end{bmatrix} \begin{bmatrix} \mathbf{x}_K \\ \mathbf{y} \end{bmatrix}, \quad (4.40)$$

with state-feedback gain $\mathbf{F}(\boldsymbol{\theta})$ according to (A.26) given by

$$\mathbf{F}(\boldsymbol{\theta}) = -\boldsymbol{\Theta} \gamma^2 \bar{\mathbf{B}}_2^T \mathbf{Z}. \quad (4.41)$$

In contrast to the quarter-vehicle control design of Section 3.5.2, the full-vehicle control design presented here uses a constant Lyapunov matrix \mathbf{Z} .

The proposed performance signals and weighting functions yield far less additional states in the generalized plant and consequently a controller with less states compared to the design schemes proposed in Do et al. (2010, p. 4656) and Do et al. (2012, p. 398). These schemes employ second-order weighting function for the body and wheel related performance signals and introduce a significant number of additional states into the controller synthesis problem. The disturbance inputs of the DI control design, namely body and wheel acceleration and damper velocity feature the advantage that they inherently better emphasize the frequency range of interest compared to the road profile height disturbance input employed in Do et al. (2010) and Poussot-Vassal et al. (2008). This property is visualized in Section 4.7 by the corresponding frequency responses of the unconstrained open-loop system and the frozen closed-loop LPV systems with $\theta_i = 1 \ \forall i \in \{1, 2, 3, 4\}$ and $\theta_i = \theta_{\min} \ \forall i \in \{1, 2, 3, 4\}$.

The tuning parameters of the DI problem are

- the scaling factors $w_{b,h}$, $w_{b,r}$ and $w_{b,p}$ of the body velocities $\dot{x}_{b,\text{CoG}}$, $\dot{x}_{b,\text{roll}}$ and $\dot{x}_{b,\text{pitch}}$, and
- the scaling factor w_w of the wheel velocities \dot{x}_w .

The optimal values of these tuning parameters are obtained as discussed in Section 4.7.

4.6 Fault-Tolerant Control Augmentation

The proposed FTC augmentation considers damper malfunctions that reduce the damper force, e.g. due to oil leakage or a loss of the electrical power supply similar to Sename et al. (2013). In Sename et al. (2013) actuator faults are described by actuator efficiency parameters and the quarter-vehicle LPV controller presented in Do et al. (2010) is extended such that it achieves closed-loop stability and a specified performance for all actuator efficiencies. The paper reports simulation results illustrating the improved performance of the FTC LPV controller. Tudón-Martinez et al. (2013) present a full-vehicle application of fault-tolerant semi-active suspension control. Similar to Sename et al. (2013) actuator malfunction is described by actuator efficiency parameters, but instead of introducing the actuator efficiency parameters into the quarter-vehicle LPV controller design, they are employed to compute appropriate compensation forces for the remaining healthy dampers. The compensation forces are added as a feedforward action to the respective damper and simultaneously the applied compensation forces are subtracted from the force limits of the quarter-vehicle LPV feedback controllers. The full-vehicle is then composed of four quarter-vehicle controllers, one for each vehicle suspension.

The fault representation particularly assumes that the fault reduces the minimum and maximum controller force constraints according to

$$\bar{\mathbf{u}}_{F_d}^{\max} = \mathbf{M}_\eta \mathbf{u}_{F_d}^{\max}, \quad (4.42)$$

and

$$\bar{\mathbf{u}}_{F_d}^{\min} = \mathbf{M}_\eta \mathbf{u}_{F_d}^{\min}, \quad (4.43)$$

with the diagonal actuator efficiency matrix $\mathbf{M}_\eta = \text{diag}([\eta_1 \dots \eta_{n_u}]^T)$ and the actuator efficiencies satisfying $\eta_i \in (0, 1] \ \forall i \in \{1, \dots, n_u\}$. Furthermore, the fault representation assumes that the failure likewise affects compression and rebound leading to

$$\eta_i = \frac{\bar{u}_{F_d,i}^{\max}}{u_{F_d,i}^{\max}} = \frac{\bar{u}_{F_d,i}^{\min}}{u_{F_d,i}^{\min}}. \quad (4.44)$$

The design target of the augmentation of the LPV controller \mathbf{K}_Θ in the event of a damper failure can be summarized as follows:

- the augmented controller should be stable for all combinations of damper failures, and
- the performance degradation due to damper failures should be minimized.

The fault-tolerant properties of the LPV controller are achieved by integrating some ideas of Sename et al. (2013) and Tudón-Martinez et al. (2013) into the full-vehicle LPV control design with saturation indicators presented in Section 4.5. A comparison of the definition of actuator efficiency in Sename et al. (2013) and of saturation indicators in Wu et al.

(2000) shows that saturation indicators can readily be used to describe actuator malfunction. The following section investigates stability of the LPV controller from (4.39) and shows the adjustment of the saturation indicator definition to account for damper malfunction. Subsequently, Section 4.6.2 presents the augmentation of the nominal controller by a force reconfiguration such that the remaining healthy dampers compensate for the force loss of a malfunctioning damper.

This work assumes the existence of a fault detection algorithm, e.g. as proposed by Fischer and Isermann (2004) and Tudón-Martinez et al. (2013) providing the necessary fault information.

4.6.1 Stability of the Nominal Controller

The analysis of the definition of actuator efficiency from Sename et al. (2013) and actuator saturation from Wu et al. (2000) reveals that saturation indicators readily describe the considered class of actuator malfunction. This is possible due to the high flexibility of the actuator force constraint representation by saturation indicators. In particular, the actuator force limits are not explicitly considered in the controller design, but just the saturation indicators. Thus the actuator force limits employed in the calculation of the saturation indicators can be updated according to the force limits of malfunctioning dampers. The saturated control signal $\bar{\sigma}(u_{F_d,i})$ with consideration of actuator malfunction can be computed by

$$\bar{\sigma}(u_{F_d,i}) = \begin{cases} u_{F_d,i} & \eta_i u_{F_d,i}^{\min}(\mathbf{x}) < u_{F_d,i} < \eta_i u_{F_d,i}^{\max}(\mathbf{x}) \\ \eta_i u_{F_d,i}^{\min}(\mathbf{x}) & \eta_i u_{F_d,i}^{\min}(\mathbf{x}) \geq u_{F_d,i} \\ \eta_i u_{F_d,i}^{\max}(\mathbf{x}) & \eta_i u_{F_d,i}^{\max}(\mathbf{x}) \leq u_{F_d,i} \end{cases}. \quad (4.45)$$

The corresponding saturation indicators $\bar{\theta}_i$ are given by

$$\bar{\theta}_i = \frac{\bar{\sigma}(u_{F_d,i})}{u_{F_d,i}}. \quad (4.46)$$

They can be computed from the saturation indicators θ_i of the nominal system according to

$$\bar{\theta}_i = \begin{cases} \theta_i & \eta_i u_{F_d,i}^{\min}(\mathbf{x}) < u_{F_d,i} < \eta_i u_{F_d,i}^{\max}(\mathbf{x}) \\ \eta_i \theta_i & \eta_i u_{F_d,i}^{\min}(\mathbf{x}) \geq u_{F_d,i} \\ \eta_i \theta_i & \eta_i u_{F_d,i}^{\max}(\mathbf{x}) \leq u_{F_d,i} \end{cases}. \quad (4.47)$$

Consequently, the LPV controller $\mathbf{K}_{\bar{\theta}}$ using saturation indicators $\bar{\theta}_i \in (0, 1] \forall i \in \{1, \dots, n_u\}$ stabilizes the closed-loop system for all combinations of damper failures.

4.6.2 Augmentation of the Nominal Controller

From the structure of the feedback controller in (4.39) and (4.41) it is clear, that the LPV controller $\mathbf{K}_{\bar{\theta}}$ reduces the controller output \mathbf{u}_{F_d} of saturated or malfunctioning actuators

by $\bar{\Theta}$ without any interference to the remaining unsaturated actuators. Even though this controller guarantees stability in the admissible parameter range as discussed in the previous section, for a reduction of the performance degradation in the event of damper malfunction it would be preferable if the controller would compensate for the lost forces \mathbf{u}_δ . Figure 4.9-left shows the structure of the nominal LPV controller $\mathbf{K}_{\bar{\Theta}}$ without force reconfiguration. The control signals of the unconstrained controller \mathbf{K}_0 are scaled with their corresponding saturation indicators yielding the control signal \mathbf{u}_{F_d} . An analysis of the four suspension force inputs of the LTI full-vehicle model \mathbf{G}_{fv} reveals a weak input redundancy with respect to body heave, roll and pitch accelerations. According to Zaccarian (2009, p. 1432), a linear plant is weakly input redundant if

$$\mathbf{G}_{fv}^* = \lim_{s \rightarrow 0} (\mathbf{C}(s\mathbf{I} - \mathbf{A})^{-1}\mathbf{B} + \mathbf{D}) \quad (4.48)$$

is finite with $*$ denoting the steady-state values of the signals and if $\text{Ker } \mathbf{G}_{fv}^*$ satisfies

$$\text{Ker } \mathbf{G}_{fv}^* \neq 0. \quad (4.49)$$

Systems \mathbf{G}_{fv} satisfying the properties stated in (4.48) and (4.49) feature a kernel such that different inputs are mapped to the same output. In contrast to strong input redundancy, the force allocation transients are visible at the plant outputs \mathbf{y} in case of weak input redundancy and thus the allocation influences stability of the augmented controller. Furthermore, the weak input redundancy is most effective at $s \rightarrow 0$ and consequently the allocation should focus on the low frequency range. The weak input redundancy can be exploited by augmenting the nominal LPV controller $\mathbf{K}_{\bar{\Theta}}$ through a force reconfiguration matrix $\mathbf{T}(\bar{\theta})$ which uses the kernel of \mathbf{G}_{fv}^* . Starting from the nominal controller, the force reconfiguration introduces cross-connections between the control signals depending on the saturation indicators. The control signal $\bar{\mathbf{u}}_{F_d}$ of the augmented controller $\bar{\mathbf{K}}_{\bar{\Theta}}$ is defined as the summation of the original control signal \mathbf{u}_{F_d} and a redistribution of the control signal \mathbf{u}_δ lost in the event of malfunction or saturation according to

$$\bar{\mathbf{u}}_{F_d} = \mathbf{u}_{F_d} + \alpha_u \bar{\mathbf{T}}_u(\bar{\theta}) \mathbf{u}_\delta, \quad (4.50)$$

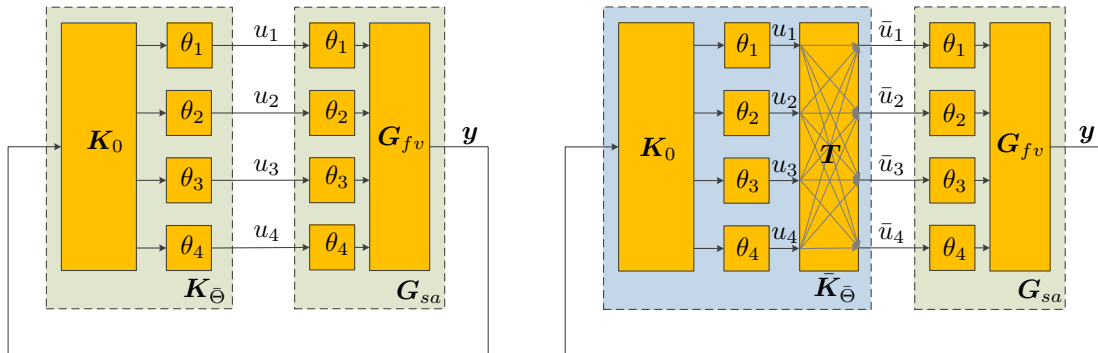


Figure 4.9: Left - structure of the nominal controller without force reconfiguration; right - structure of the augmented controller with force reconfiguration

with the scalar $\alpha_u \in [0, 1]$ and the force redistribution matrix $\bar{\mathbf{T}}_u(\bar{\boldsymbol{\theta}})$. The scalar α_u is introduced into (4.50) to provide a tuning parameter for the amount of force redistribution, i.e. $(\alpha_u \times 100)$ % of the control signal loss \mathbf{u}_δ are redistributed to the remaining healthy dampers. The control signal loss \mathbf{u}_δ can be calculated by

$$\mathbf{u}_\delta = (\mathbf{I} - \bar{\boldsymbol{\Theta}}) \mathbf{u}_0, \quad (4.51)$$

with \mathbf{u}_0 the healthy control signal. Here, the term healthy control signal is used for \mathbf{u}_0 because the output \mathbf{u}_{F_d} of the nominal controller $\mathbf{K}_{\bar{\boldsymbol{\Theta}}}$ equals \mathbf{u}_0 in the absence of malfunction or saturation due to $\bar{\boldsymbol{\Theta}} = \mathbf{I}$ and $\mathbf{u}_{F_d} = \bar{\boldsymbol{\Theta}} \mathbf{u}_0$. This relation is visualized by Figure 4.9-left. The control signal loss \mathbf{u}_δ can be alternatively expressed as a function of the output of the nominal controller \mathbf{u}_{F_d} by

$$\mathbf{u}_\delta = (\bar{\boldsymbol{\Theta}}^{-1} - \mathbf{I}) \mathbf{u}_{F_d}. \quad (4.52)$$

Due to the computation of the augmented control signal $\bar{\mathbf{u}}_{F_d}$ in (4.50) and in particular the control signal loss \mathbf{u}_δ using the saturation indicator definition of (4.47), the force redistribution covers both actuator malfunction and saturation. Figure 4.9-right depicts the structural augmentation of the nominal controller $\mathbf{K}_{\bar{\boldsymbol{\Theta}}}$ with the force reconfiguration matrix $\mathbf{T}(\bar{\boldsymbol{\theta}})$. The augmented control signal can be stated by

$$\bar{\mathbf{u}}_{F_d} = (\mathbf{I} + \mathbf{T}(\bar{\boldsymbol{\theta}})) \mathbf{u}_{F_d}, \quad (4.53)$$

as a function of the force reconfiguration matrix $\mathbf{T}(\bar{\boldsymbol{\theta}})$ and the nominal control signal \mathbf{u}_{F_d} . The force reconfiguration matrix $\mathbf{T}(\bar{\boldsymbol{\theta}})$ is related to the force redistribution matrix $\bar{\mathbf{T}}_u(\bar{\boldsymbol{\theta}})$ of (4.50) according to

$$\mathbf{T}(\bar{\boldsymbol{\theta}}) = \alpha_u \bar{\mathbf{T}}_u(\bar{\boldsymbol{\theta}}) (\bar{\boldsymbol{\Theta}}^{-1} - \mathbf{I}). \quad (4.54)$$

The derivation of the force reconfiguration individually considers the failure conditions from no damper malfunctioning to one damper malfunctioning to ultimately all dampers malfunctioning. The idea is to find a force redistribution matrix $\bar{\mathbf{T}}_u(\bar{\boldsymbol{\theta}})$ that gives a good approximation of the optimal redistribution for all failure conditions.

Firstly, the condition with no damper failure is considered. In this case, the control signal loss \mathbf{u}_δ is zero and the redistribution matrix does not affect the augmented control signal $\bar{\mathbf{u}}_{F_d}$. Consequently, the force redistribution matrix can be arbitrary, but with finite elements, i.e. $\|\bar{\mathbf{T}}_u(\bar{\boldsymbol{\theta}})\|_\infty < \infty \forall \bar{\theta}_i \in (0, 1]$.

Secondly, the conditions with one malfunctioning damper are considered. In this case, the weak input redundancy of the full-vehicle can be exploited to derive an optimal force redistribution by four separate equilibrium analyses of the LTI full-vehicle \mathbf{G}_{fv} as shown in Tudón-Martínez et al. (2013). The four resulting force redistribution matrices $\bar{\mathbf{T}}_{ui}$ can then be gathered into the redistribution matrix $\bar{\mathbf{T}}_{ug}$ according to

$$\bar{\mathbf{T}}_{ug} = \sum_{i=1}^{n_u} \bar{\mathbf{T}}_{ui}. \quad (4.55)$$

The matrices $\bar{\mathbf{T}}_{ui}$ are computed by imposing that the remaining healthy dampers compensate the effect of the control signal loss $u_{\delta,i}$ due to malfunction of the i -th damper. In particular, the design goal is to achieve the same body heave, roll and pitch accelerations \mathbf{y}_{hrp} of the healthy system and the system with one damper failure. If damper $i = 1$ is assumed faulty, this design goal can be stated by

$$\mathbf{y}_{hrp} = \begin{bmatrix} \ddot{x}_{b,\text{CoG}} \\ \ddot{x}_{b,\text{roll}} \\ \ddot{x}_{b,\text{pitch}} \end{bmatrix} = \mathbf{G}_{fv,hrp}(j0) \begin{bmatrix} u_{\delta,1} \\ 0 \\ 0 \\ 0 \end{bmatrix} = \bar{\mathbf{G}}_{fv,hrp}(j0) \begin{bmatrix} \bar{u}_{r,2} \\ \bar{u}_{r,3} \\ \bar{u}_{r,4} \end{bmatrix}, \quad (4.56)$$

with the control signals $\bar{u}_{r,j}$ to be added to the nominal control signal of the three healthy damper $j \in \{2, 3, 4\}$. The control signals $u_{r,j}$ can be expressed by

$$\begin{bmatrix} \bar{u}_{r,2} \\ \bar{u}_{r,3} \\ \bar{u}_{r,4} \end{bmatrix} = \tilde{\mathbf{T}}_{u1} \begin{bmatrix} u_{\delta,1} \\ 0 \\ 0 \\ 0 \end{bmatrix}, \quad (4.57)$$

with $\tilde{\mathbf{T}}_{u1} = \bar{\mathbf{G}}_{fv,hrp}^{-1}(j0) \mathbf{G}_{fv,hrp}(j0)$. The inversion of the 3×3 matrix $\bar{\mathbf{G}}_{fv,hrp}(j0)$ is always defined in a full-vehicle application as long as the actuators have different points of application. The matrix $\bar{\mathbf{T}}_{u1}$ used in (4.55) can now be computed by

$$\bar{\mathbf{T}}_{u1} = \left[\begin{array}{cccc} 0 & 0 & 0 & 0 \\ \hline \tilde{\mathbf{T}}_{u1} & - [\mathbf{0} & \mathbf{I}] \end{array} \right]. \quad (4.58)$$

In (4.58) the 3×4 matrix $\tilde{\mathbf{T}}_{u1}$ is extended to the 4×4 matrix $\bar{\mathbf{T}}_{u1}$. Therefore, a row of zeros is added such that any control input results in zero output of the faulty damper. Additionally, the matrix $\tilde{\mathbf{T}}_{u1}$ preserves the control signals of the control inputs $u_{\delta,2}$ to $u_{\delta,4}$ which are all zero in (4.57). This property is obstructive for the computation of $\bar{\mathbf{T}}_{ug}$ according to (4.55) and thus the identity entries are canceled in (4.58). The matrices $\bar{\mathbf{T}}_{u2}$ to $\bar{\mathbf{T}}_{u4}$ can be derived in a similar manner, e.g. the matrix $\bar{\mathbf{T}}_{u4}$ can be computed from $\tilde{\mathbf{T}}_{u4}$ by

$$\bar{\mathbf{T}}_{u4} = \left[\begin{array}{cccc} \tilde{\mathbf{T}}_{u4} & - [\mathbf{I} & \mathbf{0}] \\ \hline 0 & 0 & 0 & 0 \end{array} \right]. \quad (4.59)$$

The matrix $\bar{\mathbf{T}}_{ug}$ optimally redistributes the force losses \mathbf{u}_{δ} in case of one malfunctioning actuator and satisfies the condition $\|\bar{\mathbf{T}}_{ug}(\bar{\boldsymbol{\theta}})\|_{\infty} < \infty$.

In case of all actuators malfunctioning, however, the matrix $\bar{\mathbf{T}}_{ug}$ redistributes the force losses \mathbf{u}_{δ} from one faulty actuator to the other faulty actuators. This behavior counteracts the original controller behavior which reduces the nominal control signal \mathbf{u}_{F_d} by $\bar{\boldsymbol{\Theta}}$. In particular, a force redistribution using $\bar{\mathbf{T}}_u(\bar{\boldsymbol{\theta}}) = \bar{\mathbf{T}}_{ug}$ increases the augmented control signals $\bar{\mathbf{u}}_{F_d}$ far beyond the force limits of the actuators such that the saturation possibly

exceeds the admissible saturation indicator range. To reduce this effect, the matrix $\bar{\mathbf{T}}_{ug}$ is scaled by $\bar{\Theta}^2$ leading to the redistribution matrix $\bar{\mathbf{T}}_u = \bar{\Theta}^2 \bar{\mathbf{T}}_{ug}$. This matrix $\bar{\mathbf{T}}_u$ still optimally redistributes the force loss \mathbf{u}_δ if one actuator is malfunctioning, but no longer superimposes significant forces to other malfunctioning actuators. The augmented control signal $\bar{\mathbf{u}}_{F_d}$ can then be computed according to (4.53) with the force reconfiguration matrix

$$\mathbf{T}(\bar{\theta}) = \alpha_u \bar{\Theta}^2 \bar{\mathbf{T}}_{ug}(\bar{\theta}) (\bar{\Theta}^{-1} - \mathbf{I}). \quad (4.60)$$

In case of two or more actuators malfunctioning, the force reconfiguration matrix $\mathbf{T}(\bar{\theta})$ redistributes the control signal loss \mathbf{u}_δ from the faulty actuators to the remaining healthy actuators. This redistribution, however, is only an approximation of the optimal force redistribution. The approximation results from the design of the force reconfiguration matrix as described above which focuses on an optimal force reconfiguration of the most likely condition of one actuator malfunctioning.

To verify that the introduction of the reconfiguration of the nominal controller output does not corrupt stability of the closed-loop LPV system, the existence of the induced L_2 -norm of the modified closed-loop with

$$\bar{\mathbf{F}}(\theta) = -\gamma^2 (\mathbf{I} + \mathbf{T}(\bar{\theta})) \bar{\Theta} \bar{\mathbf{B}}_2^T \mathbf{Z} \quad (4.61)$$

is verified by calculating the performance index of the modified closed-loop. In this process, the scalar α_u acts as a tuning parameter, which is increased from zero towards one.

4.6.3 Verification of the Augmented Controller

The proposed augmented LPV controller $\bar{\mathbf{K}}_{\bar{\Theta}}$ is verified by a simulation scenario using the nonlinear simulation model discussed in Appendix E.2. The simulation scenario assumes a failure of one damper such that this damper provides only the minimal damper force and the actuator efficiency approaches zero. The vehicle model is excited by a heave, roll and pitch sine sweep with constant excitation velocity amplitude and a frequency progression from 1 Hz to 6 Hz. The force reconfiguration has been designed to reduce the body heave, roll and pitch accelerations, which define ride comfort. Therefore, the ride comfort index described in Section 4.2 is employed to assess the performance of the augmented controller. During the experiments, the parameter α_u of the augmented controller was set to $\alpha_u = 0.75$. The result of the controller assessment is shown in Table 4.1. The percentage values provided there indicate the ride comfort degradation relative to ride comfort of the nominal closed-loop without damper failure. Compared to the nominal controller $\mathbf{K}_{\bar{\Theta}}$, the augmented controller $\bar{\mathbf{K}}_{\bar{\Theta}}$ with force reconfiguration achieves a significant reduction of performance degradation for all three types of excitations.

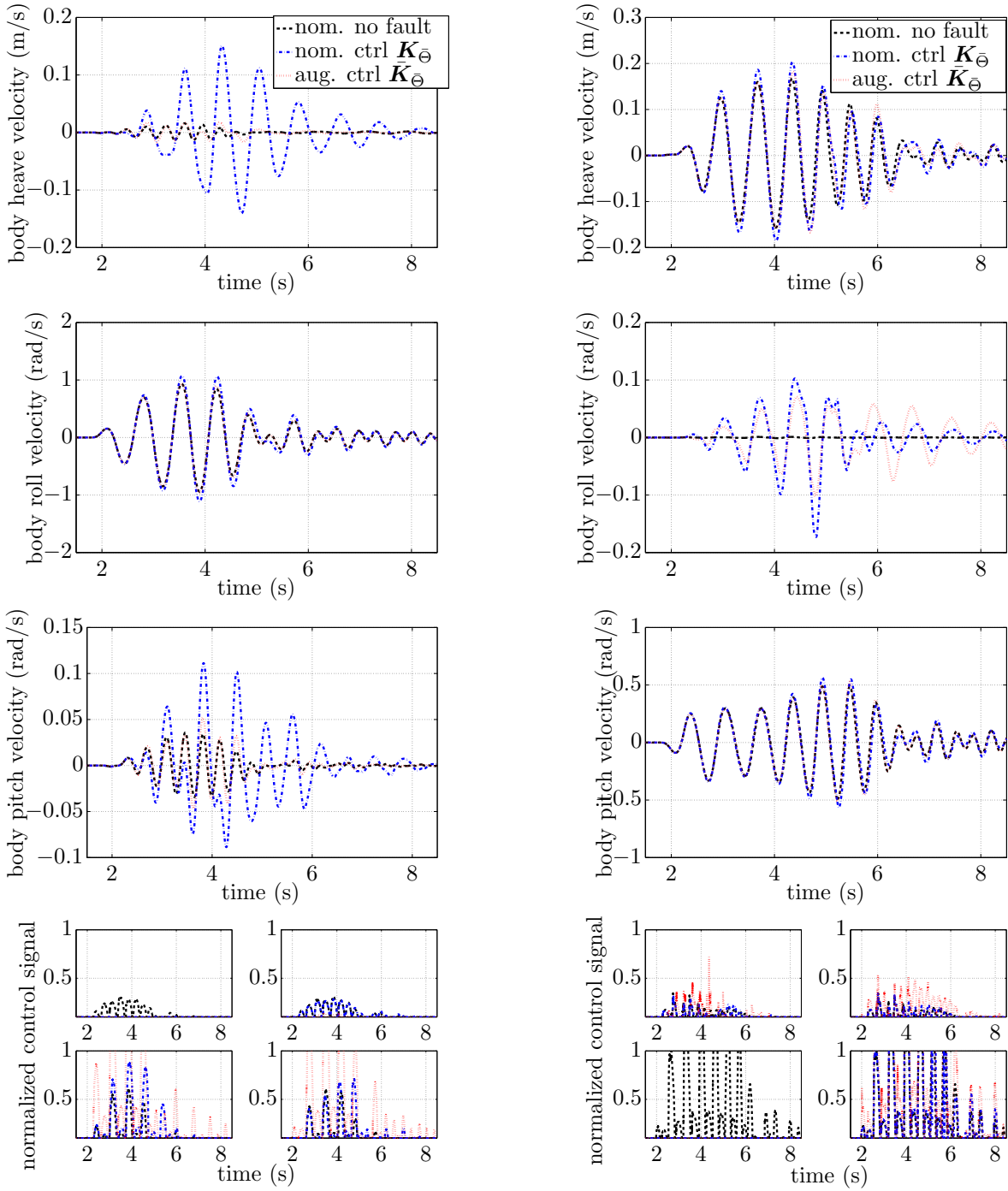
The performance improvement of the force reconfiguration, however, is not as large as reported by Tudón-Martínez et al. (2013). This difference can be attributed to the distinct ride comfort definitions, while Tudón-Martínez et al. (2013) considers the roll angle as

Table 4.1: Performance degradation due to failure of front left (FL) or rear left (RL) damper. The percentages indicate the degradation relative to the nominal closed-loop without damper failure.

	heave	roll	pitch
	FL failure	FL failure	RL failure
nom. ctrl $\mathbf{K}_{\bar{\Theta}}$	5.1 %	18.1 %	12.5 %
aug. ctrl $\bar{\mathbf{K}}_{\bar{\Theta}}$	2.0 %	2.0 %	4.8 %

ride comfort index, this work employs the ride comfort definition from ISO (2631-1:1997). Complementary to Table 4.1, Figure 4.10 shows plots of the heave, roll and pitch velocities and the controller output $\bar{\mathbf{u}}_d$ of the nominal closed-loop, and the closed-loop with damper failure with and without force reconfiguration. During the experiment depicted in Figure 4.10-left the vehicle model has been excited by the roll sweep signal. The plots of heave and pitch velocities illustrate vital amplitude reductions of the augmented controller compared to the nominal controller. The amplitude reduction of the roll velocity, however, is rather small, nevertheless, the augmented controller reduces the performance degradation by 16 %. Figure 4.10-right shows the same signals in case of a rear left damper failure and a pitch sweep excitation. Here, the augmented controller achieves small reductions of the body heave and pitch velocities and a vital reduction of the roll velocity. The improvement of the ride comfort performance degradation amounts to 7.7 %. In summary, Figure 4.10 emphasizes that the force reconfiguration reduces the asymmetry of the damper force distribution in the event of malfunction of one damper. The bottom plots of Figure 4.10 show the controller output of the four damper. As expected, the controller with force reconfiguration commands much higher control signals than the controller without reconfiguration. Due the nonlinear reference vehicle, the control signals of the rear suspensions are much higher than those of the front suspensions. Therefore, the additional control signals of the augmented controller at the rear suspensions in case of the front left damper failure are much more obvious than the additional control signals at the front suspensions in case of the rear left damper failure.

The robustness of the proposed augmented controller regarding deviations of the actual actuator efficiencies η_i and the estimated actuator efficiencies $\hat{\eta}_i$ is numerically assessed by two scenarios. The fault detection does not recognize a damper failure, e.g. the estimated actuator efficiencies supplied to the augmented controller are $\hat{\eta}_i = 1 \forall i \in \{1, \dots, n_u\}$ although the k -th damper is malfunctioning $\eta_k \rightarrow 0$. The results of this scenario correspond to the ones of the nom. controller in Table 4.1, because the augmented controller is identical to the nominal controller due to the missing fault information. The second scenario assumes a false alarm, e.g. the estimated actuator efficiency of the k -th damper approaches zero $\hat{\eta}_k \rightarrow 0$, even though the actuator is perfectly healthy $\eta_k = 1$. During this



1) roll sweep simulation with front left damper failure

2) pitch sweep simulation with rear left damper failure

Figure 4.10: Results of sweep simulations with damper failure: top - body heave, upper middle - body roll, lower middle - body pitch, and bottom - normalized control signals

scenario, the augmented controller reconfigures its output such that no damper forces are requested from the reported faulty damper and simultaneously compensates $\alpha_u \times 100\%$ of the missing force of this damper by the other dampers. The assessment of the heave, roll and pitch sweep experiment illustrated in Table 4.2 reveals that the ride comfort performance of the augmented controller subject to a false alarm degrades to similar values than in case of a real damper failure. This result is natural because the reconfiguration reduces the control signal of the presumed faulty damper. Furthermore, the results of Table 4.1 and 4.2 show that the augmented controller is stable in case of false alarms or missing fault information.

Table 4.2: Performance degradation due to false alarm (FA) of damper failure front left (FL) or rear left (RL). The percentages indicate the degradation relative to the nominal closed-loop without damper failure

	heave sweep	roll sweep	pitch sweep
	FA FL	FA FL	FA RL
aug. ctrl \bar{K}	2.0 %	2.0 %	4.7 %

4.7 Multi-Objective Controller Tuning

The controller tuning is carried out in MATLAB using the DLR MOPS optimization toolbox (Joos et al., 2002) and the nonlinear full-vehicle model presented in Appendix E.2. The controller is simulated with the vehicle model in closed-loop and ride comfort J_{cISO} and road-holding J_{rh} given in Section 4.2 are calculated from the simulation outputs. The optimization procedure is equal to the one introduced during the quarter-vehicle control design in Chapter 3. The corresponding process diagram is depicted in Figure 3.12. In contrast to the quarter-vehicle application of Section 3.6, sine sweep excitations, e.g. a heave sweep signal or a pitch sweep signal, are not well suited for full-vehicle controller tuning. The sine sweep signals mainly excite one body degree-of-freedom, while leaving the others almost unaffected. Conversely, stochastic road signals, e.g. as reported by ISO (8608:1995) simultaneously excite all body degrees-of-freedom and furthermore, these signals represent the most common excitations on real roads. To ensure that the controllers also perform well if the vehicle is excited by single events, like bumps or potholes, the simulation is conducted twice with the two excitations:

- stochastic road, and
- obstacle event.

This multi-excitation approach computes the ride comfort and road-holding criteria as the mean value of the respective criteria of the separate simulations. The optimization

problem at hand is nonconvex due to the employed nonlinear vehicle model, and thus local minima can be an issue. To still achieve a solution close to the global minimum, the optimization uses a hybrid algorithm consisting of a genetic algorithm and a subsequent local downhill method. The optimization problem is defined analog to (3.51) and (3.52) by

$$\min_{\boldsymbol{\varphi}} J_{\text{opt}}(J_c, J_{rh}) \quad \text{subject to} \quad (4.62a)$$

$$\max(|\text{eig}(\mathbf{\Gamma}_{ed}(\mathbf{P}_{\Theta,k}, \mathbf{K}_{\Theta,k}))|) < \lambda_{\max} \quad (4.62b)$$

$$\max(\Delta_{\text{obs}}) < \Delta_{\text{obs,max}}. \quad (4.62c)$$

The decision parameter vector $\boldsymbol{\varphi}$ gathers the tuning parameters of the state-observer and LPV controller design according to

$$\boldsymbol{\varphi} = [w_{e,1} \ \dots \ w_{e,n_x} \ w_n \ w_{b,h} \ w_{b,r} \ w_{b,p} \ w_w]^T. \quad (4.63)$$

The new tuning parameter w_n is introduced to trade-off measurement disturbances against road disturbances during the observer design. The measurement disturbance weight \mathbf{W}_n is computed from the predetermined scaling factors of body acceleration w_{n,\ddot{x}_b} , wheel acceleration w_{n,\ddot{x}_w} and damper velocity disturbances w_{n,\dot{x}_d} by

$$\mathbf{W}_n = \text{diag}\left([w_{n,1} \ \dots \ w_{n,n_y}]^T\right) = w_n \text{diag}\left([\mathbf{w}_{n,\ddot{x}_b}^T \ \mathbf{w}_{n,\ddot{x}_w}^T \ \mathbf{w}_{n,\dot{x}_d}^T]^T\right), \quad (4.64)$$

with $\mathbf{w}_{n,\ddot{x}_b} = w_{n,\ddot{x}_b} [1 \ 1 \ 1 \ 1]^T$, $\mathbf{w}_{n,\ddot{x}_w} = w_{n,\ddot{x}_w} [1 \ 1 \ 1 \ 1]^T$ and $\mathbf{w}_{n,\dot{x}_d} = w_{n,\dot{x}_d} [1 \ 1 \ 1 \ 1]^T$.

The parameters of the road model β_r , α_r and v_{ref} introduced in (C.6) are set as described in Section 3.6 by a preliminary investigation.

As discussed in Section 3.6, inequality constraint (4.62b) is introduced to ensure that the controller is implementable on real-time hardware with a given sample time T_s . Furthermore, inequality constraint (4.62c) prevents the controller from over-fitting to the specific optimization scenario by restricting the maximum observation error $\max(\Delta_{\text{obs}})$ of the performance signals \mathbf{y}_a . The observation error of the k -th element of the performance signals \mathbf{y}_a is described by the relative Mean Square Error (MSE) Δ_k given by

$$\Delta_k = \frac{\sum_{n=1}^N (y_{a_k,n} - \hat{y}_{a_k,n})^2}{\sum_{n=1}^N (y_{a_k,n} - y_{a_k,\text{mean}})^2}, \quad (4.65)$$

with y_{a_k} the respective signal of the nonlinear vehicle model, \hat{y}_{a_k} the corresponding observed signal and $y_{a_k,\text{mean}}$ the mean value of y_{a_k} . The maximum acceptable MSE value $\Delta_{\text{obs,max}}$ is set to $\Delta_{\text{obs,max}} = \alpha_{\text{obs}} \Delta_{\text{obs,opt}}$ with the relaxation factor $\alpha_{\text{obs}} > 1$. In this way, the major design targets ride comfort and road-holding determine the observer tuning parameters and $\Delta_{\text{obs,max}}$ only defines an upper bound of the observation error.

The optimization procedure described above is applied to the full-vehicle LPV controller (LPV FVM) and the quarter-vehicle LPV controller (LPV QVM) of Section 3.5. The quarter-vehicle LPV controller is designed in the same way as the full-vehicle controller,

i.e. with a constant nominal damping d_0 . Subsequently, the control of the full-vehicle is constructed by employing one quarter-vehicle controller for each vehicle suspension. The full-vehicle control by four separate quarter-vehicle controllers approximates the vehicle vertical dynamics by lumping the roll and pitch inertias into the quarter-vehicle body mass. The synthesis of the front and rear LPV QVM controllers is performed with the same values of the tuning parameters introduced Section 3.5.1 and 3.5.2, but the plant parameters are adjusted to the suspension, i.e. the front and rear LPV QVM controllers have different spring stiffnesses. To give a state-of-the-art performance reference, additionally the full-vehicle Skyhook-Groundhook (SH/GH) controller of Section 4.4 is implemented and its gains are tuned with the optimization described above while neglecting the inequality constraints.

A sample time $T_s = 0.5$ ms is selected for implementation on the real-time hardware to avoid restriction due to large sample times. The performance degradation depending on the sample time is illustrated in Figure 4.11 for the SH/GH controller. A similar or even worse degradation can be expected for the LPV controllers because a tighter inequality constraint (4.62b) particularly restricts the LPV observer and controller design.

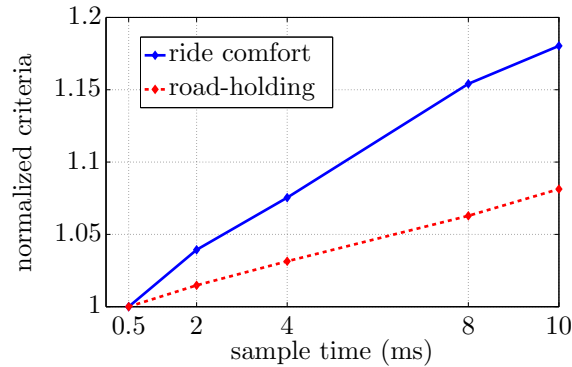


Figure 4.11: Effect of sample time on ride comfort and road-holding performance of SH/GH controller

Figure 4.12 shows the result of the Pareto optimization of ride comfort and road-holding with the nonlinear full-vehicle model. The blue markers connected by the blue solid line illustrate a variation of constant control signals $\mathbf{u}_d = 0.1 \dots 1$ A. All three controllers clearly improve ride comfort and road-holding compared to the passive suspension configurations. The LPV FVM controller achieves the best individual ride comfort and road-holding performance and in particular, the best trade-off between ride comfort and road-holding. The best achievable ride comfort of the full-vehicle and quarter-vehicle LPV controllers is comparable with only slight improvements by the LPV FVM controllers. This overall result corresponds to the expectation according to the literature, e.g. Savaresi et al. (2010), as it is well known that a SH/GH controller provides a high benchmark for ride comfort, while the rather rough system approximation involved with the Groundhook control policy limits its road-holding performance. This is overcome by

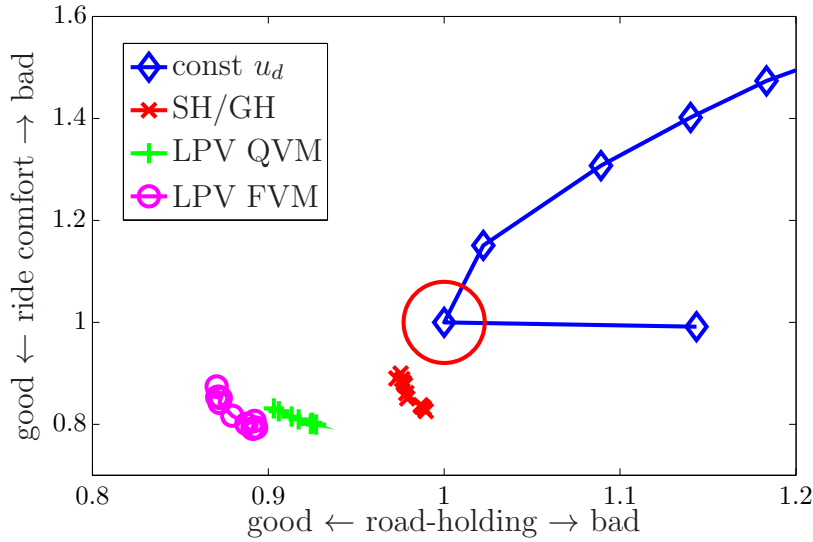


Figure 4.12: Result of Pareto optimization of ride comfort and road-holding with non-linear full-vehicle model subject to stochastic road excitation

the two model-based LPV controllers and accordingly both LPV controller feature good road-holding performance.

To verify the control design regarding the main plant disturbances; namely road disturbances, Figure 4.13 and 4.14 illustrate the frequency responses of the closed-loop with the LPV FVM controller at frozen scheduling parameter values $\theta = \theta_{\max}$ and $\theta = \theta_{\min}$. For the visualization the LPV FVM controller with the best road-holding performance is used because this controller also operates at the wheel resonance. The frequency responses of Figure 4.13 show the body heave, roll and pitch velocities excited by pure heave, roll and pitch road excitation, respectively. These excitations are generated by mapping the four independent road disturbance inputs of (4.13) to one single disturbance input according to:

$$\text{heave: } \mathbf{d}_g = [1 \ 1 \ 1 \ 1]^T d_{\text{heave}},$$

$$\text{roll: } \mathbf{d}_g = [1 \ -1 \ 1 \ -1]^T d_{\text{roll}}, \text{ and}$$

$$\text{pitch: } \mathbf{d}_g = [-1 \ -1 \ 1 \ 1]^T d_{\text{pitch}}.$$

As specified during the control design, the open-loop and the closed-loop frequency responses with $\theta = \theta_{\min}$ are almost the same as the LPV controller output is scaled towards zero by the saturation matrix. In comparison, the frequency responses of the closed-loop with $\theta = \theta_{\max}$ show that the LPV controller mainly reduces the body resonance peaks of all three transfer functions while leaving the low and high frequency responses almost unaffected. This exactly corresponds to the specified controller behavior as on the one hand the stationary system response cannot be changed by actuators with zero stationary force capabilities like semi-active dampers and on the other hand the controller should

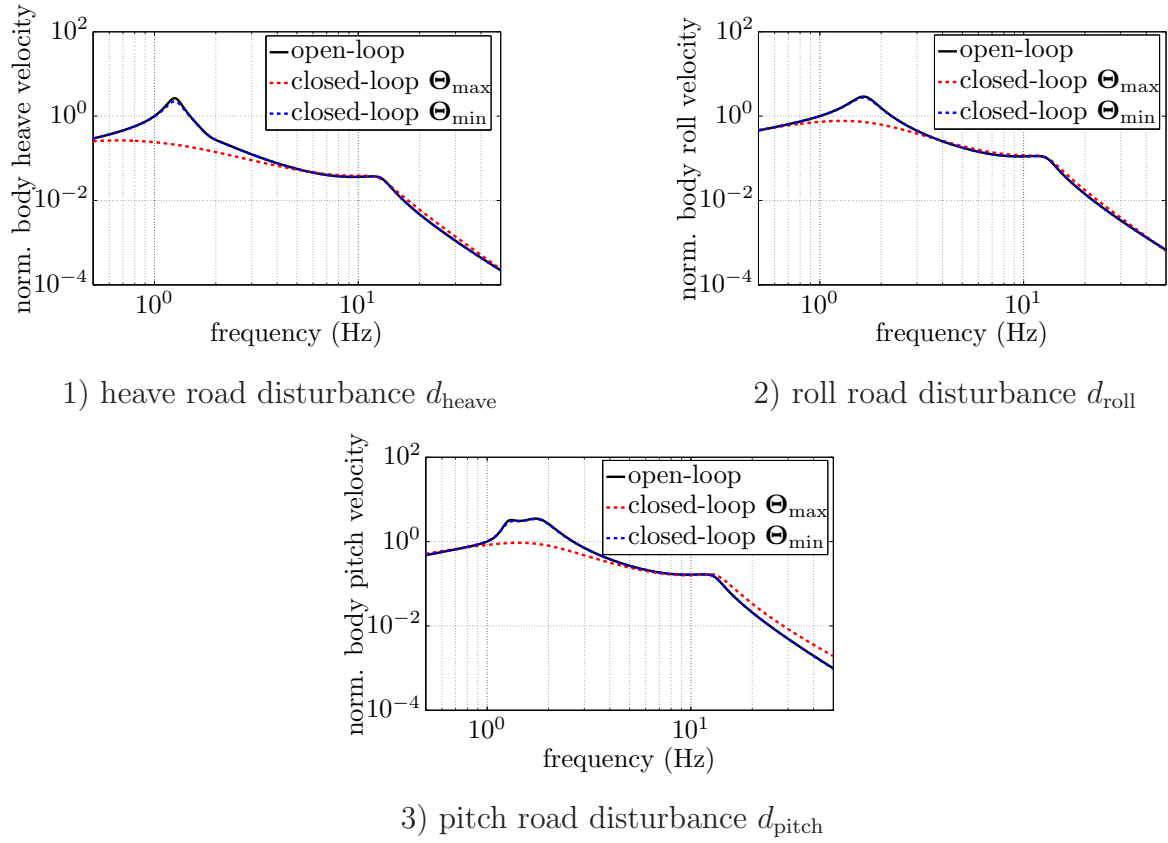


Figure 4.13: Normalized frequency responses of open-loop and closed-loop with full-vehicle from road disturbance to: top left - body heave velocity, top right - body roll velocity, and bottom - body pitch velocity

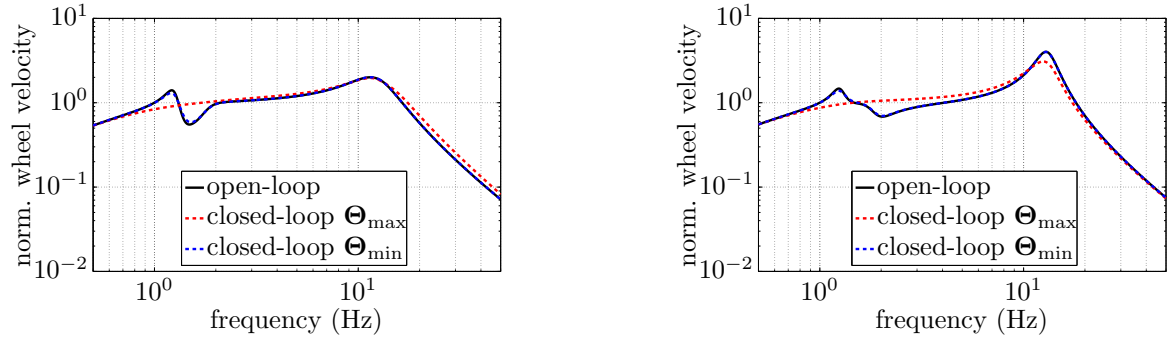


Figure 4.14: Normalized frequency responses of open-loop and closed-loop with full-vehicle from heave road disturbance d_{heave} to: left - front wheel velocity, and right - rear wheel velocity

roll-off sufficiently fast to avoid the amplification of high frequency disturbances. The frequency responses of the front and rear wheel velocities depicted in Figure 4.14 show a similar behavior with an unaffected low and high frequency closed-loop response, but in contrast to the responses of the body velocities in Figure 4.13 also the wheel resonance

peaks are mitigated, especially at the rear suspension.

In addition to the above figures, Figure 4.15, 4.16 and 4.17 illustrate the frequency response of the open loop and closed-loop system with frozen scheduling parameter $\theta = \theta_{\max}$ and $\theta = \theta_{\min}$ from linear combinations of the disturbances \mathbf{d} of plant \mathbf{P}_Θ used during the DI controller synthesis to the performance signals \mathbf{y}_a . The considered disturbances are:

$$\text{heave acceleration: } \mathbf{d} = [1 \ 1 \ 1 \ 1 \ 0 \ 0 \ 0 \ 0 \ 0 \ 0 \ 0]^T d_{a,h},$$

$$\text{wheel acceleration: } \mathbf{d} = [0 \ 0 \ 0 \ 0 \ 1 \ 1 \ 1 \ 1 \ 0 \ 0 \ 0]^T d_{a,w},$$

$$\text{damper velocity: } \mathbf{d} = [0 \ 0 \ 0 \ 0 \ 0 \ 0 \ 0 \ 0 \ 1 \ 1 \ 1]^T d_{a,d},$$

$$\text{roll acceleration: } \mathbf{d} = [1 \ -1 \ 1 \ -1 \ 0 \ 0 \ 0 \ 0 \ 0 \ 0 \ 0]^T d_{a,r}, \text{ and}$$

$$\text{pitch acceleration: } \mathbf{d} = [-1 \ -1 \ 1 \ 1 \ 0 \ 0 \ 0 \ 0 \ 0 \ 0 \ 0]^T d_{a,p}.$$

Furthermore, the figures show the corresponding performance bounds $\mathbf{W}_e(\theta)$ imposed on the frozen closed-loop system with $\theta = \theta_{\max}$ according to (4.33). The closed-loop frequency response of the body heave velocity at the grid point $\theta = \theta_{\max}$ shown in Figure 4.15 is very similar to the heave velocity resulting from the road disturbance in Figure

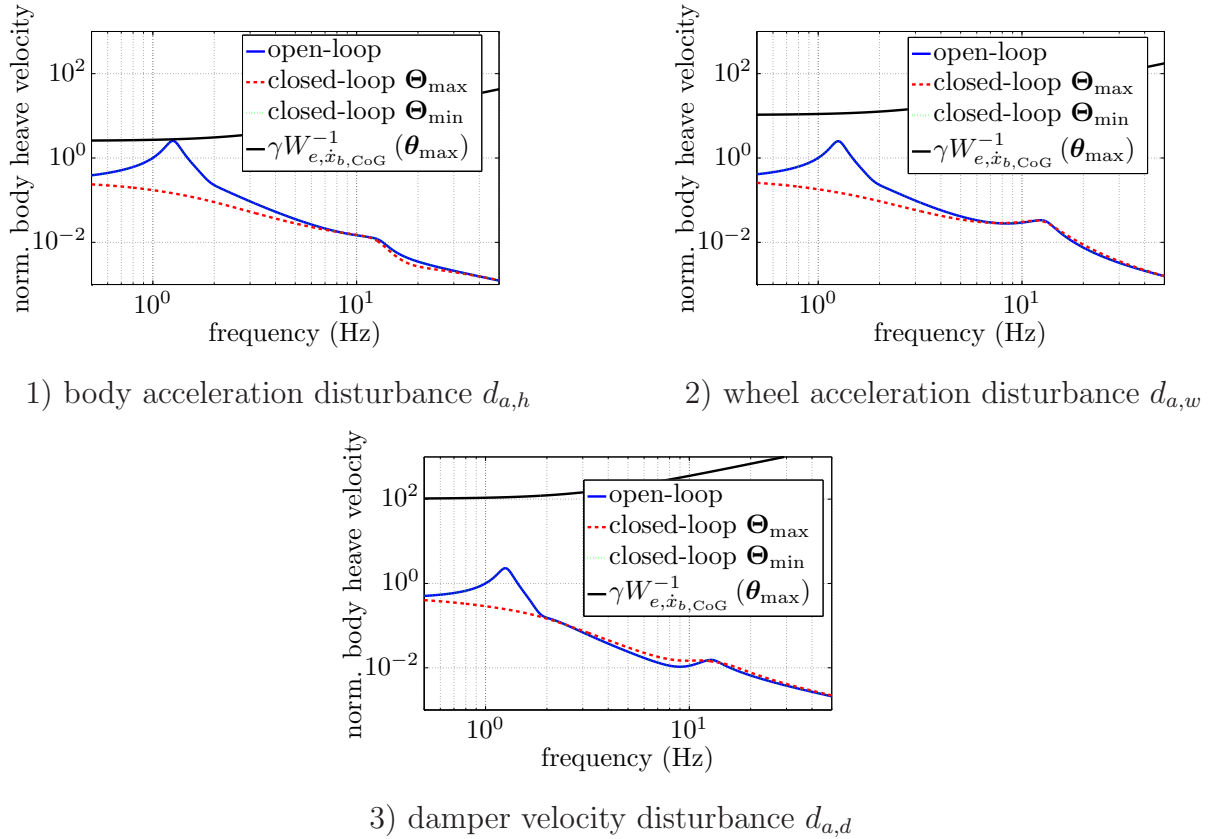


Figure 4.15: Normalized frequency responses of open-loop and closed-loop with full-vehicle from disturbances \mathbf{d} to body heave velocity

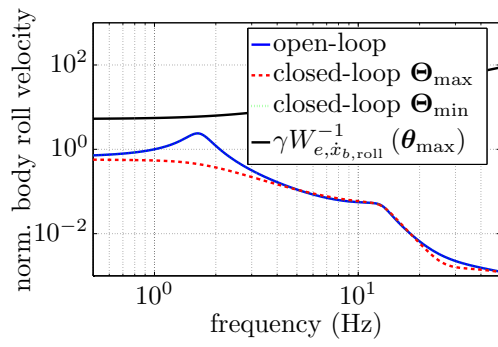
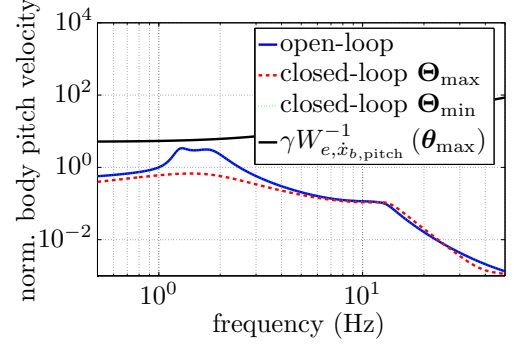
1) roll acceleration disturbance $d_{a,r}$ 2) pitch acceleration disturbance $d_{a,p}$

Figure 4.16: Normalized frequency responses of open-loop and closed-loop with full-vehicle from disturbance \mathbf{d} to: left - body roll velocity, and right - body pitch velocity

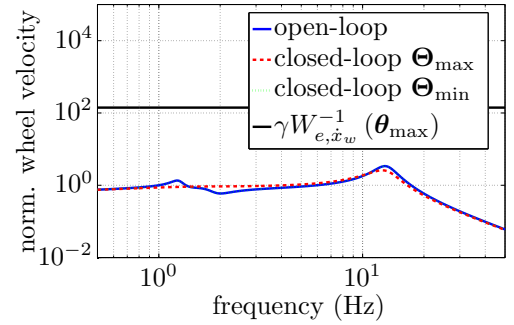
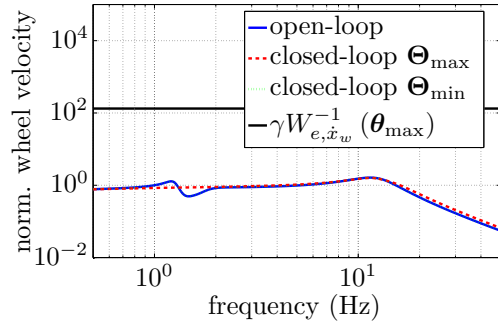


Figure 4.17: Normalized frequency responses of open-loop and closed-loop with full-vehicle from disturbance \mathbf{d} to: left - front wheel velocity, and right - rear wheel velocity

4.13-top left. The controller mainly reduces the body resonance peak and leaves the low and high frequency behavior unaffected. Figure 4.16 shows the closed-loop frequency responses of body roll and pitch velocities if excited by the roll and pitch acceleration disturbances $d_{a,r}$ and $d_{a,p}$. Again, the controller focuses on the reduction of the body resonance peaks and yields a good roll-off at higher frequencies. Figure 4.17 illustrates the closed-loop frequency responses of the front and rear wheel velocities subject to the wheel acceleration disturbance $d_{a,w}$. Compared to the closed-loop frequency responses of the body velocities, the controller shows less effect on the wheel velocities even though the controller has been tuned for optimal road-holding. This results from the trade-off between the reduction of the wheel resonance peak and the increase in amplitude in the intermediate frequency range. Finally, Figure 4.18 illustrates the closed-loop control signal \mathbf{u}_{F_d} of the front and rear dampers subject to a heave acceleration disturbance $d_{a,h}$.

4.8 Four-Post Test-Rig Experiments

The ride comfort oriented full-vehicle LPV controller is assessed by experiments with the *SC3-Bulli* on the four-post test-rig of KW as shown in Figure 1.4. The synthesized

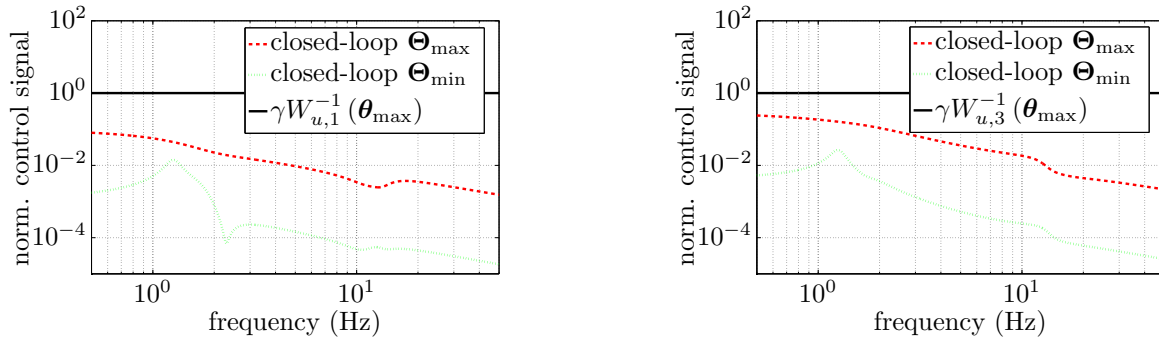


Figure 4.18: Normalized frequency responses of open-loop and closed-loop with full-vehicle from heave acceleration disturbance $\mathbf{d}_{a,h}$ to: left - front control signal, and right - rear control signal

LPV controllers and the corresponding Skyhook-Groundhook controller are implemented on a dSPACE MicroAutoBox II with a sample time of $T_s = 0.5$ ms. The logging data needed for the evaluation of ride comfort, road-holding and suspension deflection usage is recorded at a lower sample time of $T_{\log} = 1$ ms due to restrictions of the maximum sample time of the test-rig. Additionally, the assessment considers two passive suspension configurations: const. \mathbf{u}_d comfort and const. \mathbf{u}_d sport, which have been tuned together with KW during preliminary experiments such that they provide good compromises for ride comfort and sporty driving.

As introduced in Section 4.2, ride comfort is quantified according to ISO (2631-1:1997), and road-holding J_{rh} and suspension deflection usage J_d are quantified by the RMS-values of the dynamic wheel load and damper deflection, respectively. From the pool of test-rig excitations four excitations have been selected for the experimental assessment:

1. a heave sweep excitation,
2. the stochastic road excitation (also used during the controller tuning),
3. a Spanish bumps excitation, and
4. a country road segment with a long-wave bump.

4.8.1 Experiments without Damper Malfunction

The fast Fourier transforms (FFT) of the data collected during the heave sweep experiment are depicted in Figure 4.19 - 4.21. The frequency responses are computed by dividing the sine sweep sequence into seven windows and by averaging the FFTs of all windows. The frequency responses of the body heave acceleration of Figure 4.19 show that the controllers provide vital damping of the body resonance peak located between 1 Hz and 2 Hz and furthermore, exploit the performance potential of the very low minimum damper force curves in the frequency range between 2 Hz and 10 Hz. The frequency responses of the body heave acceleration also feature an invariant point at 12 Hz close before the

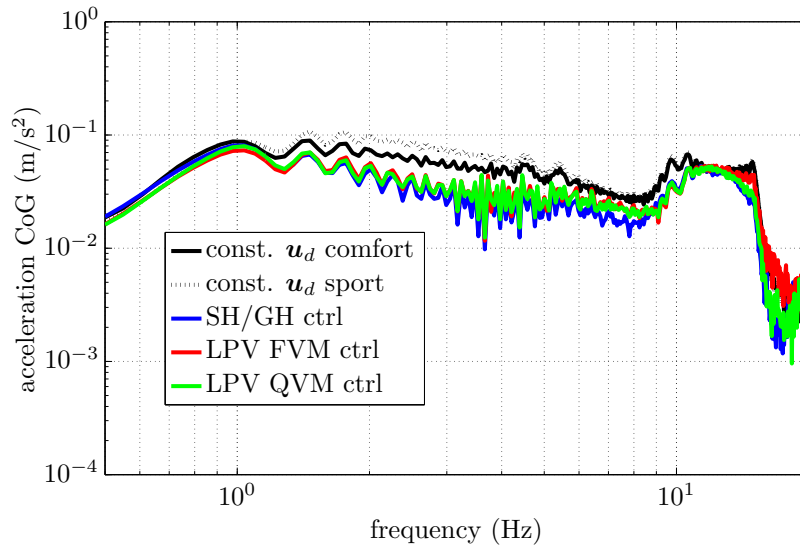


Figure 4.19: Frequency response of body heave acceleration of experimental vehicle subject to heave sweep excitation

wheel resonance frequency. This corresponds well to the frequency response of the frozen closed-loop depicted in Figure 4.13-top left, which exhibits the invariant point and the wheel resonance at almost the same frequencies. The shape of the frequency responses, however, is different and it clearly shows the nonlinearities of the experimental vehicle, especially near the wheel resonance frequency. A comparison of the experimental frequency response of the body heave acceleration of the closed-loop with SH/GH controller in Figure 4.19 with the theoretical frequency response discussed in Savaresi et al. (2010, p. 112), confirms the good parametrization of the SH/GH controller regarding ride comfort. As in Savaresi et al. (2010, p. 112), the SH/GH controller focuses its operation on the body resonance peak and rolls-off at higher frequencies. Due to the comfort-oriented parametrization of the illustrated controllers, especially the SH/GH controller, but also the quarter-vehicle LPV controller, feature only small reductions of the resonance peaks of the dynamic wheel loads at the wheel resonance frequency in Figure 4.20. The full-vehicle LPV controller, however, achieves lower amplitudes of the dynamic wheel loads at the wheel resonance frequency. The difference to the two other controllers is small at the front suspension, but significant at the rear suspension. This behavior corresponds to the result of the controller tuning in Figure 4.12 as firstly the LPV FVM controller provides the best road-holding performance and secondly the dynamic wheel loads of the simulated nonlinear vehicle model depicted in Figure 4.14 also exhibit the difference between front and rear suspensions, namely no reduction of the dynamic wheel load amplitude at the front axle versus a reduction at the rear axle. The analysis of the heave sweep experiment is completed by the frequency responses of the damper velocity depicted in Figure 4.21. These curves show that the LPV controllers feature smaller damper velocity amplitudes at the body and wheel resonance frequencies and in particular, the LPV FVM controller

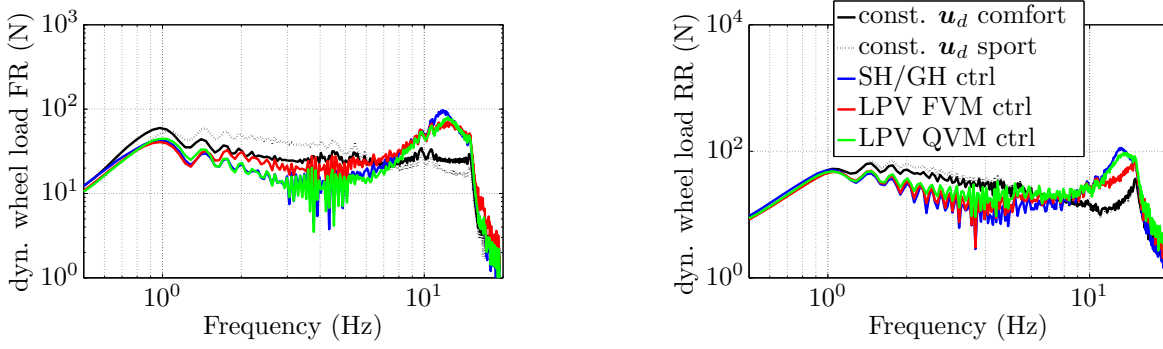


Figure 4.20: Frequency response of dynamic wheel load of experimental vehicle subject to heave sweep excitation: left - dyn. wheel load FR and right - dyn. wheel load RR

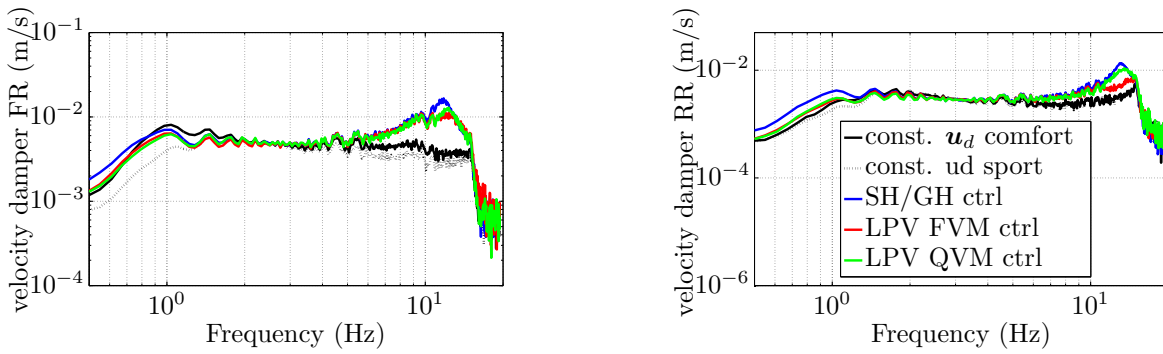


Figure 4.21: Frequency response of damper velocity of experimental vehicle subject to heave sweep excitation: left - damper velocity FR and right - damper velocity RR

vitaly reduces the damper velocity amplitudes of the rear suspensions.

The graphs in Figure 4.22 illustrate the stochastic road, Spanish bumps and country road excitations in time domain to provide an understanding for the differences between the excitations. The curves show the displacement signals of the four test-rig posts with the post position front left (FL), front right (FR), rear left (RL) and rear right (RR) denoted by 1 - 4. The stochastic road excitation is about five times longer than the other two excitations and has a total length of about 100 s. Figure 4.22-top left shows the first 20 s of the road excitation to give a legible illustration of the post displacement. The Spanish bumps excitation is a collection of single bump and pothole events. The amplitudes of the bumps and potholes are about as large as the amplitudes of the stochastic road excitation except for the first bump which is about twice as large. The country road excitation corresponds to a stochastic excitation with a superimposed long-wave bump at 12 s. The amplitude of the bump is about one third higher than the amplitudes of the Spanish bumps excitation.

The results of the evaluation of the controller performance for the three excitations are given in Table 4.3 - 4.5. The tables state the ride comfort criterion J_{ISO} , the road-holding criterion J_{rh} and the suspension deflection usage criterion J_{rh} normalized to the passive suspension configuration *const. u_d comfort*. The assessment of Table 4.3 - 4.5 shows,

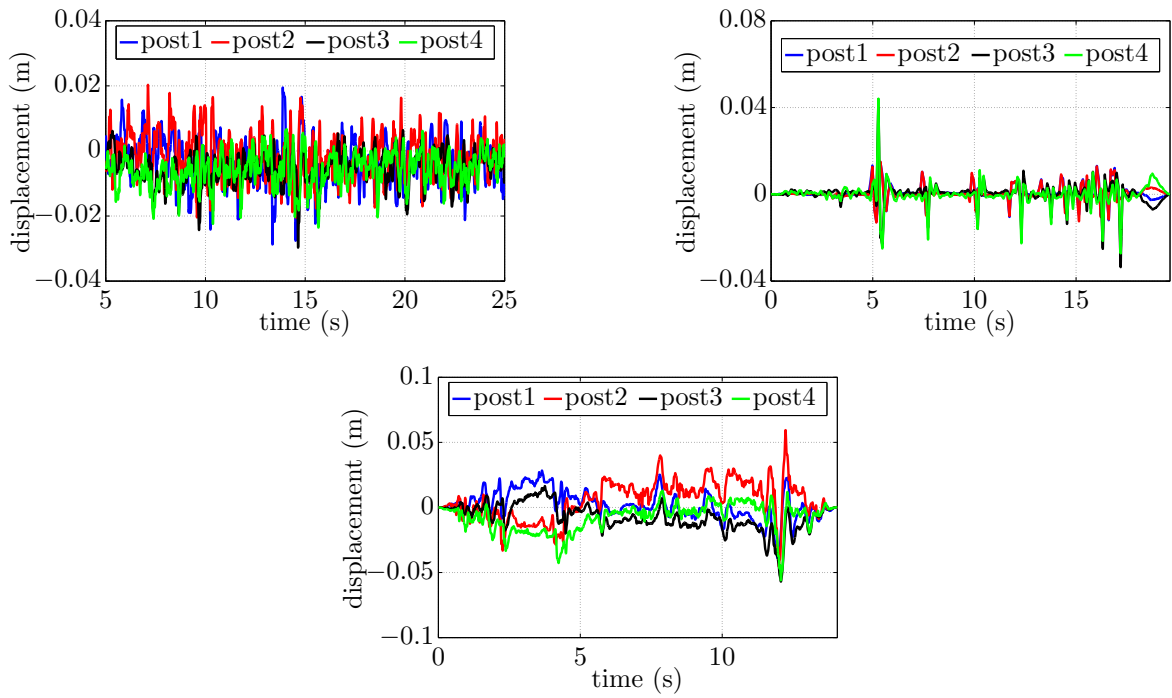


Figure 4.22: Post displacements: top left - stochastic road excitation, top right - Spanish bumps excitation, and bottom - country road with long-wave bump excitation

that the LPV FVM controller achieves the best individual results for ride comfort and road-holding, and the best trade-off between these two criteria. A closer examination of the criteria values of the most relevant stochastic road experiments shows that the LPV FVM controller improves ride comfort by about 12 % compared to the SH/GH controller and by about 3 % compared to the LPV QVM controller. The same improvement of about 9 % can be observed when evaluating road-holding of the LPV FVM and the SG/GH controller. Compared to the LPV QVM controller, however, the road-holding improvement of the LPV FVM controller of about 1 % is rather small. The assessment of the Spanish bumps and the country road with ground wave reveals a similar result. The LPV FVM controller achieves a ride comfort improvement of about 8 % for the Spanish bumps and the country road compared to the SG/GH controller. The road-holding improvement of the LPV FVM controller, however, is just 2%.

Figure 4.23 - 4.26 illustrate the behavior of the LPV FVM controller during the first large bump of the Spanish bumps excitation. The test-rig's post displacements depicted in Figure 4.23-top left show that the displacements of the left and right wheels are identical and consequently the bump mainly excites body heave and pitch. This can be confirmed by the other graphs of Figure 4.23, which show the body heave, roll and pitch accelerations. The body roll acceleration of Figure 4.23-bottom left exhibits only small amplitudes and high frequency oscillations with minor correlation to the post displacement signals. Conversely, the heave and pitch accelerations amplitudes are significant during this bump excitation and the assessment of the vehicle response with LPV FVM controller compared

Table 4.3: Performance assessment of stochastic excitation experiment; criteria in percentage relative to comfort-oriented passive suspension configuration

	ride comfort	road-holding	suspension deflection
	J_{cISO}	J_{rh}	usage J_d
const. \mathbf{u}_d comfort	100 %	100 %	100 %
const. \mathbf{u}_d sport	112 %	103 %	88 %
SH/GH controller	89 %	105 %	109 %
LPV FVM controller	77 %	96 %	96 %
LPV QVM controller	80 %	97 %	99 %

Table 4.4: Performance assessment of Spanish bumps experiment; criteria in percentage relative to comfort-oriented passive suspension configuration

	ride comfort	road-holding	suspension deflection
	J_{cISO}	J_{rh}	usage J_d
const. \mathbf{u}_d comfort	100 %	100 %	100 %
const. \mathbf{u}_d sport	115 %	119 %	92 %
SH/GH controller	76 %	80 %	93 %
LPV FVM controller	68 %	78 %	102 %
LPV QVM controller	76 %	80 %	93 %

Table 4.5: Performance assessment of country road with long-wave bump experiment; criteria in percentage relative to comfort-oriented passive suspension configuration

	ride comfort	road-holding	suspension deflection
	J_{cISO}	J_{rh}	usage J_d
const. \mathbf{u}_d comfort	100 %	100 %	100 %
const. \mathbf{u}_d sport	99 %	107 %	100 %
SH/GH controller	83 %	94 %	93 %
LPV FVM controller	75 %	92 %	80 %
LPV QVM controller	79 %	90 %	86 %

to the SH/GH controller and the passive configurations emphasizes the ride comfort improvements of the LPV FVM controller. In particular, the heave acceleration in Figure 4.23-top right reveals a vital amplitude reduction by the LPV FVM controller. Figure 4.24 and 4.25 are important to provide the entire picture of the behavior of the LPV FVM

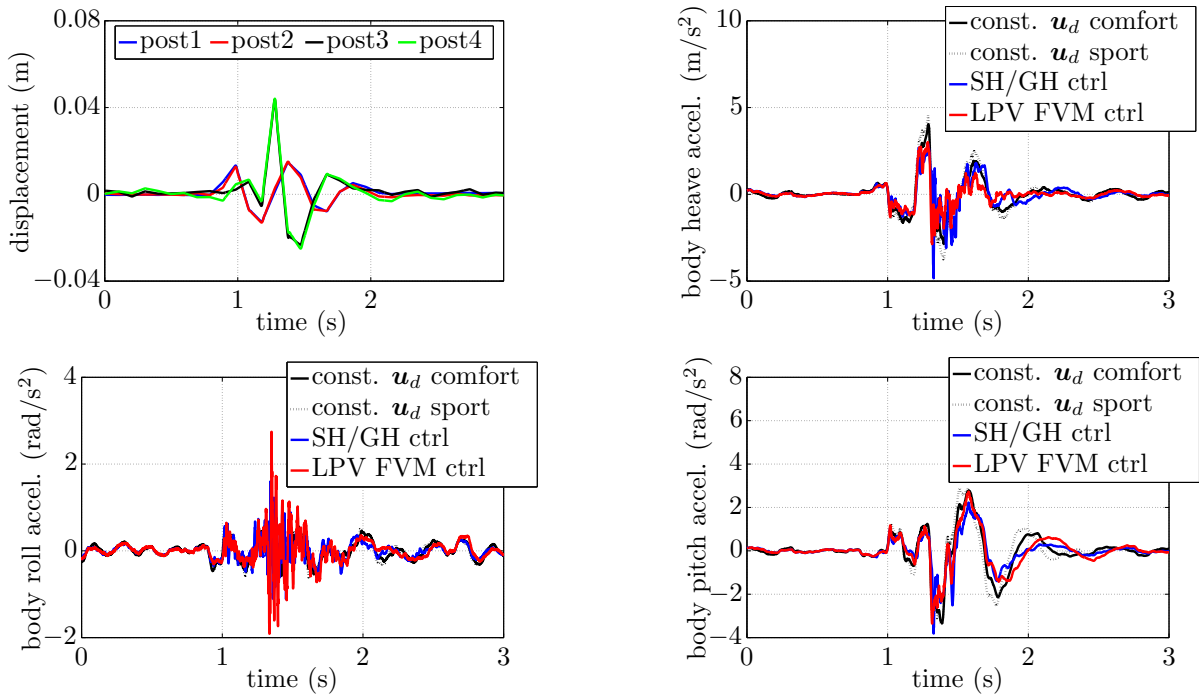


Figure 4.23: Post displacement and body accelerations of experimental vehicle subject to large bump excitation: top left - post displacements, top right - body heave acceleration, bottom left - body roll acceleration, and bottom right - body pitch acceleration

controller. Even though the controller has been tuned for optimal ride comfort, the dynamic wheel loads and also the damper velocities should not drastically increase compared to the SH/GH controller and the passive configurations; firstly to ensure a sufficient level of road-holding and secondly to avoid excessive suspension deflections approaching the bump stops. Finally, Figure 4.26 gives a comparison between the measured damper currents. Regarding the passive suspension configurations the two striking observations are firstly that the comfort-oriented setting applies damper currents distinct higher than the minimum values. This setting is necessary for ride comfort due to the very low damping

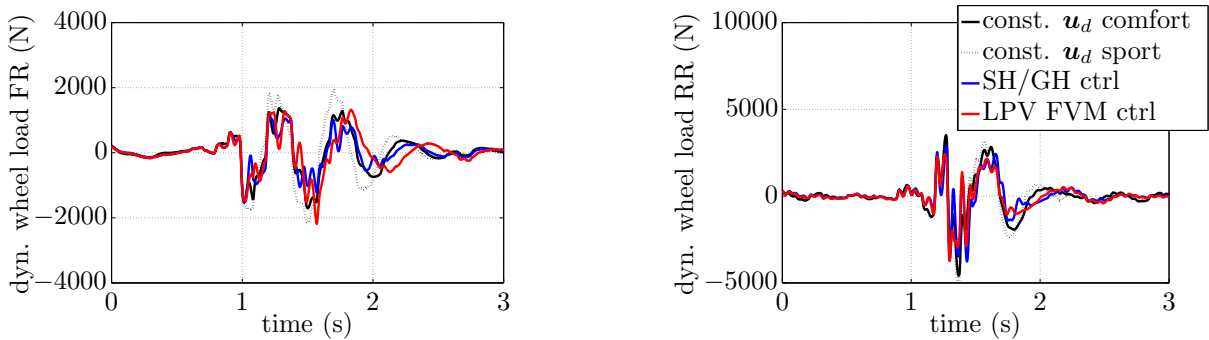


Figure 4.24: Dynamic wheel load of experimental vehicle subject to large bump excitation: left - dyn. wheel load FR and right - dyn. wheel load RR

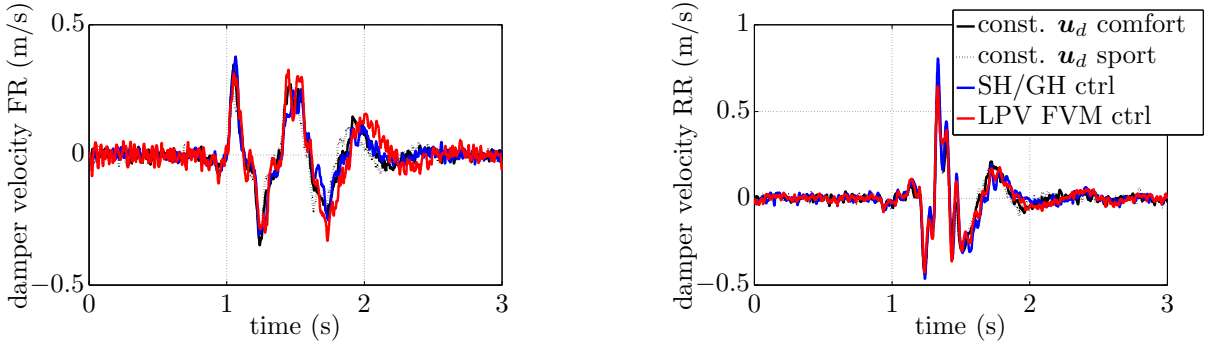


Figure 4.25: Damper velocities of experimental vehicle subject to large bump excitation: top left - damper velocity FR, bottom left - damper velocity RR

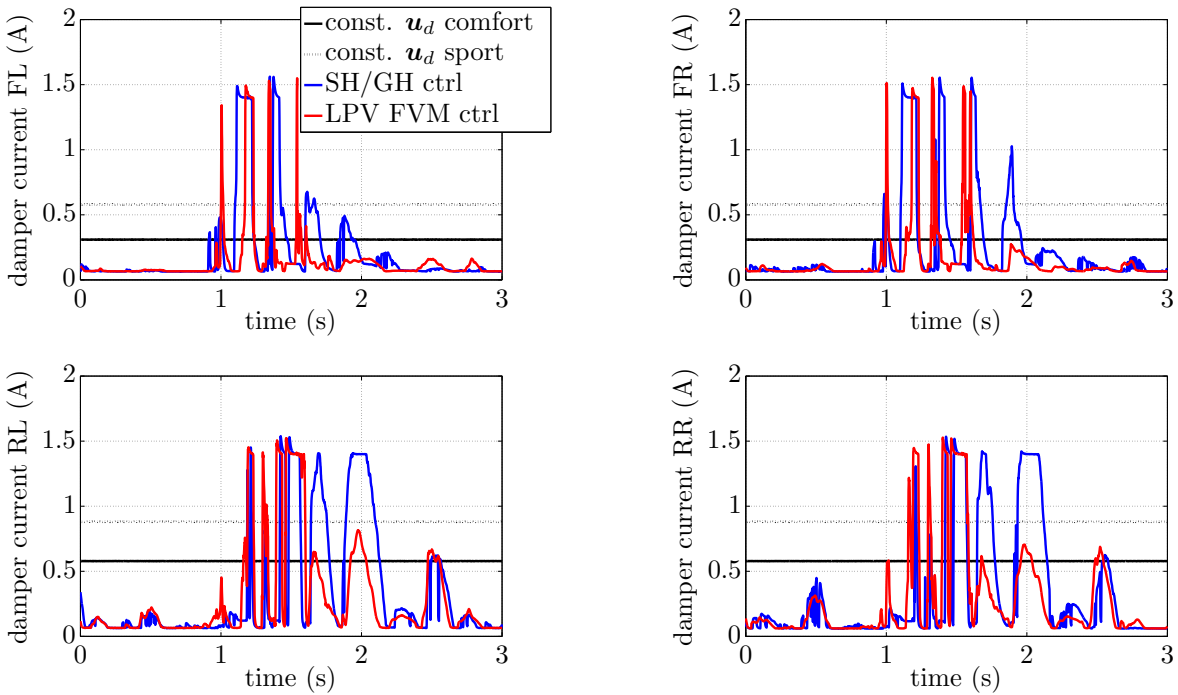


Figure 4.26: Damper current of experimental vehicle subject to large bump excitation: top left - damper current FL, top right - damper current FR, bottom left - damper current RL, and bottom right - damper current RR

provided by the minimum force curves of the semi-active dampers as discussed Appendix E.1. Secondly, the rear damper currents of both passive configurations are slightly higher than those of the front dampers to achieve a good pitch balance of the vehicle. The comparison of the LPV FVM controller and the SH/GH controller shows that both controllers operate the vehicle with minimum damper forces if the disturbances are small, but command control signals beyond the actuator capacities of 1.4 A such that the maximum damper forces are applied for some milliseconds.

In summary, the experimental results correspond well to the expectations of the controller tuning. In particular, the developed LPV FVM controller achieves a consistent improve-

ment of ride comfort and road-holding for all excitations. The achieved road-holding, however is not as good as expected from the controller tuning. The deviation between simulation and experimental results can be addressed to the approximations, in particular to the negligence of the effects of the elastokinematics of the suspensions employed during the development of the linear and nonlinear vehicle models and during control design.

4.8.2 Experiments with Damper Malfunction

In addition to the experiments with functioning semi-active dampers, this section investigates the controller performance in case of malfunction of the rear right damper such that only the minimum damper forces are available, e.g. due to an electrical failure or malfunction of the electro-hydraulic valve. This experiment assumes that the damper fault has been detected and the fault information has been provided to the LPV controller represented by $\bar{\theta}_4 = \theta_{\min}$. During the experiment the testing vehicle is excited by the first large bump of the Spanish bump sequence depicted in Figure 4.27-top left. The statistical assessment presented in Table 4.6 shows that the augmented LPV FVM controller with force reconfiguration performs best during the experiments. In particular, the ride comfort degradation due to the damper failure of the LPV FVM controller with force reconfiguration is only 7 % compared to the experiment with the LPV FVM controller without damper failure. Furthermore, the ride comfort criterion of the LPV FVM controller is 13 % better than the criterion of the SH/GH controller and about 30 % better than the passive suspension configuration const. \mathbf{u}_d comfort. Conversely, the road-holding and suspension usage criteria of the LPV FVM controller are worse compared to the SH/GH controller and the passive suspension configurations. This result corresponds to the design goals of the controller augmentation developed in Section 4.6, which focuses on improving ride comfort neglecting road-holding and suspension deflection usage.

Figure 4.27 - 4.29 illustrate the counterparts with rear right damper malfunction to Figure 4.23 - 4.26 without damper malfunction. The effect of the rear right damper failure is most

Table 4.6: Performance assessment of large bump excitation experiment with rear right damper failure; criteria in percentage relative to the LPV FVM controller without damper failure

	ride comfort J_{cISO}	road-holding J_{rh}	suspension deflection usage J_d
const. \mathbf{u}_d comfort	137 %	120 %	95 %
const. \mathbf{u}_d sport	166 %	135 %	87 %
SH/GH controller	120 %	107 %	96 %
LPV FVM controller	107 %	116 %	103 %

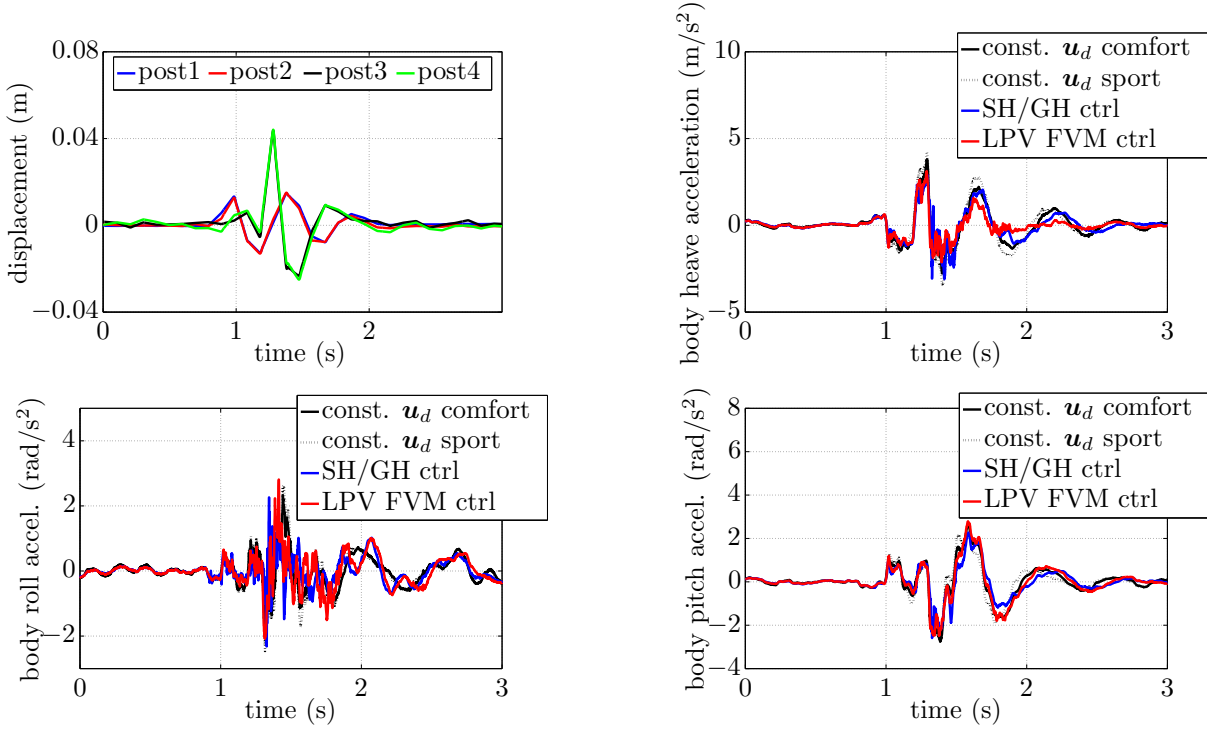


Figure 4.27: Post displacement and body accelerations of experimental vehicle with rear right damper failure subject to large bump excitation: top left - post displacements, top right - body heave acceleration, bottom left - body roll acceleration, and bottom right - body pitch acceleration

obvious at the dynamic wheel load of the rear right wheel depicted in Figure 4.28, which heavily oscillates compared with the dynamic wheel load without damper failure in Figure 4.24. Figure 4.29 visualizes the damper currents recorded during the experiment. Due to the simulated failure of the rear right damper, the corresponding damper current is almost zero. The comparison with Figure 4.26 shows that the force reconfiguration particularly increases the damper current of the rear left damper, but also that the reconfiguration is heavily restricted by the force limits of the semi-active dampers. The experiment, nevertheless, illustrates the suitability of the proposed augmented LPV FVM control design for fault-tolerant control.

4.9 Discussion and Conclusion

This chapter presents a new active fault-tolerant full-vehicle LPV controller for a car equipped with semi-active dampers. The controller employs actuator efficiencies and saturation indicators to incorporate failures and the restrictive damper force constraints in the LPV framework. In particular, this chapter proposes augmented saturation indicators which integrate the actuator efficiency and saturation indicator concept into one joint concept. To improve the performance of the LPV controller, the controller is extended by a saturation indicator dependent force reconfiguration matrix which explores the weak

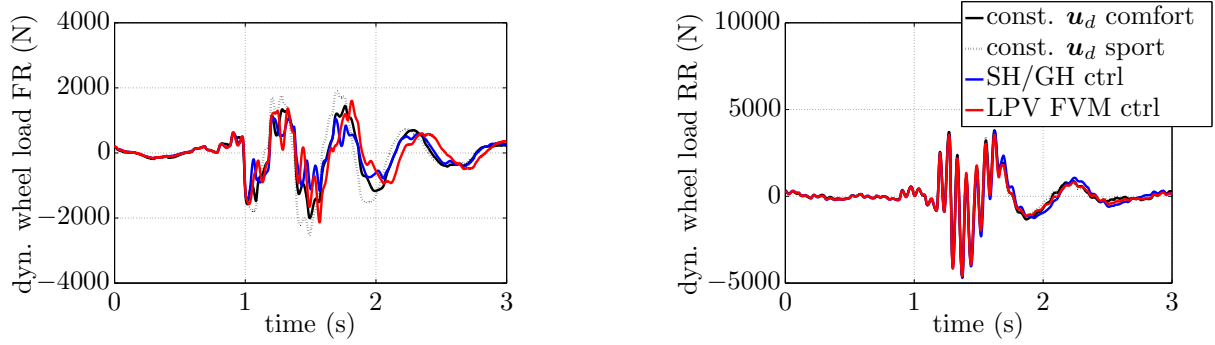


Figure 4.28: Dynamic wheel load of experimental vehicle with rear right damper failure subject to large bump excitation: left - dyn. wheel load FR and right - dyn. wheel load RR

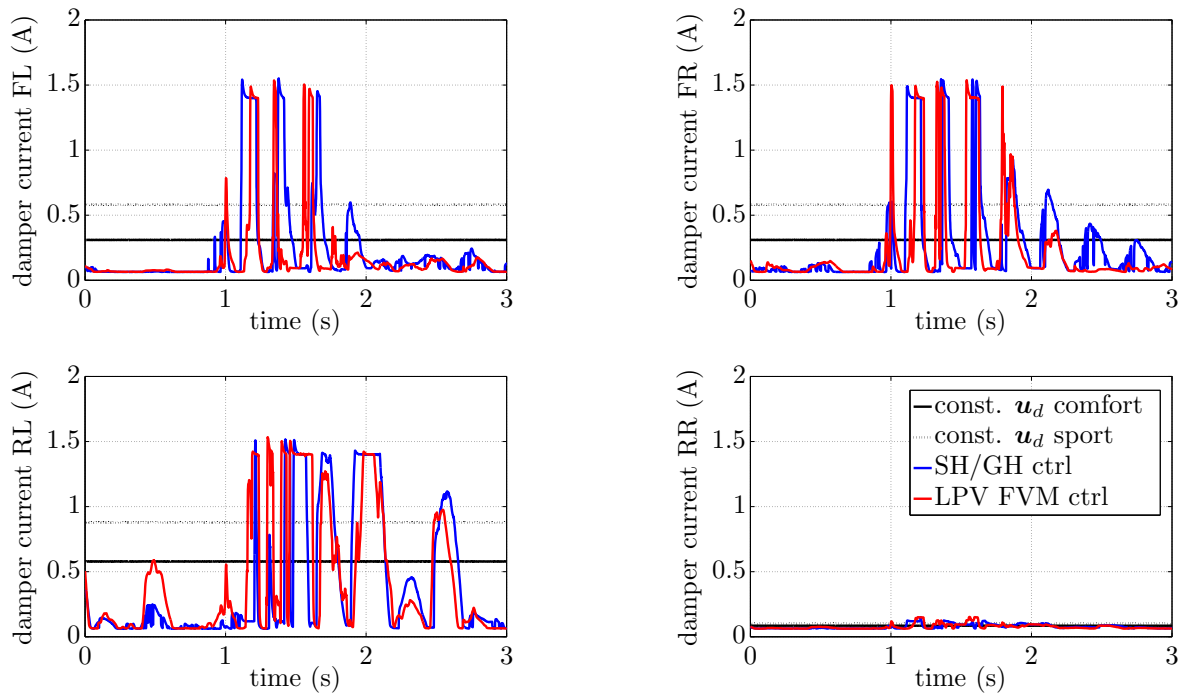


Figure 4.29: Damper current of experimental vehicle with rear right damper failure subject to large bump excitation; top left - damper current FL, top right - damper current FR, bottom left - damper current RL, and bottom right - damper current RR

actuator redundancy provided by four semi-active dampers. The proposed controller features guaranteed stability and performance for all admissible conditions of saturation and malfunction.

To reduce the computational cost during controller synthesis and code execution on real-time hardware, the LPV output-feedback control design adopts a Disturbance-Information scheme and employs a wide-meshed grid based on the minimum grid density necessary for controller stability established in Section 2.5. The Disturbance-Information scheme features the advantageous property that the output-feedback controller can be synthesized

in a two-step approach, namely an observer design as the first step and a state-feedback controller design as the second step. The observer based state-feedback structure of the resulting controller simplifies the implementation of the controller.

The fault-tolerance properties of the LPV controller are verified by a simulation study comparing the performance of the nominal LPV controller without consideration of actuator malfunction and the augmented LPV controller. The results of this investigation confirm the feasibility of the proposed controller augmentation to reduce the performance degradation in case of actuator failures.

Furthermore, the full-vehicle LPV controller is validated by experiments with the *SC3-Bulli* of SR on a four-post test-rig. The results show that the augmented full-vehicle LPV controller with force reconfiguration achieves a vital improvement of the trade-off between ride comfort and road-holding compared to a full-vehicle Skyhook-Groundhook controller. Moreover, an experiment with an assumed damper failure emphasizes the fault-tolerant control properties of the full-vehicle LPV controller with force reconfiguration. The comparison of the damper control signals without and with damper failure illustrates the control signal shift from the faulty damper to the remaining healthy dampers, but also that the reconfiguration is heavily restricted by the control signal limits of the semi-active dampers. The experiment, nevertheless, confirms the suitability of the proposed augmented LPV control design for fault-tolerant control.

5 Roll Disturbance Feedforward Control

The two main disturbances to be attenuated by the semi-active suspension controller are road disturbances and driver-induced load disturbances. As discussed in Chapter 1, driver-induced disturbances, similar to road disturbances, significantly affect ride comfort, road-holding and vehicle handling. The driver-induced disturbances considered in this chapter are roll disturbances which emerge from the steering inputs of the driver, e.g. when driving on a curvy country road. The road disturbances and driver-induced disturbances have distinct transmission paths and frequency ranges meaning that the relevant frequency range of road disturbances is 0.5 - 20 Hz, while the relevant frequency range of driver-induced disturbances is 0.1 - 3 Hz. In most vehicle applications, road disturbances as considered in Chapter 3 and 4 are unknown at runtime, but driver-induced disturbances can be estimated from the driver inputs by a suitable vehicle model like the single-track model. Moreover, the authors in Williams and Haddad (1997) and Brezas and Smith (2014) emphasize that feedback controllers which minimize the effect of road disturbances only achieve medium ride comfort and road-holding regarding driver-induced disturbances and vice versa. Smith and Wang (2002) address the control design of an active suspension system in the presence of both road disturbances and driver-induced disturbances by a special parametrization of an LTI controller for decoupled tuning of the two disturbance transmission paths. In this way, independent performance goals can be defined for each disturbance transmission path, e.g. ride comfort as defined in Section 4.2 for the road disturbance path and a well damped roll response for the driver-induced roll disturbances. Compared to road disturbances, driver-induced disturbances are easier to compensate since they can be estimated from the driver inputs and the vehicle states. This knowledge can be exploited by a two-degree-of-freedom control structure with a disturbance feedforward path. Brezas and Smith (2014) present a two-degree-of-freedom LQ control design of an active suspension system which simultaneously considers both road and driver-induced disturbances. In particular, they observed that the LQ controller with feedforward path achieves a significant improvement of ride comfort and road-holding regarding driver-induced disturbances. In Brezas et al. (2015), the authors adjust their approach to semi-active suspensions and present experimental results of a cornering manoeuvre. Alternatively, the authors in Ahmadian and Simon (2004) present a so-called steering input augmentation (SIA) of a Skyhook control such that the SIA-Skyhook controller increases its control signal proportional to the steering input. This concept is closer to industry than the preceding ones and its potential to enhance the roll stability is validated by lane change experiments.

In contrast to Brezas and Smith (2014), this work pursues a feedforward-feedback decoupling approach as theoretically described in Prempain and Postlethwaite (2001, p. 18-19), i.e. the separate design of the feedforward and feedback path. The two-step control design has the appealing property that the feedback controller can focus on the attenuation of unknown disturbances and the feedforward filter can achieve fast tracking and attenuation of known disturbances. As proposed in Prempain and Postlethwaite (2001), the feedfor-

ward filter can be obtained by solving the Full-Information (FI) problem introduced in Appendix A. The FI control approach is simple and naturally extends to LPV plants as shown in Prempain and Postlethwaite (2001, p. 23). Moreover, the FI control approach can be applied to a multitude of feedforward design problems as illustrated by the LPV helicopter control design application presented in Prempain and Postlethwaite (2000) and the LPV missile control design example given in Theis et al. (2015). Regarding a two degree-of-freedom control design, the FI control approach facilitates the coherent application of the saturation indicator concept to both the feedforward and feedback control design. In this way, the feedforward filter can be designed consistent to the feedback controller such that the feedforward filter and the feedback controller simultaneously reduce their contribution to the control signal in the event of saturation according to the value of the saturation indicators. The resulting two-degree-of-freedom LPV controller attains guaranteed stability for all admissible saturation conditions and good performance regarding the rejection of both disturbances.

The feedforward control design presented in this work focuses on shaping the body response of the vehicle in the face of roll disturbances induced by the steering inputs of the driver. The feedforward filter takes the expected lateral vehicle acceleration as input and generates appropriate damper forces. The expected lateral vehicle acceleration is estimated from the steering angle by a roll disturbance estimator which uses a simple single-track model.

The feedforward control design discussed in this chapter elaborates the Full-Information problem based feedforward control design presented in Fleps-Dezasse et al. (2018).

5.1 Roll Disturbance Feedforward Control Structure

Figure 5.1 illustrates the augmentation of the semi-active suspension controller developed in Chapter 4 with the LPV feedforward filter \mathbf{N}_Θ . The combined control force \mathbf{u}_J of the two-degree-of-freedom semi-active suspension controller is defined as the summation of the control force $\boldsymbol{\epsilon}_u$ of the original feedback controller and the control force \mathbf{u}_m of the feedforward filter \mathbf{N}_Θ with d_r being the roll disturbance input signal. Both, the feedback controller and the feedforward filter are scheduled by the saturation indicators $\boldsymbol{\theta}$. The roll disturbance d_r is estimated from the front wheel steering angle δ_F by a roll disturbance estimator which is based on a single-track model. Compared to the feedback control structure of Chapter 4, the output of the feedback controller is denoted $\boldsymbol{\epsilon}_u$ because the observer is fed by the modified measurements $\boldsymbol{\epsilon}_y$, which are calculated as the difference between the measurements \mathbf{y} and the estimated measurements \mathbf{y}_m of the feedforward filter. Similar to the full-vehicle feedback control design of Chapter 4, the saturation block and the inverse damper model are gathered in an augmented plant, which is then employed for the LPV feedforward filter design.

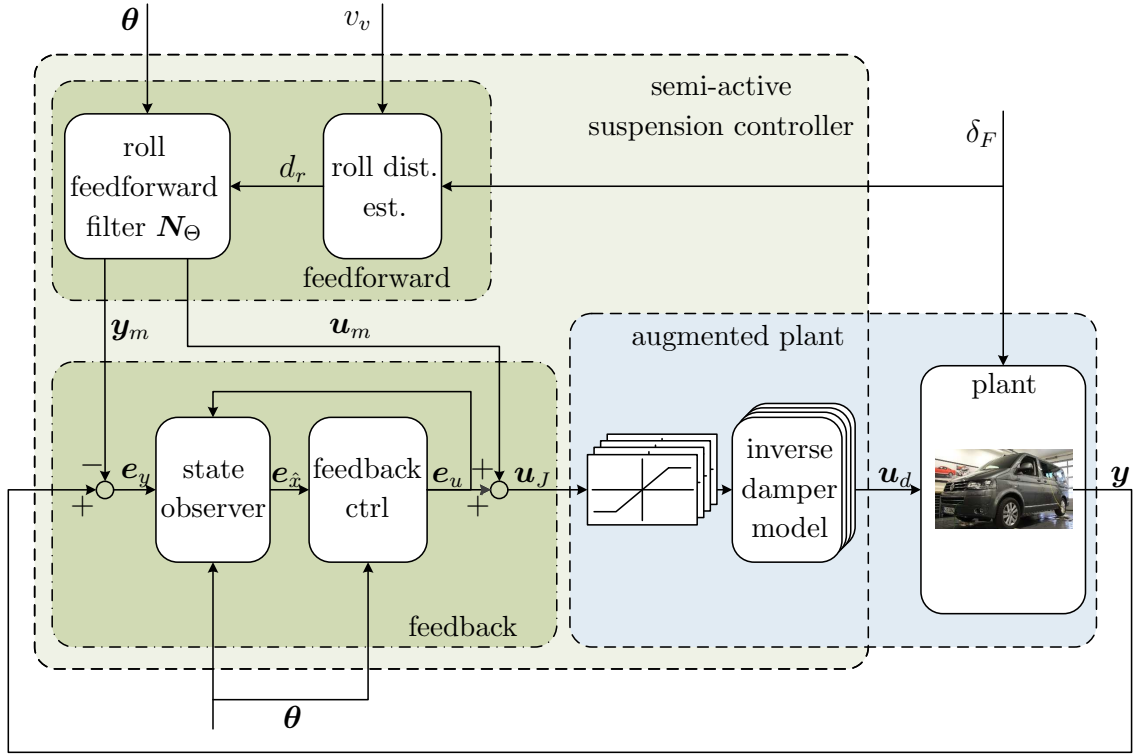


Figure 5.1: Two degree-of-freedom control structure of full-vehicle equipped with four semi-active suspensions

5.2 Vehicle Model with Roll Disturbance Input

The roll disturbances induced by the steering inputs of the driver are modeled as proposed in Brezas and Smith (2014, p. 550) by introducing the additional roll moment input d_r into the full-vehicle model of Section 4.3. Accordingly, equation 4.11 describing the body roll dynamics extends to

$$I_{xx}\ddot{x}_{b,\text{roll}} = d_r + \sum_i l_{\text{roll},i} (k_{b,i} (x_{w,i} - x_{bs,i}) + d_{0,i} (\dot{x}_{w,i} - \dot{x}_{bs,i}) + F_{s,i}), \quad (5.1)$$

with $i = 1, 2, 3, 4$ denoting the respective suspension unit. This simple extension covers the effect of driver-induced roll disturbances on the vehicle body, but neglects the additional transmission paths to the wheels. The roll moment distribution between both transmission paths is determined by the suspension kinematics, more precisely by the distance between the body CoG and the vehicle roll axis. Regarding semi-active suspension control, however, only the response of the vehicle body to roll disturbances can be essentially shaped by adjusting the damper forces. Using (5.1) and the equations of the full-vehicle model from Section 4.3, the vehicle model with roll disturbance \mathbf{G}_r can be stated in state-space notation by

$$\dot{\mathbf{x}} = \mathbf{A}\mathbf{x} + \mathbf{B}_1 d_r + \bar{\mathbf{B}}_2 \Theta \mathbf{u}_J, \quad (5.2)$$

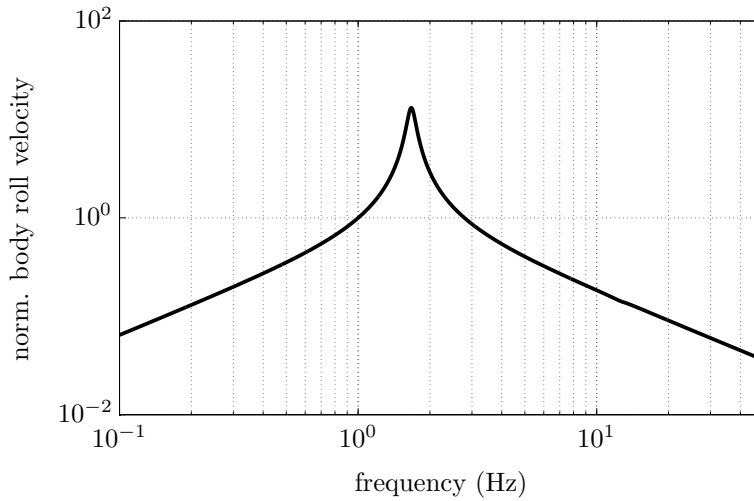


Figure 5.2: Transfer function from roll disturbance input d_r to angular roll velocity of vehicle body $\dot{x}_{b,\text{roll}}$

with the control input \mathbf{u}_J , the roll disturbance moment input d_r , the saturation indicator matrix Θ and the state vector

$$\mathbf{x} = [x_{b,\text{roll}} \ \dot{x}_{b,\text{roll}} \ x_{w,1} \ \dot{x}_{w,1} \ \dots \ x_{w,4} \ \dot{x}_{w,4} \ x_{F_d,1} \ \dots \ x_{F_d,4}]. \quad (5.3)$$

Compared to the states of the full-vehicle model of Section 4.3, the state vector of \mathbf{G}_r neglects the body heave and pitch degrees-of-freedom because they are not excited by the roll disturbance input. The vehicle model with roll disturbance input generates the measurements \mathbf{y} employed during the feedback control design presented in Section 4.5 according to

$$\mathbf{y} = \mathbf{C}_2 \mathbf{x} + \mathbf{D}_{21} d_r, \quad (5.4)$$

with the output matrix \mathbf{C}_2 and the disturbance feedthrough matrix \mathbf{D}_{21} . The vehicle model given in (5.2) includes the first-order actuator dynamics introduced in (3.18). Therefore, the control signal \mathbf{u}_J has no direct feedthrough to the measurements \mathbf{y} .

Figure 5.2 illustrates the frequency response from the roll disturbance moment input d_r to the angular roll velocity of the body $\dot{x}_{b,\text{roll}}$ of \mathbf{G}_r . Obviously, the frequency response of the vehicle body subject to the roll disturbance input d_r approximately corresponds to a mass-spring-damper system. The body motion is only weakly damped by the nominal body damping d_0 , and shows a good roll-off at high frequencies and a zero steady-state gain.

5.3 Roll Disturbance Feedforward Control Design

Figure 5.3 shows the interconnection of a two-degree-of-freedom controller consisting of the feedback controller \mathbf{K}_Θ and the feedforward filter \mathbf{N}_Θ with the vehicle model with

roll disturbance input \mathbf{G}_r where \mathbf{J}_m is given by

$$\mathbf{J}_m = \begin{bmatrix} \mathbf{0} & \mathbf{I} & \mathbf{0} & \mathbf{I} \\ -\mathbf{I} & \mathbf{0} & \mathbf{I} & \mathbf{0} \end{bmatrix}. \quad (5.5)$$

The feedforward filter \mathbf{N}_Θ generates the reference measurements \mathbf{y}_m and the feedforward control signal \mathbf{u}_m from the roll disturbance input d_r . Starting from the solution of the FI problem, the feedforward filter \mathbf{N}_Θ is obtained as the interconnection of the FI controller \mathbf{K}_{FI} with system \mathbf{P}_N according to

$$\mathbf{N}_\Theta = \mathbf{\Gamma}_{ed}(\mathbf{P}_N, \mathbf{K}_{FI}), \quad (5.6)$$

with \mathbf{P}_N given by

$$\begin{bmatrix} \dot{\mathbf{x}} \\ \begin{bmatrix} \mathbf{y}_m \\ \mathbf{u}_m \end{bmatrix} \\ \begin{bmatrix} \mathbf{x} \\ d_r \end{bmatrix} \end{bmatrix} = \begin{bmatrix} \mathbf{A} & \mathbf{B}_1 & \bar{\mathbf{B}}_2 \Theta \\ \begin{bmatrix} \mathbf{C}_2 \\ \mathbf{0} \\ \mathbf{I} \\ \mathbf{0} \end{bmatrix} & \begin{bmatrix} \mathbf{0} \\ \mathbf{0} \\ \mathbf{0} \\ I \end{bmatrix} & \begin{bmatrix} \mathbf{0} \\ \mathbf{I} \\ \mathbf{0} \\ \mathbf{0} \end{bmatrix} \end{bmatrix} \begin{bmatrix} \mathbf{x} \\ d_r \\ \mathbf{u}_m \end{bmatrix}. \quad (5.7)$$

The system \mathbf{P}_N particularly estimates the input of the FI controller \mathbf{K}_{FI} from the roll disturbance input d_r such that the control signal \mathbf{u}_m of \mathbf{K}_{FI} minimizes the effect of the disturbance d_r on the plant \mathbf{G}_r . Naturally, in the absence of disturbances d_r , the control structure of Figure 5.3 recovers the closed-loop with pure feedback. Moreover, as stated in Prempain and Postlethwaite (2001, p. 21), for a perfectly known plant and the reference measurements satisfying

$$\mathbf{y}_m = \mathbf{G}_r \begin{bmatrix} \mathbf{u}_m \\ d_r \end{bmatrix}, \quad (5.8)$$

it is possible to achieve perfect rejection of the known disturbances d_r . By perfect disturbance rejection it is meant that for zero-state initial condition, the reference measurements \mathbf{y}_m of the feedforward filter equal the measurements \mathbf{y} of \mathbf{G}_r and the control signal \mathbf{u}_J equals the control signal \mathbf{u}_m of the feedforward filter. In case of non-zero initial states of feedforward filter and plant, \mathbf{y} and \mathbf{u} will asymptotically tend towards \mathbf{y}_m and \mathbf{u}_m , respectively.

The objective of the semi-active suspension control design is the rejection of driver-induced roll disturbances. The performance criteria are ride comfort, road-holding and vehicle handling. In a full-vehicle context ride comfort can be characterized according to ISO (2631-1:1997) by the vehicle body heave, roll and pitch accelerations. The body heave and pitch motions are only weakly excited by the considered roll disturbances and can be neglected during the computation of the ride comfort criterion J_{cISO} . Compared to Section 4.2, the criterion simplifies to

$$J_{\text{cISO}} = \sqrt{\frac{1}{T} \int_0^T |\ddot{x}_{b,\text{roll}}(t)|^2 dt}. \quad (5.9)$$

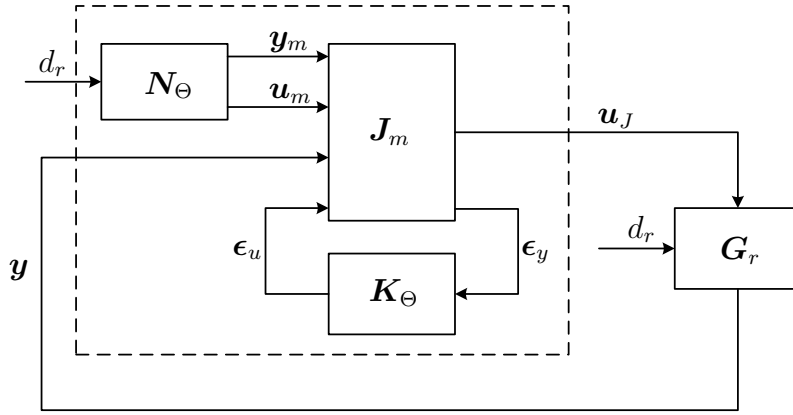


Figure 5.3: Two-degree-of-freedom closed-loop interconnection

The bar of $\ddot{x}_{b,\text{roll}}$ indicates that the RMS value of the body roll acceleration is computed after filtering the signal by the weighting filter given in ISO (2631-1:1997). The road-holding criterion J_{rh} of a vehicle can be determined from the RMS value of the vectorial dynamic wheel load signal \mathbf{F}_{wl} as described in Section 4.2. The vehicle handling properties can be only indirectly affected by semi-active suspension control. The authors in Williams and Haddad (1995) discuss the contribution of suspension control which results from a reduction of the (dynamic) wheel load transfer. In particular, they argue that the lateral force capability of an axle decreases due to the wheel load transfer during cornering. The main reason for this effect is the degressive side force characteristic of tires. Consequently, the increase in side force due to the higher wheel load of one tire of the axle is smaller than the decrease in side force due to the lower wheel load of the other tire of the axle. This effect reduces the maximum side force capability of the vehicle. The driver then has to compensate the larger side slip angles of the tires by larger steering inputs to still follow the road. The RMS value J_h of the front wheel steering angle given by

$$J_h = \sqrt{\frac{1}{T} \int_0^T |\delta_F(t)|^2 dt}, \quad (5.10)$$

is thus a good indicator of the vehicle handling properties.

The three design targets presented above can be simultaneously realized by the feed-forward filter as their individual design specifications are very similar. With respect to vehicle handling, the front wheel steering angle would be the first choice as performance signal \mathbf{e}_a of the FI control design. Unfortunately, the front wheel steering angle is not part of the control design problem with vehicle model \mathbf{G}_r . However, vehicle handling can be improved by a reduction of the wheel load transfer which is directly correlated to the body roll motion. During the FI control design, the body roll velocity is employed as performance signal. The roll velocity sufficiently emphasizes the body roll resonance peak and offers a better roll-off than the roll acceleration. Compared to the roll angle,

the roll velocity features a zero steady-state gain with respect to the roll disturbance input d_r . This is an essential property during the feedforward filter design of a semi-active suspension because the dampers cannot produce any steady-state forces at constant roll angles.

The body roll velocity performance signal is weighted by the saturation indicator dependent weight $W_{a,\text{roll}}(\boldsymbol{\theta})$ given by

$$W_{a,\text{roll}}(\boldsymbol{\theta}) = w_{b,\text{roll}} \left(\frac{1}{n_u} \sum_{i=1}^{n_u} \theta_i \right) G_{pt1,\text{roll}}, \quad (5.11)$$

with the scaling factor $w_{b,\text{roll}}$ and the first-order low-pass filter $G_{pt1,\text{roll}}$ similar to (3.43), but with a cut-off frequency of 10 Hz. The saturation indicator dependence of $W_{a,\text{roll}}(\boldsymbol{\theta})$ is realized such that the performance signal is scaled by the mean value of the saturation indicators $\boldsymbol{\theta}$ as in (4.37) of the feedback control design. In this way, the performance requirement is relaxed if the actuators are saturated. The control effort weighting function $\mathbf{W}_u(\boldsymbol{\theta})$ given by

$$\mathbf{W}_u(\boldsymbol{\theta}) = \boldsymbol{\Theta}^{-1}, \quad (5.12)$$

is again realized as introduced in Section 2.4 such that the feedforward filter achieves the desired behavior, i.e. the controller reduces its output with increasing actuator saturation. Figure 5.4 illustrates the weighting scheme of the feedforward filter design with the roll disturbance model \mathbf{G}_r comprised of the saturation block and the unconstrained roll disturbance model $\bar{\mathbf{G}}_r$. The saturation block limits the control signal \mathbf{u}_m yielding the constrained control signal $\boldsymbol{\sigma}(\mathbf{u}_m)$ which can be computed from the saturation indicator matrix $\boldsymbol{\Theta}$ by

$$\boldsymbol{\sigma}(\mathbf{u}_m) = \boldsymbol{\Theta} \mathbf{u}_m. \quad (5.13)$$

The generalized FI plant \mathbf{P}_r gathering the vehicle model \mathbf{G}_r and the weighting functions $W_{a,\text{roll}}(\boldsymbol{\theta})$ and $\mathbf{W}_u(\boldsymbol{\theta})$ can be stated by

$$\begin{bmatrix} \dot{\mathbf{x}} \\ \begin{bmatrix} e_a \\ \mathbf{e}_u \end{bmatrix} \\ \begin{bmatrix} \mathbf{x} \\ d_r \end{bmatrix} \end{bmatrix} = \begin{bmatrix} \mathbf{A} & \mathbf{B}_1 & \bar{\mathbf{B}}_2 \boldsymbol{\Theta} \\ \begin{bmatrix} C_{11}(\boldsymbol{\theta}) \\ \mathbf{0} \\ \mathbf{I} \\ \mathbf{0} \end{bmatrix} & \begin{bmatrix} 0 \\ \mathbf{0} \\ \mathbf{0} \\ I \end{bmatrix} & \begin{bmatrix} 0 \\ \mathbf{I} \\ \mathbf{0} \\ \mathbf{0} \end{bmatrix} \end{bmatrix} \begin{bmatrix} \mathbf{x} \\ d_r \\ \mathbf{u}_m \end{bmatrix}. \quad (5.14)$$

As discussed in Appendix A.4.5 and theoretically deduced in Prempain and Postlethwaite (2001, p. 22), the feedforward filter corresponding to the FI problem (5.14) can be designed via a state-feedback controller synthesis if the disturbances d_r have no direct feedthrough to the performance signals e_a and \mathbf{e}_u . In the proposed feedforward filter design with $\mathbf{W}_u(\boldsymbol{\theta}) = \boldsymbol{\Theta}^{-1}$, this condition is always satisfied as long as $W_{a,\text{roll}}(\boldsymbol{\theta})$ is strictly proper. Once the optimal state-feedback gain $\mathbf{F}(\boldsymbol{\theta})$ is determined, the feedforward filter

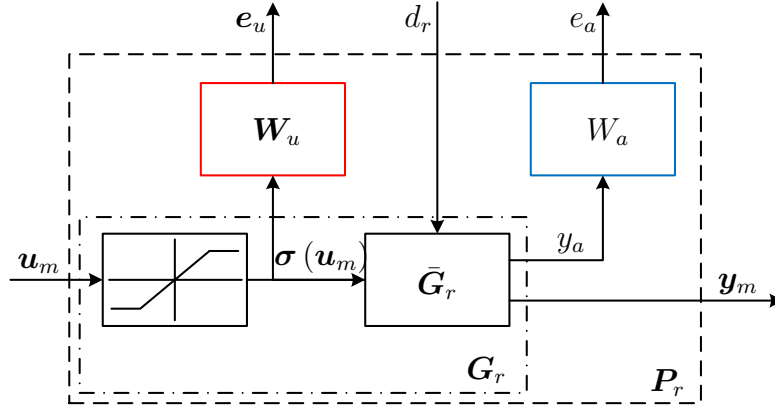


Figure 5.4: Weighting scheme of feedforward control design

N_Θ can be constructed according to (5.6). The corresponding state-feedback gain $F(\theta)$ is given by

$$F(\theta) = -\Theta\gamma^2\bar{B}_2^T Z, \quad (5.15)$$

with Lyapunov matrix Z resulting from the controller synthesis.

Figure 5.5 illustrates the frequency response of the roll velocity of the interconnection of the vehicle model G_r with feedforward filter N_Θ for the grid points $\theta = \theta_{\min}$ and $\theta = \theta_{\max}$. According to the design specification, the feedforward filter with $\theta = \theta_{\max}$ significantly reduces the roll velocity resonance peak of the vehicle, while the response with feedforward filter $N_{\Theta_{\min}}$ resembles the open-loop system. This behavior results from the state-feedback gain (5.15) of the feedforward filter which linearly reduces its control signal

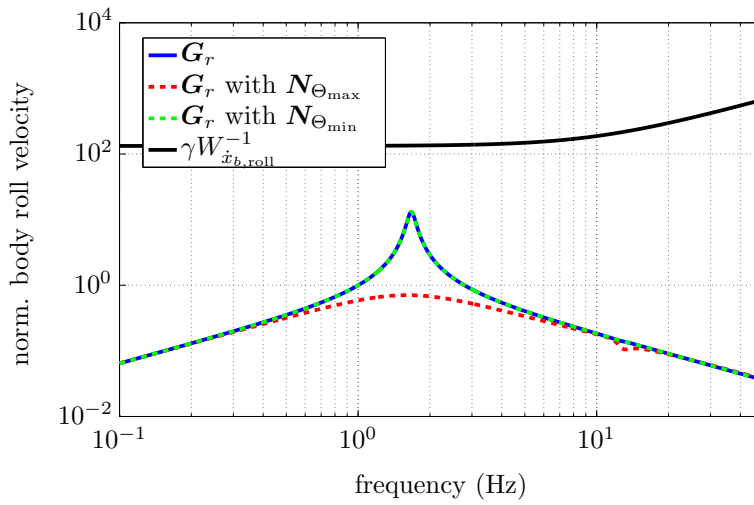


Figure 5.5: Frequency response of plant G_r from roll disturbance moment input d_r to angular roll velocity $\dot{x}_{b,roll}$ with and without feedforward filter N_Θ

\mathbf{u}_m according to the value of the saturation indicators $\boldsymbol{\theta}$ until the effect of the feedforward filter vanishes. Due to the equal saturation indicator dependent weighting schemes of the feedback and feedforward control design, the feedback and feedforward control signals are equally reduced in the event of saturation according to the saturation indicators and the two-degree-of-freedom controller achieves guaranteed stability for all admissible saturation indicators. Furthermore, the feedback controller and the feedforward filter equivalently contribute to the constrained control signal such that the feedforward filter does not dominate the constrained closed-loop system.

5.4 Simulation Results

To verify the performance benefit of the two-degree-of-freedom controller with feedforward filter \mathbf{N}_Θ , this section investigates a lane-change scenario. The investigation is enabled by extending the simulation model of the *SC3-Bulli* introduced in Appendix E.2 by a roll disturbance moment input. The vehicle model is then excited by the lateral acceleration depicted in Figure 5.6-top. The roll disturbance moment resulting from the lateral acceleration is computed according to (F.1).

Table 5.1: Performance assessment of two-degree-of-freedom controller with feedforward filter during simulation of lane-change scenario

	ride comfort J_{cISO}	road holding J_{rh}	RMS roll angle	RMS roll velocity
const. \mathbf{u}_d comfort	100 %	100 %	100 %	100 %
const. \mathbf{u}_d sport	64 %	77 %	67 %	63 %
LPV FVM ctrl	71 %	82 %	78 %	73 %
LPV FVM ctrl with \mathbf{N}_Θ	57 %	74 %	61 %	57 %

Table 5.1 presents the results of the simulation scenario. In addition to the criteria ride comfort and road-holding employed during feedback control design, the evaluation of the controller performance considers the RMS values of the roll angle and roll velocity of the vehicle body. In contrast to the investigation with road disturbances of Chapter 4, the comfort-oriented passive suspension configuration achieves the worst performance throughout all four criteria. At first glance, especially the bad ride comfort performance is surprising because the comfort-oriented passive suspension has been tuned to achieve good ride comfort. Unfortunately, good ride comfort regarding road disturbances and driver-induced disturbances corresponds to different passive damper configurations. This

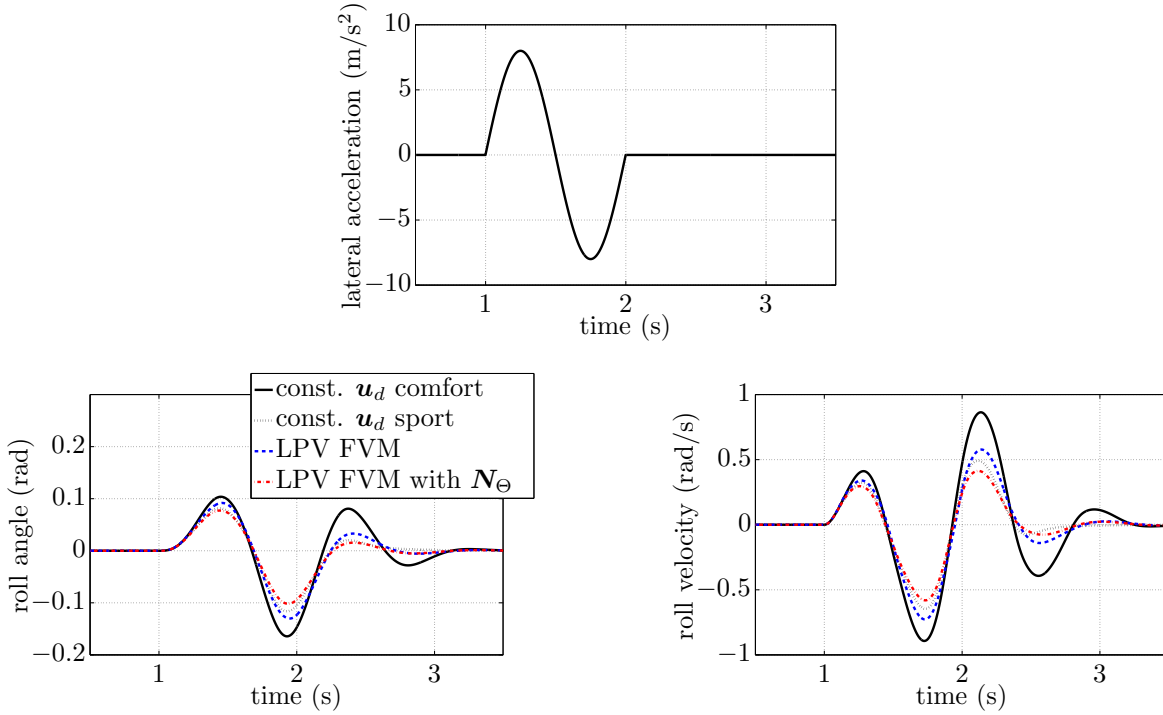


Figure 5.6: Simulation of lane change manoeuvre: top - lateral acceleration, bottom left - body roll angle, and bottom right - body angular roll velocity

is further emphasized by the very good performance of the sporty-oriented passive suspension configuration. The behavior can be justified by two reasons:

1. the transmission path of driver-induced disturbances to the body roll velocity shows a much better roll-off after the body resonance frequency (Figure 5.2) than the transmission path of road disturbances, and
2. the driver-induced disturbances are mainly low frequency disturbances up to 3 Hz.

Accordingly, the LPV FVM feedback controller tuned for good ride comfort regarding road disturbances, shows only medium performance regarding driver-induced disturbances. This is overcome by the two-degree-of-freedom LPV FVM controller with feedforward filter N_Θ , which improves the ride comfort and the RMS criteria of the roll angle and the roll velocity by at least 14 %, and road-holding by 8 % compared to the LPV controller without feedforward filter. Moreover, the LPV FVM controller with N_Θ achieves a slightly better performance than the sporty passive suspension configuration. This shows that the feedforward filter could be parametrized even more aggressive to further improve the performance regarding driver-induced disturbances. During combined road and driver-induced disturbances, however, an aggressive feedforward filter reduces the overall performance of the LPV FVM controller. Figure 5.6 - 5.9 illustrate the results of Table 5.1 by time series plots of the body roll angle, body roll velocity, damper velocities, dynamic wheel loads and control signals. As suggested by the results of Table 5.1 the sporty passive suspension configuration and the LPV FVM controller with N_Θ achieve the smallest

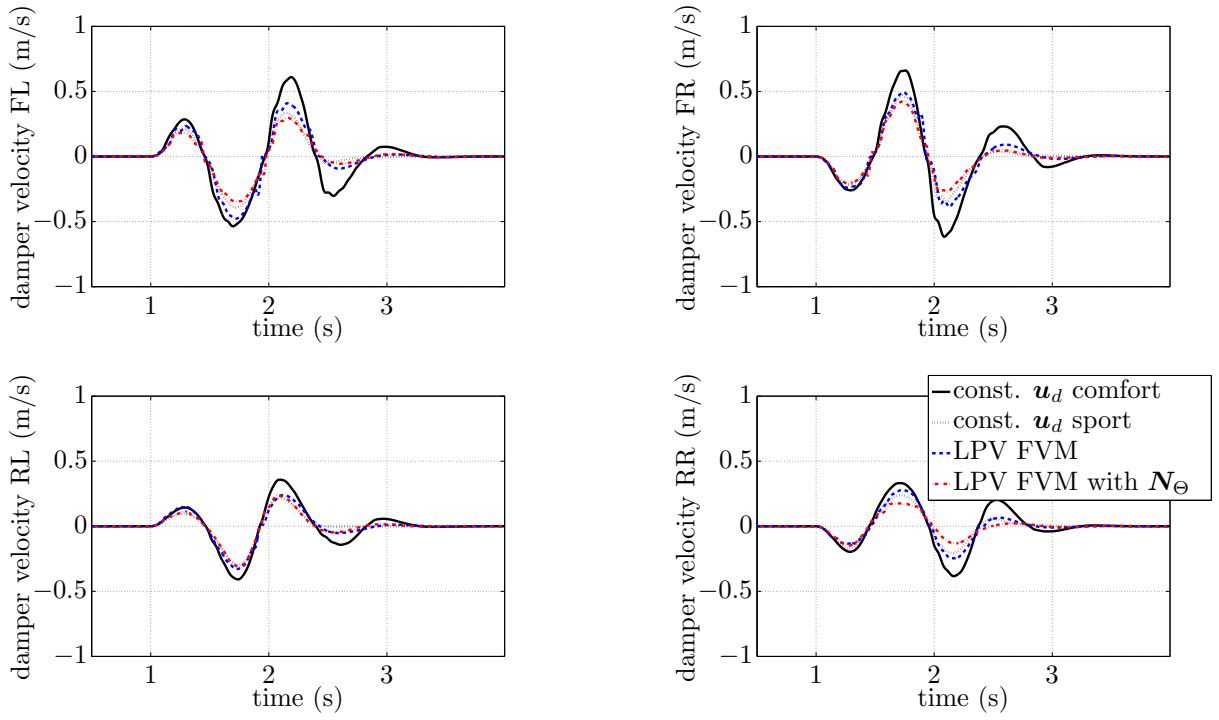


Figure 5.7: Simulation of lane change manoeuver: top left - damper velocity FL, top right - damper velocity FR, bottom left - damper velocity RL, and bottom right - damper velocity RR

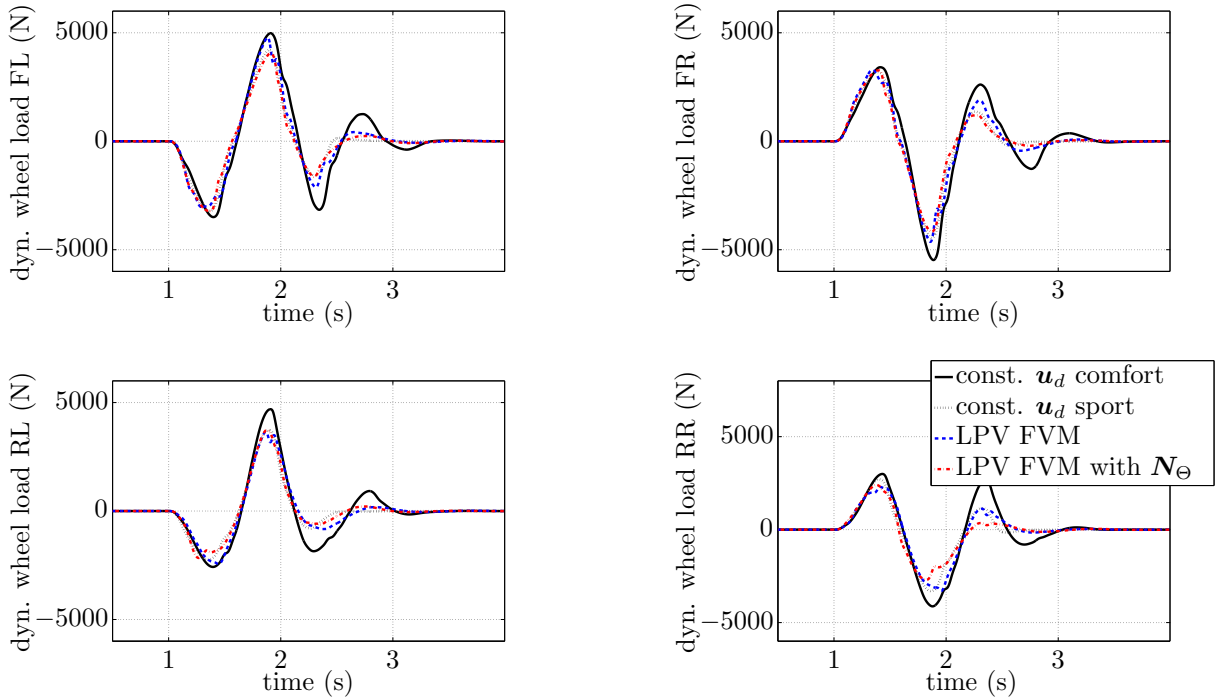


Figure 5.8: Simulation of lane change manoeuver: top left - dyn. wheel load FL, top right - dyn. wheel load FR, bottom left - dyn. wheel load RL, and bottom right - dyn. wheel load RR

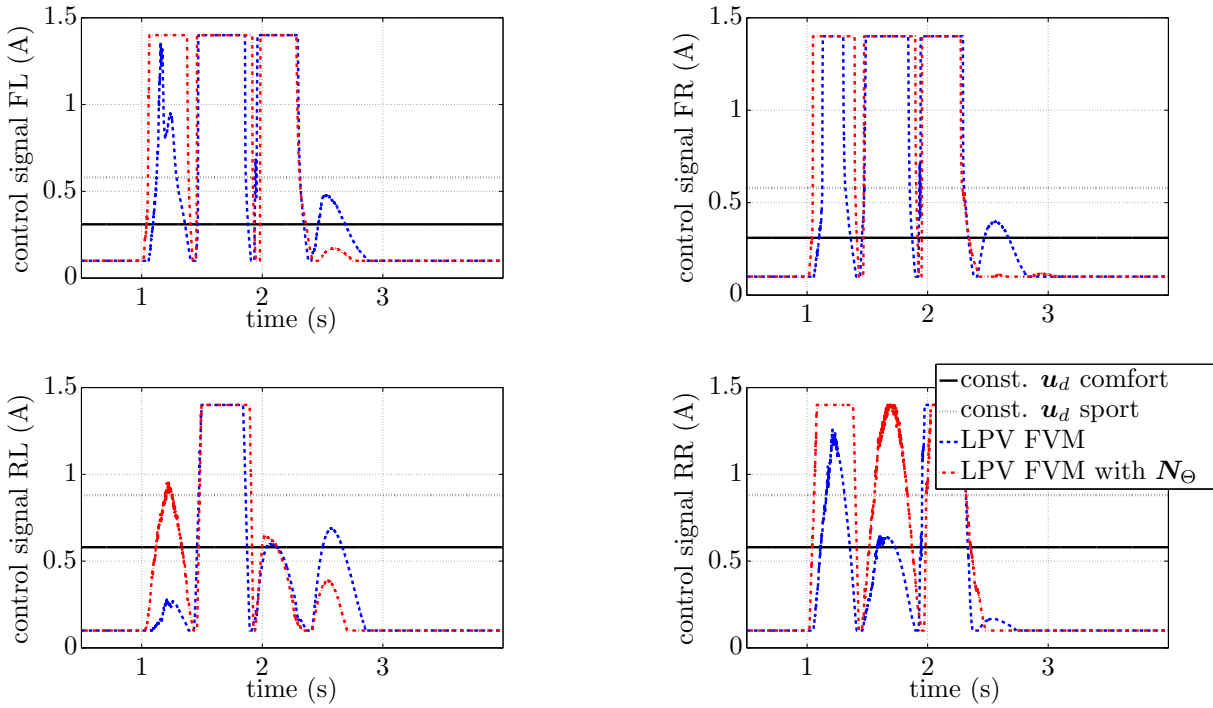


Figure 5.9: Simulation of lane change manoeuvre: top left - control signal FL, top right - control signal FR, bottom left - control signal RL, and bottom right - control signal RR

roll angles and roll angle velocities. The effect of the feedforward filter \mathbf{N}_Θ is particularly obvious from the control signals depicted in Figure 5.9. Due to the feedforward filter \mathbf{N}_Θ , the LPV FVM controller with \mathbf{N}_Θ commands much higher control signals and stabilizes the body roll motion.

The control signals of the rear suspensions additionally visualize the vital asymmetry of the force map of the rear semi-active dampers, which provide large rebound forces and only small compression forces. Therefore, the commanded damper current during compression is much higher than during rebound operation of the dampers.

5.5 Experimental Results

The proposed two-degree-of-freedom controller is evaluated by double lane change experiments with the *SC3-Bulli* introduced in Appendix E. The lane change manoeuvres are set-up according to ISO (3888-2:2011). The corresponding test track and parameters are given in Figure 5.10 and Table 5.2. The lane change defined by ISO (3888-2:2011) resembles an obstacle avoidance manoeuvre and is performed at a vehicle speed of 50 km/h.

The roll disturbance acting on the vehicle is estimated by the roll disturbance estimator presented in Appendix F. The roll disturbance estimator uses a single-track model to compute the expected lateral acceleration a_{yS} of a virtual acceleration sensor located a position S along the longitudinal vehicle axis. The position of the virtual acceleration sen-

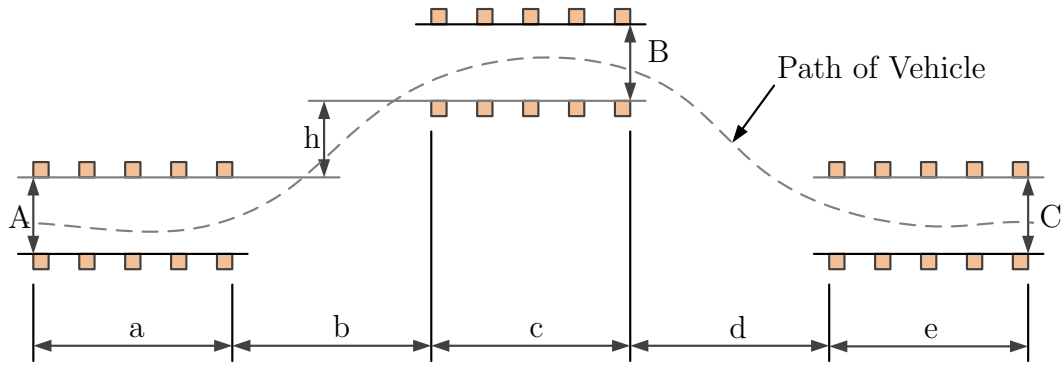


Figure 5.10: Experiment set-up ISO (3888-2:2011) lane change

Table 5.2: Parameters of lane change manoeuvres according to ISO (3888-2:2011); all quantities in (m)

a	b	c	d	e	A	B	C	h
12	13.5	11	12.5	12	$1.1b_v + 0.25$	$b_v + 1$	3	1

sor is used as a tuning parameter. It is determined by preliminary experiments according to the evaluation of the vehicle handling properties by the test driver.

Figure 5.11-top illustrates the measured lateral acceleration and the estimated lateral acceleration of the single-track model (STM) of the experiments with the passive suspension configuration const. \mathbf{u}_d comfort. The figure provides a cross-validation of the performance of the single-track model and confirms its suitability to estimate the vehicle lateral acceleration. Figure 5.11-bottom shows the measured lateral accelerations and steering angles of the four suspension configurations const. \mathbf{u}_d comfort, const. \mathbf{u}_d sport, LPV FVM and LPV FVM with feedforward filter \mathbf{N}_Θ of the lane change manoeuvres. Throughout all four runs, the lateral accelerations and steering angles match very well during the first 2.5 s of the experiments. The vehicle with const. \mathbf{u}_d sport and LPV FVM with feedforward filter \mathbf{N}_Θ , however, is essentially easier to drive and less steering angle is needed by the driver from 2.5 s onwards to the end of the manoeuvre. This behavior is consistent with the discussion of the vehicle handling properties in Section 5.3. The attenuation of the body roll motion reduces the dynamics wheel load transfer and consequently the tire side slip angles during the lane change manoeuvre. Simultaneously, the resulting lateral acceleration and the roll disturbance are also smaller. This behavior further enhances the performance of the suspension configurations const. \mathbf{u}_d sport and LPV FVM with feedforward filter \mathbf{N}_Θ .

Table 5.3 gives a comparison of ride comfort and the RMS values of the body roll angle, the body roll velocity and the steering angle of the ISO (3888-2:2011) lane change

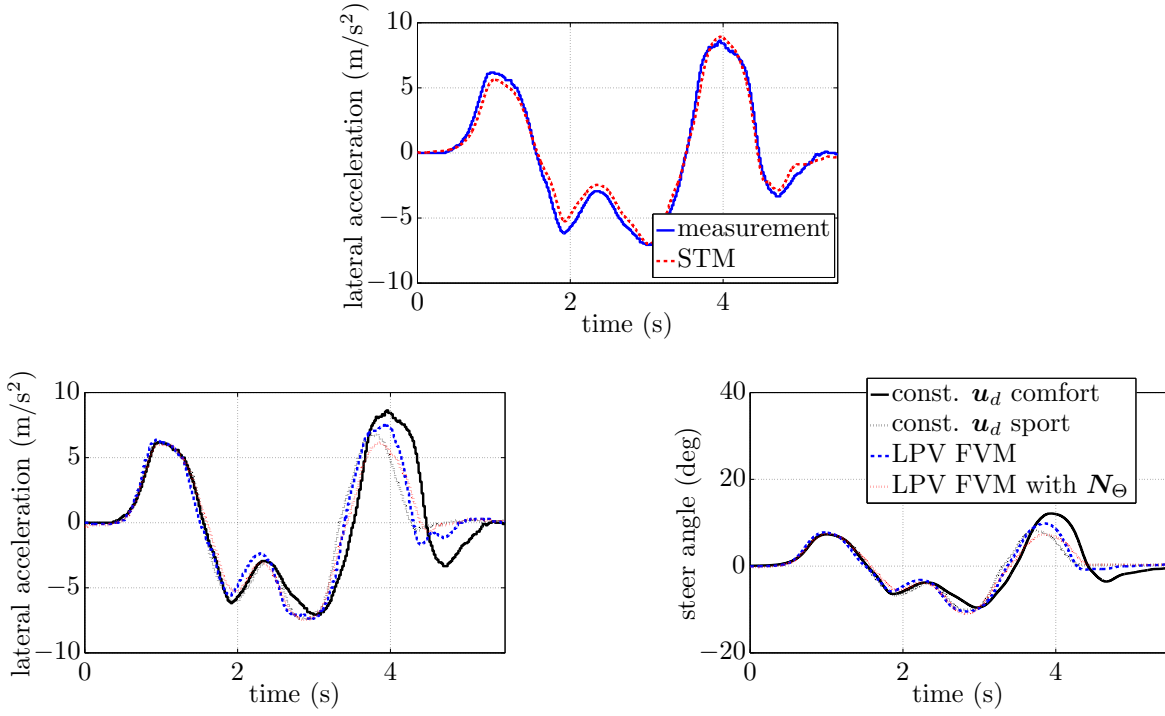


Figure 5.11: ISO (3888-2:2011) double lane change at a vehicle speed of 50 km/h: top - single-track model estimation, bottom left - lateral acceleration, and bottom right - front wheel steering angle

manoeuvre. Compared to the LPV FVM controller without feedforward filter, the two-degree-of-freedom controller improves ride comfort by 15 % and reduces the RMS values of the body roll angle and velocity by the same magnitude compared to the LPV controller without feedforward. Moreover, the RMS value of the steering angle is also reduced by

Table 5.3: ISO (3888-2:2011) double lane change at a vehicle speed of 50 km/h: performance assessment of two-degree-of-freedom controller with feedforward filter

	ride comfort J_{cISO}	RMS roll angle	RMS roll velocity	RMS steer angle
const. \mathbf{u}_d comfort	100 %	100 %	100 %	100 %
const. \mathbf{u}_d sport	88 %	78 %	81 %	84 %
LPV FVM ctrl	94 %	97 %	96 %	91 %
LPV FVM ctrl with \mathbf{N}_Θ	79 %	76 %	81 %	78 %

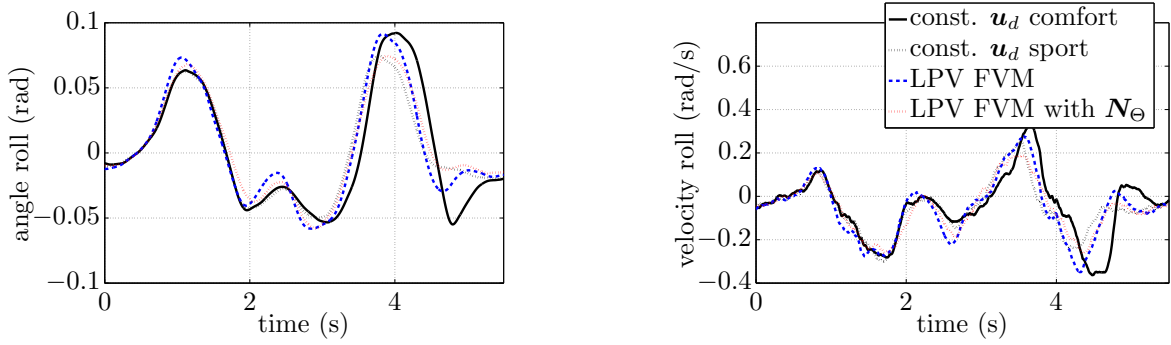


Figure 5.12: ISO (3888-2:2011) double lane change at a vehicle speed of 50 km/h: left - body roll angle, right - body angular roll velocity

about 20 %. Figure 5.12 illustrates the corresponding body roll angle and velocity of the four configurations and Figure 5.13 shows the damper current. As expected, the two-degree-of-freedom controller commands much higher control signals to attenuate the roll disturbance.

In summary, the results of the double lane change manoeuvre correspond well to the simulation results of Section 5.4. Even though the paths of the vehicle through the test track vary from experimental run to run due to imperfect driver inputs, the individual runs exhibit just small variations of the lateral acceleration at the beginning of the experiment.

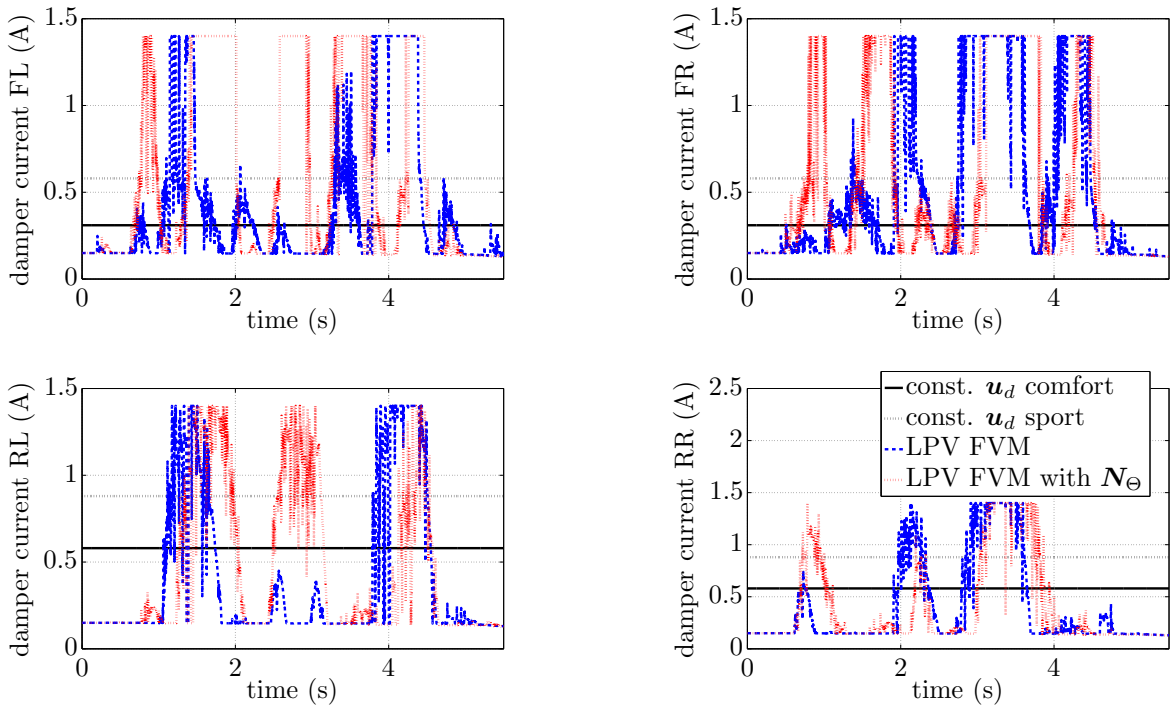


Figure 5.13: ISO (3888-2:2011) double lane change at a vehicle speed of 50 km/h: top left - damper current FL, top right - damper current FR, bottom left - damper current RL, and bottom right - damper current RR

Moreover, the LPV controller with feedforward filter features a vital improvement of ride comfort of 15 % compared to the LPV controller without feedforward filter. This improvement is distinctly larger than the ride comfort variation due to the imperfect driver input of experimental runs with the same suspension configuration.

5.6 Discussion and Conclusion

This chapter augments the full-vehicle LPV controller presented in Chapter 4 by an LPV feedforward filter. The feedforward filter is designed by a Full-Information problem and aims at an attenuation of the effect of driver-induced roll disturbances on ride comfort and vehicle handling. Equally to the LPV feedback controller of Chapter 4, the feedforward filter employs saturation indicator parameters that incorporate the restrictive force constraints of semi-active dampers in the control design. In this way, the control signal of the feedforward filter also linearly reduces in the event of saturation depending on the saturation indicators. The resulting two-degree-of-freedom controller features guaranteed stability for all admissible saturation indicators. Moreover, the equal saturation indicator dependent weighting schemes of the feedback and feedforward control design achieve an equivalent contribution of the feedback controller and the feedforward filter to the constrained control signal.

The proposed two-degree-of-freedom LPV controller is validated by lane change experiments with SR's *SC3-Bulli* experimental vehicle. The results show a vital improvement of ride comfort and also a reduced body roll angle and velocity compared to the LPV controller without feedforward filter.

6 Conclusion and Outlook

This work elaborates the control design for a passenger car equipped with four semi-active dampers. The typical software implementation of a vertical dynamics control algorithm has been introduced in Chapter 1 Figure 1.3. As discussed there, the presented control design focuses on the *feedback controller* and the *roll feedforward* control. All other functions are mandatory parts of the entire vertical dynamics control algorithm and are realized according to the state-of-the-art with minor adaptations to the application.

6.1 Conclusion

The main design goals of the vertical dynamics control problem are ride comfort, road-holding and handling of the vehicle subject to road and driver-induced disturbances. To exploit the performance potential of the vehicle with four semi-active dampers, the design goals are addressed by a two-degree-of-freedom controller. The feedback control part of the two-degree-of-freedom structure, called *feedback controller* in Figure 1.3, focuses on the attenuation of the unknown road disturbances, while the feedforward part, called *roll feedforward* control, minimizes the effect of the estimated driver-induced roll disturbances. The vital control design challenges introduced by the restrictive state-dependent force limitations of the semi-active dampers are overcome by a rigorous LPV control design utilizing saturation indicator parameters. The two-degree-of-freedom LPV controller features the following advantageous properties.

- The controller explicitly considers the actuator force limitations by saturation indicators and thus achieves a vital improvement of the design targets compared to a full-vehicle Skyhook-Groundhook controller
- The controller guarantees stability and performance of the closed-loop in the event of actuator saturation.
- The controller allows for the individual tuning of the body heave, roll and pitch degrees-of-freedom based on a full-vehicle controller synthesis model.
- The controller reconfigures its control signal in case of saturation or malfunction of the semi-active dampers.
- The controller allows for the separate specification of design goals regarding road disturbances and driver-induced disturbances.

In order to achieve these properties, the presented LPV controller extends existing anti-windup LPV control approaches by saturation indicator dependent weighting functions. In particular, the saturation indicator dependence is realized such that the resulting LPV controller features a linear dependence on the saturation indicators. In this way, the

controller linearly reduces its control signal in the event of saturation. Moreover, the presented control design investigates the minimum required saturation indicator grid density to guarantee quadratic stability and introduces saturation transformer parameters to extend the applicability of the saturation indicator concept to arbitrary time-varying actuator constraints. The presented control design additionally integrates the saturation indicator concept and the actuator efficiency concept to augment the full-vehicle controller to an active fault-tolerant LPV controller. The augmentation of the saturation indicator concept guarantees stability of the controller in the presence of saturation nonlinearities and actuator malfunction. Furthermore, the active fault-tolerant controller reduces the ride comfort degradation in the event of actuator malfunction by reconfiguring the force distribution among the semi-active dampers. Finally, the coherent design of the feedback controller and the feedforward filter, both utilizing saturation indicators to describe the actuator constraints and equivalent saturation indicator dependent weighting functions, results in equal contribution of the feedback controller and the feedforward filter to the constrained control signal. This property of the entire two-degree-of-freedom controller is achieved by the consistent linear dependence of the feedback controller and the feedforward filter on the saturation indicators such that the control signals of both are linearly reduced in the event of saturation.

The proposed LPV control design is experimentally investigated in three steps. Firstly, a quarter-vehicle test-rig assessment verifies the fundamental suitability of the anti-windup LPV control design with saturation indicators for the semi-active suspension control problem. Secondly, the active fault-tolerant full-vehicle LPV controller is validated by experiments on a four-post test-rig with SR's *SC3-Bulli* experimental vehicle. Thirdly, double lane change experiments confirm the attenuation of driver-induced roll disturbances by the LPV feedforward filter. In summary, the experiments show that the proposed two-degree-of-freedom controller improves ride comfort and road-holding by 10 % compared to a full-vehicle Skyhook-Groundhook controller. The feedforward filter enhances the performance of the LPV feedback controller regarding driver-induced roll disturbances by 15 %.

6.2 Outlook and Future Work

As part of this work, the proposed full-vehicle LPV controller has been implemented on a dSPACE MicroAutoBox II and integrated in the *SC3-Bulli* experimental vehicle of SR. In addition to the experimental assessments presented in Chapters 4 and 5, the full-vehicle LPV controller has collected about 1000 km on highways and country roads. During these test drives the controller confirmed its good performance and its easy integration into vertical dynamics control algorithms. Compared to full-vehicle Skyhook-Groundhook controllers, however, some challenges remain on the way to industrialization. On the one hand, the implementation on automotive electronic control units (ECU) has to be verified. Automotive ECUs provide far less computational power and memory than the dSPACE MicroAutoBox. This may be a vital issue for the integration of the full-vehicle LPV

controller, even though the observer-based state-feedback structure mitigates these issues due to the distinct separation between observer and controller. On the other hand, immediate controller tuning during test drives is common practice during the parametrization of semi-active damper controllers. This requirement is easily satisfied by a Skyhook-Groundhook controller which features tunable gain parameters to determine the control signal height. In contrast, the LPV controller presented in this work has to be synthesized with every adjustment of the tuning parameters. This can be overcome by introducing further scheduling parameters which are dedicated to enable an online adaption of the control targets. The effect of the tuning parameters, however, is less transparent and the application engineer needs some insight into the LPV control design.

The proposed LPV controller can easily incorporate plant nonlinearities like air spring characteristics and nonlinear suspension kinematics by additional scheduling parameters. This improves the performance of the LPV controller in applications with highly nonlinear plants. Despite the direct consideration of nonlinearities and the reported good performance of the LPV controller, however, the question: “How optimal is the LPV controller in a semi-active suspension application?” remains. The question is difficult to answer due to the highly nonlinear experimental vehicle, e.g. the semi-active dampers and the kinematics and elastokinematics of the suspensions. During the LPV control design only the most essential nonlinearity, the semi-active damper, has been explicitly considered. In order to find the optimal control signal for a given disturbance scenario, offline trajectory optimization might be a feasible approach.

The saturation indicator concept can be readily adjusted for vertical dynamics applications with fully-active actuators or a combination of semi-active dampers with slowly-active actuators. As discussed in Koch et al. (2010), the combination of a semi-active damper with a slowly-active actuator offers a vital potential for improvement of ride comfort compared to a suspension configuration with only semi-active dampers. The advantages of the combined suspension are mainly the additional functions offered by the slowly-active actuators like load leveling and active suppression of low frequency body oscillations. Regarding fully-active suspension systems, the presented LPV controller provides a good starting point for the control design. Naturally, the explicit consideration of actuator constraints is crucial for fully-active actuators which also offer limited force capability. Compared to the semi-active damper application, an application with fully-active actuators may introduce the additional design goal of stationary accuracy. In that case, the proposed anti-windup LPV control approach has to incorporate a windup feedback signal according to Wu et al. (2000) and the weighting functions have to be adjusted such that the low frequency range is emphasized if required.

The fault-tolerant control augmentation of the LPV controller can also readily be employed in an application with active actuators. Due to the less restrictive force constraints, the performance degradation of the fault-tolerant LPV controller should be even smaller than in the presented semi-active damper application. In both applications, the fault-tolerant controller needs a fault-detection and diagnosis (FDD) algorithm which provides

the fault information.

The augmentation of the LPV controller by the LPV feedforward filter which aims at a reduction of the effect of driver-induced roll disturbances constitutes the first step towards the cooperation of the vertical dynamics controller with the planar vehicle control algorithms. The feedforward filter reduces the body roll motion and improves the tire road contact. Thus, the tires can transmit larger longitudinal and lateral forces which results in an improved planar vehicle dynamics. In such a cooperation, the planar vehicle control algorithms could provide the expected longitudinal and lateral accelerations to the vertical dynamics controller. This information could then be used to compute the driver-induced disturbance inputs of the feedforward filters. Equally, the vertical dynamics algorithm could provide an estimate of the dynamic wheel load to the planar dynamics algorithms such that the longitudinal and lateral force capabilities of the tire could be assessed more easily. Moreover, the integration of vertical vehicle dynamics and planar vehicle dynamics control algorithms into one central controller could achieve vital performance improvements in both fields. The main challenge of such an integrated vehicle control approach arises from the significant increase in complexity of the control problem due to the high-order full-vehicle model and the numerous design goals.

LPV control methods continue to be intensively investigated in the scientific community and the numerous publications contain interesting developments like the integration of LPV and MPC methods described in Satzger et al. (2017). As discussed in Mohammadpour and Scherer (2012) and Sename et al. (2013), most nonlinear control problems can be cast into LPV control problems and it's up to control engineers to explore the vast possibilities of LPV methods.

A LPV Control Design

This chapter introduces the basic LPV theory and methods required for the control design in the subsequent chapters. The chapter focuses on LPV control methods that specify performance by the closed-loop input-to-output response (Apkarian et al., 1995; Apkarian and Gahinet, 1995; Wu et al., 1996; Becker and Packard, 1994). The presented LPV methods conceptually expand well-known sub-optimal H_∞ control theory of LTI plants (Gahinet and Apkarian, 1994) to LPV plants, such that loop-shaping techniques presented in Skogestad and Postlethwaite (2005, p. 399 ff.) can be employed to achieve the desired closed-loop behavior. In particular, quadratic Lyapunov stability of LTI plants is extended to quadratic Lyapunov stability of LPV plants, and finally to parameter-dependent Lyapunov stability. The stability conditions together with the induced L_2 -norm performance index are formulated in an LPV version of the Bounded Real Lemma. This theorem states a sufficient condition in terms of an infinite dimensional parameter-dependent matrix inequality to analyze stability and performance of the closed-loop system (Wu, 1995, p. 67-70). The most common approaches according to Hoffmann and Werner (2015, p. 419) to transform the infinite dimensional matrix inequality into a finite dimensional one can be classified into

- polytopic LPV control approaches,
- multiplier-based LFT LPV control approaches, and
- gridding-based LPV control approaches.

The LPV control design theory used in this work was developed as part of the PhD thesis of Wu (1995). It pursues a gridding-based LPV control design which can be applied to a large variety of LPV plants. Hughes and Wu (2012) provide a recent application example with a brief review of the theory.

A.1 Definition of LPV Systems

LPV systems generalize standard LTI systems to linear plants with time-varying parameters $\boldsymbol{\rho}(t)$ called scheduling parameters. The scheduling parameters are assumed to continuously evolve in time and to be measurable or estimable in real-time. Furthermore, the rates of variation of the scheduling parameters are assumed to be bounded according to

$$|\dot{\rho}_i(t)| \leq \dot{\rho}_{\max,i} \quad \forall i \in \{1, 2, \dots, n_\rho\} \quad \forall t \in \mathbb{R}^+ \quad (\text{A.1})$$

with n_ρ the number of scheduling parameters and the rate bounds $\dot{\rho}_{\max,i} > 0$. The scheduling parameter vector itself belongs to a compact set $\mathcal{P} \subset \mathbb{R}^{n_\rho}$. In the remainder of this thesis, the notation $\boldsymbol{\rho} \in \mathcal{F}_\rho$ denotes time-varying trajectories with bounded rates in the parameter variation set \mathcal{F}_ρ . Using the scheduling parameter $\boldsymbol{\rho}$, Definition A.1 states a

general continuous-time LPV system whose state-space matrices are continuous functions of the scheduling parameters $\boldsymbol{\rho}$ and their derivatives $\dot{\boldsymbol{\rho}}$.

Definition A.1. An n_x -th order linear parameter-varying (LPV) system $\mathbf{\Gamma}_{ed}$ is given by

$$\begin{bmatrix} \dot{\mathbf{x}} \\ \mathbf{e} \end{bmatrix} = \begin{bmatrix} \mathbf{A}(\boldsymbol{\rho}, \dot{\boldsymbol{\rho}}) & \mathbf{B}(\boldsymbol{\rho}, \dot{\boldsymbol{\rho}}) \\ \mathbf{C}(\boldsymbol{\rho}, \dot{\boldsymbol{\rho}}) & \mathbf{D}(\boldsymbol{\rho}, \dot{\boldsymbol{\rho}}) \end{bmatrix} \begin{bmatrix} \mathbf{x} \\ \mathbf{d} \end{bmatrix}, \quad (\text{A.2})$$

with $\mathbf{A} \in \mathcal{C}_0(\mathbb{R}^{n_\rho} \times \mathbb{R}^{n_\rho}, \mathbb{R}^{n_x \times n_x})$, $\mathbf{B} \in \mathcal{C}_0(\mathbb{R}^{n_\rho} \times \mathbb{R}^{n_\rho}, \mathbb{R}^{n_x \times n_d})$, $\mathbf{C} \in \mathcal{C}_0(\mathbb{R}^{n_\rho} \times \mathbb{R}^{n_\rho}, \mathbb{R}^{n_e \times n_x})$, $\mathbf{D} \in \mathcal{C}_0(\mathbb{R}^{n_\rho} \times \mathbb{R}^{n_\rho}, \mathbb{R}^{n_e \times n_d})$ and $\boldsymbol{\rho} \in \mathcal{F}_\rho$, and the vectors \mathbf{x} , \mathbf{e} and \mathbf{d} of appropriate dimension.

Remark. The time-dependence of matrices and vectors, e.g. $\boldsymbol{\rho}(t)$ is omitted in equations if the time-dependence is clear from the context.

Compared to LTV systems whose system matrices $\mathbf{A}(t)$, $\mathbf{B}(t)$, $\mathbf{C}(t)$, and $\mathbf{D}(t)$ are general functions of time, the system matrices of LPV systems feature a prescribed dependence on the scheduling parameters $\boldsymbol{\rho}$. The interest in LPV systems is motivated by the fact that nonlinear dynamics can be often cast into LPV systems by choosing a suitable set of scheduling variables. LPV systems whose scheduling parameters are functions of the system state $\boldsymbol{\rho}(t) = f(\mathbf{x}(t))$ are called quasi-LPV systems. During controller synthesis, the state-dependent scheduling parameters of quasi-LPV systems are treated as exogenous signals just as scheduling parameters of ordinary LPV systems. The drawback of this approximation may be a more conservative controller, however, the advantages of LPV methods outweigh in most applications (Huang and Jadbabaie, 1999, p. 87). In the remainder, this thesis does not distinguish between quasi-LPV systems and LPV systems with real exogenous scheduling parameters.

A.2 Stability of LPV Systems

Compared to the stability analysis of LTI systems, the stability analysis of LPV systems is more involved, because the analysis has to cover the whole parameter variation set \mathcal{F}_ρ . In particular, stability of time-varying systems such as LTV and LPV systems cannot be verified by separately analyzing frozen systems, e.g. in the LPV case $\mathbf{\Gamma}_{ed}(\boldsymbol{\rho}_k)$ with fixed parameter vectors $\boldsymbol{\rho}_k$. Even if the system matrix $\mathbf{A}(\boldsymbol{\rho}_k)$ of the frozen systems is *Hurwitz*, stability of the LPV system cannot be inferred as discussed in Amato (2006, p. 13). Nevertheless, the stability of LPV systems can be analyzed by means of the well-known Lyapunov stability theory. According to Wu (1995, p. 4 and p. 54 ff.), Lyapunov stability of LPV systems can be divided into quadratic stability of LPV systems with constant Lyapunov matrices and quadratic stability of LPV systems with parameter-dependent Lyapunov matrices. Throughout this work, quadratic stability of LPV systems with constant Lyapunov matrices is called quadratic stability, while quadratic stability of LPV systems with parameter-dependent Lyapunov matrices is called parameter-dependent stability. The two concepts gradually extend quadratic Lyapunov stability of LTI systems:

firstly to quadratic stability of LPV systems and subsequently to parameter-dependent stability of LPV systems.

A.2.1 Quadratic Lyapunov Stability

Similar to Lyapunov stability of LTI systems, quadratic Lyapunov stability of LPV systems involves a single constant Lyapunov matrix, but the Lyapunov conditions have to hold over the compact parameter set \mathcal{P} . The quadratic Lyapunov stability conditions of LPV system without explicit dependence on scheduling parameter derivatives

$$\begin{bmatrix} \dot{\mathbf{x}} \\ \mathbf{e} \end{bmatrix} = \begin{bmatrix} \mathbf{A}(\boldsymbol{\rho}) & \mathbf{B}(\boldsymbol{\rho}) \\ \mathbf{C}(\boldsymbol{\rho}) & \mathbf{D}(\boldsymbol{\rho}) \end{bmatrix} \begin{bmatrix} \mathbf{x} \\ \mathbf{d} \end{bmatrix}, \quad (\text{A.3})$$

with $\boldsymbol{\rho} \in \mathcal{P}$, $\mathbf{A} \in \mathcal{C}_0(\mathbb{R}^{n_\rho}, \mathbb{R}^{n_x \times n_x})$, $\mathbf{B} \in \mathcal{C}_0(\mathbb{R}^{n_\rho}, \mathbb{R}^{n_x \times n_d})$, $\mathbf{C} \in \mathcal{C}_0(\mathbb{R}^{n_\rho}, \mathbb{R}^{n_e \times n_x})$, and $\mathbf{D} \in \mathcal{C}_0(\mathbb{R}^{n_\rho}, \mathbb{R}^{n_e \times n_d})$ and the vectors \mathbf{x} , \mathbf{e} and \mathbf{d} of appropriate dimension can be deduced from the Lyapunov conditions of nonlinear systems. The stability conditions with quadratic Lyapunov function $v(\mathbf{x})$ are firstly

$$v(\mathbf{x}) = \mathbf{x}^T \mathbf{Z} \mathbf{x} > 0 \quad \forall \mathbf{x} \neq 0 \text{ and } v(0) = 0, \quad (\text{A.4})$$

with positive definite Lyapunov matrix $\mathbf{Z} > 0$ and $\mathbf{Z} \in \mathbb{R}^{n_x \times n_x}$ and secondly

$$\dot{v}(\mathbf{x}, \boldsymbol{\rho}) < 0 \quad \forall \mathbf{x} \neq 0 \text{ and } \boldsymbol{\rho} \in \mathcal{P}. \quad (\text{A.5})$$

The conditions can be summarized in the following definition.

Definition A.2 (Quadratic stability of LPV systems). The LPV system Γ_{ed} given in (A.3) without explicit dependence on the scheduling parameter derivatives is quadratically stable if there exists a positive definite matrix $\mathbf{Z} > 0$ and $\mathbf{Z} \in \mathbb{R}^{n_x \times n_x}$, such that for all $\boldsymbol{\rho} \in \mathcal{P}$

$$\mathbf{A}^T(\boldsymbol{\rho}) \mathbf{Z} + \mathbf{Z} \mathbf{A}(\boldsymbol{\rho}) < 0. \quad (\text{A.6})$$

This definition of quadratic stability can be found in Becker and Packard (1994, p. 206) and (Wu, 1995, p. 4). The conditions hold for arbitrary state trajectories and for arbitrarily fast rates of variation of the scheduling parameters as long as $\boldsymbol{\rho} \in \mathcal{P}$.

A.2.2 Parameter-Dependent Lyapunov Stability

In many control applications, the scheduling parameters are a continuous and slowly varying function of time, e.g. the velocity of an airplane or passenger car. In these applications, the quadratic stability approach with constant Lyapunov function and arbitrarily fast parameter variation rates may result in extremely conservative designs or may not be able to prove stability at all. This is emphasized by Wu (1995, p. 55-57), who shows an example of an LPV system with parameter-dependent state-feedback whose stability cannot

be proven by quadratic Lyapunov stability with a constant Lyapunov matrix, but nevertheless by considering the maximum parameter variation rates quadratic stability can be proven by a suitable parameter-dependent Lyapunov function. This is possible as the stability analysis can exploit the additional degrees-of-freedom introduced by a parameter-dependent Lyapunov matrix which leads to a far less conservative results. Definition A.3 states the quadratic Lyapunov stability conditions based on the parameter-dependent Lyapunov function $v(\mathbf{x}, \boldsymbol{\rho}) = \mathbf{x}^T \mathbf{Z}(\boldsymbol{\rho}) \mathbf{x}$ as described in Wu (1995, p. 58 ff.).

Definition A.3 (Parameter-dependent stability of LPV systems). The LPV system $\mathbf{\Gamma}_{ed}$ given in (A.2) is quadratically stable via a parameter-dependent Lyapunov function in $\mathcal{P} \times \dot{\mathcal{P}}$ if there exists a continuously differentiable matrix function $\mathbf{Z}(\boldsymbol{\rho}) > 0$ with $\mathbf{Z}(\boldsymbol{\rho}) \in \mathcal{C}_1(\mathbb{R}^{n_\rho}, \mathbb{R}^{n_x \times n_x})$, such that for all $\boldsymbol{\rho} \in \mathcal{P}$ and β_i with $|\beta_i| \leq \dot{\rho}_{\max,i} \quad \forall i \in \{1, 2, \dots, n_\rho\}$

$$\mathbf{A}^T(\boldsymbol{\rho}, \boldsymbol{\beta}) \mathbf{Z}(\boldsymbol{\rho}) + \mathbf{Z}(\boldsymbol{\rho}) \mathbf{A}(\boldsymbol{\rho}, \boldsymbol{\beta}) + \sum_{i=1}^{n_\rho} \frac{\partial \mathbf{Z}(\boldsymbol{\rho})}{\partial \rho_i} \beta_i < 0. \quad (\text{A.7})$$

A similar definition of quadratic Lyapunov stability via parameter-dependent Lyapunov functions is presented in Amato (2006, p. 93). In Definition A.3, the derivatives of the scheduling parameters $\dot{\boldsymbol{\rho}} \in \dot{\mathcal{P}}$ are substituted by $\boldsymbol{\beta} \in \dot{\mathcal{P}}$ to emphasize that the scheduling parameters $\boldsymbol{\rho}$ and their derivatives $\boldsymbol{\beta}$ are treated as independent parameters during the stability analysis. The stability condition has to be verified for all $(\boldsymbol{\rho}, \boldsymbol{\beta}) \in \mathcal{P} \times \dot{\mathcal{P}}$.

Each of Definition A.2 and A.3 by itself provides only sufficient conditions for exponential stability of LPV systems (Amato, 2006, p. 94). This means that both conditions are conservative in the sense that there are LPV systems whose exponential stability property cannot be verified by them. Nevertheless, the conditions recover the necessary and sufficient conditions for exponential stability of LTI systems presented in Gahinet and Apkarian (1994, p. 6).

A.3 Induced L_2 -Norm Performance

The induced L_2 -norm of LPV system $\mathbf{\Gamma}_{ed}$ given in (A.2) characterizes the worst-case energy gain from its input \mathbf{d} to its output \mathbf{e} . Figure A.1 illustrates the L_2 -norm of the LPV system $\mathbf{\Gamma}_{ed}$. Mathematically, the induced L_2 -norm of the LPV system $\mathbf{\Gamma}_{ed}$ for all admissible scheduling parameter trajectories $\boldsymbol{\rho} \in \mathcal{F}_\rho$ is defined as

$$\|\mathbf{\Gamma}_{ed}(\boldsymbol{\rho}, \dot{\boldsymbol{\rho}})\|_{i2} = \sup_{\substack{\boldsymbol{\rho} \in \mathcal{F}_\rho, \|\mathbf{d}\|_2 \neq 0, \\ \mathbf{d} \in \mathcal{L}_2}} \frac{\|\mathbf{e}\|_2}{\|\mathbf{d}\|_2} = \sup_{\substack{\boldsymbol{\rho} \in \mathcal{F}_\rho, \|\mathbf{d}\|_2 \neq 0, \\ \mathbf{d} \in \mathcal{L}_2}} \frac{\|\mathbf{\Gamma}_{ed}(\boldsymbol{\rho}, \dot{\boldsymbol{\rho}}) \mathbf{d}\|_2}{\|\mathbf{d}\|_2} < \gamma, \quad (\text{A.8})$$

with the induced L_2 -norm performance level γ . The conditions $\|\mathbf{d}\|_2 \neq 0$ and $\mathbf{d} \in \mathcal{L}_2$ ensure that the L_2 -norm of the input signal \mathbf{d} is well defined. A proof of the existence of an upper bound of the induced L_2 -norm of a stable LPV system $\mathbf{\Gamma}_{ed}$, i.e. $\gamma < \infty$, can be found in Wu (1995, p. 61 ff.). The induced L_2 -norm is a generalization of the

\mathcal{H}_∞ -norm known from LTI systems to LPV systems. Consequently, the induced L_2 -norm of LTI systems is equal to their \mathcal{H}_∞ -norm. The close relation of the induced L_2 -norm to the \mathcal{H}_∞ -norm facilitates the application of well-known design techniques like loop-shaping to the design of LPV controllers. In particular, the \mathcal{H}_∞ -norm is equal to the maximum singular value of the LTI system $\|\mathbf{\Gamma}_{\text{lti}}\|_\infty = \sup_{\omega \in \mathbb{R}} \varsigma_{\max}(\mathbf{\Gamma}_{\text{lti}}(j\omega))$ and can be interpreted as the minimal upper bound of the worst-case energy gain of the LTI system.

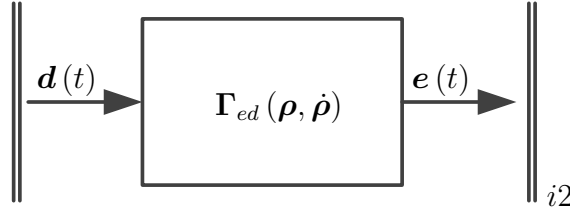


Figure A.1: Induced L_2 -Norm of LPV system $\mathbf{\Gamma}_{ed}$

The generalized Bounded Real Lemma formulated in Wu (1995, p. 63) and Wu et al. (1996, p. 985) states a sufficient condition to analyze the induced L_2 -norm of an LPV system.

Theorem A.1 (Generalized Bounded Real Lemma of LPV systems). *Consider a compact set $\mathcal{P} \subset \mathbb{R}^{n_\rho}$, finite non-negative bounds $\dot{\rho}_{\max,i}$ with $i \in \{1, 2, \dots, n_\rho\}$ and the LPV system $\mathbf{\Gamma}_{ed}$ in (A.2). If there exists a continuously differentiable function $\mathbf{Z}(\boldsymbol{\rho}) \in \mathcal{C}_1(\mathbb{R}^{n_\rho}, \mathbb{R}^{n_x \times n_x})$ such that $\mathbf{Z}(\boldsymbol{\rho}) > 0$ and*

$$\begin{bmatrix} \mathbf{A}^T(\boldsymbol{\rho}, \boldsymbol{\beta}) \mathbf{Z}(\boldsymbol{\rho}) + \mathbf{Z}(\boldsymbol{\rho}) \mathbf{A}(\boldsymbol{\rho}, \boldsymbol{\beta}) + \sum_{i=1}^{n_\rho} \frac{\partial \mathbf{Z}(\boldsymbol{\rho})}{\partial \rho_i} \beta_i & \mathbf{Z}(\boldsymbol{\rho}) \mathbf{B}(\boldsymbol{\rho}, \boldsymbol{\beta}) & \gamma^{-1} \mathbf{C}^T(\boldsymbol{\rho}, \boldsymbol{\beta}) \\ \mathbf{B}^T(\boldsymbol{\rho}, \boldsymbol{\beta}) \mathbf{Z}(\boldsymbol{\rho}) & -\mathbf{I}_{n_d} & \gamma^{-1} \mathbf{D}^T(\boldsymbol{\rho}, \boldsymbol{\beta}) \\ \gamma^{-1} \mathbf{C}(\boldsymbol{\rho}, \boldsymbol{\beta}) & \gamma^{-1} \mathbf{D}(\boldsymbol{\rho}, \boldsymbol{\beta}) & -\mathbf{I}_{n_e} \end{bmatrix} < 0 \quad (\text{A.9})$$

for all $\boldsymbol{\rho} \in \mathcal{P}$ and $|\beta_i| \leq \dot{\rho}_{\max,i} \quad \forall i \in \{1, 2, \dots, n_\rho\}$, then

1. the function $\mathbf{A}(\boldsymbol{\rho}, \boldsymbol{\beta})$ is parametrically-dependent stable over \mathcal{P} , and
2. there exists a scalar δ with $0 \leq \delta < \gamma$ such that $\|\mathbf{\Gamma}_{ed}(\boldsymbol{\rho}, \boldsymbol{\beta})\|_{i2} \leq \delta$

Proof. The proof of this theorem can be found in Wu (1995, p. 63 ff.) and Wu et al. (1996, p. 985-986). \square

A comparison of Theorem A.1 with Definition A.3 shows that parameter-dependent stability is contained in the generalized Bounded Real Lemma. Equally, by restricting \mathbf{Z} in Theorem A.1 to constant positive-definite matrices $\mathbf{Z} > 0$ with $\mathbf{Z} \in \mathbb{R}^{n_x \times n_x}$, the theorem obviously contains quadratic stability of LPV systems (A.3) without explicit dependence on the scheduling parameter derivatives discussed in Section A.2.1. Furthermore, Theorem A.1 recovers the necessary and sufficient conditions of the LTI version of the Bounded Real Lemma described in Gahinet and Apkarian (1994, p. 6).

A.4 LPV Controller Synthesis

The controller design interconnects the open-loop LPV plant \mathbf{P} and the LPV controller \mathbf{K} according to the general control configuration illustrated in Figure 2.1. The resulting closed-loop system is denoted by $\mathbf{\Gamma}_{ed}(\mathbf{P}, \mathbf{K})$. In this configuration, the measurements \mathbf{y} of the open-loop plant \mathbf{P} drive the controller \mathbf{K} yielding the control signal \mathbf{u} . The performance of the controller is specified by the induced L_2 -norm of the closed-loop system $\mathbf{\Gamma}_{ed}$ with the disturbance input \mathbf{d} shaped by the filter \mathbf{W}_d and the performance output \mathbf{e} weighted by the filter \mathbf{W}_e .

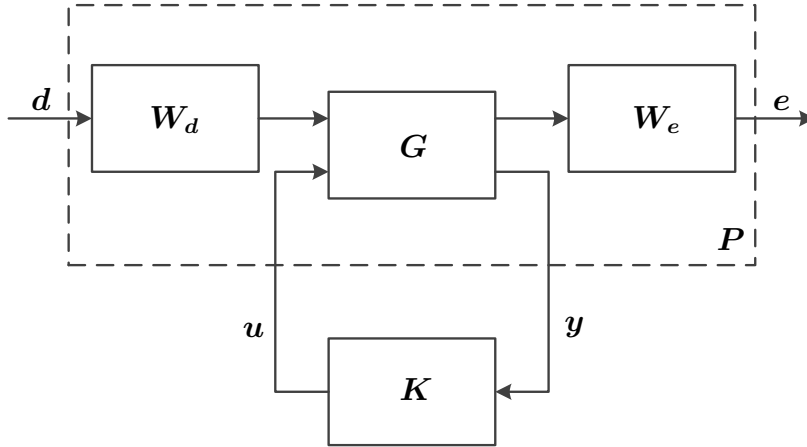


Figure A.2: General control configuration

The close relation of the induced L_2 -norm and the \mathcal{H}_∞ -norm facilitates the application of loop-shaping techniques during the design of LPV controllers. Hence, LPV controllers can be developed according to the two-stage loop-shaping design process well-established in \mathcal{H}_∞ control, see e.g. Kwakernaak (1993, p. 261 ff.) and Skogestad and Postlethwaite (2005, p. 399 ff.). In this process, the original open-loop LPV plant \mathbf{G} is augmented by input and output weighting filters \mathbf{W}_d and \mathbf{W}_e to specify the desired closed-loop shape. In comparison to LTI systems, the frequency response of LPV systems is only defined for frozen scheduling parameters $\boldsymbol{\rho}_k$. The application of loop-shaping, which specifies design objectives in frequency domain, nevertheless, achieves a successful control design because LPV control approaches with induced L_2 -norm performance index generalize LMI based \mathcal{H}_∞ control from LTI to LPV systems. Furthermore, the induced L_2 -norm inherently defines an upper bound for all frozen LPV systems $\mathbf{\Gamma}_{ed}(\boldsymbol{\rho}_k)$. In the literature, the augmented open-loop plant \mathbf{P} is referred to as a generalized plant and its state-space representation is given by

$$\begin{bmatrix} \dot{\mathbf{x}} \\ \mathbf{e} \\ \mathbf{y} \end{bmatrix} = \begin{bmatrix} \mathbf{A}(\boldsymbol{\rho}) & \mathbf{B}_1(\boldsymbol{\rho}) & \mathbf{B}_2(\boldsymbol{\rho}) \\ \mathbf{C}_1(\boldsymbol{\rho}) & \mathbf{D}_{11}(\boldsymbol{\rho}) & \mathbf{D}_{12}(\boldsymbol{\rho}) \\ \mathbf{C}_2(\boldsymbol{\rho}) & \mathbf{D}_{21}(\boldsymbol{\rho}) & \mathbf{D}_{22}(\boldsymbol{\rho}) \end{bmatrix} \begin{bmatrix} \mathbf{x} \\ \mathbf{d} \\ \mathbf{u} \end{bmatrix}, \quad (\text{A.10})$$

with $\boldsymbol{\rho} \in \mathcal{F}_\rho$, $\mathbf{x} \in \mathbb{R}^{n_x}$, $\mathbf{d} \in \mathbb{R}^{n_d}$, $\mathbf{e} \in \mathbb{R}^{n_e}$, $\mathbf{u} \in \mathbb{R}^{n_u}$, and $\mathbf{y} \in \mathbb{R}^{n_y}$. The corresponding state-space matrices are continuous functions of the scheduling parameters $\boldsymbol{\rho}$ and of appropriate dimensions.

Throughout the control design of this work, the generalized plant \mathbf{P} has to satisfy the following assumptions:

- (a1) $\mathbf{D}_{11}(\boldsymbol{\rho}) = \mathbf{0}$, $\mathbf{D}_{22}(\boldsymbol{\rho}) = \mathbf{0}$,
- (a2) $\mathbf{D}_{12}(\boldsymbol{\rho})$ full column rank for all $\boldsymbol{\rho} \in \mathcal{P}$,
- (a3) $\mathbf{D}_{21}(\boldsymbol{\rho})$ full row rank for all $\boldsymbol{\rho} \in \mathcal{P}$,
- (a4) the pair $(\mathbf{A}(\boldsymbol{\rho}), \mathbf{B}_2(\boldsymbol{\rho}))$ parameter-dependent stabilizable, and
- (a5) the pair $(\mathbf{A}(\boldsymbol{\rho}), \mathbf{C}_2(\boldsymbol{\rho}))$ parameter-dependent detectable.

Assumption (a1) restricts the generalized plant \mathbf{P} to systems without direct feedthrough of the control signals \mathbf{u} to the measurements \mathbf{y} and furthermore without direct feedthrough of the disturbance inputs \mathbf{d} to the performance outputs \mathbf{e} . As discussed in Wu (1995, p.68), the relaxation of assumptions (a2) and (a3) leads to a singular controller synthesis problem. Using assumptions (a1) - (a3) the open-loop generalized plant can be rewritten as

$$\begin{bmatrix} \dot{\mathbf{x}} \\ \begin{bmatrix} \mathbf{e}_a \\ \mathbf{e}_u \\ \mathbf{y} \end{bmatrix} \end{bmatrix} = \begin{bmatrix} \mathbf{A}(\boldsymbol{\rho}) & \mathbf{B}_{11}(\boldsymbol{\rho}) & \mathbf{B}_{12}(\boldsymbol{\rho}) & \mathbf{B}_2(\boldsymbol{\rho}) \\ \begin{bmatrix} \mathbf{C}_{11}(\boldsymbol{\rho}) \\ \mathbf{C}_{12}(\boldsymbol{\rho}) \\ \mathbf{C}_2(\boldsymbol{\rho}) \end{bmatrix} & \begin{bmatrix} \mathbf{0} \\ \mathbf{0} \\ \mathbf{0} \end{bmatrix} & \begin{bmatrix} \mathbf{0} \\ \mathbf{0} \\ \mathbf{I}_{n_{d2}} \end{bmatrix} & \begin{bmatrix} \mathbf{0} \\ \mathbf{I}_{n_u} \\ \mathbf{0} \end{bmatrix} \end{bmatrix} \begin{bmatrix} \mathbf{x} \\ \begin{bmatrix} \mathbf{d}_1 \\ \mathbf{d}_2 \\ \mathbf{u} \end{bmatrix} \end{bmatrix}, \quad (\text{A.11})$$

with $\boldsymbol{\rho} \in \mathcal{F}_\rho$, $\mathbf{d}_1 \in \mathbb{R}^{n_{d1}}$, $\mathbf{d}_2 \in \mathbb{R}^{n_{d2}}$, $\mathbf{e}_a \in \mathbb{R}^{n_{ea}}$, and $\mathbf{e}_u \in \mathbb{R}^{n_{eu}}$. This step particularly exploits assumptions (a2) and (a3) by norm-preserving transformations of the disturbance inputs \mathbf{d} and the performance outputs \mathbf{e} , and invertible transformations of the control signals \mathbf{u} and measurements \mathbf{y} such that $\mathbf{D}_{12}(\boldsymbol{\rho}) = [\mathbf{0} \ \mathbf{I}_{n_u}]^T$ and $\mathbf{D}_{21}(\boldsymbol{\rho}) = [\mathbf{0} \ \mathbf{I}_{n_{d2}}]$ as described in Wu (1995, p. 25 and p. 68) and Becker and Packard (1994, p. 209). These transformations are not only advantageous during controller synthesis from a computational point of view, but also from a design point of view as the performance outputs \mathbf{e} of the transformed plant given in (A.11) are structured into the performance signals \mathbf{e}_a and the control effort signals \mathbf{e}_u according to $\mathbf{e} = [\mathbf{e}_a^T \ \mathbf{e}_u^T]^T$. To sum up, assumptions (a1) - (a3) substantially simplify the control design as discussed in Doyle et al. (1989, p. 834) and should only be relaxed if essential for the application. The LPV control design presented in Chapters 3, 4 and 5 directly achieves open-loop generalized plants \mathbf{P} corresponding to (A.11) by a suitable formulation of the control design problem.

The analytical assessment of the stabilizability and detectability assumptions (a4) and (a5) of the LPV system, e.g. by evaluating the stronger notions of controllability and observability is much more involved for LPV systems than for LTI systems. In particular, because the generalized controllability matrix and observability matrix include time

derivatives of the pair $(\mathbf{A}(\boldsymbol{\rho}), \mathbf{B}_2(\boldsymbol{\rho}))$ and $(\mathbf{A}(\boldsymbol{\rho}), \mathbf{C}_2(\boldsymbol{\rho}))$, respectively. In this work, the plant models are large, and stabilizability and detectability are implicitly checked during the controller synthesis as proposed in Wu (1995, p. 97 ff.).

The definition of the finite dimensional controller \mathbf{K} of Figure A.2 given below can be found in Wu (1995, p. 69).

Definition A.4 (Parameter-dependent controller). Given a compact set $\mathcal{P} \subset \mathbb{R}^{n_\rho}$ and an integer $n_K \geq 0$, denote the parametrically-dependent, n_K -dimensional linear feedback controller as \mathbf{K} with the continuous functions $\mathbf{A}_K \in \mathcal{C}_0(\mathbb{R}^{n_\rho} \times \mathbb{R}^{n_\rho}, \mathbb{R}^{n_K \times n_K})$, $\mathbf{B}_K \in \mathcal{C}_0(\mathbb{R}^{n_\rho} \times \mathbb{R}^{n_\rho}, \mathbb{R}^{n_K \times n_y})$, $\mathbf{C}_K \in \mathcal{C}_0(\mathbb{R}^{n_\rho} \times \mathbb{R}^{n_\rho}, \mathbb{R}^{n_u \times n_K})$ and $\mathbf{D}_K \in \mathcal{C}_0(\mathbb{R}^{n_\rho} \times \mathbb{R}^{n_\rho}, \mathbb{R}^{n_u \times n_y})$. The controller $\mathbf{K}(\boldsymbol{\rho}, \dot{\boldsymbol{\rho}})$ depends on the scheduling parameters and their derivatives, and is given by

$$\begin{bmatrix} \dot{\mathbf{x}}_K \\ \mathbf{u} \end{bmatrix} = \begin{bmatrix} \mathbf{A}_K(\boldsymbol{\rho}, \dot{\boldsymbol{\rho}}) & \mathbf{B}_K(\boldsymbol{\rho}, \dot{\boldsymbol{\rho}}) \\ \mathbf{C}_K(\boldsymbol{\rho}, \dot{\boldsymbol{\rho}}) & \mathbf{D}_K(\boldsymbol{\rho}, \dot{\boldsymbol{\rho}}) \end{bmatrix} \begin{bmatrix} \mathbf{x}_K \\ \mathbf{y} \end{bmatrix}. \quad (\text{A.12})$$

with $\boldsymbol{\rho} \in \mathcal{F}_\rho$, and \mathbf{x}_K are the n_K -dimensional controller states.

Using Definition A.4, the closed-loop system $\boldsymbol{\Gamma}_{ed}(\mathbf{P}, \mathbf{K})$ with state $\mathbf{x}_{\text{clp}} = [\mathbf{x} \ \mathbf{x}_K]^T$ can be expressed as

$$\begin{bmatrix} \dot{\mathbf{x}}_{\text{clp}} \\ \mathbf{e} \end{bmatrix} = \begin{bmatrix} \mathbf{A}_{\text{clp}}(\boldsymbol{\rho}, \dot{\boldsymbol{\rho}}) & \mathbf{B}_{\text{clp}}(\boldsymbol{\rho}, \dot{\boldsymbol{\rho}}) \\ \mathbf{C}_{\text{clp}}(\boldsymbol{\rho}, \dot{\boldsymbol{\rho}}) & \mathbf{D}_{\text{clp}}(\boldsymbol{\rho}, \dot{\boldsymbol{\rho}}) \end{bmatrix} \begin{bmatrix} \mathbf{x}_{\text{clp}} \\ \mathbf{d} \end{bmatrix}. \quad (\text{A.13})$$

with

$$\mathbf{A}_{\text{clp}}(\boldsymbol{\rho}, \dot{\boldsymbol{\rho}}) = \begin{bmatrix} \mathbf{A}(\boldsymbol{\rho}) + \mathbf{B}_2(\boldsymbol{\rho}) \mathbf{D}_K(\boldsymbol{\rho}, \dot{\boldsymbol{\rho}}) \mathbf{C}_2(\boldsymbol{\rho}) & \mathbf{B}_2(\boldsymbol{\rho}) \mathbf{C}_K(\boldsymbol{\rho}, \dot{\boldsymbol{\rho}}) \\ \mathbf{B}_K(\boldsymbol{\rho}, \dot{\boldsymbol{\rho}}) \mathbf{C}_2(\boldsymbol{\rho}) & \mathbf{A}_K(\boldsymbol{\rho}, \dot{\boldsymbol{\rho}}) \end{bmatrix}, \quad (\text{A.14})$$

$$\mathbf{B}_{\text{clp}}(\boldsymbol{\rho}, \dot{\boldsymbol{\rho}}) = \begin{bmatrix} \mathbf{B}_{11}(\boldsymbol{\rho}) & \mathbf{B}_{12}(\boldsymbol{\rho}) + \mathbf{B}_2(\boldsymbol{\rho}) \mathbf{D}_K(\boldsymbol{\rho}, \dot{\boldsymbol{\rho}}) \\ \mathbf{0} & \mathbf{B}_K(\boldsymbol{\rho}, \dot{\boldsymbol{\rho}}) \end{bmatrix}, \quad (\text{A.15})$$

$$\mathbf{C}_{\text{clp}}(\boldsymbol{\rho}, \dot{\boldsymbol{\rho}}) = \begin{bmatrix} \mathbf{C}_{11}(\boldsymbol{\rho}) & \mathbf{0} \\ \mathbf{C}_{12}(\boldsymbol{\rho}) + \mathbf{D}_K(\boldsymbol{\rho}, \dot{\boldsymbol{\rho}}) \mathbf{C}_2(\boldsymbol{\rho}) & \mathbf{C}_K(\boldsymbol{\rho}, \dot{\boldsymbol{\rho}}) \end{bmatrix}, \text{ and} \quad (\text{A.16})$$

$$\mathbf{D}_{\text{clp}}(\boldsymbol{\rho}, \dot{\boldsymbol{\rho}}) = \begin{bmatrix} \mathbf{0} & \mathbf{0} \\ \mathbf{0} & \mathbf{D}_K(\boldsymbol{\rho}, \dot{\boldsymbol{\rho}}) \end{bmatrix}. \quad (\text{A.17})$$

The fundamental question of the control design problem is to determine if there exists a controller \mathbf{K} according to Definition A.4 and a parameter-dependent Lyapunov function such that the closed-loop satisfies Theorem A.1.

During the formulation of the state-feedback problem and the output-feedback problem, the analysis condition of the generalized Bounded Real Lemma (Theorem A.1) is reformulated as a group of linear matrix inequalities (LMI) of the performance index γ , the controller and the continuously-differentiable Lyapunov function. The minimal upper bound γ of the induced L_2 -norm of the LPV system $\boldsymbol{\Gamma}_{ed}(\mathbf{P}, \mathbf{K})$ can then be computed

by using these LMI conditions to form a convex optimization problem. Unfortunately, the optimization problem is infinite-dimensional firstly due to the open dependence of the parameter-dependent Lyapunov matrix on the scheduling parameters $\boldsymbol{\rho}$ and secondly due to the infinite-dimensional parameter space of the scheduling parameters themselves. As mentioned in the introduction of this chapter, the three most common types of relaxation of the infinite-dimensional scheduling parameter space into a finite-dimensional one are classified into polytopic, LFT-based and gridding-based LPV methods. The gridding-based LPV approach presented in Wu (1995, p. 87 ff.) and Wu et al. (1996, p. 993 ff.) pursued in this work approximates the parameter space by a finite number of grid points. Additionally, the infinite function space of the parameter-dependent Lyapunov function is approximated with a finite number of basis functions according to

$$\mathbf{Z}(\boldsymbol{\rho}) = \sum_{i=1}^{n_f} f_i(\boldsymbol{\rho}) \mathbf{Z}_i, \quad (\text{A.18})$$

with $f_i(\boldsymbol{\rho})$ the continuously differentiable basis functions, \mathbf{Z}_i the corresponding coefficient matrices and n_f the number of basis functions. As a result, the optimization problem becomes finite dimensional and can be efficiently solved using Semi-Definite Programming (SDP). An SDP is an optimization problem with linear cost function and LMI constraints. With respect to LPV controller synthesis, the SDP is defined as

$$\min_{\gamma, \mathbf{K}, \mathbf{Z}} \gamma \quad \text{s. t.} \quad (\text{A.19a})$$

$$\|\Gamma_{ed}(\mathbf{P}(\boldsymbol{\rho}), \mathbf{K}(\boldsymbol{\rho}, \dot{\boldsymbol{\rho}}))\|_{i_2} < \gamma \quad \forall \boldsymbol{\rho} = \{\boldsymbol{\rho}_1, \boldsymbol{\rho}_2, \dots, \boldsymbol{\rho}_{n_g}\} \quad \text{and} \quad \forall \dot{\boldsymbol{\rho}} = \{\boldsymbol{\nu}_1, \boldsymbol{\nu}_2, \dots, \boldsymbol{\nu}_{n_\nu}\}, \quad (\text{A.19b})$$

with n_g the number of grid points, ν_i denoting the vertices of the space of scheduling parameter derivatives and n_ν the number of vertices. The optimization calculates the LPV controller \mathbf{K} that minimizes the induced L_2 -norm performance index γ of the closed-loop system Γ_{ed} constructed by interconnecting the open-loop plant \mathbf{P} and the controller \mathbf{K} as illustrated in Figure A.2. The requirement of LMI constraints of SDPs restrict conditions (A.19b) to matrix inequalities with an affine dependence on the decision variables γ , \mathbf{K} and \mathbf{Z} .

A.4.1 State-Feedback Problem

This section presents the parameter-dependent state-feedback problem illustrated in Figure A.3, i.e. the feedback control problem where the full plant state vector \mathbf{x} is available either from measurements or through estimation. A detailed presentation of the state-feedback problem can be found in Wu (1995, p. 70 ff.) and Amato (2006, p. 130 and 134). The state-feedback problem with controller \mathbf{K}_x according to

$$\mathbf{u} = \mathbf{F}(\boldsymbol{\rho}) \mathbf{x} \quad (\text{A.20})$$

is stated in the following definition.

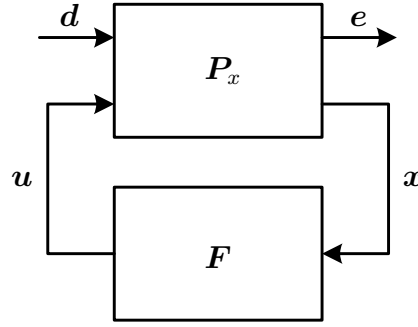


Figure A.3: General control configuration state-feedback problem

Definition A.5 (Parameter-dependent state-feedback problem). Consider a compact set $\mathcal{P} \subset \mathbb{R}^{n_\rho}$, the performance level $\gamma > 0$, and the LPV system \mathbf{P}_x

$$\begin{bmatrix} \dot{x} \\ e \end{bmatrix} = \begin{bmatrix} \mathbf{A}(\rho) & \mathbf{B}_1(\rho) & \mathbf{B}_2(\rho) \\ \mathbf{C}_1(\rho) & \mathbf{0} & \mathbf{D}_{12}(\rho) \end{bmatrix} \begin{bmatrix} x \\ d \\ u \end{bmatrix}. \quad (\text{A.21})$$

with $\rho \in \mathcal{F}_\rho$. The parameter-dependent state-feedback problem is solvable if there exist continuously differentiable matrix functions $\mathbf{Z}(\rho) \in \mathcal{C}_1(\mathbb{R}^{n_\rho}, \mathbb{R}^{n_x \times n_x})$ and $\mathbf{F}(\rho, \beta) \in \mathcal{C}_0(\mathbb{R}^{n_\rho} \times \mathbb{R}^{n_\rho}, \mathbb{R}^{n_u \times n_x})$ such that for all $\rho \in \mathcal{P}$ and $|\beta_i| \leq \dot{\rho}_{\max, i} \quad \forall i \in \{1, 2, \dots, n_\rho\}$, $\mathbf{Z}(\rho) > 0$ and

$$\begin{bmatrix} \mathbf{A}_F^T(\rho, \beta) \mathbf{Z}(\rho) + \mathbf{Z}(\rho) \mathbf{A}_F(\rho, \beta) + \sum_{i=1}^{n_\rho} \frac{\partial \mathbf{Z}(\rho)}{\partial \rho_i} \beta_i & \mathbf{Z}(\rho) \mathbf{B}_1(\rho) & \gamma^{-1} \mathbf{C}_F^T(\rho, \beta) \\ \mathbf{B}_1^T(\rho) \mathbf{Z}(\rho) & -\mathbf{I}_{n_d} & \mathbf{0} \\ \gamma^{-1} \mathbf{C}_F(\rho, \beta) & \mathbf{0} & -\mathbf{I}_{n_e} \end{bmatrix} < 0 \quad (\text{A.22})$$

with $\mathbf{A}_F(\rho, \beta) = \mathbf{A}(\rho) + \mathbf{B}_2(\rho) \mathbf{F}(\rho, \beta)$ and $\mathbf{C}_F(\rho, \beta) = \mathbf{C}_1(\rho) + \mathbf{D}_{12}(\rho) \mathbf{F}(\rho, \beta)$.

Unfortunately, condition (A.22) is not affine in the decision variables γ , \mathbf{F} and \mathbf{Z} and hence cannot be cast into a SDP optimization. This issue is overcome by reformulating the existence condition such that they depend only on state-space data of the open-loop system as shown in (Wu, 1995, p. 71). Using assumption (a2), (A.21) can be rewritten as

$$\begin{bmatrix} \dot{x} \\ e_a \\ e_u \end{bmatrix} = \begin{bmatrix} \mathbf{A}(\rho) & \mathbf{B}_1(\rho) & \mathbf{B}_2(\rho) \\ \mathbf{C}_{11}(\rho) & \mathbf{0} & \mathbf{0} \\ \mathbf{C}_{12}(\rho) & \mathbf{0} & \mathbf{I} \end{bmatrix} \begin{bmatrix} x \\ d \\ u \end{bmatrix} \quad (\text{A.23})$$

similar to (A.11). The existence conditions of the state-feedback controller \mathbf{K}_x can then be expressed by LMIs of the state-space data of the open-loop (A.23). The reformulated conditions are summarized in the following theorem.

Theorem A.2 (LMI conditions of the parameter-dependent state-feedback problem). Consider a compact set $\mathcal{P} \subset \mathbb{R}^{n_\rho}$, the performance level $\gamma > 0$, and the LPV system \mathbf{P}_x in (A.23). The parameter-dependent state-feedback problem is solvable if and only if there exists a continuously differentiable function $\mathbf{X}(\boldsymbol{\rho}) \in \mathcal{C}_1(\mathbb{R}^{n_\rho}, \mathbb{R}^{n_x \times n_x})$ such that for all $\boldsymbol{\rho} \in \mathcal{P}$, $\mathbf{X}(\boldsymbol{\rho}) > 0$ and

$$\begin{bmatrix} \mathbf{X}(\boldsymbol{\rho}) \hat{\mathbf{A}}^T(\boldsymbol{\rho}) + \hat{\mathbf{A}}^T(\boldsymbol{\rho}) \mathbf{X}(\boldsymbol{\rho}) - \partial \mathbf{X}(\boldsymbol{\rho}) - \mathbf{H}_{B_2}(\boldsymbol{\rho}) & \mathbf{X}(\boldsymbol{\rho}) \mathbf{C}_{11}^T(\boldsymbol{\rho}) & \gamma^{-1} \mathbf{B}_1(\boldsymbol{\rho}) \\ \mathbf{C}_{11}(\boldsymbol{\rho}) \mathbf{X}(\boldsymbol{\rho}) & -\mathbf{I}_{n_{e_1}} & \mathbf{0} \\ \gamma^{-1} \mathbf{B}_1^T(\boldsymbol{\rho}) & \mathbf{0} & -\mathbf{I}_{n_d} \end{bmatrix} < 0 \quad (\text{A.24})$$

with

$$\begin{aligned} \hat{\mathbf{A}}(\boldsymbol{\rho}) &= \mathbf{A}(\boldsymbol{\rho}) - \mathbf{B}_2(\boldsymbol{\rho}) \mathbf{C}_{12}(\boldsymbol{\rho}), \\ \mathbf{H}_{B_2}(\boldsymbol{\rho}) &= \mathbf{B}_2(\boldsymbol{\rho}) \mathbf{B}_2^T(\boldsymbol{\rho}), \\ \partial \mathbf{X}(\boldsymbol{\rho}) &= \sum_{i=1}^{n_\rho} \pm \left(\frac{\partial \mathbf{X}(\boldsymbol{\rho})}{\partial \rho_i} \rho_{\max, i} \right). \end{aligned}$$

Proof. The proof of Theorem A.2 can be found in Wu (1995, p. 72 ff.). \square

As shown during the proof of Theorem A.2, the resulting state-feedback controller naturally takes on the parameter-dependent state-feedback gain $\mathbf{F}(\boldsymbol{\rho})$ given by

$$\mathbf{F}(\boldsymbol{\rho}) = -(\gamma^2 \mathbf{B}_2^T(\boldsymbol{\rho}) \mathbf{Z}(\boldsymbol{\rho}) + \mathbf{C}_{12}(\boldsymbol{\rho})) = -(\mathbf{B}_2^T(\boldsymbol{\rho}) \mathbf{X}^{-1}(\boldsymbol{\rho}) + \mathbf{C}_{12}(\boldsymbol{\rho})), \quad (\text{A.25})$$

with $\mathbf{X}(\boldsymbol{\rho}) = \gamma^{-2} \mathbf{Z}^{-1}(\boldsymbol{\rho})$. In contrast to the general LPV controller of Definition A.12, the optimal state-feedback gain $\mathbf{F}(\boldsymbol{\rho})$ does not depend on derivatives of the scheduling parameters. The state-feedback gain $\mathbf{F}(\boldsymbol{\rho})$ of the original state-feedback problem given in (A.21) is obtained from (A.25) by undoing the transformation of the control signal which yields

$$\mathbf{F}(\boldsymbol{\rho}) = -(\mathbf{D}_{12}^T(\boldsymbol{\rho}) \mathbf{D}_{12}(\boldsymbol{\rho}))^{-1} (\gamma^2 \mathbf{B}_2^T(\boldsymbol{\rho}) \mathbf{Z}(\boldsymbol{\rho}) + \mathbf{D}_{12}^T(\boldsymbol{\rho}) \mathbf{C}_1(\boldsymbol{\rho})). \quad (\text{A.26})$$

A.4.2 State-Observer Problem

This section presents the state-observer problem and shows the duality between the state-observer problem and the state-feedback problem. The objective of the state-observer problem is to find the observer gain $\mathbf{L}(\boldsymbol{\rho})$ that minimizes the induced L_2 -norm from the disturbances \mathbf{d} to the weighted observation errors $\Delta \mathbf{e}$ of the closed-loop system $\Gamma_{\Delta ed}(\mathbf{P}_o, \mathbf{O})$. The considered observer \mathbf{O} features the structure of a classical Luenberger observer given by

$$\dot{\hat{\mathbf{x}}} = (\mathbf{A}(\boldsymbol{\rho}) - \mathbf{L}(\boldsymbol{\rho}) \mathbf{C}_2(\boldsymbol{\rho})) \hat{\mathbf{x}} + \mathbf{L}(\boldsymbol{\rho}) \mathbf{y} + \mathbf{B}_2(\boldsymbol{\rho}) \mathbf{u} \quad (\text{A.27a})$$

$$\hat{\mathbf{y}} = \mathbf{C}_2(\boldsymbol{\rho}) \hat{\mathbf{x}}, \quad (\text{A.27b})$$

with the matrices $\mathbf{A}(\rho)$, $\mathbf{B}_2(\rho)$ and $\mathbf{C}_2(\rho)$ as defined in the general plant (A.10) and satisfying assumption (a5).

The differential error equation of the observer can be derived by substituting the derivative of the plant state $\dot{\mathbf{x}}$ and the derivative of the observer state $\dot{\hat{\mathbf{x}}}$ into $\Delta\dot{\mathbf{x}} = \dot{\mathbf{x}} - \dot{\hat{\mathbf{x}}}$. The resulting differential error equation is given by

$$\Delta\dot{\mathbf{x}} = (\mathbf{A}(\rho) + \mathbf{L}(\rho) \mathbf{C}_2(\rho)) \Delta\mathbf{x} + \mathbf{B}_1(\rho) \mathbf{d} + \mathbf{L}(\rho) \mathbf{D}_{21}(\rho) \mathbf{d} \quad (\text{A.28a})$$

$$\Delta\mathbf{y} = \mathbf{C}_2(\rho) \Delta\mathbf{x}. \quad (\text{A.28b})$$

Next, the differential error equation can be used to formulate the observer design prob-

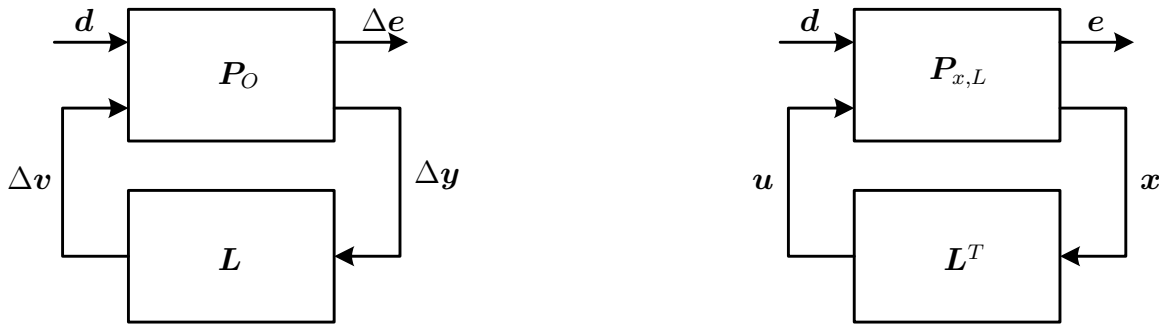


Figure A.4: General control configuration state-observer problem

lem in the general control framework as illustrated in Figure A.4-left. In this configuration, the observation error $\Delta\mathbf{y}$ multiplied with the observer gain $\mathbf{L}(\rho)$ yields the state correction $\Delta\mathbf{v}$ according to

$$\Delta\mathbf{v} = \mathbf{L}(\rho) \Delta\mathbf{y} = \mathbf{L}(\rho) (\mathbf{C}_2(\rho) \Delta\mathbf{x} + \mathbf{D}_{21}(\rho) \mathbf{d}). \quad (\text{A.29})$$

The generalized plant \mathbf{P}_o of the observer problem can be stated as

$$\begin{bmatrix} \Delta\dot{\mathbf{x}} \\ \Delta\mathbf{e} \\ \Delta\mathbf{y} \end{bmatrix} = \begin{bmatrix} \mathbf{A}(\rho) & \mathbf{B}_1(\rho) & \mathbf{I} \\ \mathbf{C}_1(\rho) & \mathbf{0} & \mathbf{0} \\ \mathbf{C}_2(\rho) & \mathbf{D}_{21}(\rho) & \mathbf{0} \end{bmatrix} \begin{bmatrix} \Delta\mathbf{x} \\ \mathbf{d} \\ \Delta\mathbf{v} \end{bmatrix}. \quad (\text{A.30})$$

From the general results on duality for LTV systems presented in Kalman (1963, p. 163), duality of the LPV state-observer problem and the LPV state-feedback problem follows as special case. A discussion of duality of state-feedback and state-observation for LTI systems can be found e.g. in Zhou et al. (1996, p. 295 ff.). Duality means, that the state-observer problem can be reformulated as a state-feedback problem, see Figure A.4 - right. The duality becomes clear by comparing the state-feedback and the state-observer conditions derived from the Bounded Real Lemma given in Theorem A.9. In the following the conditions for quadratic stability are considered for simplicity, duality for parameter-dependent stability can be shown in an analogous manner. The Schur

complement (Amato, 2006, p. 178) of the state-feedback condition in (A.22) can be expressed as

$$\mathbf{A}_F^T(\boldsymbol{\rho}) \mathbf{Z}(\boldsymbol{\rho}) + \mathbf{Z}(\boldsymbol{\rho}) \mathbf{A}_F(\boldsymbol{\rho}) + \gamma^{-2} \mathbf{C}_F^T(\boldsymbol{\rho}) \mathbf{C}_F(\boldsymbol{\rho}) + \mathbf{Z}(\boldsymbol{\rho}) \mathbf{B}_1(\boldsymbol{\rho}) \mathbf{B}_1^T(\boldsymbol{\rho}) \mathbf{Z}(\boldsymbol{\rho}) < 0. \quad (\text{A.31})$$

In the same way, the Schur complement of the state-observer condition derived by substituting $\boldsymbol{\Gamma}_{\Delta ed}(\mathbf{P}, \mathbf{O})$ into the Bounded Real Lemma in Theorem A.9 is given by

$$\mathbf{A}_L^T(\boldsymbol{\rho}) \mathbf{V}(\boldsymbol{\rho}) + \mathbf{V}(\boldsymbol{\rho}) \mathbf{A}_L(\boldsymbol{\rho}) + \gamma^{-2} \mathbf{C}_1^T(\boldsymbol{\rho}) \mathbf{C}_1(\boldsymbol{\rho}) + \mathbf{V}(\boldsymbol{\rho}) \mathbf{B}_L(\boldsymbol{\rho}) \mathbf{B}_L^T(\boldsymbol{\rho}) \mathbf{V}(\boldsymbol{\rho}) < 0, \quad (\text{A.32})$$

with $\mathbf{A}_L^T(\boldsymbol{\rho}) = \mathbf{A}(\boldsymbol{\rho}) + \mathbf{L}(\boldsymbol{\rho}) \mathbf{C}_2(\boldsymbol{\rho})$ and $\mathbf{B}_L^T(\boldsymbol{\rho}) = \mathbf{B}_1(\boldsymbol{\rho}) + \mathbf{L}(\boldsymbol{\rho}) \mathbf{D}_{21}(\boldsymbol{\rho})$. After left-right multiplication of (A.32) with $\gamma^{-1} \mathbf{V}^{-1}(\boldsymbol{\rho})$ and substitution of $\gamma^{-1} \mathbf{V}^{-1}(\boldsymbol{\rho})$ with $\gamma^{-1} \mathbf{V}^{-1}(\boldsymbol{\rho}) = \mathbf{Z}(\boldsymbol{\rho})$, (A.32) can be reformulated as

$$\mathbf{A}_L(\boldsymbol{\rho}) \mathbf{Z}(\boldsymbol{\rho}) + \mathbf{Z}(\boldsymbol{\rho}) \mathbf{A}_L^T(\boldsymbol{\rho}) + \gamma^{-2} \mathbf{B}_L(\boldsymbol{\rho}) \mathbf{B}_L^T(\boldsymbol{\rho}) + \mathbf{Z}(\boldsymbol{\rho}) \mathbf{C}_1^T(\boldsymbol{\rho}) \mathbf{C}_1(\boldsymbol{\rho}) \mathbf{Z}(\boldsymbol{\rho}) < 0. \quad (\text{A.33})$$

A comparison of the latter state-observer condition (A.33) and the state-feedback condition in (A.31) reveals that the state-observer problem can be solved as state-feedback problem by substituting

$$\mathbf{A}_F(\boldsymbol{\rho}) = \mathbf{A}_L^T(\boldsymbol{\rho}) \quad (\text{A.34a})$$

$$\mathbf{B}_1(\boldsymbol{\rho}) = \mathbf{C}_1^T(\boldsymbol{\rho}) \quad (\text{A.34b})$$

$$\mathbf{C}_F(\boldsymbol{\rho}) = \mathbf{B}_L^T(\boldsymbol{\rho}). \quad (\text{A.34c})$$

into the state-feedback problem. The solution of the modified state-feedback problem is the transpose observer gain $\mathbf{L}^T(\boldsymbol{\rho})$.

A.4.3 Separation Principle

In LTI system theory, the separation principle states that any combination of a stable state-observer and a stable state-feedback controller yields a stable closed-loop system as described in Aström and Murray (2008, p. 211 ff.). This property of observer-based state-feedback controllers can be generalized to LPV systems as shown in Wu (1995, p. 36 ff.). The separation principle for LPV systems is summarized in the following theorem:

Theorem A.3 (Separation principle of LPV systems). *Given the LPV system \mathbf{P} in (A.10) satisfying assumptions (a1) - (a5). The observer-based state-feedback controller \mathbf{K}_{OS} given by*

$$\begin{bmatrix} \dot{\hat{\mathbf{x}}} \\ \mathbf{u} \end{bmatrix} = \begin{bmatrix} \mathbf{A}(\boldsymbol{\rho}) + \mathbf{B}_2(\boldsymbol{\rho}) \mathbf{F}(\boldsymbol{\rho}) - \mathbf{L}(\boldsymbol{\rho}) \mathbf{C}_2(\boldsymbol{\rho}) & \mathbf{L}(\boldsymbol{\rho}) \\ \mathbf{F}(\boldsymbol{\rho}) & \mathbf{0} \end{bmatrix} \begin{bmatrix} \hat{\mathbf{x}} \\ \mathbf{y} \end{bmatrix}, \quad (\text{A.35})$$

comprised of a state-feedback controller \mathbf{K}_x with state-feedback gain $\mathbf{F}(\boldsymbol{\rho})$ and a state-observer \mathbf{O} with state-observer gain $\mathbf{L}(\boldsymbol{\rho})$, parameter-dependently stabilizes the closed-loop system $\boldsymbol{\Gamma}_{ed}(\mathbf{P}, \mathbf{K}_{OS})$ for all $\boldsymbol{\rho} \in \mathcal{P}$ and $|\beta_i| \leq \dot{\rho}_{\max, i} \quad \forall i \in \{1, 2, \dots, n_\rho\}$,

(a) if and only if the closed-loop with state-feedback $\Gamma_{ed}(\mathbf{P}_x, \mathbf{K}_x)$ is parameter-dependent stable, i.e. there exists a continuously differentiable matrix function $\mathbf{Z}(\boldsymbol{\rho}) \in \mathcal{C}_1(\mathbb{R}^{n_\rho}, \mathbb{R}^{n_x \times n_x})$ with $\mathbf{Z}(\boldsymbol{\rho}) > 0$ such that $\mathbf{A}_F(\boldsymbol{\rho}) = \mathbf{A}(\boldsymbol{\rho}) + \mathbf{B}_2(\boldsymbol{\rho}) \mathbf{F}(\boldsymbol{\rho})$ and $\mathbf{Z}(\boldsymbol{\rho})$ satisfy condition (A.7) of Definition A.3 for all $\boldsymbol{\rho} \in \mathcal{P}$ and $|\beta_i| \leq \dot{\rho}_{\max,i} \quad \forall i \in \{1, 2, \dots, n_\rho\}$, and

(b) if and only if the observation error dynamics is parameter-dependent stable, i.e. there exists a continuously differentiable matrix function $\mathbf{V}(\boldsymbol{\rho}) \in \mathcal{C}_1(\mathbb{R}^{n_\rho}, \mathbb{R}^{n_x \times n_x})$ with $\mathbf{V}(\boldsymbol{\rho}) > 0$ such that $\mathbf{A}_L(\boldsymbol{\rho}) = \mathbf{A}(\boldsymbol{\rho}) - \mathbf{L}(\boldsymbol{\rho}) \mathbf{C}_2(\boldsymbol{\rho})$ and $\mathbf{V}(\boldsymbol{\rho})$ satisfy condition (A.7) of Definition A.3 for all $\boldsymbol{\rho} \in \mathcal{P}$ and $|\beta_i| \leq \dot{\rho}_{\max,i} \quad \forall i \in \{1, 2, \dots, n_\rho\}$.

Proof. The closed-loop system $\Gamma_{ed}(\mathbf{P}, \mathbf{K}_{OS})$ can be expressed by

$$\begin{bmatrix} \dot{\mathbf{x}} \\ \dot{\hat{\mathbf{x}}} \\ \mathbf{e} \end{bmatrix} = \left[\begin{array}{cc|c} \mathbf{A}(\boldsymbol{\rho}) & \mathbf{B}_2(\boldsymbol{\rho}) \mathbf{F}(\boldsymbol{\rho}) & \mathbf{B}_1(\boldsymbol{\rho}) \\ \mathbf{L}(\boldsymbol{\rho}) \mathbf{C}_2(\boldsymbol{\rho}) & \mathbf{A}(\boldsymbol{\rho}) + \mathbf{B}_2(\boldsymbol{\rho}) \mathbf{F}(\boldsymbol{\rho}) - \mathbf{L}(\boldsymbol{\rho}) \mathbf{C}_2(\boldsymbol{\rho}) & \mathbf{L}(\boldsymbol{\rho}) \mathbf{D}_{21}(\boldsymbol{\rho}) \\ \mathbf{C}_1(\boldsymbol{\rho}) & \mathbf{D}_{12}(\boldsymbol{\rho}) \mathbf{F}(\boldsymbol{\rho}) & \mathbf{0} \end{array} \right] \begin{bmatrix} \mathbf{x} \\ \hat{\mathbf{x}} \\ \mathbf{d} \end{bmatrix}. \quad (\text{A.36})$$

Next, the closed-loop dynamics matrix $\mathbf{A}_{\text{clp}}(\boldsymbol{\rho})$ can be brought to a triangular structure by a state transformation according to

$$\begin{bmatrix} \mathbf{x} \\ \boldsymbol{\eta}_K \end{bmatrix} = \begin{bmatrix} \mathbf{I} & \mathbf{0} \\ \mathbf{I} & -\mathbf{I} \end{bmatrix} \begin{bmatrix} \mathbf{x} \\ \mathbf{x}_K \end{bmatrix}. \quad (\text{A.37})$$

The states of the transformed closed-loop are the original open-loop plant state \mathbf{x} and the observation error $\boldsymbol{\eta}_K = \mathbf{x} - \hat{\mathbf{x}}$. The transformed closed-loop system can then be stated as

$$\begin{bmatrix} \dot{\mathbf{x}} \\ \dot{\boldsymbol{\eta}}_K \\ \mathbf{e} \end{bmatrix} = \left[\begin{array}{cc|c} \mathbf{A}(\boldsymbol{\rho}) + \mathbf{B}_2(\boldsymbol{\rho}) \mathbf{F}(\boldsymbol{\rho}) & -\mathbf{B}_2(\boldsymbol{\rho}) \mathbf{F}(\boldsymbol{\rho}) & \mathbf{B}_1(\boldsymbol{\rho}) \\ \mathbf{0} & \mathbf{A}(\boldsymbol{\rho}) + \mathbf{L}(\boldsymbol{\rho}) \mathbf{C}_2(\boldsymbol{\rho}) & \mathbf{H}_\eta(\boldsymbol{\rho}) \\ \mathbf{C}_1(\boldsymbol{\rho}) + \mathbf{D}_{12}(\boldsymbol{\rho}) \mathbf{F}(\boldsymbol{\rho}) & -\mathbf{D}_{12}(\boldsymbol{\rho}) \mathbf{F}(\boldsymbol{\rho}) & \mathbf{0} \end{array} \right] \begin{bmatrix} \mathbf{x} \\ \boldsymbol{\eta}_K \\ \mathbf{d} \end{bmatrix}, \quad (\text{A.38})$$

with $\mathbf{H}_\eta = \mathbf{B}_1(\boldsymbol{\rho}) - \mathbf{L}(\boldsymbol{\rho}) \mathbf{D}_{21}(\boldsymbol{\rho})$. The triangular structure of the closed-loop dynamics matrix $\mathbf{A}_{\text{clp}}(\boldsymbol{\rho})$ in (A.38) lends itself to conclude stability of the closed-loop $\Gamma_{ed}(\mathbf{P}, \mathbf{K}_{OS})$ since the matrices $\mathbf{A}(\boldsymbol{\rho}) + \mathbf{B}_2(\boldsymbol{\rho}) \mathbf{F}(\boldsymbol{\rho})$ and $\mathbf{A}(\boldsymbol{\rho}) + \mathbf{L}(\boldsymbol{\rho}) \mathbf{C}_2(\boldsymbol{\rho})$ are parameter-dependent stable by assumption and the matrix $-\mathbf{B}_2(\boldsymbol{\rho}) \mathbf{F}(\boldsymbol{\rho})$ is norm bounded. \square

Further details regarding the separation principle of LPV systems and a similar proof of Theorem A.3 are provided by Wu (1995, p. 36 ff.) and Amato (2006, p. 124). There exists also extensive literature, see Åström and Kumar (2014, p. 18), on the separation principle regarding linear quadratic Gaussian (LQG) control, i.e. the combination of a Kalman filter with a linear state-feedback controller. A discussion of the separation principle for LTV systems can be found in Kwakernaak and Sivan (1972, p. 378).

A.4.4 Special Control Problem: Disturbance-Information

The Disturbance-Information problem represents a special type of output-feedback control problem. It is extensively discussed in Zhou et al. (1996, p. 297 ff. and p. 423

ff.) and Doyle et al. (1989, p. 837 and p. 844 ff.) together with three corresponding special problems: the Full-Information, the Full-Control and the Output-Estimation problem. In the literature, the Disturbance-Information problem is often referred to as Disturbance-Feedforward problem, e.g. in Zhou et al. (1996), however, to clearly distinguish the feedback control of Chapters 3 and 4 from the feedforward control of Chapter 5, the expression “Feedforward” in the term Disturbance-Feedforward is replaced by “Information” throughout this work. Even though, Zhou et al. (1996) and Doyle et al. (1989) discuss the Disturbance-Information problem for LTI systems, the results can be readily extended to LPV systems as shown in Prempain and Postlethwaite (2001, p. 23) and Saupe (2013, p. 133 ff.). Applications of the Disturbance-Information problem and the Full-Information problem to LPV systems can be found in Prempain and Postlethwaite (2000), Saupe and Pfifer (2011) and Theis et al. (2015).

The state-space realization of a generalized plant \mathbf{P}_{DI} corresponding to a Disturbance-Information problem is given by

$$\begin{bmatrix} \dot{\mathbf{x}} \\ \mathbf{e} \\ \mathbf{y} \end{bmatrix} = \begin{bmatrix} \mathbf{A}(\boldsymbol{\rho}) & \mathbf{B}_1(\boldsymbol{\rho}) & \mathbf{B}_2(\boldsymbol{\rho}) \\ \mathbf{C}_1(\boldsymbol{\rho}) & \mathbf{0} & \mathbf{D}_{12}(\boldsymbol{\rho}) \\ \mathbf{C}_2(\boldsymbol{\rho}) & \mathbf{I} & \mathbf{0} \end{bmatrix} \begin{bmatrix} \mathbf{x} \\ \mathbf{d} \\ \mathbf{u} \end{bmatrix}. \quad (\text{A.39})$$

The DI plant has to satisfy the assumptions

(b1) $(\mathbf{A}(\boldsymbol{\rho}) - \mathbf{B}_1(\boldsymbol{\rho})\mathbf{C}_2(\boldsymbol{\rho}))$ parameter-dependent stable, and

(b2) $\mathbf{D}_{21}(\boldsymbol{\rho}) = \mathbf{I}$,

Assumption (b1) and (b2) can be easily satisfied by properly adjusting the input disturbances \mathbf{d} and their weighting function \mathbf{W}_d illustrated in Figure A.2. In particular, assumption (b2) determines the measurements \mathbf{y} as a linear combination of the system states \mathbf{x} and the disturbances \mathbf{d} according to

$$\mathbf{y} = \mathbf{C}_2(\boldsymbol{\rho})\mathbf{x} + \mathbf{d}, \quad (\text{A.40})$$

such that the disturbances \mathbf{d} have an identity feedthrough to the measurements \mathbf{y} , and assumption (b1) is satisfied if e.g. $\mathbf{B}_1(\boldsymbol{\rho})$ is the state-observer gain of the related state-observer problem. The closed-loop interconnection of plant \mathbf{P}_{DI} with DI controller \mathbf{K}_{DI} is depicted in Figure A.5.

One advantageous property of DI controllers is that they can be constructed by the sequential synthesis of a state-observer and a state-feedback controller as described in Saupe (2013, p. 133 ff.). In contrast to ad-hoc observer-based state-feedback controllers \mathbf{K}_{OS} , discussed in Section A.4.3, DI controllers \mathbf{K}_{DI} achieve a guaranteed performance index γ of the closed-loop system $\boldsymbol{\Gamma}_{ed}(\mathbf{P}_{DI}, \mathbf{K}_{DI})$ equivalently to general output-feedback controllers. This property of DI controllers is stated in the following theorem.

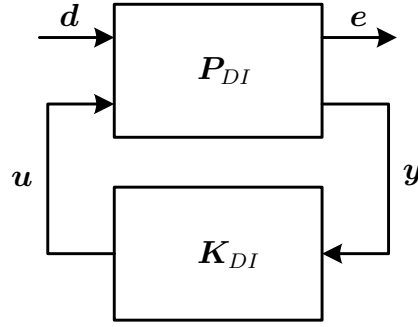


Figure A.5: General control configuration Disturbance-Information (DI) problem

Theorem A.4 (Performance of Disturbance-Information controllers). *Consider the LPV system P_{DI} in (A.39) satisfying assumptions (a1) - (a5) and (b1) - (b2). The DI output-feedback controller K_{DI} given by*

$$\begin{bmatrix} \dot{\mathbf{x}}_K \\ \mathbf{u} \end{bmatrix} = \begin{bmatrix} \mathbf{A}(\rho) + \mathbf{B}_2(\rho) \mathbf{F}(\rho) - \mathbf{B}_1(\rho) \mathbf{C}_2(\rho) & \mathbf{B}_1(\rho) \\ \mathbf{F}(\rho) & \mathbf{0} \end{bmatrix} \begin{bmatrix} \mathbf{x}_K \\ \mathbf{y} \end{bmatrix}, \quad (\text{A.41})$$

comprised of a state-feedback controller K_x with state-feedback gain $\mathbf{F}(\rho)$, parameter-dependently stabilizes the closed-loop system $\Gamma_{ed}(P_{DI}, K_{DI})$ and renders its induced L_2 -norm less than the performance index γ for all $\rho \in \mathcal{P}$ and $|\beta_i| \leq \dot{\rho}_{\max,i} \ \forall i \in \{1, 2, \dots, n_\rho\}$, if and only if the closed-loop with state-feedback $\Gamma_{ed}(P_x, K_x)$ is parameter-dependent stable and its induced L_2 -norm less than the performance index γ , i.e. there exists a continuously differentiable matrix function $\mathbf{Z}(\rho) \in \mathcal{C}_1(\mathbb{R}^{n_\rho}, \mathbb{R}^{n_x \times n_x})$ with $\mathbf{Z}(\rho) > 0$ such that $\mathbf{A}_F(\rho) = \mathbf{A}(\rho) + \mathbf{B}_2(\rho) \mathbf{F}(\rho)$ and $\mathbf{Z}(\rho)$ satisfy condition (A.22) of Definition A.5 for all $\rho \in \mathcal{P}$ and $|\beta_i| \leq \dot{\rho}_{\max,i} \ \forall i \in \{1, 2, \dots, n_\rho\}$.

Proof. The proof of Theorem A.4 uses the state transformation (A.37) introduced as part of the proof of the separation principle in Section A.4.3. After the state transformation, the states of the transformed closed-loop represent the original open-loop plant states \mathbf{x} and the errors between the plant states and the controller states $\boldsymbol{\eta}_K = \mathbf{x} - \mathbf{x}_K$. Due to the structure of the DI controller (A.41), the controller states \mathbf{x}_K can be interpreted as the states of an observer with observer gain $\mathbf{B}_1(\rho)$ and consequently $\boldsymbol{\eta}_K$ corresponds to the observation errors. The transformed closed-loop system can be stated by

$$\begin{bmatrix} \dot{\mathbf{x}} \\ \dot{\boldsymbol{\eta}}_K \\ \mathbf{e} \end{bmatrix} = \left[\begin{array}{cc|c} \mathbf{A}(\rho) + \mathbf{B}_2(\rho) \mathbf{F}(\rho) & -\mathbf{B}_2(\rho) \mathbf{F}(\rho) & \mathbf{B}_1(\rho) \\ \mathbf{0} & \mathbf{A}(\rho) + \mathbf{B}_1(\rho) \mathbf{C}_2(\rho) & \mathbf{0} \\ \hline \mathbf{C}_1(\rho) + \mathbf{D}_{12}(\rho) \mathbf{F}(\rho) & \mathbf{D}_{12}(\rho) \mathbf{F}(\rho) & \mathbf{0} \end{array} \right] \begin{bmatrix} \mathbf{x} \\ \boldsymbol{\eta}_K \\ \mathbf{d} \end{bmatrix}. \quad (\text{A.42})$$

As shown during the proof of the separation principle in Section A.4.3, parameter-dependent stability of the closed-loop system can be easily concluded by exploring the upper triangular structure of the dynamics matrix since stability of $\mathbf{A}(\rho) + \mathbf{B}_1(\rho) \mathbf{C}_2(\rho)$

is guaranteed through assumption (b1) and stability of $\mathbf{A}(\boldsymbol{\rho}) + \mathbf{B}_2(\boldsymbol{\rho})\mathbf{F}(\boldsymbol{\rho})$ is given as $\mathbf{F}(\boldsymbol{\rho})$ is obtained from the solution of the associated state-feedback problem. As stated in Wu (1995, p. 38), the closed-loop system is stable if its dynamics matrix has stable diagonal entries and the off-diagonal matrix is norm bounded.

In contrast to the general closed-loop (A.38) with ad-hoc observer-based state-feedback controller \mathbf{K}_{OS} , the observation errors $\boldsymbol{\eta}_K$ are not affected by the disturbances \mathbf{d} in the closed-loop (A.42) with DI controller due to $\mathbf{H}_\eta = \mathbf{0}$. Consequently, the dynamics of $\boldsymbol{\eta}_K$ have no influence on the induced L_2 -norm of the closed-loop $\|\boldsymbol{\Gamma}_{ed}(\mathbf{P}_{DI}, \mathbf{K}_{DI})\|_{i_2}$ and $\boldsymbol{\eta}_K$ can be removed from the design problem yielding a state-feedback problem with plant \mathbf{P}_x . \square

As described in Skogestad and Postlethwaite (2005, p. 415), controllers with observer-based state-feedback structure have several advantages compared to general output-feedback controllers:

- The functionality of the controller can be described more easily, especially to people who are not familiar with advanced control theory.
- The computational complexity of the controller synthesis is reduced compared to the design of a general output-feedback controller.
- The observer-based state-feedback structure can be exploited during the implementation of the controller.
- The observer can be easily augmented with known disturbance signals.
- The observer can be tuned and verified with measurement data to ensure good performance on the real plant.

In summary these properties make the design of observer-based controllers like ad-hoc observer-based state-feedback controllers or DI controllers very attractive in complex applications, e.g. in applications which require high-order plant models.

Remark. Even though, the choice of input weights \mathbf{W}_d of a DI problem is not restricted to weights yielding the disturbance input matrix $\mathbf{B}_1(\boldsymbol{\rho})$ equal to a precalculated state-observer gain $\mathbf{L}(\boldsymbol{\rho})$, this selection of the input weight is natural due to the structure of the resulting controller.

Remark. As discussed in Skogestad and Postlethwaite (2005, p. 409) and Sefton and Glover (1990, p. 303) for LTI systems, observer-based state-feedback controllers have the particularly nice property not to be subject to pole-zero cancellations in the closed-loop system. This can also be concluded from the remarks on poles and zeros in Skogestad and Postlethwaite (2005, p. 141 and p. 146 item 7). There the authors state that systems with outputs containing direct information about the full state vector, i.e. $\mathbf{C}_2 = \mathbf{I}$ and $\mathbf{D}_{22} = \mathbf{0}$, have no zeros.

A.4.5 Special Control Problem: Full-Information

The Full-Information problem represents a special type of control problem where the plant states \mathbf{x} and the disturbances \mathbf{d} are available as measurements. As shown in Zhou et al. (1996, p. 297 ff. and p. 423 ff.) and Doyle et al. (1989, p. 837 and p. 844 ff.), the Full-Information problem is equivalent to the Disturbance-Information problem in the sense that the closed-loop interconnections of the FI plant \mathbf{P}_{FI} with FI controller \mathbf{K}_{FI} depicted in Figure A.6 and the closed-loop interconnections of the DI plant \mathbf{P}_{DI} with the DI controller \mathbf{K}_{DI} depicted in Figure A.5 result in equivalent closed-loop systems

$$\Gamma_{ed}(\mathbf{P}_{FI}, \mathbf{K}_{FI}) = \Gamma_{ed}(\mathbf{P}_{DI}, \mathbf{K}_{DI}), \quad (\text{A.43})$$

if the initial conditions of plant and controller are identical.

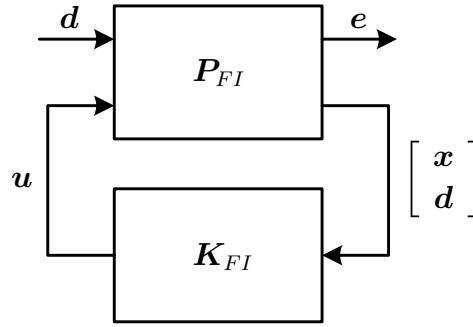


Figure A.6: General control configuration Full-Information (FI) problem

The generalized plant \mathbf{P}_{FI} corresponding to the general control configuration depicted in Figure A.6 can be expressed by

$$\begin{bmatrix} \dot{\mathbf{x}} \\ \mathbf{e} \\ \begin{bmatrix} \mathbf{x} \\ \mathbf{d} \end{bmatrix} \end{bmatrix} = \begin{bmatrix} \mathbf{A}(\rho) & \mathbf{B}_1(\rho) & \mathbf{B}_2(\rho) \\ \mathbf{C}_1(\rho) & \mathbf{0} & \mathbf{D}_{12}(\rho) \\ \begin{bmatrix} \mathbf{I} \\ \mathbf{0} \end{bmatrix} & \begin{bmatrix} \mathbf{0} \\ \mathbf{I} \end{bmatrix} & \begin{bmatrix} \mathbf{0} \\ \mathbf{0} \end{bmatrix} \end{bmatrix} \begin{bmatrix} \mathbf{x} \\ \mathbf{d} \\ \mathbf{u} \end{bmatrix}, \quad (\text{A.44})$$

with the general assumptions (a1) - (a4) and the specific FI assumptions:

(c1) $(\mathbf{A}(\rho), \mathbf{B}_1(\rho))$ parameter-dependent stabilizable, and

(c2) $\mathbf{C}_2(\rho) = [\mathbf{I} \ \mathbf{0}]^T$, $\mathbf{D}_{21}(\rho) = [\mathbf{0} \ \mathbf{I}]^T$.

Figure A.7 further emphasizes the equivalence of the FI and the DI problem by illustrating the interconnection of both problems. The DI controller \mathbf{K}_{DI} can be expressed as the interconnection of the FI controller \mathbf{K}_{FI} with the dynamical system \mathbf{V}_O according to

$$\mathbf{K}_{DI} = \mathbf{K}_{FI} \mathbf{V}_O. \quad (\text{A.45})$$

The system \mathbf{V}_O given by

$$\begin{bmatrix} \dot{\mathbf{x}} \\ \mathbf{x} \\ \mathbf{d} \end{bmatrix} = \left[\begin{array}{c|cc} \mathbf{A}(\rho) - \mathbf{B}_1(\rho)\mathbf{C}_2(\rho) & \mathbf{B}_1(\rho) & \mathbf{B}_2(\rho) \\ \hline \mathbf{I} & \mathbf{0} & \mathbf{0} \\ -\mathbf{C}_2(\rho) & \mathbf{I} & \mathbf{0} \end{array} \right] \begin{bmatrix} \mathbf{x} \\ \mathbf{y} \\ \mathbf{u} \end{bmatrix}. \quad (\text{A.46})$$

calculates the system states \mathbf{x} and disturbances \mathbf{d} from the measurements \mathbf{y} and control signals \mathbf{u} . Depending on the interpretation of Figure A.7 as FI problem or DI problem \mathbf{V}_O is part of the plant forming \mathbf{P}_{FI} or integrated into the DI controller forming \mathbf{K}_{DI} . In the latter case, \mathbf{V}_O represents an observer estimating the system states \mathbf{x} and disturbances \mathbf{d} .

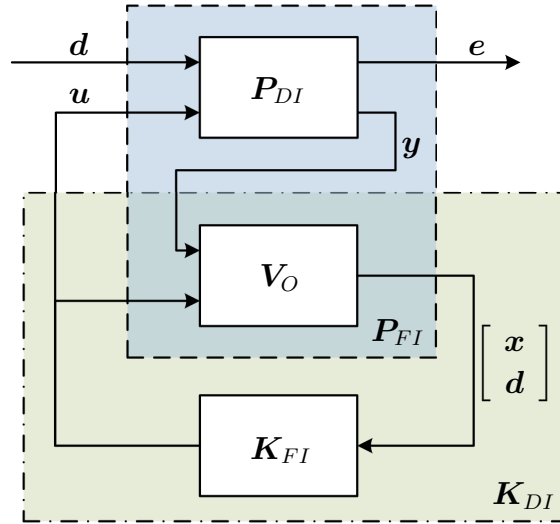


Figure A.7: Equivalence of Full-Information controller \mathbf{K}_{FI} and Disturbance-Information controller \mathbf{K}_{DI}

Conversely, the FI controller \mathbf{K}_{FI} can be computed from the DI controller \mathbf{K}_{DI} according to

$$\mathbf{K}_{FI} = \mathbf{K}_{DI} [\mathbf{C}_2(\rho) \ \mathbf{I}], \quad (\text{A.47})$$

with $\mathbf{C}_2(\rho)$ of the DI plant in (A.39). Moreover as shown in Prempain and Postlethwaite (2001, p. 22), for proper FI plants like (A.44), i.e. with $\mathbf{D}_{11} = \mathbf{0}$, the FI controller \mathbf{K}_{FI} can be designed via a pure state-feedback synthesis and therefore reduces to

$$\mathbf{K}_{FI} = [\mathbf{F}(\rho) \ \mathbf{0}]. \quad (\text{A.48})$$

Of course, this result corresponds to the expectation due to the equivalence between FI and DI controllers which naturally implies that if the DI controller can be designed by a state-feedback synthesis, likewise can the FI controller.

A.4.6 Computational Considerations

As mentioned in the introduction of this chapter, the LPV control design presented in this thesis pursues a gridding approach as proposed in Wu (1995, p. 87 ff.) and Wu et al. (1996, p. 993 ff.). This LPV approach is applicable to a large variety of nonlinear control problems and in particular does not impose as restrictive assumptions on the LPV plants as polytopic LPV methods. The gridding-based LPV control approach has been implemented in the MATLAB toolbox LPVTools by Hjartarson et al. (2013, 2015).

As discussed in Wu (1995, p. 87 ff.), the gridding approach involves two approximation steps to formulate the controller synthesis as a tractable convex optimization problem. Firstly, the infinite dimensional function space of the parameter-dependent Lyapunov function has to be approximated with a finite number of basis functions and secondly the infinite dimensional scheduling parameter space \mathcal{P} has to be approximated with a finite number of grid points. The grid density employed during the controller synthesis is crucial for a successful control design. Unfortunately, there is a design conflict between the accuracy of the approximation of the scheduling parameter space and the computational cost of the controller synthesis. Hence, the required grid density constitutes an important design parameter and is generally determined during a preliminary analysis. This preliminary analysis is usually as simple as a variation of the grid density from loose to dense until the induced L_2 -norm stays almost the same. The controller design is then performed as a two-stage process: firstly the tuning parameters are determined with a rather loose grid and subsequently the controller is verified with the required high grid density.

The main drawback of the gridding-based LPV methods arises from the complexity of the controller synthesis and implementation. This is obvious because the number of grid points h_P of the overall grid of an LPV plant \mathbf{P} is determined by

$$h_P = \prod_{i=1}^{n_\rho} h_i \quad (\text{A.49})$$

with the number of grid points h_i of scheduling parameter ρ_i . For example, the optimization of a state-feedback controller with constant Lyapunov function consists of h_P LMIs as given in (A.24). Additionally, if a parameter-dependent Lyapunov function $\mathbf{X}(\boldsymbol{\rho})$ is employed, the worst-case partial derivative of the Lyapunov matrix $\partial \mathbf{X}(\boldsymbol{\rho})$ has to be determined at each grid point. Unfortunately, the worst-case of $\partial \mathbf{X}(\boldsymbol{\rho})$ is unknown, but can be found by evaluating $\partial \mathbf{X}(\boldsymbol{\rho})$ at all vertices of the polytope formed by the maximum rates of the scheduling parameters $\dot{\rho}_{\max,i} \forall i \in \{1, 2, \dots, n_\rho\}$. Consequently, the number of LMIs of the controller optimization problem with parameter-dependent Lyapunov function is $2^{n_\rho} \times h_P$ and thus 2^{n_ρ} times larger than the number of LMIs of the controller optimization with constant Lyapunov function. The complexity of the controller optimization problem is further increased by the additional decision variables of the coefficient matrices of the basis functions used to approximate the function space of the parameter-dependent Lyapunov function. To illustrate the effect of a parameter-dependent Lyapunov function on

the number of decision variables, an example with linear basis functions is considered

$$\mathbf{X}(\boldsymbol{\rho}) = \mathbf{X}_0 + \rho_1 \mathbf{X}_1 + \dots + \rho_{n_\rho} \mathbf{X}_{n_\rho}. \quad (\text{A.50})$$

Compared to a controller design with constant Lyapunov function \mathbf{X}_0 and n_{d0} decision variables, the number of decision variables in the controller design problem with linear basis functions increases by $n_\rho \times n_{d0}$. The definition of appropriate basis functions is therefore essential for a successful control design exploring the performance benefit of parameter-dependent Lyapunov functions. Up to now, the definition of basis functions relies on the experience of the control engineer as there exists no theoretical rigor in determining the best basis functions.

To sum up, the complexity issues during implementation and synthesis of LPV controllers limit the applicability of LPV control to plants with few scheduling parameters and few states. The applicability can be extended to slightly larger plants with more states and scheduling parameters by designing observer-based state-feedback controllers like the DI controller instead of general output-feedback controllers due to the reduced size of the involved LMIs. A detailed discussion of implementation and synthesis complexity can be found in Hoffmann and Werner (2015, p. 421 ff.).

B Semi-Active Force Actuator

This work employs semi-active force actuators, henceforth called semi-active dampers, to improve ride comfort and road-holding of passenger cars. As ordinary passive dampers, semi-active dampers are subject to the passivity constraint, meaning that they cannot inject energy to the suspension system. This property distinguishes semi-active suspensions from active ones, which feature pneumatic, hydraulic or electro-mechanic force actuators and are able to lift the vehicle. Table B.1 gives a comparison between passive, semi-active and active suspensions regarding their most vital properties from a control perspective similar to Fischer and Isermann (2004, p. 1356) and Savaresi et al. (2010, p. 24). Current state-of-the-art semi-active dampers have high bandwidths of up to 100 Hz and large controllable areas bounded by their minimum and maximum force curves (denoted by the black dashed lines in the figures in Table B.1). They offer a significant potential to mitigate the design conflict between ride comfort and road-holding and thus improve the overall performance. In contrast to active suspensions, however, semi-active suspensions cannot achieve an equal performance and moreover cannot provide additional functionality like load-leveling.

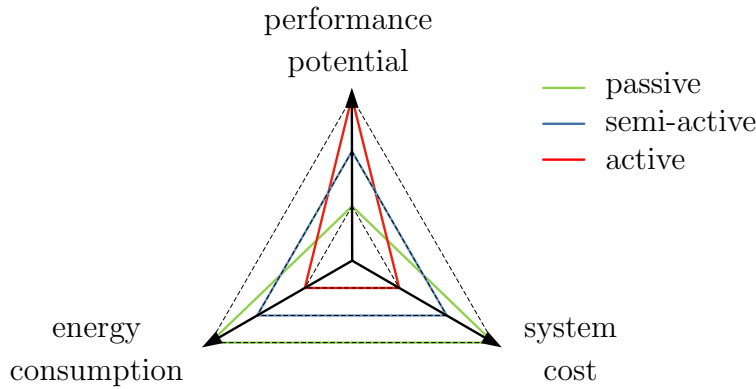
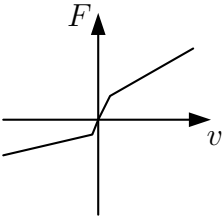
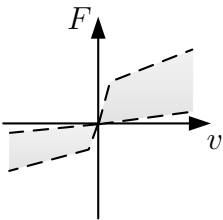
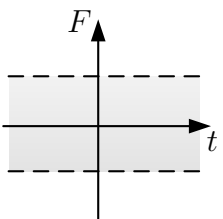
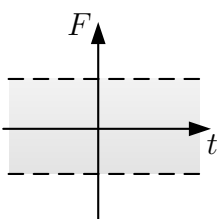


Figure B.1: Conflict triangle of suspension types; large values indicate better performance, lower energy consumption and lower system cost

Figure B.1 illustrates the conflict triangle consisting of performance potential, energy consumption and system cost of passive, semi-active and active suspensions. Compared to active suspensions, semi-active suspensions provide much better performance-to-cost and performance-to-energy consumption trade-offs. This makes their integration in passenger cars very attractive and has contributed to their wide spreading in the automotive market. Additionally, semi-active suspensions can be combined with a slowly-active suspension to exploit their complementary properties and achieve a similar performance than a fully-active suspension, but with lower system cost and energy consumption (Koch et al., 2010).

Table B.1: Classification of electronically controlled suspensions

Suspension type	Force constraint	Actuator bandwidth	Power request	Performance potential
passive		-	0 W	o
semi-active		20-100 Hz	< 50 W	++
slowly active		1-5 Hz	< 5 kW	+
fully active		20-30 kW	5-10 kW	+++

B.1 Semi-Active Damper Technology

Automotive industry and academia to-date investigate three types of semi-active damper technologies:

- electro-hydraulic (EH) dampers: these dampers are equipped with an solenoid valve to modify the cross section in the orifice and hence change its flow resistance,
- magneto-rheologic (MR) dampers: these dampers are equipped with a solenoid which generates a magnetic field to modify the viscosity of the MR fluid and hence change the flow resistance in the orifices,
- electro-rheologic (ER) dampers: these dampers are equipped with a parallel-tube

condensator which generates an electric field to modify the viscosity of the ER fluid and hence change the flow resistance in the orifices.

The dampers employed for the experiments in this work are EH dampers. Therefore, this section briefly explains their principle structure and function. On the left-hand side Figure B.2 shows a mono-tube EH damper with a controllable piston valve and on the right-hand side Figure B.2 shows a mono-tube EH damper with a controllable external valve. The main difference regarding the controlled solenoid valve between the damper with the internal controlled valve and the external controlled valve is the oil flow direction. The flow through the internal solenoid valve goes in both directions depending on the current damper state, e.g. compression or rebound, while the flow through the external solenoid valve goes only in one direction independent of the current damper state. This property allows to specifically optimize the external valve for its flow direction and simplifies the design of the solenoid valve. The drawbacks of course are the additional space required by the housing of the external valve as obvious from Figure B.2 and the larger oil flow distances between the compression and rebound cambers.

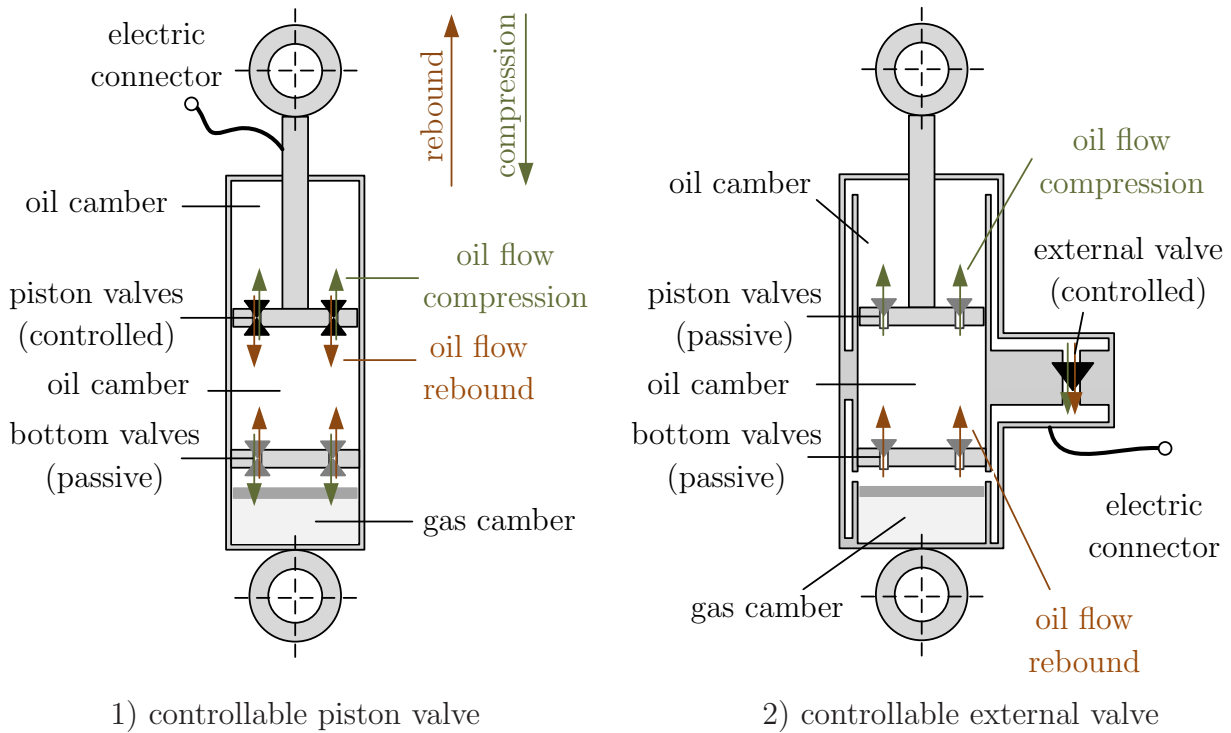


Figure B.2: Schematic of semi-active dampers with controllable electro-hydraulic valves

B.2 Semi-Active Damper Model

The common component models for semi-active dampers can be separated into the following groups depending on the kind of modeling:

- full physical models: these models consist of detailed models of the mechanic, electric and hydraulic subsystems. The hydraulic subsystem constitutes the most involved part due to the complex fluid flow, especially through the passive and controlled valves,
- semi-physical models: these models partly cover the mechanic and electric subsystem and approximate the hydraulic subsystem by an empirical model, and
- black-box models: these models are purely empirical models without any physical insight.

Descriptions of a physical damper models can be found in Duym et al. (1997) and Duym (2000). These models are useful during damper design to facilitate the layout of the fluid flow, especially of the orifices, however, their computational complexity makes them inappropriate for control design. Conversely, semi-physical and black-box models feature a drastically reduced computational complexity, while still accurately modeling the input-output behavior of the semi-active damper. An extensive overview of semi-physical models can be found in Spencer et al. (1997) and Butz and von Stryk (2001). These two papers give an introduction to semi-active damper modeling and describe several semi-physical models like the Bingham and the Bouc-Wen damper models. A simple semi-physical look-up table based damper model is developed in Unger (2012). The authors in Savaresi et al. (2005) develop a black-box damper model based on a nonlinear autoregressive exogenous (ARX) description and show that the ARX model slightly outperforms a Bouc-Wen model according to Spencer et al. (1997).

This work does not develop new damper models. Nevertheless, the suitability of existing damper models for the forthcoming semi-active damper control design has been investigated during the preliminary study presented in Fleps-Dezasse et al. (2014). The crucial selection criteria for the damper model are:

- appropriate accuracy of the control input to force output behavior, in particular, coverage of the asymmetric compression and rebound characteristic of state-of-the-art automotive dampers,
- easy invertibility of the input-to-output response, and
- real-time capable computational complexity.

These criteria are best met by the extended Bouc-Wen model from Spencer et al. (1997) and a simple look-up table based model as used in Unger (2012). The Bouc-Wen model has been experimentally validated for symmetric compression and rebound characteristics, e.g. in Savaresi et al. (2005) and Guglielmino et al. (2008) and is widely acknowledged to accurately model semi-active dampers. Therefore, the preliminary study in Fleps-Dezasse et al. (2014) compared a simple look-up table based model with the more sophisticated extended Bouc-Wen model.

The output force of a semi-active damper is a function of the control signal u_d , in case of an EH-damper the current through the solenoid valve, and the damper states x_{damper} . The most important damper state is the damper velocity \dot{x}_d , but also the damper position x_d and acceleration \ddot{x}_d may have a vital effect on the output force, e.g. if the gas volume inside the damper generates significant forces. The output force of a semi-active damper can be mathematically stated by

$$F_d = f(u_d, x_{\text{damper}}). \quad (\text{B.1})$$

The look-up table based damper model, called force map (FM) model, considers only mandatory variables. It treats the damper velocity \dot{x}_d and the control signal u_d as input signals and requires no additional signals such as the damper position and acceleration. Consequently, the force map model approximates the damper force by

$$F_d \approx f_{FM}(u_d, \dot{x}_d). \quad (\text{B.2})$$

The force map damper model f_{FM} stated in (B.2) should also account for the dynamics of the damper force during control signal transients. This is achieved by a proper pre-filtering of the control signal u_d with the transfer function $G_{u_d}(s)$ as proposed in Spencer et al. (1997). The force map model $f_{FM}(u_d, \dot{x}_d)$ with 2D-look-up table $f_{2D}(u_d, \dot{x}_d)$ and constrained control signal $\sigma(u_d)$ can be expressed as

$$f_{FM}(u_d, \dot{x}_d) = f_{2D}(u_d, \dot{x}_d) G_{u_d}(s) \sigma(u_d). \quad (\text{B.3})$$

The saturation function σ is defined as introduced in (2.4). Figure B.3 illustrates a normalized 2D-look-up table $f_{2D}(u_d, \dot{x}_d)$ in a damper force vs damper velocity diagram with incrementally increasing control signal. The 2D-look-up table easily considers

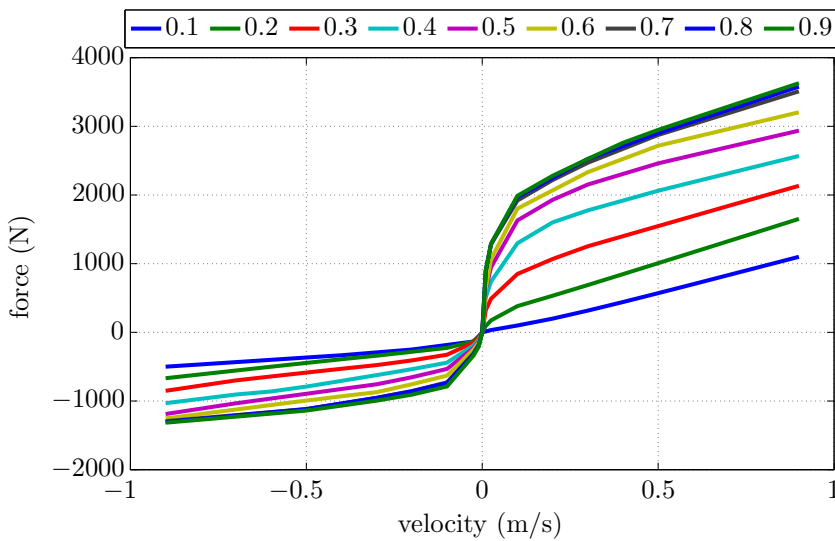


Figure B.3: Force map $f_{2D}(u_d, \dot{x}_d)$ of semi-active damper with normalized control signal $u_d \in [0.1, 0.9]$

- asymmetric compression and rebound forces,
- nonlinear damper force to damper velocity relations, and
- nonlinear damper force to control signal relations.

Due to these properties the force map damper model achieves a similar modeling accuracy as the much more complex extended Bouc-Wen model. The results of the damper model investigation with constant control signals from Fleps-Dezasse et al. (2014) depicted in Appendix B.4 emphasize the high accuracy of the force map model.

B.3 Inverse Semi-Active Damper Model

The controllers developed in this work all generate a demand value F_{sa} for the damper force. The controller output signal F_{sa} is subsequently transformed into the control signal u_d of the semi-active damper by the inverse semi-active damper model $g_{2D}(F_{sa}, \dot{x}_d)$ as depicted by the control structure in Figure 3.1. The inverse semi-active damper model $g_{2D}(F_{sa}, \dot{x}_d)$ is computed from the force map damper model $f_{FM}(u_d, \dot{x}_d)$ by point-wise inverting the damper force map shown in Figure B.3 for each damper velocity grid point i according to

$$u_d = g_{2D}(F_{sa}, \dot{x}_{d,i}) = f_{2D}^{-1}(u_d, \dot{x}_{d,i}) \quad \forall i \in \{1, 2, \dots, n_{\dot{x}_d}\}, \quad (\text{B.4})$$

with $n_{\dot{x}_d}$ the overall number of damper velocity grid points. Figure B.4 illustrates the underlying concept of the control input transformation from the damper control signal u_d to the controller output signal F_{sa} . The computation of the inverse damper model neglects the control signal dynamics $G_{u_d}(s)$ and saturation $\sigma(u_d)$ modeled by the force map damper model $f_{FM}(u_d, \dot{x}_d)$. These two properties of semi-active dampers are directly considered during the LPV control design. Therefore, the inverse damper model is essentially represented by the control signal map shown in Figure B.5. The major

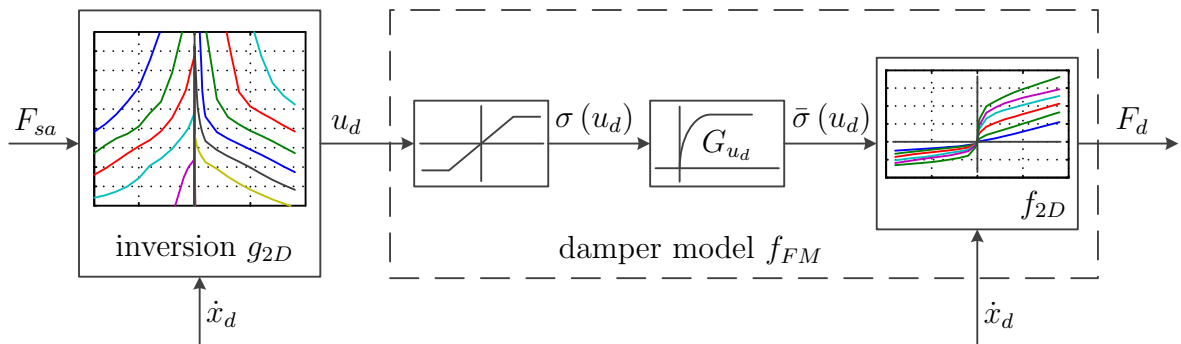


Figure B.4: Inversion of force map damper model

difficulty during the computation of the control signal map $g_{2D}(F_{sa}, \dot{x}_d)$ constitutes the

force singularity of the damper force map depicted in Figure B.3 at zero damper velocity. The inversion (B.4) of the damper force map at zero damper velocity yields an infinite control signal u_d for any controller output F_{sa} . This behavior may be not an issue during simulation due to

$$g_{2D}(F_{sa}, \dot{x}_{d,i}) f_{2D}^{-1}(u_d, \dot{x}_{d,i}) = 1 \quad \forall i \in \{1, 2, \dots, n_{\dot{x}_d}\}, \quad (\text{B.5})$$

in hardware applications, however, such a behavior is not desirable, because the control signal u_d is the physical output of the damper power electronics unit. The increase of the control signal u_d to its maximum near zero damper velocity deteriorates the energy consumption of the semi-active suspension system. Additionally, the ride comfort and road-holding performance are also affected due to the imperfect cancellation between the inverse damper model and the real semi-active damper. Unger (2012, p.101 and 134-135) describes a common approach to overcome this issue by suppressing the control signal u_d near zero damper velocity with a damper velocity dependent scaling. This approach has the drawback that the damper control signal u_d is essentially independent of the controller output F_{sa} near zero damper velocity. In contrast, the control signal map $g_{2D}(F_{sa}, \dot{x}_d)$ depicted in Figure B.5 is computed from a modified force map $f_{2D}(u_d, \dot{x}_d)$ with relaxed singularity. The relaxation is achieved by modifying the force curves of the force map in Figure B.3 such that the force curves have a small offset at zero velocity. As a result, the inverse damper model $g_{2D}(F_{sa}, \dot{x}_d)$ computed from the relaxed force map outputs finite control signals u_d and the inverse damper model requires no additional control signal suppression.

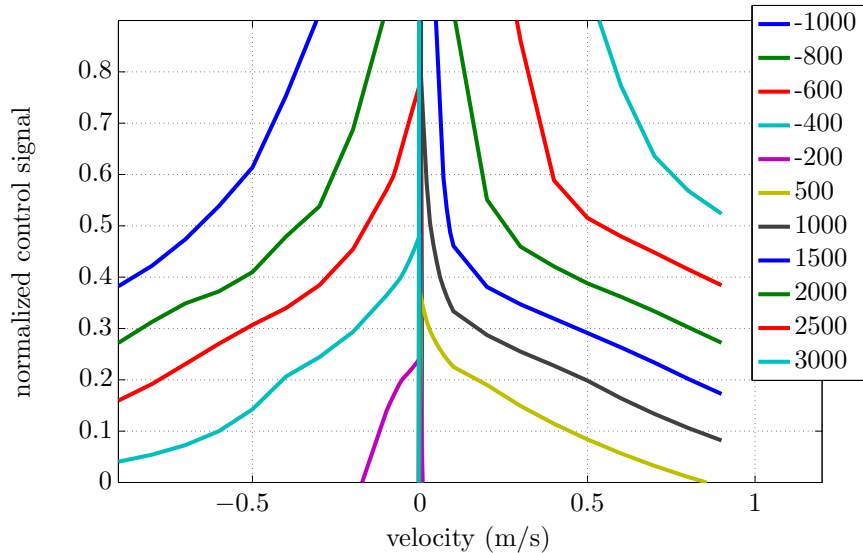


Figure B.5: Control signal map of inverse semi-active damper model $g_{2D}(F_d, \dot{x}_d)$

B.4 Results of Semi-Active Damper Model Assessment

This section presents the results of the Bouc-Wen and force map damper model assessment from Fleps-Dezasse et al. (2014).

The top plots of Figure B.6 show the time series of the damper force if the damper is excited by a sine sweep signal. The control signal is constant during the whole experiment and set to $u_d = 0.1$ on the left plots and to $u_d = 0.5$ on the right ones. The plots in the middle show the same experiments with the damper force plotted over damper deflection and the bottom plots show the damper force plotted over damper velocity. As expected because of the inherent limitation of the force map damper model, the force map model predicts the mean damper force with very high accuracy, but cannot reproduce the hysteresis of the damper. The influence of the hysteresis is particularly obvious for low damper velocities in the plots in Figure B.6-right. Nevertheless, the overall modeling accuracy of the force map model is perfectly sufficient.

The pre-filter $G_{u_d}(s)$ is selected such that the predicted damper force due to control signal changes at constant damper velocities matches the measured damper force. For the EH dampers employed in this work, a first-order low-pass dynamics with input delay represents a sufficiently good approximation of the damper behavior. This is emphasized by the control signal step experiments illustrated in Figure B.7. The left plot in Figure B.7 shows the control signal and the right plot the related damper force measurements and the predicted damper forces by the extended Bouc-Wen and the force map damper model. Due to the appropriate pre-filtering of the control signal with $G_{u_d}(s)$ the damper models achieves a high accuracy during control signals transients.

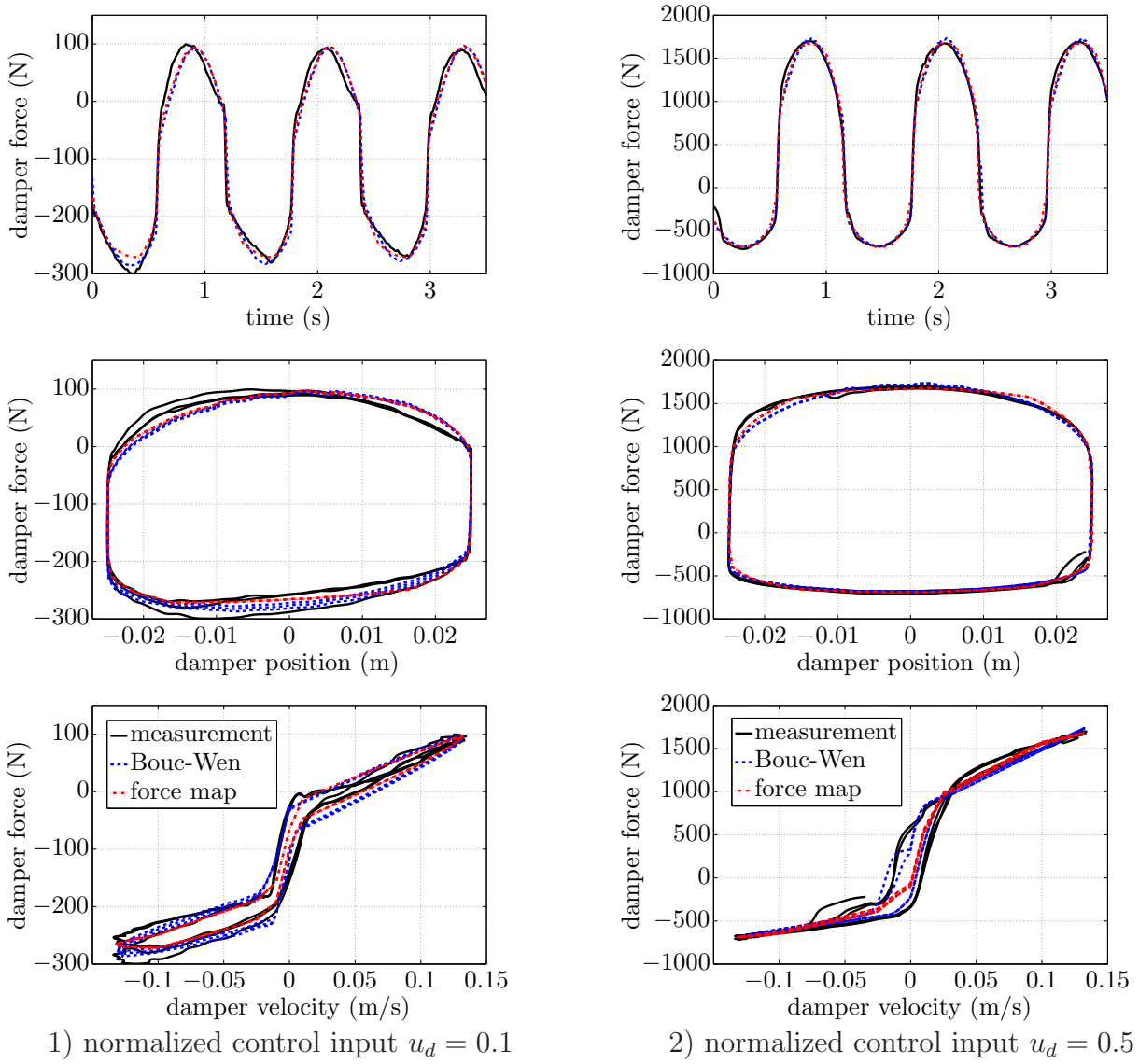


Figure B.6: Accuracy of reproducing measurement data of Bouc-Wen and force map damper models for constant control signals u_d

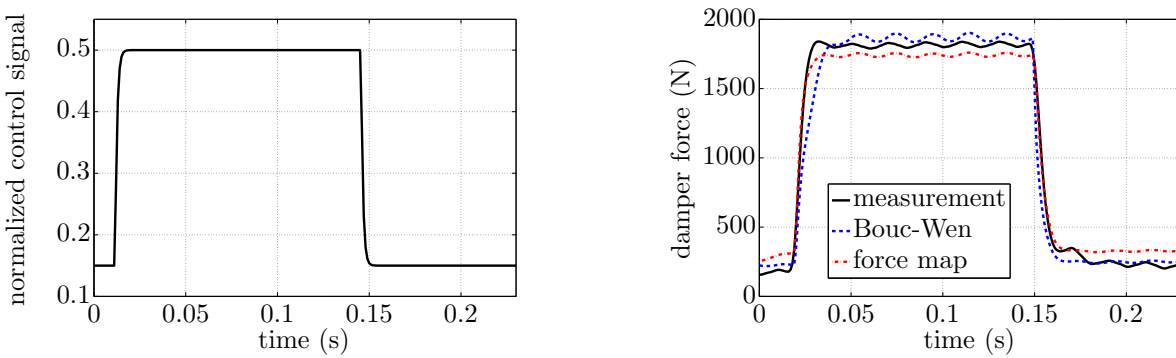


Figure B.7: Accuracy of reproducing control signal steps of Bouc-Wen and force map damper models for constant damper velocities \dot{x}_d

C Vertical Dynamics Road Excitations

Due to the nonlinearities of the semi-active damper, the performance criteria introduced in Section 3.2 not only depend on system properties like body and wheel masses, but strongly depend on road excitation properties like amplitude and frequency spectrum. The dependence on the excitation can be emphasized by considering the damper force curve of a medium constant control signal, e.g. $u_d = 0.3$, of the force map of the semi-active damper depicted in Figure B.3. The degressive damper force behavior leads to a strong damped system behavior for small excitation amplitudes, e.g. if the damper velocities stay below 0.2 m/s. Conversely, the system exhibits a distinct weaker damped behavior if the road excitations yield damper velocities around 1 m/s. A detailed discussion of road excitations relevant for suspension design is presented in Mitschke and Wallentowitz (2004, p. 280 ff.). The most essential road excitations regarding semi-active damper control are stochastic road, sine sweep and bump excitations.

C.1 Stochastic Road Excitation

The evaluation of measured road profile data reported in ISO (8608:1995) shows that road profiles of common roads like highways, country roads and urban roads can be described by stochastic signals with given power spectral density (PSD). Even though the PSD of individual roads is unique, in general as shown in ISO (8608:1995) and Mitschke and Wallentowitz (2004, p. 289 ff.), the PSD $\Phi_h(\Omega)$ of all types of roads can be approximated by a simple formula

$$\Phi_h(\Omega) = \Phi_h(\Omega_0) \left(\frac{\Omega}{\Omega_0} \right)^{-w}. \quad (\text{C.1})$$

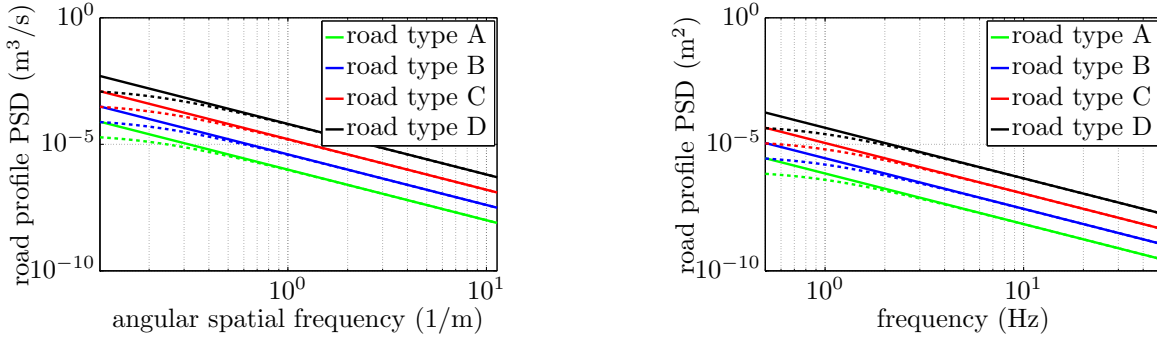
This representation expresses the road profile PSD $\Phi_h(\Omega)$ as a function of the angular spatial frequency Ω . ISO (8608:1995) defines the reference angular spatial frequency $\Omega_0 = 1 \text{ m}^{-1}$ and the exponent $w = 2$ for all road types. The advantage of describing the road profile PSD Φ_h as a function of the angular spatial frequency Ω is that the actual values of the road profile PSD $\Phi_h(\Omega)$ are independent of the vehicle speed v_v . The angular spatial frequency $\Omega = \frac{1}{L}$ is defined as the reciprocal of the wave length L and related to the frequency ω by

$$\omega = v_v \Omega. \quad (\text{C.2})$$

The road profile PSD $\Phi_h(\omega)$ with respect to ω can be computed from $\Phi_h(\Omega)$ according to

$$\Phi_h(\omega) = \frac{1}{v_v} \Phi_h(\Omega). \quad (\text{C.3})$$

Figure C.1 illustrates the approximations of $\Phi_h(\Omega)$ and $\Phi_h(\omega)$ of the road types A - very good, B - good, C - medium and D - bad as defined by ISO (8608:1995). In the double-logarithmic plots both representations of the road profile PSDs show a linear decrease



Road profile PSD as function of the angular spatial frequency Ω

Road profile PSD at a vehicle speed $v_v = 100$ km/h as function of the frequency ω

Figure C.1: Road profile PSD: solid lines - approximated PSD Φ_h according to (C.1); dashed lines approximated PSD $\bar{\Phi}_h$ according to (C.4) with $\beta_r = 0.2$

of the road profile amplitude with increasing frequency. Additionally, the dashed curves in Figure C.1 show a modified approximation $\bar{\Phi}_h$ of the road profile PSD with finite amplitude for $\Omega = 0$ discussed in Mitschke and Wallentowitz (2004, p. 297 ff.). This modified road profile PSD $\bar{\Phi}_h$ is given by

$$\bar{\Phi}_h(\Omega) = \frac{\alpha_r}{\beta_r^2 + \Omega^2}, \quad (\text{C.4})$$

with the parameter $\alpha_r = \Phi_h(\Omega_0)$ and the parameter $\beta_r > 0$. The generation of the plots in Figure C.1 has been done with $\beta_r = 0.2$. The PSD defined by (C.4) can be realized by a first-order low pass filter as shown in Unger (2012, p. 9). This filter can be expressed as a function of the travel distance l_s according to

$$\frac{\delta}{\delta l_s} x_g(l_s) = -\beta_r x_g(l_s) + \sqrt{\alpha_r} \xi(l_s). \quad (\text{C.5})$$

For a given vehicle speed v_v , the travel distance dependent filter in (C.5) can be reformulated as a function of time given by

$$\dot{x}_g = -\beta_r v_v x_g + \sqrt{\alpha_r v_v} \xi. \quad (\text{C.6})$$

The input signal ξ driving the road profile height x_g is a white noise signal with unit PSD. The characterization of stochastic road excitations according to (C.6) will be employed in the following LPV controller design to shape the road disturbance input.

C.2 Sine Sweep Excitation

Experiments with sine sweep excitations provide a means to assess the frequency response of nonlinear systems like semi-active suspension systems. Even though, the frequency response of the suspension system may change depending on the amplitude and frequency

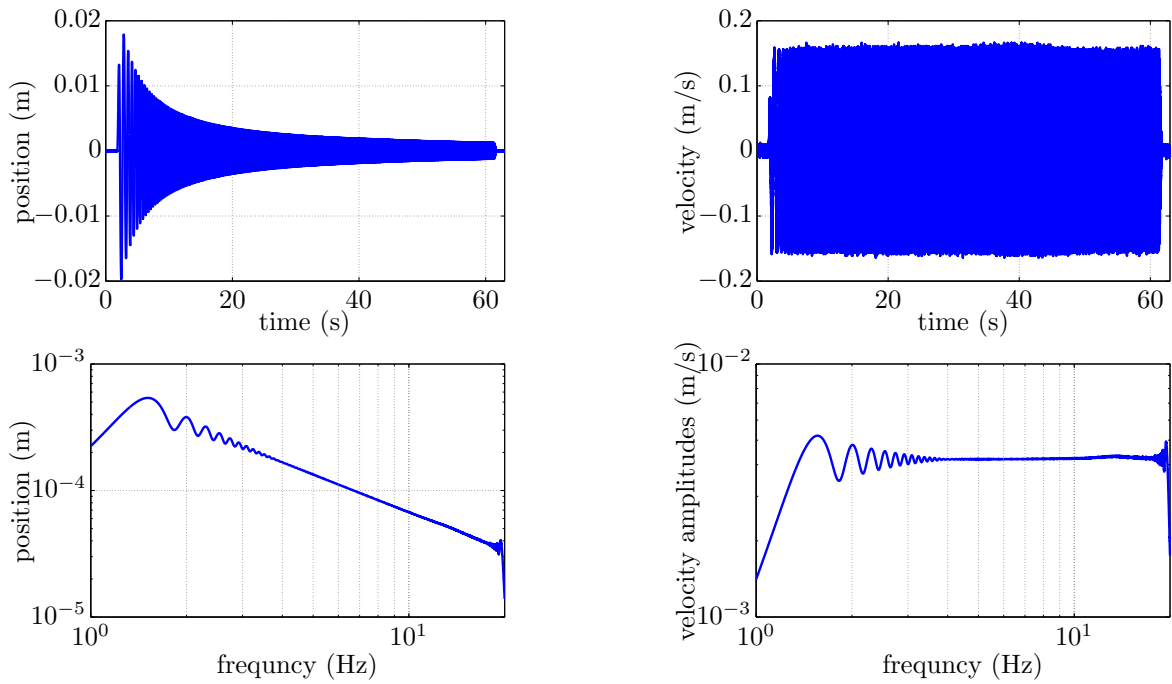


Figure C.2: Illustration of sine sweep excitation with amplitude spectrum similar to stochastic road excitations according to ISO 8608:1995: top - time series plots; bottom - frequency domain plots

progression of the sine sweep, if properly defined, sine sweep excitations allow to analyze the frequency behavior of suspension systems as discussed in Savaresi et al. (2010, p. 76 ff.). Sine sweep signals suitable for the development of semi-active suspension controllers should cover the relevant frequency range $f \in [0.5 \ 20]$ Hz. Moreover, the body and wheel resonance frequencies should both be roughly equivalently excited. The latter property can be achieved by adjusting the amplitude of the sine sweep signal such that it decreases with increasing frequency similar to the amplitude of the road profile PSD shown in Figure C.1. In particular, the sine sweep amplitudes should also linearly roll-off if plotted in a double-logarithmic manner. Figure C.2 illustrates the time series plot and the corresponding frequency domain plot of the sine sweep excitation employed in this work. The frequency domain curves show that the selected sine sweep signal gives a good approximation of the linear roll-off for frequencies larger than 3 Hz, but is subject to small amplitude oscillation for lower frequencies. These oscillations result from the trade-off between the total signal length and the frequency resolution at low frequencies. A detailed discussion of the use of sine sweep signals to compute a “nonlinear frequency response” can be found in Savaresi et al. (2010, p. 76 ff.) and Bunte (2011).

D The Quarter-Vehicle Test-Rig

The performance of the LPV controller is experimentally investigated using the quarter-vehicle test-rig of the *University of the Federal Armed Forces* in Munich shown in Figure D.1. A description of the test-rig setup and the control algorithm of the hydraulic cylinder can be found in Ahmed and Svaricek (2013) and Ahmed and Svaricek (2014).

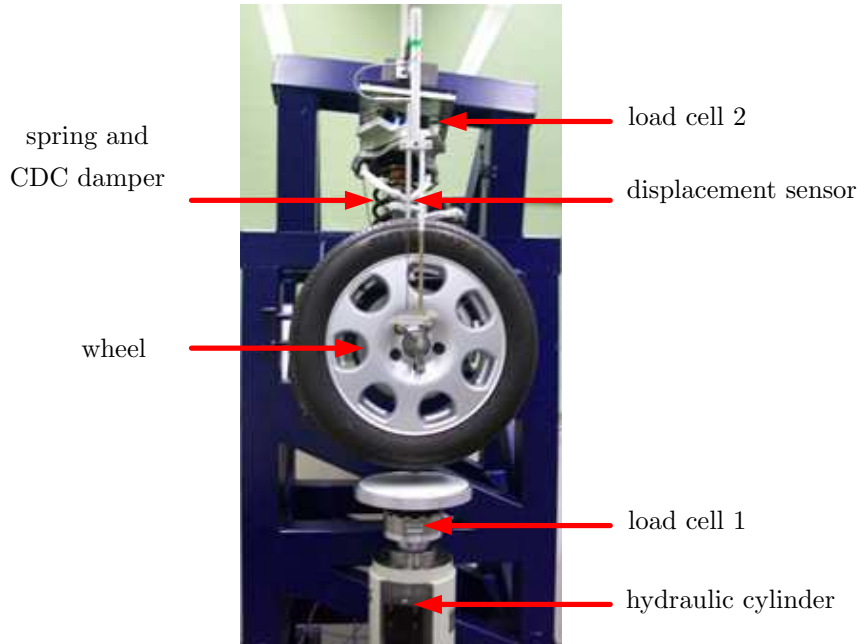


Figure D.1: Quarter-vehicle test-rig of the *University of the Federal Armed Forces* in Munich

D.1 Hardware and Software Setup

The quarter-vehicle test-rig consists of a McPherson suspension with spring, and semi-active damper that is assembled together and mounted at a fixed frame. The wheel acceleration is measured using an accelerometer with a range of ± 50 g and a resolution of 0.005 g rms. A load cell with a range of ± 50 kN is placed under the wheel for measuring the dynamic wheel load (load cell 1). To measure forces acting on the chassis another load cell is mounted between the suspension strut and frame (load cell 2). The suspension deflection is measured by a displacement sensor with a range of 200 mm. The generation of road profiles is carried out by a hydraulic servo system, which is controlled using the Non-Model based Adaptive Control (NMAC) algorithm given in Ahmed and Svaricek (2014) at a sampling rate of 1000 Hz.

No body mass was applied to the quarter-vehicle test-rig, as can be seen in Figure D.1. The chassis acceleration is obtained virtually based on a predefined body mass value and

the measured contact force of load cell 2. This set-up features the advantage to operate the test-rig with different body mass values without any hardware changes. The virtual body acceleration $\ddot{x}_{b,tr}$ is determined by

$$\ddot{x}_{b,tr} = \frac{1}{\bar{m}_b} F_{b,tr}, \quad (D.1)$$

with the virtual body mass \bar{m}_b and the measured contact force $F_{b,tr}$. With the assumption of a perfectly known initial body position and velocity, the body position x_b of a reference quarter-vehicle is equivalent to the position $x_{b,tr}$ of the virtual body obtained by double integration of the virtual chassis acceleration $\ddot{x}_{b,tr}$. The major challenge resulting from the virtual body mass constitutes the realization of the reference quarter-vehicle spring displacement and damper velocity at the test-rig. Therefore, the wheel position $x_{w,tr}$ at the test-rig has to fulfill

$$x_{w,tr} = x_w - x_b, \quad (D.2)$$

with wheel position x_w and body position x_b of the reference quarter-vehicle. Moreover, the tire deformation of the test-rig and the reference quarter-vehicle should be identical such that

$$x_{p,tr} - x_{w,tr} = x_g - x_w, \quad (D.3)$$

with the post position $x_{p,tr}$ of the test-rig and the road profile x_g . By substituting (D.2) in (D.3), it can be deduced that in order to realize condition (D.3) the virtual body position $x_{b,tr}$ must be subtracted from the road profile x_g yielding

$$x_{p,tr} = x_g - x_b. \quad (D.4)$$

The block diagram shown in Figure D.2 illustrates the operation of the test-rig. As derived in (D.1) - (D.4), the demand value of the post position $x_{p,tr}$ of the test-rig is not simply the road profile x_g , but a synthetic signal comprised of the road profile x_g and the position of the virtual body $x_{b,tr}$. According to Kuncz (2007), the approximations involved with the virtual body mass result in a relative amplitude error of the LTI test-rig model compared to the LTI reference quarter-vehicle of 2 % at the body resonance frequency and of 16 % at the wheel resonance frequency. Due to measurement errors, like noise and biases, and nonlinearities, the deviation between the reference quarter-vehicle and the quarter-vehicle with virtual body mass are expected to be larger at the test-rig.

The control of the test-rig is carried out using a DS1103 real time computer from dSPACE with the processor PPC 750GX 1 GHz. The controllers themselves are implemented on a dSPACE MicroAutoBox II at a sampling rate of 1000 Hz. The sensor signals and the control signal are exchanged as analog signals between the real-time platforms.

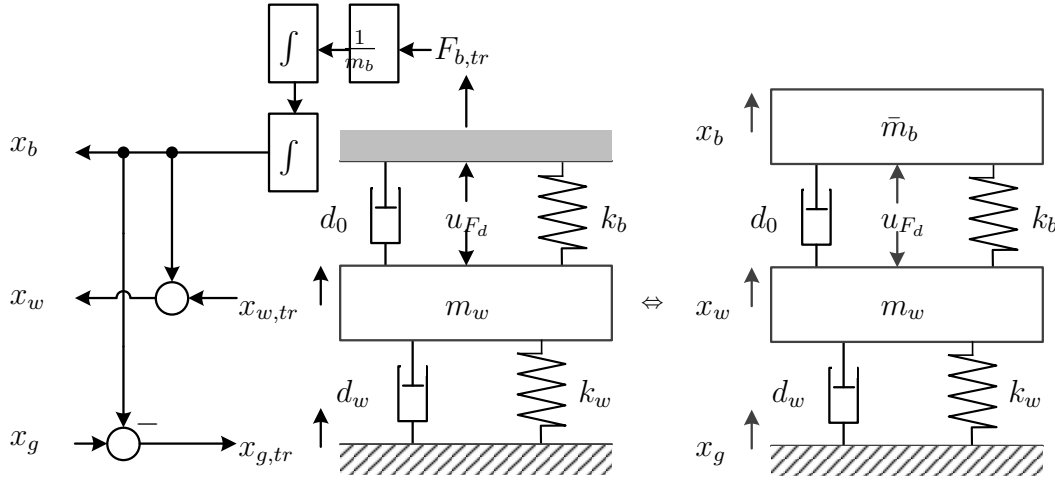


Figure D.2: Block diagram illustrating the test-rig operation

D.2 Modeling and Simulation

To tune and verify the performance of the LPV controller according to Section 3.5.1 and 3.5.2 before the test-rig experiments, the reference quarter-vehicle is implemented in Modelica (Otter, 2013; Fleps-Dezasse and Brembeck, 2013). The semi-active damper is modeled by the force map damper model introduced in Section B.2 and the linear suspension spring with bump stops is modeled by a 1D look-up table. Table D.1 summarizes the parameters of the quarter-vehicle test-rig and corresponding reference quarter-vehicle. Additionally, Figure D.3 shows the minimum and maximum damper force characteristics of the semi-active damper at the test-rig. A closer examination of the reference quarter-

Table D.1: Quarter-vehicle test-rig model: symbols and parameters

Symbol	Quantity	Value	Unit
\bar{m}_b	(quarter) body mass	350	kg
m_w	wheel mass	50	kg
k_b	suspension spring stiffness	30000	N/m
k_w	tire stiffness	180000	N/m
d_w	tire damping	200	Ns/m
ω_d	damper bandwidth	50	rad/s

vehicle properties with a constant damping of $d_{b,\text{lti}} = 1500$ Ns/m, which approximates the minimum damper characteristics, reveals that the LTI reference quarter-vehicle features a body resonance frequency of about 1.5 Hz and a damping ratio D calculated by

$$D = \frac{d_{b,\text{lti}}}{2\sqrt{k_b\bar{m}_b}} \quad (\text{D.5})$$

of $D = 0.23$. As described in Mitschke and Wallentowitz (2004, p. 261), this damping ratio already corresponds to a comfortable passenger car, i.e. the minimum damping of the semi-active damper already provides sufficient damping of the body and wheel resonance amplitudes. Regarding semi-active suspension control design, this basic suspension setting tightens the performance margin as discussed in Section 3.7.

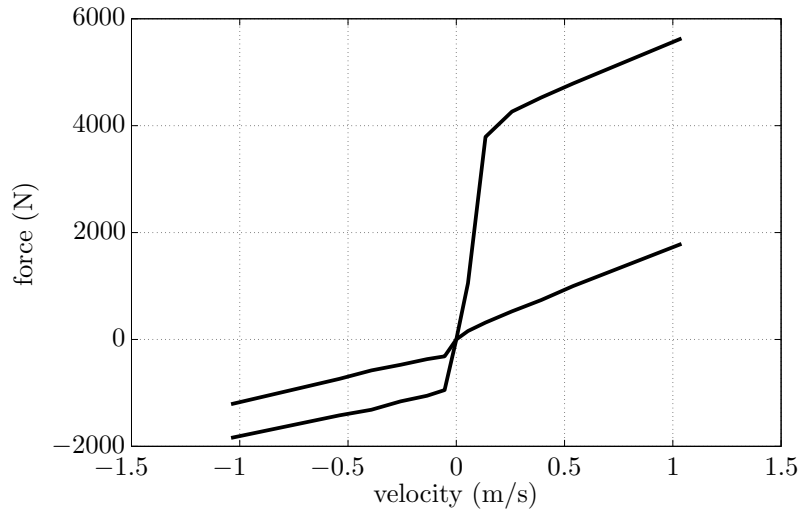


Figure D.3: Force map of semi-active damper at quarter-vehicle test-rig

E The SC3-Bulli Experimental Vehicle

The performance of the developed LPV controller is validated by experiments with the *SC3-Bulli* experimental vehicle of SR shown in Figure 1.4. The *SC3-Bulli* constitutes SRs testing vehicle for *safety critical connected control* with the vertical dynamics topic being the first application.

E.1 Hardware and Software Setup

The experimental vehicle is equipped with the semi-active dampers from its successor model, namely the VW T6 van, where they are offered as supplemental equipment. Figure E.1-right depicts the normalized minimum and maximum force characteristics of the front and rear semi-active dampers. Both damper characteristics feature asymmetrical compression and rebound forces and a nonlinear force-over-velocity relationship. Compared to the semi-active damper of the quarter-vehicle test-rig of Section D, the minimum damping curves of the front and rear suspensions are much lower and can be approximated by a linear body damping of about $d_{b,lti} = 500$ Ns/m. The corresponding damping ratio D of the vehicle body heave motion given by

$$D = \frac{4d_{b,lti}}{2\sqrt{4k_b m_b}}, \quad (\text{E.1})$$

and calculated with the parameters from Table E.2 is $D \approx 0.1$. Complemented by very low static and sliding friction forces, the minimum curves provide insufficient damping and the vehicle oscillates heavily if operated in this configuration. Nevertheless, semi-active dampers with such a low minimum damping are perfectly suitable for semi-active suspension control as discussed in Section 4.7. Due to the large payload of the experimental vehicle, especially the rear dampers have large rebound forces to provide sufficient damping at maximum payload. The current of the electromagnetic valve of each damper is controlled by a SISO controller with proportional and integral action with anti-windup. A damper current of $u_d = 0.1$ A corresponds to minimum damping and a damper current of $u_d = 1.4$ A to maximum damping. Figure E.1-left shows the spring characteristics of the front and rear suspensions. To prevent large suspension strokes and minimize bump stop interferences at maximum payload, the rear springs feature a stiffer and more progressive characteristic than the front springs. The front axle of the *SC3-Bulli* is realized by classical McPherson suspension systems with the semi-active damper mounted inside the body spring and the rear suspension systems are realized by transverse control arms. The *SC3-Bulli* is equipped with a dSPACE MicroAutoBox II which runs the semi-active suspension control algorithm. The damper demand signals calculated on the MicroAutoBox are then processed by a power electronics unit. The power electronics generates the current of the electromagnetic valves and provides current measurements to the MicroAutoBox. As input signals to the control algorithms, the *SC3-Bulli* offers wheel acceleration measurements, suspension height measurements and body acceleration measurements.

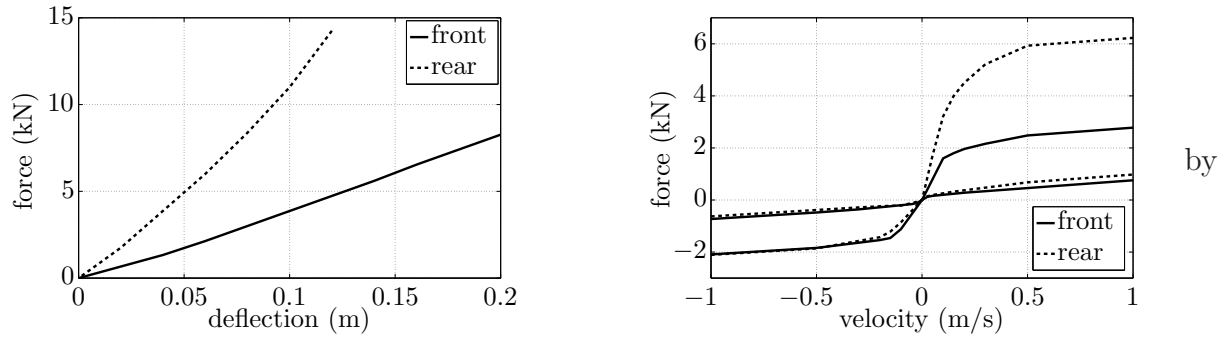


Figure E.1: Left - suspension spring characteristic, right - semi-active damper characteristic of *SC3-Bulli*

Table E.1 illustrates the corresponding specifications of the body and wheel acceleration and the suspension height sensors. All sensors are standard automotive components: the acceleration sensors are from Continental (2016) and the suspension height sensors are parts of the VW T6 van.

Table E.1: Sensor specification *SC3-Bulli*

	quantity	range	sensitivity	output
body accelerometer	4	± 1.6 g	0.9375 V/g	analog
wheel accelerometer	4	± 15 g	0.133 V/g	analog
height sensor	4	$3 \times \pm 60$ deg	$\frac{1,6\text{deg}}{\text{percentage duty cycle}}$	PWM (800 Hz)

E.2 Modeling and Simulation

In addition to the linear full-vehicle model presented in Section 4.3, a nonlinear full-vehicle model is implemented in Modelica (Otter, 2013; Fleps-Dezasse and Tobolář, 2015). This model is used for off-line simulation of the closed-loop behavior and for controller tuning. The model includes the most essential nonlinearities like

- the semi-active dampers,
- the nonlinear spring characteristics, and
- the transmission between wheel position and spring and damper deflection,

but neglects the elastokinematics of the suspension systems and the bump stops due to missing component information. Furthermore, the nonlinear full-vehicle model approximates the tires by linear spring-damper elements and features no planar vehicle motions

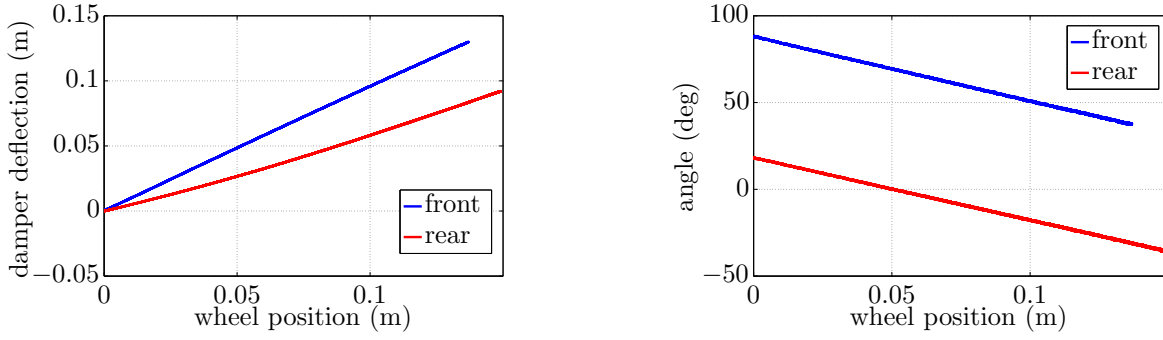


Figure E.2: Left - damper deflection over vertical wheel position, right - height sensor output over vertical wheel position

like yaw and longitudinal or lateral displacements. Figure E.2 depicts the measured transmission of the front and rear damper deflection relative to the wheel position with fixed body position. Both curves show an approximately linear relationship between damper deflection and wheel position. After negligence of the static offset of the curves, the slopes of the curves correspond to the transmission ratios between damper deflection and wheel position. The transmission ratio of the front damper $r_{\text{damper},f}$ is almost one, while the transmission ratio of the rear damper is $r_{\text{damper},r} = 0.58$. The small rear transmission ratio significantly reduces the effect of the corresponding damper forces as shown in (4.25). In addition to the damper deflection related transmission ratios, the nonlinear full-vehicle model also accounts for the spring deflection related transmission ratios $r_{\text{spring},f}$ and $r_{\text{spring},r}$. At the front suspension the spring and the damper are coaxially mounted and consequently $r_{\text{damper},f} = r_{\text{spring},f}$. Conversely, the springs and dampers have different mounting positions at the rear suspensions and separate transmission ratios have to be considered as stated in Table E.2. The nonlinear full-vehicle model also considers a

Table E.2: Symbols and parameters of *SC3-Bulli* vehicle model

Symbol	Quantity	Value	Unit
m_b	body mass	2400	kg
I_{xx}	roll inertia	850	kgm ²
I_{yy}	pitch inertia	2500	kgm ²
m_w	wheel mass	50	kg
$\bar{k}_{b,f} / \bar{k}_{b,r}$	suspension spring stiffness (front/ rear)	30/ 100	kN/m
k_w	tire stiffness	280	kN/m
d_w	tire damping	300	Ns/m
ω_d	damper bandwidth	80	Hz
$r_{\text{spring},f} / r_{\text{spring},r}$	transmission ratio spring (front/ rear)	0.95/ 0.75	-
$r_{\text{damper},f} / r_{\text{damper},r}$	transmission ratio damper (front/ rear)	0.95/ 0.58	-

simple approximation of sliding friction of each damper given by

$$F_{sf,i} = F_{sf,\text{nom}} \tanh\left(\frac{\dot{x}_{d,i}}{\dot{x}_{d,\text{ref}}}\right), \quad (\text{E.2})$$

with the nominal friction force $F_{sf,\text{nom}}$ determined during measurements on the damper test-rig. The parameter $\dot{x}_{d,\text{ref}}$ determines the transition from negative to positive damper velocities. To generate realistic measurements as input to the controllers, the simulated sensor signals of the vehicle model are corrupted by white noise and additionally the acceleration sensor signals are corrupted by small biases.

The vehicle model is simulated by a fourth-order *Runge-Kutta* algorithm with a step size $T_{\text{nFVM}} = 0.5$ ms.

F Estimation of the Roll Disturbance Moment

The roll disturbance moment d_r acting on the vehicle body due to the steering inputs of the driver can be computed from the corresponding lateral vehicle acceleration a_y according to

$$d_r = t_\tau a_y, \quad (\text{F.1})$$

with the transmission factor t_τ determined by

$$t_\tau = -m_b (h_{b,\text{CoG}} - h_{\text{roll}}). \quad (\text{F.2})$$

The transmission factor t_τ transforms the lateral acceleration into a lateral force acting on the vehicle body using the body mass m_b and furthermore, into the roll disturbance moment through the lever arm between the point of application of the lateral force and the vehicle roll axis. The lever arm of the lateral force corresponds to the vertical distance between the vehicle CoG and the roll axis.

In Figure 5.1, the roll disturbance moment d_r acting on the vehicle is provided by the roll disturbance estimator subsystem. This function gathers (F.1) and the expected lateral acceleration estimated by a linear single-track model processing the steering angle input of the driver. The linear single-track model presented in Mitschke and Wallentowitz (2004, p. 547 ff.) and Schramm et al. (2014, p. 223 ff.) approximates the planar motion of a passenger car. The main limitations of the single-track model as listed in Schramm et al. (2014, p. 223 ff.) are:

- constant longitudinal velocity of the vehicle CoG along the trajectory,
- negligence of body heave, roll and pitch motion,
- left and right tires conflated to one single tire per front and rear axle, and
- constant wheel-load distribution front to rear.

Table F.1: Single-track model: symbols and parameters

Symbol	Quantity	Value	Unit
m_v	vehicle mass	2600	kg
I_{zz}	yaw inertia	3007	kg
$c_{\alpha F}$	cornering stiffness front	96000	N/m
$c_{\alpha R}$	cornering stiffness rear	199000	N/m
l_{vF}	distance vehicle CoG to front axle	1.37	m
l_{vR}	distance vehicle CoG to rear axle	1.63	m
l_S	distance vehicle CoG to sensor	1.37	m
t_d	output delay	0.1	s

As discussed in Mitschke and Wallentowitz (2004, p. 560 ff.), the validity of the linear single-track model is limited to lateral accelerations of the vehicle CoG smaller than $a_{yCoG} = 4 \text{ m/s}^2$. This property, however, does not impose significant restrictions during the presented application because the lateral accelerations attained by drivers mostly stay below $a_{yCoG} = 4 \text{ m/s}^2$ (Mitschke and Wallentowitz, 2004, p. 559 ff.). The following equations present the state-space description of the linear single-track model with front steering angle input δ_F and the system states \mathbf{x}_{STM} given by

$$\mathbf{x}_{STM} = \begin{bmatrix} \dot{\psi} & \beta_{STM} \end{bmatrix}^T. \quad (\text{F.3})$$

The states of the single-track model are composed of the yaw rate $\dot{\psi}$ and the vehicle side slip angle β_{STM} which characterizes the angle between the direction of the velocity of the vehicle CoG and the vehicle's longitudinal axis. The single-track model outputs the lateral acceleration a_{yS} of a virtual acceleration sensor S with distance l_S along the longitudinal axis from the vehicle CoG. Positive values of l_S indicate a location to the front of the vehicle, e.g. $l_S = l_{vF}$ means that the virtual acceleration sensor is located at the front wheels. The state-space representation of the linear single-track model is then given by

$$\begin{bmatrix} \dot{\mathbf{x}}_{STM} \\ a_{yS} \end{bmatrix} = \begin{bmatrix} \mathbf{A}_{STM} & \mathbf{B}_{STM} \\ \mathbf{C}_{STM} & D_{STM} \end{bmatrix} \begin{bmatrix} \mathbf{x}_{STM} \\ \delta_F \end{bmatrix}, \quad (\text{F.4})$$

with the related state-space matrices

$$\mathbf{A}_{STM} = \begin{bmatrix} -\frac{c_{\alpha F} l_{vF}^2 + c_{\alpha R} l_{vR}^2}{I_{zz} v_v} & -\frac{c_{\alpha F} l_{vF} - c_{\alpha R} l_{vR}}{I_{zz}} \\ -1 - \frac{c_{\alpha F} l_{vF} - c_{\alpha R} l_{vR}}{m_v v_v^2} & -\frac{c_{\alpha F} + c_{\alpha R}}{m_v v_v} \end{bmatrix}, \quad (\text{F.5})$$

$$\mathbf{B}_{STM} = \begin{bmatrix} \frac{c_{\alpha F} l_{vF}}{I_{zz}} & \frac{c_{\alpha F}}{m_v v_v} \end{bmatrix}^T, \quad (\text{F.6})$$

$$\mathbf{C}_{STM} = \begin{bmatrix} -\left(\frac{c_{\alpha F} l_{vF} - c_{\alpha R} l_{vR}}{m_v v_v} + l_S \frac{c_{\alpha F} l_{vF}^2 + c_{\alpha R} l_{vR}^2}{I_{zz} v_v} \right) & -\left(\frac{c_{\alpha F} + c_{\alpha R}}{m_v} + l_S \frac{c_{\alpha F} l_{vF} - c_{\alpha R} l_{vR}}{I_{zz}} \right) \end{bmatrix}, \quad (\text{F.7})$$

and

$$D_{STM} = \frac{c_{\alpha F}}{m_v} + l_S \frac{c_{\alpha F} l_{vF}}{I_{zz}}. \quad (\text{F.8})$$

Table F.1 introduces the corresponding symbols and parameters of the single-track model. Figure F.1 and F.2 illustrate the two reference manoeuvres which have been employed to tune the parameters of the single-track model. The first manoeuvre roughly corresponds to a constant radius cornering with increasing vehicle speed and the second manoeuvre consists of several steering angle step inputs. Overall, the parametrized single-track model achieves a high accuracy in reproducing measured lateral accelerations. In particular, as emphasized by Figure F.2-bottom right, the simulated transient response of the linear single-track model corresponds very well to the measured transient response of the vehicle. Equally, the simulated and measured steady-state lateral accelerations during the constant radius cornering manoeuvre depicted in Figure F.1-bottom right also agree with high accuracy.

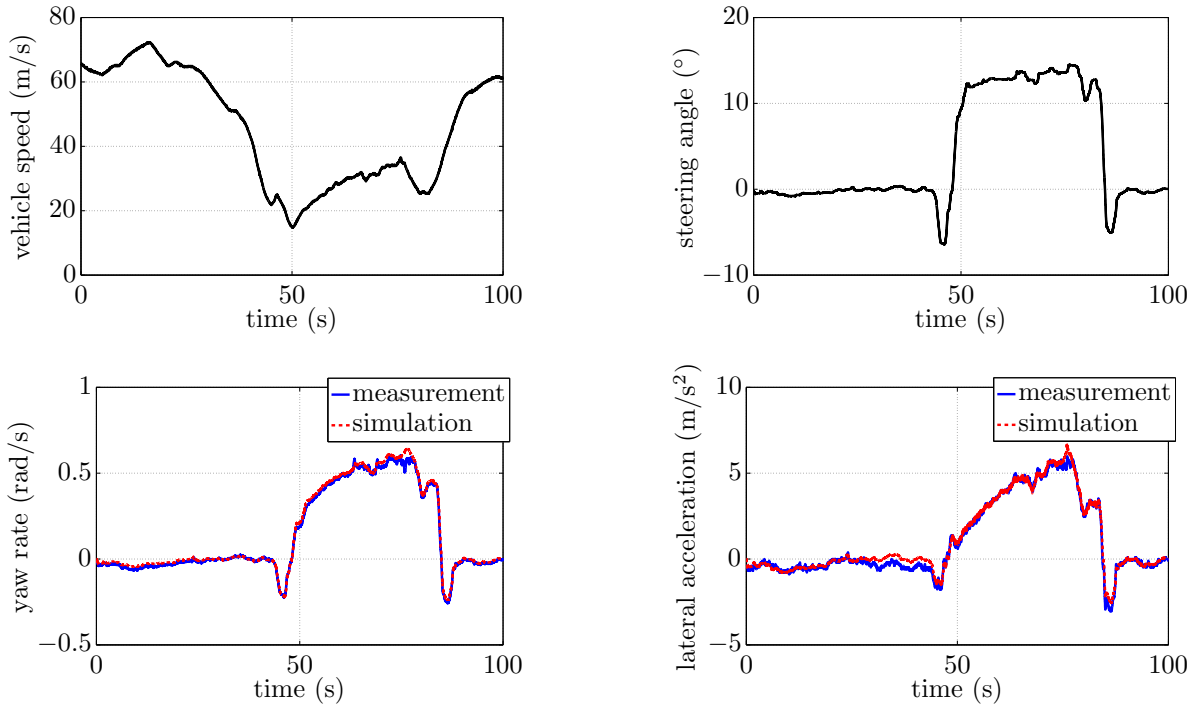


Figure F.1: Estimation error of single-track model with parameters according to Table F.1 during quasi steady-state cornering at a constant radius

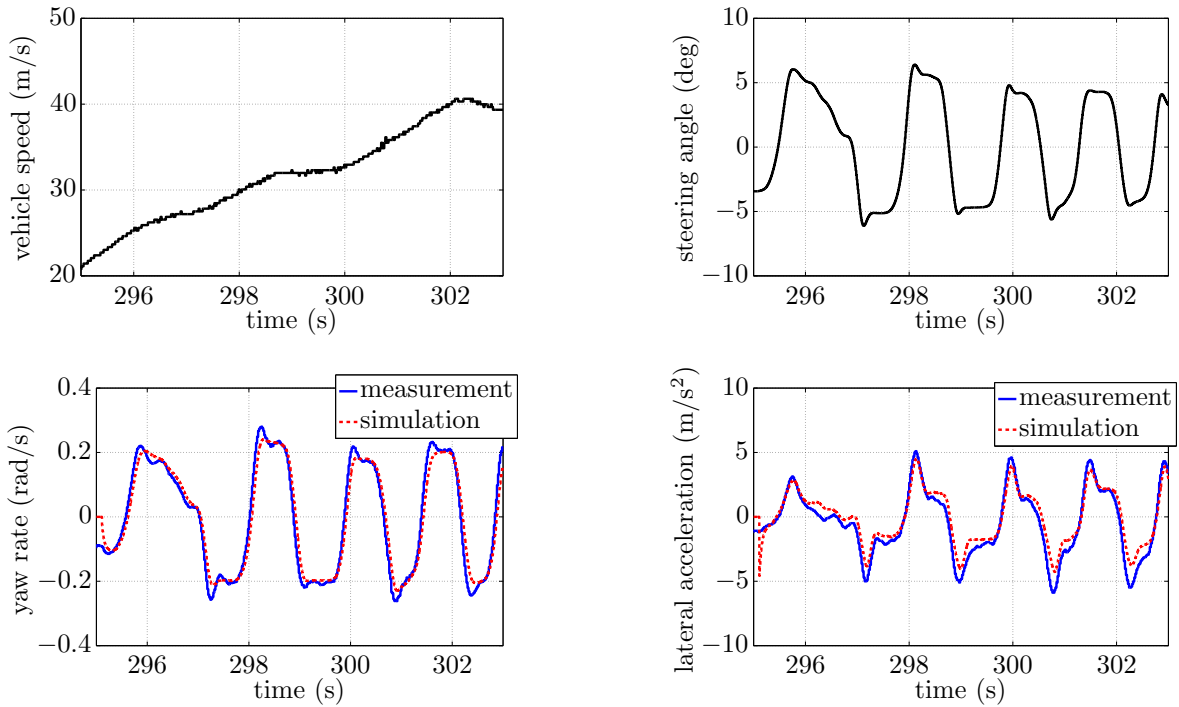


Figure F.2: Estimation error of single-track model with parameters according to Table F.1 during steering angle steps

G Gain-Scheduled H_∞ Control vs LPV Control

This section presents a comparison between the LPV controller design presented in Chapter 3 and 4 and corresponding H_∞ controllers. Firstly, the induced L_2 and H_∞ performance levels of a state-feedback LPV controller and H_∞ controller are compared in a quarter-vehicle application. Secondly, the ride comfort and road-holding performance of the full-vehicle LPV controller of Section 4.5 is compared to a gain-scheduled H_∞ controller.

G.1 γ -Performance Level Comparison

Figure G.1 gives a comparison between the body velocity and wheel velocity frequency responses of the closed-loop with the H_∞ controller of the unconstrained system and closed-loop with the LPV controller with frozen saturation indicators θ_{\min} and θ_{\max} . Both controllers, the H_∞ controller and the LPV controller are designed as state-feedback controllers assuming the availability of the plant state as measurements. As in Chapter 3 and 4, the control design problem is formulated in generalized plant notation. For the example here, the quarter-vehicle plant presented in (3.19) is extended by the road disturbance model (C.6) and the nominal damping d_0 is assumed constant. The LPV and H_∞ control design problems minimize the induced L_2 and H_∞ -norms of the closed-loop systems with road disturbance input d_g and body velocity performance signal e_a . The generalized plant of the LPV control design problem is given by

$$\begin{bmatrix} \dot{\mathbf{x}} \\ \begin{bmatrix} e_a \\ e_u \end{bmatrix} \end{bmatrix} = \begin{bmatrix} \mathbf{A} & \mathbf{B}_1 & \bar{\mathbf{B}}_2\theta \\ \mathbf{C}_{11}(\theta) & \begin{bmatrix} 0 \\ 0 \end{bmatrix} & \begin{bmatrix} 0 \\ I \end{bmatrix} \end{bmatrix} \begin{bmatrix} \mathbf{x} \\ d_g \\ u_{F_d} \end{bmatrix}, \quad (\text{G.1})$$

with the state vector $\mathbf{x} = [x_b \ \dot{x}_b \ x_w \ \dot{x}_w \ x_{F_d} \ x_g]^T$ and the matrices

$$\mathbf{A}(d_0) = \begin{bmatrix} 0 & 1 & 0 & 0 & 0 & 0 \\ \frac{-k_b}{m_b} & \frac{-d_0}{m_b} & \frac{k_b}{m_b} & \frac{d_0}{m_b} & \frac{1}{m_b} & 0 \\ 0 & 0 & 0 & 1 & 0 & 0 \\ \frac{k_b}{m_w} & \frac{d_0}{m_w} & \frac{-k_b-k_w}{m_w} & \frac{-d_0-d_w}{m_w} & -\frac{1}{m_w} & \frac{k_w-d_w\beta_r v_{\text{ref}}}{m_w} \\ 0 & 0 & 0 & 0 & -\omega_d & 0 \\ 0 & 0 & 0 & 0 & 0 & -\beta_r v_{\text{ref}} \end{bmatrix}, \quad (\text{G.2})$$

$$\mathbf{B}_1 = \begin{bmatrix} 0 & 0 & 0 & \frac{d_w\alpha_r v_{\text{ref}}}{m_w} & 0 & \alpha_r v_{\text{ref}} \end{bmatrix}^T, \quad (\text{G.3})$$

$$\bar{\mathbf{B}}_2 = \begin{bmatrix} 0 & 0 & 0 & 0 & \omega_d & 0 \end{bmatrix}^T \text{ and} \quad (\text{G.4})$$

$$\mathbf{C}_{11} = \begin{bmatrix} 0 & w_b\theta & 0 & 0 & 0 & 0 \end{bmatrix}. \quad (\text{G.5})$$

The above generalized plant includes the control effort weight

$$W_u = \theta^{-1}, \quad (\text{G.6})$$

introduced in Chapter 2 and weights the body velocity performance signal by

$$W_a = w_b \theta. \quad (\text{G.7})$$

The LPV controller is synthesized with a constant Lyapunov matrix and a grid density of two points, namely θ_{\min} and θ_{\max} . The H_∞ controller is synthesized with the unconstrained plant by setting the saturation indicator to one, i.e. $\theta = 1$.

As expected according to the discussion in Section A.4, the H_∞ performance level γ_∞ is smaller than the induced L_2 -norm performance level γ_θ of the LPV control design. Furthermore, the H_∞ controller achieves a better attenuation of the body resonance peak of the unconstrained system. In the LPV case the unconstrained system corresponds to $\theta = 1$.

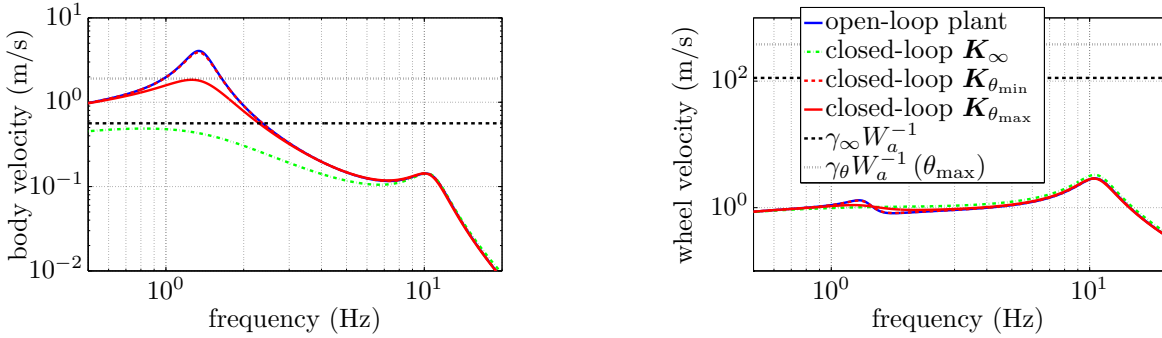


Figure G.1: Comparison of frequency responses of body and wheel velocity of closed-loop with H_∞ control of the unconstrained system and closed-loop with LPV control of system with frozen saturation indicators θ_{\min} and θ_{\max}

The evaluation of the performance levels provides some insight into the amount of conservatism of the LPV control design with saturation indicators compared to an H_∞ control design. The assessment, however, is only valid for the unconstrained closed-loop system, i.e. without consideration of the actuator force constraints. The H_∞ controller can be adjusted to application with actuator constraints by the clipping approach as introduced in Section 1.1.3. This ad-hoc adjustment, however, entails the loss of the original performance and stability properties of the H_∞ controller. In contrast, the mathematically rigorous LPV control design offers performance and stability guarantees for the fast saturation indicator variations present in semi-active suspensions and for all admissible actuator saturation conditions.

G.2 Ride Comfort and Road-holding Performance Comparison

In semi-active suspension design, the performance level of the controller synthesis is far less important than the actual ride comfort and road-holding performance. Therefore, in

addition to the previous section, this section investigates the ride comfort and road-holding performance of the full-vehicle LPV controller \mathbf{K}_θ of Section 4.5 and a gain-scheduled H_∞ controller \mathbf{K}_{gsH_∞} . The gain-scheduled H_∞ controller is designed with the same grid as the LPV controller, but instead of one LPV controller for the entire admissible saturation indicator range, separate H_∞ controllers for each grid point are synthesized. Similar to the LPV controller, the controller output is then obtained by interpolation of the grid points. Both controllers are tuned by the optimization procedure described in Section 4.7. The achievable Pareto fronts of the controllers are depicted in Figure G.2. Figure G.2-left shows the evaluation of the multi-excitations and Figure G.2-right shows the evaluation of the stochastic road excitation. In contrast to the investigation of the γ -performance levels in the previous section, the ride comfort and road-holding performance of the LPV controller and the gain-scheduled H_∞ controller are almost identical. This shows that, at least in the considered semi-active suspension application, a proper tuning of the controller parameters can overcome the conservatism of the LPV control design noticed in the previous section.

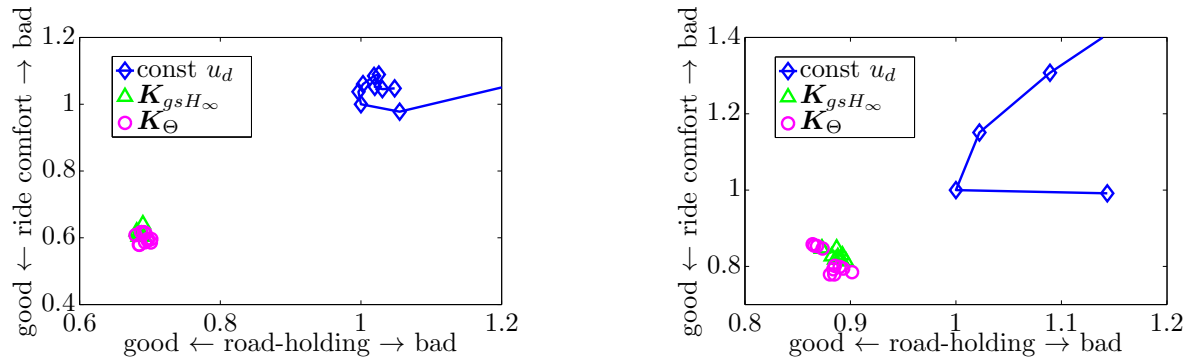


Figure G.2: Comparison of Pareto fronts of ride comfort and road-holding of full-vehicle gain-scheduled H_∞ controller and LPV controller; left - Pareto fronts of multi-excitation optimization and right - Evaluation of stochastic road excitation

H Robust Performance of the Full-Vehicle LPV Controller

This section investigates the robust performance of the full-vehicle LPV controller of Chapter 4. To this end, firstly the body mass of the nonlinear full-vehicle model of Section E.2 is varied from 2200 kg to 3000 kg and the ride comfort performance as defined in Section 4.2 is evaluated. This investigation emulates typical body mass variation of the *SC3-Bulli* starting from the nominal body mass of 2400 kg, e.g. due to additional payloads. Secondly, the effect of an imperfect inverse damper model is evaluated. For this investigation it is assumed that the imperfect inverse damper model results in a scaling of the damper control signal \mathbf{u}_d , i.e. the multiplication of the inverse damper model and the damper model according to (B.5) amounts to values distinct from one.

Figure H.1 shows the results of both simulation investigations with the nonlinear vehicle model subject to the stochastic road excitation. As expected, the ride comfort performance of both the Skyhook-Groundhook (SH/GH) controller and the full-vehicle LPV controller improves with increasing body mass due to the better isolation regarding road disturbances. Moreover, the ride comfort performance of the full-vehicle LPV controller shows a slightly larger improvement of ride comfort, which indicates that the full-vehicle LPV controller features a better robust performance regarding body mass variation than the Skyhook-Groundhook controller. Figure H.1-right shows the result of the investigation of the imperfect inverse semi-active damper model. Overall, the ride comfort performance of both controllers exhibits good robustness regarding the considered scaling error resulting from the inverse semi-active damper model. The Skyhook-Groundhook controller, however, seems to be slightly more insensitive to these errors.

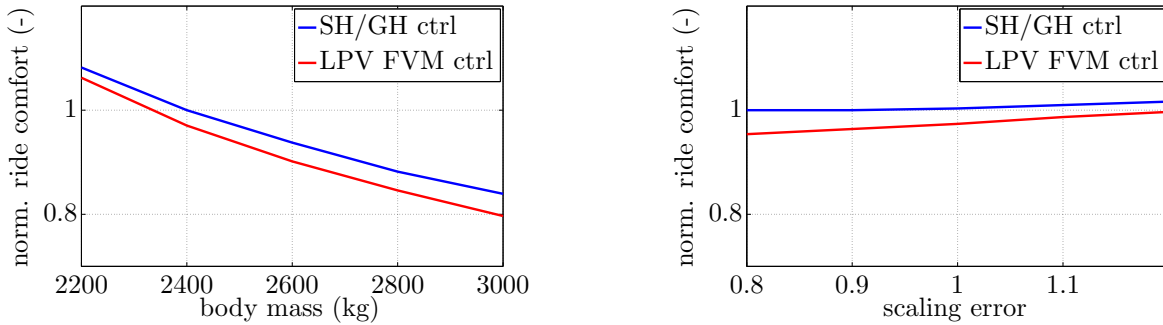


Figure H.1: Robust performance investigation of full-vehicle LPV controller: left - variation of body mass, and right - scaling error of inverse damper model

I Implementation in Simulink

This section presents two screenshots of the implementation of the vertical dynamics algorithm in Simulink. Figure I.1 shows the top level of the Simulink model and Figure I.2 illustrates the implementation of the full-vehicle LPV controller. The overall vertical dynamics software consists of seven main subsystems:

sensors_and_can: this subsystem collects the input signals from the sensors and the vehicle CAN bus and converts them to physically meaningful signals,

prepare_inputs: this subsystem estimates the lateral acceleration of the vehicle from the steering angle and the vehicle speed and handles the offsets of the accelerometers,

params_and_adaptions: this subsystem calculates the road index and determines most of the parameters of the damper control algorithm,

vehicle_CtrlAlgo: this subsystem incorporates the full-vehicle LPV controller or the Skyhook-Groundhook controller,

damper_mode_selector: this subsystem determines the operating modes of the dampers, namely const. u_d comfort, const. u_d sport, controlled comfort, etc.

damper_CtrlAlgo: this subsystem features the local damper current controller,

to_Damper: this subsystem outputs the demand values of each damper.

This modular architecture allows for an easy substitution of subsystems and functions like the Skyhook-Groundhook controller and the LPV controller. Furthermore, the vertical dynamics software can be easily adapted to the requirements of new application, e.g. by removing some of the subsystems or adding new ones.

Figure I.2 shows the implementation of the full-vehicle LPV controller with feedforward consisting of the main subsystems:

observer: this subsystem collects the input signals from the sensors and estimates the states of the full-vehicle,

LPV_stateFeedback: this subsystem computes the LPV state-feedback gain using look-up tables,

roll_feedforward: this subsystem incorporates the LPV feedforward filter,

calc_theta: this subsystem calculates the saturation indicators.

The structure of the controller particularly emphasizes the advantages of DI controllers compared to general output-feedback controller. In particular, DI controllers can be implemented by separate subsystems for the observer and for the state-feedback part.

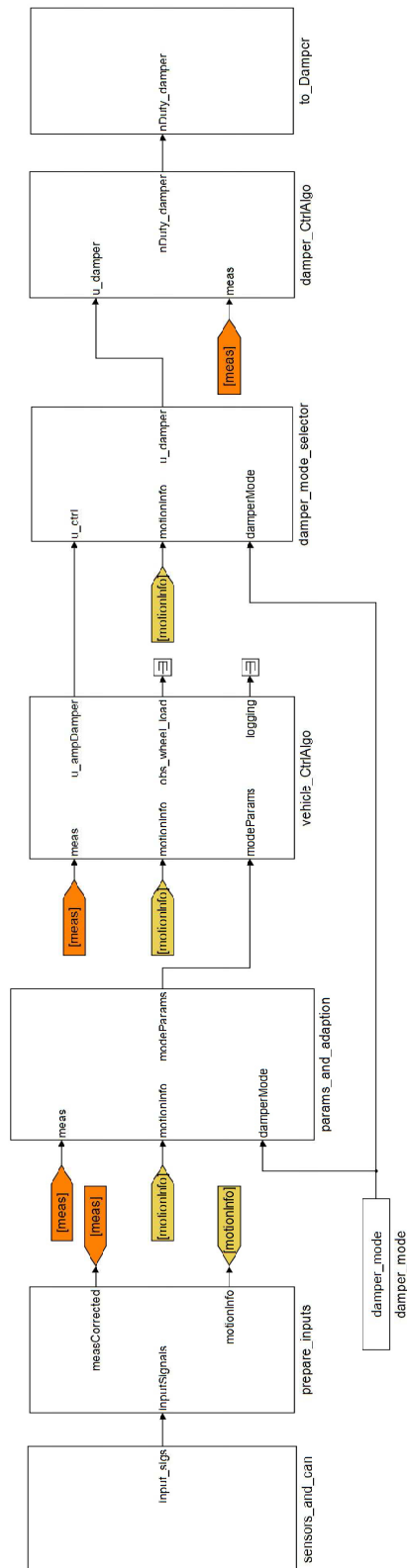


Figure I.1: Overview of Simulink implementation of the vertical dynamics algorithm

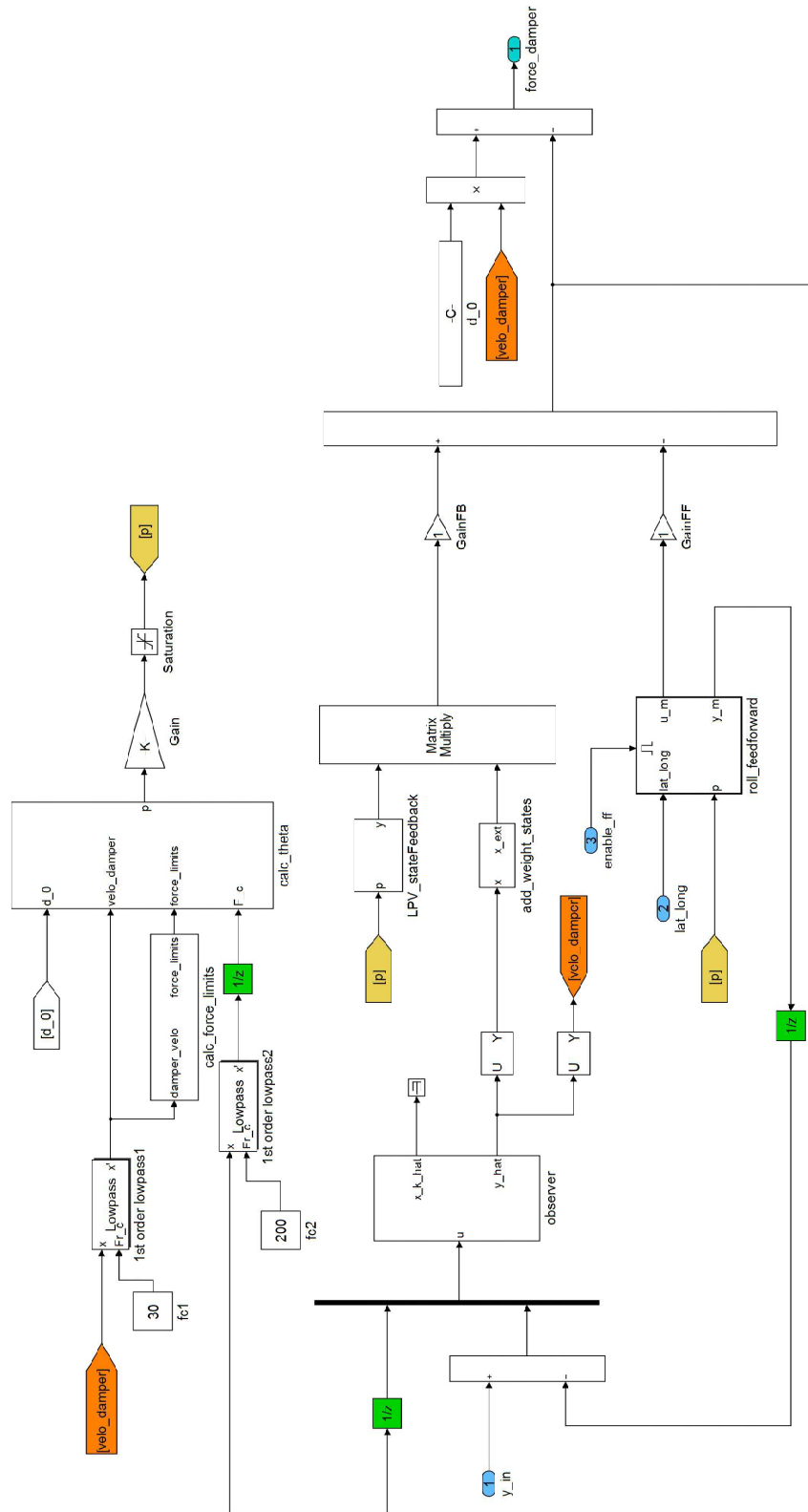


Figure I.2: Simulink implementation of the full-vehicle LPV controller with feedforward

References

- Ahmadian, M.** and **E. Blanchard**. 2011. Non-dimensionalised closed-form parametric analysis of semi-active vehicle suspensions using a quarter-car model. *Vehicle System Dynamics* 49(1-2). 219–235.
- Ahmadian, M.** and **C. A. Pare**. 2000. A quarter-car experimental analysis of alternative semiactive control methods. *J. of Intelligent Material Systems and Structures* 11(8). 604–612.
- Ahmadian, M., B. Reichert, X. Song** and **S. S. Southward**. 2000. No-jerk semi-active skyhook control method and apparatus. European Patent Application No. 99310141.9, 16.12.1999.
- Ahmadian, M.** and **D. E. Simon**. 2004. Can semiactive dampers with skyhook control improve roll stability of passenger vehicles?. *SAE Technical Paper*. SAE International.
- Ahmed, M.** and **F. Svaricek**. 2013. Adaptive robust gain scheduled control of vehicle semi-active suspension for improved ride comfort and road handling. *Proc. of the IEEE Int. Conf. on Mechatronics (ICM)*. Vicenza, Italy. 376–381.
- Ahmed, M.** and **F. Svaricek**. 2014. Adaptive anti-windup approach for vehicle semi-active suspension. *Proc. of the 6th IEEE Int. Conf. on Modelling, Identification Control (ICMIC)*. Melbourne, Australia. 265–270.
- Amato, F.** 2006. *Robust Control of Linear Systems Subject to Uncertain Time-Varying Parameters*. 1 Auflage. Heidelberg: Springer-Verlag.
- Apkarian, P.** and **P. Gahinet**. 1995. A convex characterization of gain-scheduled H_∞ controllers. *IEEE Transactions on Automatic Control* 40(5). 853–864.
- Apkarian, P., P. Gahinet** and **G. Becker**. 1995. Self-scheduled H_∞ control of linear parameter-varying systems: a design example. *Automatica* 31(9). 1251–1261.
- Aström, K. J.** and **P. Kumar**. 2014. Control: A perspective. *Automatica* 50(1). 3–43.
- Aström, K. J.** and **R. M. Murray**. 2008. *Feedback Systems*. 1 Auflage. Princeton: University Press.
- Aström, K. J.** and **L. Rundqwist**. 1989. Integrator windup and how to avoid it. *Proc. of the American Control Conference (ACC)*. Pittsburgh, Pennsylvania, United States. 1693–1698.
- Becker, G.** and **A. Packard**. 1994. Robust performance of linear parametrically varying systems using parametrically-dependent linear feedback. *Systems & Control Letters* 23(3). 205–215.

- Brezas, P.** and **M. C. Smith**. 2014. Linear quadratic optimal and risk-sensitive control for vehicle active suspensions. *IEEE Transactions on Control Systems Technology* 22(2). 543–556.
- Brezas, P., M. C. Smith** and **W. Houtt**. 2015. A clipped-optimal control algorithm for semi-active vehicle suspensions: Theory and experimental evaluation. *Automatica* 53. 188–194.
- Bünthe, T.** 2011. Recording of model frequency responses and describing functions in modelica. *Proc. of the 8th Int. Modelica Conference*. Dresden, Germany. 686–696.
- Butz, T.** and **O. von Stryk**. 2001. Modelling and simulation of electro- and magnetorheological fluid dampers. *Journal of Engineering Mechanics* 82(1). 3–20.
- Canale, M., M. Milanese** and **C. Novara**. 2006. Semi-active suspension control using “fast” model-predictive techniques. *IEEE Transactions on Control Systems Technology* 14(6). 1034–1046.
- Choi, S. B., H. K. Lee** and **E. G. Chang**. 2001. Field test results of a semi-active suspension system associated with skyhook controller. *Mechatronics* 11(3). 345–353.
- Continental, A.** 2016. Acceleration sensor (bsz 04). http://www.continental-automotive.com/www/automotive_de_en/themes/commercial_vehicles/chassis_safety/passive_safety/acceleration_sensor_en.html; accessed: 2016-11-16.
- Do, A.-L., J. M. G. da Silva, O. Sename** and **L. Dugard**. 2011. Control design for LPV systems with input saturation and state constraints: An application to a semi-active suspension. *Proc. of the 50th IEEE Conf. on Decision and Control and European Control Conference (CDC-ECC)*. Atlanta, Georgia, USA. 3416–3421.
- Do, A.-L., C. Poussot-Vassal, O. Sename** and **L. Dugard**. 2013. LPV control approaches in view of comfort improvement of automotive suspensions equipped with mr dampers. *Robust Control and Linear Parameter Varying Approaches*, hg. von O. Sename, P. Gáspár and J. Bokor. *Lecture Notes in Control and Information Sciences*. 437. 183–212. Berlin, Heidelberg: Springer.
- Do, A.-L., O. Sename** and **L. Dugard**. 2010. An LPV control approach for semi-active suspension control with actuator constraints. *Proc. of the American Control Conference (ACC)*. Baltimore, Maryland, USA. 4653–4658.
- Do, A.-L., O. Sename** and **L. Dugard**. 2012. LPV modeling and control of semi-active dampers in automotive systems. *Control of Linear Parameter Varying Systems with Applications*, hg. von J. Mohammadpour and C. W. Scherer. 381–411. Boston, MA: Springer US.

- Do, A.-L., C. Spelta, S. M. Savaresi, O. Sename, L. Dugard and D. Delvecchio.** 2010. An LPV control approach for comfort and suspension travel improvements of semi-active suspension systems. *Proc. of the 49th IEEE Conf. on Decision and Control (CDC)*. Orlando, Florida, USA. 5560–5565.
- Doyle, J. C., K. Glover, P. P. Khargonekar and B. A. Francis.** 1989. State-space solutions to standard H_2 and H_∞ control problems. *IEEE Transactions on Automatic Control* 34(8). 831–847.
- Doyle, J. C., R. S. Smith and D. F. Enns.** 1987. Control of plants with input saturation nonlinearities. *Proc. of the American Control Conference (ACC)*. Minneapolis, Minnesota, United States. 1034–1039.
- Duym, S. R. W., R. Stiens and K. Reybrouck.** 1997. Evaluation of shock absorber models. *Vehicle System Dynamics* 27(2). 109–127.
- Duym, S. W. R.** 2000. Simulation tools, modelling and identification, for an automotive shock absorber in the context of vehicle dynamics. *Vehicle System Dynamics* 33(4). 261–285.
- Fialho, I. J. and G. J. Balas.** 2000. Design of nonlinear controllers for active vehicle suspensions using parameter-varying control synthesis. *Vehicle System Dynamics* 33(5). 351–370.
- Fialho, I. J. and G. J. Balas.** 2002. Road adaptive active suspension design using linear parameter-varying gain-scheduling. *IEEE Transactions on Control Systems Technology* 10(1). 43–54.
- Fischer, D. and R. Isermann.** 2004. Mechatronic semi-active and active vehicle suspensions. *Control Engineering Practice* 12(11). 1353–1367.
- Fleps-Dezasse, M., M. M. Ahmed, J. Brembeck and F. Svaricek.** 2016. Experimental evaluation of linear parameter-varying semi-active suspension control. *Proc. of the IEEE Int. Conf. on Control Applications (CCA)*. Buenos Aires, Argentina. 77–84.
- Fleps-Dezasse, M. and J. Brembeck.** 2013. Model based vertical dynamics estimation with modelica and FMI. *Proc. of the 7th Int. IFAC Symp. on Advances in Automotive Control (AAC)* 341–346.
- Fleps-Dezasse, M. and J. Brembeck.** 2016. LPV control of full-vehicle vertical dynamics using semi-active dampers. *Proc. of the 8th Int. IFAC Symp. on Advances in Automotive Control (AAC)*. Kolmarden, Sweden. 432–439.
- Fleps-Dezasse, M., T. Bunte, F. Svaricek and J. Brembeck.** 2018. Lpv feedforward control of semi-active suspensions for improved roll stability. *Control Engineering Practice* 78. 1–11.

- Fleps-Dezasse, M., F. Svaricek and J. Brembeck.** 2017. Damper fault-tolerant linear parameter-varying semi-active suspension control. *Proc. of the IFAC World Congress (WC)*. Toulouse, France. 8592–8599.
- Fleps-Dezasse, M. and J. Tobolář.** 2015. Identification of a nonlinear full vehicle model for semi-active damper controller synthesis. *Proc. of the 24th Int. Symp. on Dynamics of Vehicles on Roads and Tracks*. Graz, Austria. 711–720.
- Fleps-Dezasse, M., J. Tobolář and J. Pitzer.** 2014. Modelling and parameter identification of a semi-active vehicle damper. *Proc. of the 10th Int. Modelica Conference*. Lund, Sweden. 283–292.
- Gahinet, P. and P. Apkarian.** 1994. A linear matrix inequality approach to H_∞ control. *Int. J. of Robust and Nonlinear Control* 4(4). 421–448.
- Gáspár, P. and Z. Szabó.** 2013. Design of a hierarchical controller for suspension systems. *Robust Control and Linear Parameter Varying Approaches*, hg. von O. Sename, P. Gáspár and J. Bokor. *Lecture Notes in Control and Information Sciences*. 437. 311–328. Berlin, Heidelberg: Springer.
- Giorgetti, N., A. Bemporad, H. E. Tseng and D. Hrovat.** 2006. Hybrid model predictive control application towards optimal semi-active suspension. *Int. J. of Control* 79(5). 521–533.
- Grimm, G., J. Hatfield, I. Postlethwaite, A. R. Teel, M. C. Turner and L. Zaccarian.** 2003. Antiwindup for stable linear systems with input saturation: an lmi-based synthesis. *IEEE Transactions on Automatic Control* 48(9). 1509–1525.
- Guglielmino, E., T. Sireteanu, C. W. Stammers, G. Ghita and M. Giuclea.** 2008. *Semi-active Suspension Control*. 1 Auflage. London: Springer-Verlag.
- Hedrick, J. K. and T. Butsuen.** 1990. Invariant properties of automotive suspensions. *Proc. of the Institution of Mechanical Engineers, Part D: Journal of Automobile Engineering 1989-1996 (vols 203-210)* 204(14). 21–27.
- Heißing, B. and M. Ersoy.** 2011. *Chassis Handbook: Fundamentals, Driving Dynamics, Components, Mechatronics, Perspectives*. ATZ/MTZ-Fachbuch. ATZ/MTZ-Fachbuch. Wiesbaden: Vieweg+Teubner Verlag.
- Hjartarson, A., P. J. Seiler and A. Packard.** 2015. LPVTools: A toolbox for modeling, analysis, and synthesis of parameter varying control systems. *Proc. of the 1st IFAC Workshop on Linear Parameter Varying Systems (LPVS)*. Grenoble, France. 139–145.
- Hjartarson, A., P. J. Seiler, A. Packard and G. J. Balas.** 2013. LPV aeroservoelastic control using the LPVTools toolbox. *Proc. of the AIAA Atmospheric Flight Mechanics (AFM) Conf.*. Boston, MA., USA. 139–145.

- Hoffmann, C.** and **H. Werner.** 2015. A survey of linear parameter-varying control applications validated by experiments or high-fidelity simulations. *IEEE Transactions on Control Systems Technology* 23(2). 416–433.
- Hrovat, D.** 1997. Survey of advanced suspension developments and related optimal control applications. *Automatica* 33(10). 1781–1817.
- Hu, T.** and **Z. Lin.** 2001. *Control Systems with Actuator Saturation*. 1 Auflage. Basel: Birkhäuser.
- Huang, Y.** and **A. Jadbabaie.** 1999. Nonlinear H_∞ control: An enhanced quasi-LPV approach. *Proc. of the IFAC World Congress (WC)*. Beijing, China. 85–90.
- Hughes, H. D.** and **F. Wu.** 2012. LPV h_{∞} control for flexible hypersonic vehicle. *Control of Linear Parameter Varying Systems with Applications*, hg. von J. Mohammadpour and C. W. Scherer. 413–444. Boston, MA: Springer US.
- Isermann, R.** 2005. *Mechatronic Systems*. 1 Auflage. London: Springer-Verlag.
- Isermann, R.** 2006. *Fault-Diagnosis Systems*. 1 Auflage. Berlin Heidelberg: Springer-Verlag.
- ISO 2631-1:1997. *Mechanical vibration and shock – evaluation of human exposure to whole-body vibration – part 1: General requirements*. Standard. International Organization for Standardization.
- ISO 3888-2:2011. *Passenger cars – test track for a severe lane-change manoeuvre – part 2: Obstacle avoidance*. Standard. International Organization for Standardization.
- ISO 8608:1995. *Mechanical vibration – road surface profiles – reporting of measured data*. Standard. International Organization for Standardization.
- Joos, H.-D., J. Bals, G. Looye, K. Schnepfer** and **A. Varga.** 2002. A multiobjective optimisation-based software environment for control systems design. *Proc. of the IEEE Int. Symp. on Computer Aided Control System Design*. Glasgow, Scotland. 7–14.
- Kalman, R. E.** 1963. Mathematical description of linear dynamical systems. *Journal of the Society for Industrial and Applied Mathematics; Series A: Control* 1(2). 152–192.
- Karnopp, D.** 1983. Active damping in road vehicle suspension systems. *Vehicle System Dynamics* 12(6). 291–311.
- Karnopp, D., M. J. Crosby** and **R. A. Harwood.** 1974. Vibration control using semi-active force generators. *Int. J. of Engineering for Industry* 96(2). 619–626.

- Koch, G., O. Fritsch and B. Lohmann.** 2010. Potential of low bandwidth active suspension control with continuously variable damper. *Control Engineering Practice* 18(11). 1251–1262. Special Issue on Automotive Control Applications, 2008 IFAC World Congress.
- Koo, J.-H., M. Ahmadian, M. Setareh and T. Murray.** 2004. In search of suitable control methods for semi-active tuned vibration absorbers. *J. of Vibration and Control* 10(2). 163–174.
- Kortüm, W., M. Valásek, Z. Šika, W. Schwartz, P. Steinbauer and O. Vaculín.** 2002. Semi-active damping in automotive systems: design-by-simulation. *Int. J. of Vehicle Design* 28(1/2/3). 103–120.
- Kuncz, D.** 2007. *Möglichkeiten zum abgleich der prüfstandsdaten mit viertelfahrzeug*. Report. Department of Aerospace Engineering, Group of Control Engineering, University of the Federal Armed Forces Munich.
- Kwakernaak, H.** 1993. Robust control and h_∞ -optimization - tutorial paper. *Automatica* 29(2). 255–273.
- Kwakernaak, H. and R. Sivan.** 1972. *Linear Optimal Control Systems*. Interscience. Interscience. New York: Wiley.
- Lu, J. and M. DePoyster.** 2002. Multiobjective optimal suspension control to achieve integrated ride and handling performance. *IEEE Transactions on Control Systems Technology* 10(6). 807–821.
- Lunze, J. and J. H. Richter.** 2008. Reconfigurable fault-tolerant control: A tutorial introduction. *European Journal of Control* 14(5). 359–386.
- Margolls, D. L.** 1982. The response of active and semi-active suspensions to realistic feedback signals. *Vehicle System Dynamics* 11(5-6). 267–282.
- Mitschke, M. and H. Wallentowitz.** 2004. *Dynamik der Kraftfahrzeuge*. VDI-Buch. VDI-Buch. 4 Auflage. Heidelberg: Springer-Verlag.
- Mohammadpour, J. and C. W. Scherer.** 2012. *Control of Linear Parameter Varying Systems with Applications*. 1 Auflage. New York: Springer US.
- Nedachi, Y., J. Ishikawa and H. Yoshino.** 2016. Suspension control device of vehicle. Japanese Patent Application No. JP20150055850, 19.03.2015.
- Nguyen, M. Q., J. M. G. da Silva, O. Sename and L. Dugard.** 2015a. Semi-active suspension control problem: Some new results using an LPV h_∞ state feedback input constrained control. *Proc. of the 54th IEEE Conf. on Decision and Control (CDC)*. Osaka, Japan. 863–868.

- Nguyen, M. Q., J. M. G. da Silva, O. Sename and L. Dugard. 2015b. A state feedback input constrained control design for a 4-semi-active damper suspension system: a quasi-LPV approach. *Proc. of the 8th IFAC Symp. on Robust Control Design (ROCOND)*. Bratislava, Slovakia. 259–264.
- Otter, M. 2013. *Multi-domain Modeling and Simulation*. Springer. London. 1–14.
- Poussot-Vassal, C., S. M. Savaresi, C. Spelta, O. Sename and L. Dugard. 2010. A methodology for optimal semi-active suspension systems performance evaluation. *Proc. of the 49th IEEE Conf. on Decision and Control (CDC)*. Orlando, Florida, USA. 2892–2897.
- Poussot-Vassal, C., O. Sename, L. Dugard, P. Gáspár, Z. Szabó and J. Bokor. 2008. A new semi-active suspension control strategy through LPV technique. *Control Engineering Practice* 16(12). 1519–1534.
- Poussot-Vassal, C., C. Spelta, O. Sename, S. M. Savaresi and L. Dugard. 2012. Survey and performance evaluation on some automotive semi-active suspension control methods: A comparative study on a single-corner model. *Annual Reviews in Control* 36(1). 148–160.
- Prempain, E. and I. Postlethwaite. 2000. A new two-degree-of-freedom gain scheduling method applied to the lynx mk7. *Proc. of the Institution of Mechanical Engineers, Part I: Journal of Systems and Control Engineering* 214(4). 299–311.
- Prempain, E. and I. Postlethwaite. 2001. Feedforward control: a full-information approach. *Automatica* 37(1). 17–28.
- Rajamani, R. 2012. *Vehicle Dynamics and Control*. 2 Auflage. Boston, MA: Springer US.
- Rill, G. 2012. *Road vehicle dynamics: Fundamentals and modeling*. Ground vehicle engineering series. Boca Raton, FL: CRC Press.
- Sammier, D., O. Sename and L. Dugard. 2003. Skyhook and h_∞ control of semi-active suspensions: Some practical aspects. *Vehicle System Dynamics* 39(4). 279–308.
- Sankaranarayanan, V., M. E. Emekli, B. A. Gilvenc, L. Guvenc, E. S. Ozturk, E. S. Ersolmaz, I. E. Eyol and M. Sinal. 2008. Semiactive suspension control of a light commercial vehicle. *IEEE/ASME Transactions on Mechatronics* 13(5). 598–604.
- Satzger, C., R. de Castro and A. Knoblach. 2017. Robust linear parameter varying model predictive control and its application to wheel slip control. *Proc. of the IFAC World Congress (WC)*. Toulouse, France. 1514–1520.
- Saupe, F. 2013. *Linear parameter varying control design for industrial manipulators*. Dissertation. Technical University Hamburg-Harburg. Düsseldorf.

- Saupe, F.** and **H. Pfifer**. 2011. Applied LPV control exploiting the separation principle for the single axis positioning of an industrial manipulator. *Proc. of the IEEE Int. Conf. on Control Applications (CCA)*. Denver, CO, USA. 1476–1481.
- Savaresi, S. M., S. Bittanti** and **M. Montiglio**. 2005. Identification of semi-physical and black-box non-linear models: the case of mr-dampers for vehicles control. *Automatica* 41(1). 113–127.
- Savaresi, S. M., C. Poussot-Vassal, L. Dugard, O. Sename** and **C. Spelta**. 2010. *Semi-Active Suspension Control Design for Vehicles*. 1 Auflage. Oxford: Elsevier.
- Savaresi, S. M.** and **C. Spelta**. 2007. Mixed sky-hook and add: Approaching the filtering limits of a semi-active suspension. *J. of Dynamic Systems, Measurement, and Control* 129(4). 382–392.
- Schramm, D., M. Hiller** and **R. Bardini**. 2014. *Vehicle Dynamics: Modeling and Simulation*. 1 Auflage. Heidelberg: Springer-Verlag.
- Sefton, J.** and **K. Glover**. 1990. Pole/zero cancellations in the general h_∞ problem with reference to a two block design. *Systems & Control Letters* 14(4). 295–306.
- Sename, O., P. Gáspár** and **J. Bokor**. 2013. *Robust Control and Linear Parameter Varying Approaches: Application to Vehicle Dynamics*. 1 Auflage. Berlin, Heidelberg: Springer.
- Sename, O., J. C. Tudón-Martínez** and **S. Fergani**. 2013. LPV methods for fault-tolerant vehicle dynamic control. *Proc. of the IEEE Conference on Control and Fault-Tolerant Systems (SysTol)*. Nice, France. 631–636.
- Shamma, J. S.** 1988. *Analysis and design of gain scheduled control systems*. Dissertation. Massachusetts Institute of Technology, Dept. of Mechanical Engineering. Cambridge.
- Shamma, J. S.** and **M. Athans**. 1991. Guaranteed properties of gain scheduled control for linear parameter-varying plants. *Automatica* 27(3). 559–564.
- Skogestad, S.** and **I. Postlethwaite**. 2005. *Multivariable Feedback Control: Analysis and Design*. 2 Auflage. Chichester: Wiley-Blackwell.
- Smith, M. C.** and **F.-C. Wang**. 2002. Controller parameterization for disturbance response decoupling: application to vehicle active suspension control. *IEEE Transactions on Control Systems Technology* 10(3). 393–407.
- Spelta, C., S. M. Savaresi** and **L. Fabbri**. 2010. Experimental analysis of a motorcycle semi-active rear suspension. *Control Engineering Practice* 18(11). 1239–1250. Special Issue on Automotive Control Applications, 2008 IFAC World Congress.

- Spencer, B. J., S. Dyke, M. Sain and J. Carlson.** 1997. Phenomenological model for magnetorheological dampers. *Journal of Engineering Mechanics* 123(3). 230–238.
- Theis, J., H. Pfifer, A. Knoblach, F. Saupe and H. Werner.** 2015. Linear parameter-varying feedforward control: A missile autopilot design. *Proc. of the AIAA Conf. on Guidance, Navigation, and Control*. Kissimmee, Florida. 1–9.
- Tseng, H. E. and D. Hrovat.** 2015. State of the art survey: active and semi-active suspension control. *Vehicle System Dynamics* 53(7). 1034–1062.
- Tudón-Martinez, J. C., S. Varrier, O. Sename, R. Morales-Menendez, J.-J. Martinez and L. Dugard.** 2013. Fault tolerant strategy for semi-active suspension with LPV accommodation. *Proc. of the IEEE Conference on Control and Fault-Tolerant Systems (SysTol)*. Nice, France. 116–130.
- Unger, A.** 2017. Method for operating a wheel suspension system. US Patent Application No. US201515317343, 05.06.2015.
- Unger, A., F. Schimmack, B. Lohmann and R. Schwarz.** 2013. Application of LQ-based semi-active suspension control in a vehicle. *Control Engineering Practice* 21(12). 1841–1850.
- Unger, A. F.** 2012. *Serientaugliche quadratisch optimale Regelung für semiaktive Pkw-Fahrwerke*. Dissertation. Technical University Munich. Göttingen.
- Valášek, M., W. Kortüm, Z. Šika, L. Magdolen and O. Vaculín.** 1998. Development of semi-active road-friendly truck suspensions. *Control Engineering Practice* 6(6). 735–744.
- Valášek, M., M. Novák, Z. Šika and O. Vaculín.** 1997. Extended ground-hook - new concept of semi-active control of truck's suspension. *Vehicle System Dynamics* 27(5-6). 289–303.
- Venhovens, P. J. T.** 1994. *Optimal Control of Vehicle Suspensions*. Dissertation. Delft University of Technology, Faculty of Mechanical Engineering and Marine Technology. Delft.
- Weist, U., J. Missel, S. Cytrynski, D. Mehren, T. Schwarz and S. Kern.** 2013. Fahrkomfort der extraklasse. *ATZextra* 18(5). 124–128.
- Williams, D. E. and W. M. Haddad.** 1995. Nonlinear control of roll moment distribution to influence vehicle yaw characteristics. *IEEE Transactions on Control Systems Technology* 3(1). 110–116.
- Williams, D. E. and W. M. Haddad.** 1997. Active suspension control to improve vehicle ride and handling. *Vehicle System Dynamics* 28(1). 1–24.

- Wu, F.** 1995. *Control of Linear Parameter Varying Systems*. Dissertation. Engineering-Mechanical Engineering. Berkeley.
- Wu, F., K. M. Grigoriadis and A. Packard.** 2000. Anti-windup controller design using linear parameter-varying control methods. *Int. J. of Control* 73(12). 1104–1114.
- Wu, F., X. H. Yang, A. Packard and G. Becker.** 1996. Induced L_2 -norm control for LPV systems with bounded parameter variation rates. *Int. J. of Robust and Nonlinear Control* 6(9-10). 983–998.
- Yi, K. and B. S. Song.** 1999. A new adaptive sky-hook control of vehicle semi-active suspensions. *Proc. of the Institution of Mechanical Engineers, Part D: Journal of Automobile Engineering* 213(3). 293–303.
- Zaccarian, L.** 2009. Dynamic allocation for input redundant control systems. *Automatica* 45(6). 1431–1438.
- Zhang, Y. and J. Jiang.** 2008. Bibliographical review on reconfigurable fault-tolerant control systems. *Annual Reviews in Control* 32(2). 229–252.
- Zhou, K., J. C. Doyle and K. Glover.** 1996. *Robust and Optimal Control*. Upper Saddle River, N.J.: Prentice Hall.